Consejo Superior de Investigaciones Científicas (CSIC)
Institut de Ciències de la Terra "Jaume Almera"
Departament d'Estructura i Dinàmica de la Terra

Universitat de Barcelona
Departament de Geodinàmica i Geofísica
Programa de doctorat Ciències de la Terra. Bienni 2002-2004

DEVELOPMENT OF NUMERICAL METHODS TO DETERMINE THE LITHOSPHERIC STRUCTURE COMBINING GEOPOTENTIAL, LITHOSTATIC AND HEAT TRANSPORT EQUATIONS. APPLICATION TO THE GIBRALTAR ARC SYSTEM

Memoria presentada por Javier Fullea Urchulutegui para optar al grado de Doctor

Directores:

Manel Fernàndez Ortiga

Hermann Zeyen

Tutor:

Francesc Sàbat Montserrat

Barcelona, Diciembre 2007

Agradecimientos

Este trabajo no habría sido posible sin la ayuda inestimable de mis directores de tesis: Manel Fernàndez y Hermann Zeyen. A Manel le agradezco la paciencia y el tiempo dedicados a ejercer su magisterio sobre este humilde aprendiz, iniciándole así en los modos y maneras de esta artesanía moderna que es la labor científica. A Hermann, que me acogió amablemente durante dos estancias veraniegas en el *Departement de Sciences de la Terre, Paris-Sud*, le debo toda la parte técnica de la tesis e innúmeras horas de dedicación.

Quisiera agradecer a mi antigua profesora de la UCM, Ana Negredo, el haberme introducido en el ambiente científico a través de un estimulante trabajo de investigación de final de carrera, y a Jaume Vergés sus valiosos comentarios geológicos.

Agradezco al Ministerio de Educación y Ciencia la financiación de esta tesis a través de una beca FPU, y al Institut de Cienciès de la Terra Jaume Almera, perteneciente al CSIC, el haberme proporcionado todos los medios materiales para la consecución de la misma.

Esta tesis debe mucho al software libre, *sensu lato*. Es decir, tanto a aquellos que generosamente ponen su código a disposición de la comunidad de usuarios para que éstos lo hagan evolucionar, como a aquellos que utilizan la libre disponibilidad de los programas como eficaz banco de pruebas para ulteriores desarrollos comerciales. Por tanto, mi gratitud para con Linux, los autores de Generic Mapping Tools (GMT) e Intel (Compilador Fortran 90 para Linux).

Agradezco a los compañeros, pasados y presentes, del Jaume Almera el haberme hecho grata la estancia en la ciudad condal. Mención especial merece mi buen amigo y camarada Mario, excelente y eximio individuo con el que tantas horas he pasado charlando, dentro y fuera del trabajo, y que tantos ratos me ha ofrecido su buen corazón, seguro cabo con el que aferrarme a la *joliè de la vie*, mientras las tempestades de la tristeza azotaban mi alma. Y las horas que has echado para enseñarme Linux y GMT no se las salta un romaní. Un especial recuerdo también para mi compañera de despacho, Leire, a quien considero como una hermana mayor, y cuya tesis y la mía, fatalmente unidas temática y espacio-temporalmente, parecen haber superado la maldición del depatx 250. Te agradezco haberme enseñado la palabra *zirrikitu* y las lecciones improvisadas de geología. Al Dr. Yeisi (JC A(l)fonso, te regalo la l que siempre me robas del apellido) le agradezco el haberme descubierto las excelencias de la buena cerveza, y el haberme inoculado la fiebre ochentera. Otrosí su dilatado *background* geofísico y petrológico, que tan útil me ha resultado. El hierático Dr. Arrow (Isaac) también me ha servido de seguro maestro en el manejo del ordenador, y le quiero agradecer su estilismo funcional-revolucionario, su lucidez en el análisis del mundo científico, y su palillo. Al Dr. Zlotnik, porteño quijotesco, le quiero agradecer su efusividad en las noches de mala vida y su asesoramiento, profesional, en materia de programación. Al chaba banyolí, pero netamente internacional, Gaspà Dos Veces Toro, le agradezco su animosidad fiestera y su chulería castiza, rara vez enturbiadas. Al Dr. Saura, melena *par excellence* del Gironès, le agradezco el ser co-lector de un libro irlandés maldito por lo denso, su exquisita educación, y su asesoramiento técnico, que tantas veces me ayudó a desfacer el nudo Wordiano. A David, fotolog master, le agradezco la parada y fonda generosamente ofrecidas, así como la oportunidad de ver en directo a una ilustre pareja de aborígenes rockeros e irreverentes. A las amazonas de la ciencia ipalomer y bgaite, les agradezco el mal genio (pero buen corazón y excelente disposición como proveedora de *papers* de las antípodas), y el haberme brindado la posibilidad de leer al

jalisciense más internacional editado en sus propios pagos, respectivamente. Al "jodido" Dr. Emami le agradezco las conversaciones sobre Zoroastro, y a Stephàne su discreción y *savoir faire*. A la tétrada consagrada, y futuro de la Geofísica ibérica, Ivone, Daniel GC, Marta y Antonio, les agradezco su buen hacer y el ejemplo de que, al final y con la precariedad como bandera, los buenos ganan: sois unos científicos de cajales. A la vieja guardia del Almera de los tiempos heroicos (Manu, Charlie, Ignacio, Rafa, Valen, Jose etc.) le agradezco el haber generado una mitología becaria homérica, que nos ha permitido tocar el material de los sueños a los amanuenses de esta época gris y medievalizante. Un recuerdo también para los compañeros más recientes: Lluís, Anne, Emilio, Caroline, Naiara, Jordi etc.

A mis amigos de Madrid, camaradas desde los tiempos universitarios, les debo infinitas horas de diversión y apoyo, y muchas cosas más, difíciles de expresar por escrito. Sencillamente, os quiero, y me gustaría que mi vida siguiera formando parte de la vuestra, aunque medien miles de km (no me lo toméis en cuenta, la edad me está volviendo asquerosamente sentimental). Al proto doctor Rísquez, ingenio de Moratalaz y fénix de las Ecuaciones de Maxwell, le agradezco la camaradería política (¡¡son 13 años de sintonía y evolución conjunta!!), su bondad extremada y desbordante, así como los buenos ratos que hemos pasado pergeñando ecuaciones y modelos disparatados en los lugares más inverosímiles. Al hombre-móvil Álvaro Ruano, cruzado ocasional y subscriptor honorario del Marca, Ché de las hamburguesas, le agradezco el que se pase la vida intentando parecer un malvado cínico e insensible para disimular ese buen corazón que tantas veces le ha perdido. Hemos hecho prácticas "a rajatabla", virguerías con el Fifa y, aunque me has hecho conocer el frío suelo de Toledo para no deshacer una cama, conozco pocas personas más generosas que tú (y, además, me ofreciste el mejor consejo sentimental de mi vida). ¿Qué decir de mi pequeño amigo Jose, probablemente el mayor experto mundial en Álgebra vivo, titán memorioso, madridista honrado y fervoroso, prodigio del recorte verbal castizo e ingenioso? Conocimos juntos la vaselina abellanística por un error de aula en aquel otoño iniciático del 95 (¡¡primera persona que conocí en la carrera!!). A Juanma, Lord Prosper, otrora hombre-H, le agradezco su locuacidad radiofónica, las muchas horas de buena conversación de madrugada en el Ford Fiesta, y el haberme presentado al inefable Segovia de Huete. Al forestal Abraham, topógrafo de la meseta, le agradezco haberme dejado formar parte de los tiempos etílicos en que se forjó su leyenda de copar-field a golpe de Negrita, y el haberme dado la oportunidad de conducir, por una vez en mi vida, un BMW. El filósofo melómano y socrático David, Miles Davis de San Blas, me introdujo en el mundo de la Filmoteca y el billar, así como en Materialismo Filosófico bueniano; le agradezco el haberse comido de cabo a rabo un bocadillo de barra entera en mi casa (pero, para qué lo vas a cortar, no le hagas daño al pan…) y su gerontofilia reciente. Al ingeniero Marqueta, avezado ciclista y acreedor del prestigioso "cero remarcado" de Gascón en Mecánica I, le agradezco haberme enseñado como se come de verdad la carne con las manos y el arte del lanzamiento de croquetas en una épica jornada en el barrio de Oporto. Mi buen Dimas de Corral, *top ten* de Física, eterno estudiante, cristo dos pistolas de las residencias universitarias, quiero agradecerte la oportunidad que me diste de conocer un viñedo, tu inocencia rural y tu atletismo irredento. Finalmente a Johonny y Juanito les agradezco el haber abierto recientemente embajada en Ucrania.

Agradezco a mis padres su apoyo incondicional e incesante durante todos estos años, su paciencia infinita, su cariño, y su bondad desinteresada. Siempre habéis sido puerto donde recalar en tiempos difíciles. Y siempre lo seréis. Mi afecto especial para los dos canes de mi vida que guardaron y guardan el sueño y la alegría de mis progenitores: Crom, noble teutón de morro chato y electrizante, y Pip, bretón montaraz.

Alicia, *ma ringa, ma sha*. En el invierno de mi corazón, arrasado por la soledad, el hastío y la indiferencia, brotaste como una extraña y fragante flor, la más hermosa, la más inesperada del jardín de las almas; despertaste mi interés por la vida y los asuntos de los hombres; no me pesaron los trabajos del cortejo, oíslo cimarrón, pues mis pies bailan ligeros elevados sobre la tierra, nunca tan amable, nunca tan feraz. Corona y cetro, cetro y corona, excuso decir que este trabajo es tan tuyo como mío, pues tú eres yo, y yo soy tú, sustancia imponderable, sutilísima, eterna.

Por último, y en un acto de inmodestia audaz e inusitada, quiero agradecerme esta tesis a mí mismo. Por haber tenido paciencia y soportado mis incesantes desfallecimientos y escarceos varios, pues es dilatado y vasto el campo de las distracciones que amenaza el alma de los jóvenes doctorandos. No ha sido fácil enderezar, durante todos estos años, la voluntad a un fin único y, como si de una larga marcha se tratase, hemos tenido que comer suela de alpargata y sacrificar a algunos hombres (otros yo, sombras del pasado), *ad majorem scientia gloriam*, se entiende.

TABLE OF CONTENTS

Chapter 1

INTRODUCTION

1. INTRODUCTION

1.1 PREVIOUS WORK

1.1.1 Geophysical modelling

Detailed modelling of the present-day lithospheric structure is of paramount importance to understand the evolution of the Earth in the context of plate tectonics. The lithosphere is composed of crust and upper mantle. The crustal layer can be constrained by field measurements and boreholes, which provide direct observations of the uppermost crust, while seismic techniques offer reliable data at greater depths, up to the crust-mantle boundary. Unfortunately, the lithospheric mantle is more scarcely known and little direct data are available. Numerical modelling using the information provided by geophysical observables such as elevation, gravity and geoid anomalies, and surface heat flow (SHF), is straightforward and is a relatively low cost procedure to improve our knowledge of the lithospheric mantle, which can complement other indirect techniques like seismic tomography.

Forward lithospheric modelling of the present day crustal and lithospheric structure has been the subject of several works, and a number of numerical codes are available. Zeyen and Fernàndez (1994) presented a 2D algorithm to determine the steady state thermal structure of the lithosphere integrating thermal, gravity and local isostasy analyses. Later works integrated also the geoid anomaly in the algorithm to obtain a better constrain of the deep lithospheric structure (Torne et al. 1995; Fernàndez et al., 2004). However, the 2D approach is only suitable when lithospheric variations across the profile are small in comparison to variations along the profile. Other works provide a full 3D frame to model the lithospheric structure using different data sets. 3GRAINS is a program that allows 3D interactive modelling of the lithosphere's density structure using gravity anomalies (Snopek and Casten, 2005). IGMAS is a 3D tool for the interpretation of geoid, gravity and magnetic data that uses a polyhedron approach to model the lithospheric structure (e.g. Götze and Lahmeyer, 1988; Schmidt and Götze, 1999). However, the aforementioned 3D modelling tools do not include the temperature distribution, which is a key parameter to model the lithospheric mantle density (e.g. Parsons and Sclater, 1977; Schubert et al., 2001; Afonso et al., 2005).

1.1.2 Study area: the Gibraltar Arc System region

Traditionally, the Gibraltar Arc System region (GAS) has been considered as a zone comprising the Alboran Basin, the Betic and Rif orogens and the Gulf of Cadiz. However, in this thesis, we consider that the adjacent Atlas Mountains could play an important role in the geodynamic evolution of the area. Therefore, and in the scope of this thesis, we will consider that the Alboran Basin, the Betic and Rif orogens, the Gulf of Cadiz, the Guadalquivir and Rharb foreland basins, and the Atlas Mountains compose the GAS region.

The GAS region has been the subject of several studies: seismic reflection/refraction profiles (e.g. Banda et al., 1993; Comas et al., 1997; Simancas et al., 2003), seismic tomography (e.g.; Blanco and Spakman, 1993; Bijwaard et al., 1998; Calvert et al., 2000; Marone et al., 2004), gravity modelling (e.g. Torne et al., 2000; Gràcia et al., 2003) and heat flow (Polyak et al., 1996; Fernàndez et al., 1998b; Rimi et al., 1998). These studies show a thin crust and lithosphere under the easternmost part of the Alboran Basin, with a steep thickening towards the Betic and Rif arcuate thrust belt (Torne et al., 2000). Recent integrated lithospheric models along 2D profiles indicate a rather flat lithosphere-asthenosphere boundary in the SW Iberian margin (Fernàndez et al., 2004) and a pronounced lithospheric thickening beneath the Gulf of Cadiz (Zeyen et al., 2005). The crustal root beneath the Atlas Mountains (e.g. Makris et al., 1985; Wigger et al., 1992) is not thick enough to isostatically support the high topography and a thin, hot, lower density lithosphere is invoked in order to achieve full isostatical compensation (Seber et al., 2001; Teixell et al., 2003; Frizon de Lamotte et al., 2004; Teixell et al., 2005; Zeyen et al., 2005).

Seismic tomography studies depict a positive P-wave velocity anomaly from about 200 km to 700 km depth beneath the Gibraltar Arc, the Betics, the Rif, and the Alboran Basin (Blanco and Spakman, 1993; Bijwaard and Spakman, 2000; Calvert et al., 2000; Spakman and Wortel, 2004). Furthermore, a low velocity anomaly situated between about 40 and 100 km depth is observed by some authors beneath the Atlas and the Alboran Basin (Blanco and Spakman, 1991; Seber et al., 1996b; Calvert et al, 2000; Gurría and Mezcua et al., 2000). However, the resolution of the seismic tomography models is low in the Gulf of Cadiz and the North African margin owing to the sparse ray-path coverage and the poor seismic station coverage.

1.2 OBJECTIVES

The objectives of this thesis are twofold: the development of numerical methods to determine the lithospheric structure combining geopotential, lithostatic and heat transport equations, and the application of these methods to the study area, the Gibraltar Arc System region. The final product should be a useful 3D tool to analyse the lithosphere integrating, in a consistent manner, the thermal field, elevation, geoid and gravity anomalies, and SHF. In this sense, four main goals are:

1) Development of a numerical code to compute Bouguer anomalies from publicly available satellite-derived free air data in both continental and marine areas.

2) Development of a 1D method to calculate a first order lithospheric structure using elevation and geoid anomaly as input data.

3) Development of a 3D interactive code to perform lithospheric forward modelling, integrating SHF, gravity and geoid anomalies, and elevation.

4) Obtain a 3D image of the lithosphere geometry over the study region independent from seismic tomography in order to improve our knowledge of the deep, present day, lithospheric structure of the GAS region, and discuss the different geodynamic models proposed to explain its origin.

1.3 STRUCTURE OF THE THESIS

Chapter 2 provides a brief review of the theoretical concepts related to the contents of the thesis: the Earth's crust and lithosphere, the gravitational field, the thermal field and isostasy.

Chapter 3 introduces the study area, the Gibraltar Arc System, from a geological and geophysical point of view. Main structural aspects are depicted in the geological setting. Elevation, free air anomaly and geoid anomaly maps of the area are analysed and, FA2BOUG, a computer code to calculate Bouguer anomaly in both land and marine areas using satellite-derived free air data as input, is presented. The program is applied, together with available measured land data, to produce a complete Bouguer anomaly map of the GAS region.

Chapter 4 deals with a method based on the combination of elevation and geoid anomaly data that allows for a rapid calculation of the crustal and lithospheric thickness over large regions under the assumption of local isostasy, thermal steady state, linear vertical density gradient for the crust, and temperature dependent mantle density. The resulting lithospheric model serves as starting point for the 3D model developed in the following chapters.

Chapter 5 presents GEO3Dmod, a computer program intended to perform interactive 3D lithospheric forward modelling, integrating SHF, elevation, gravity anomaly and geoid anomaly. The program consists of two modules. The first one (GEO3Dmod) resolves the direct problem, i.e. given a lithospheric model (a set of layers with different properties), it calculates the 3D thermal and density structure of the lithosphere and the associated geophysical observables. The second one (GEO3Dmod_INTF) is a graphical interface designed to visualize and modify the lithospheric structure according to the differences between calculated and measured geophysical observables.

GEO3Dmod is applied in Chapter 6 to the GAS region in order to obtain a 3D lithospheric regional model of the study area integrating gravity, geoid anomaly, elevation and SHF. The results obtained are discussed in the context of the different geodynamic models proposed to explain the origin and evolution of the GAS region.

Chapter 7 summarizes the main conclusions from the previous chapters and outline the possible future work.

This PhD thesis is a contribution of the Group of Dynamic of the Lithosphere (GDL), and has been supported by a FPU grant from the Spanish Ministerio de Educación y Ciencia within the projects MARSIBAL-II (REN2001-3868-C03-02/MAR), WESTMED (REN2002-11230-E-MAR), SAGAS (CTM2005-08071-C03-03/MAR), and ESF-EuroMARGINS (01-LEC-EMA 22F). In the context of this thesis, three papers have been written in collaboration with other authors. Two of them have been published in C. R. Geosciences (Fullea et al., 2006), and Tectonophysics (Fullea et al., 2007), and correspond to the contents of Chapter 4. The third one is under revision in Computer and Geosciences and is developed in Chapter 3: **Fullea, J**., Fernàndez, M., Zeyen, H. (2007). *"FA2BOUG-a FORTRAN 90 code to compute Bouguer gravity anomalies from gridded free air anomalies: application to the Atlantic-Mediterranean transition zone***".**

Chapter 2

FUNDAMENTALS

2. FUNDAMENTALS

In this thesis we integrate the following geophysical observables to model the lithospheric structure: elevation, gravity anomalies (free air and Bouguer), geoid anomaly, and surface heat flow (SHF). The idea is to take advantage of the fact that elevation, gravity anomaly and geoid anomaly depend on density distribution with different distance dependence. Elevation reflects the average density of the lithospheric column under the assumption of local isostasy. Gravity anomalies depend on the inverse of the square of the distance to mass anomalies, whereas geoid anomalies diminish only inversely proportional to the distance. Hence, gravity anomalies are particularly sensitive to mass changes at crustal levels while geoid anomaly is influenced by lateral density variations in a wider range of depths. SHF data, in spite of their significant lateral short wavelength variability due to near surface effects (ground water flow, climate, and sedimentation/erosion), and scarce geographical distribution, constitute another parameter to control the temperature distribution within the lithosphere depending on its thickness and the distribution of heat-producing elements.

2.1 GENERAL DEFINITIONS: EARTH'S CRUST AND LITHOSPHERE

The crust is the outermost and less dense layer of the Earth and is characterized by rocks with P-wave seismic velocities lower than 7.6 km/s, and, for the most part, densities lower than 3100 kg m^{-3}. It consists mostly of sediments, gneisses, granite, granodiorite, gabbro, amphibolite, granulite and volcanic material for the continental crust, and of sediments, basalts, gabbros and some serpentinites for the oceanic crust. From a mineralogical point of view the oxides of the three elements silicon, aluminium, and calcium dominate in the crust. The continental crust is usually divided into two layers: an upper crust with P-wave seismic velocities 4.5-6.4 km/s and densities 2670-2810 kg m^{-3}, and a lower crust ranging from 6-7.5 km/s and 2850-2950 kg m^{-3}. The oceanic crust is composed by a grabbroic layer with typical velocities of 6.6-7.2 km/s, overlain by basaltic pillow lavas and sheeted dykes with an average velocity of 4.5 km/s. A low velocity sedimentary layer is usually present in the crust showing a wide variety of density values (2000-2600 kg m^{-3}).

The lithosphere is the long-term rigid outer layer of the Earth and the fundamental unit of plate tectonics. It comprises the crust and a portion of the uppermost mantle. There is no unique way of defining the lithosphere: it is a

seismic, thermal, mechanical, and chemical boundary layer, according to the different possible geophysical and petroligical properties under study. From a seismological point of view, the lithosphere is defined as the high velocity material that overlies the upper mantle Low Velocity Zone. This definition is more suitable for oceanic rather than continental areas (Anderson, 1989; Carlson et al., 2005). Thermally, the lithosphere is the part of the uppermost mantle in which the heat transfer by conduction predominates over convective processes. Its base is commonly defined as a particular isotherm (usually 1300-1350 ºC) determined by the intersection between a conductive geotherm and a mantle adiabat (Schubert et al., 2001). In this sense, the asthenosphere would be the layer beneath the lithosphere in which heat transfer is due mainly to convection, implying a more ductile behaviour than the lithosphere. The mechanical lithosphere can be defined as a layer not affected by the convection beneath it, in geological time scales. According to the elastic properties, the lithosphere can be defined as an elastic plate able to support stresses higher than 5 MPa resting on an inviscid or viscous fluid. From a geochemical point of view the lithosphere-asthenosphere boundary (LAB) would be the maximum depth at which low-Y (<10 ppm) garnets are derived (Griffin et al., 1999). This definition coincides pretty well with the thermal definition.

In this thesis, and for modelling purposes, we have adopted the thermal definition of the lithosphere according to global studies explaining the bathymetry and subsidence of the oceanic floor (Parsons and Sclater, 1977). Therefore, increasing temperature results in decreasing density of the lithospheric mantle through the following relationship:

$$\rho_m(z) = \rho_a\left(1 + \alpha\left[T_a - T_m(z)\right]\right) \qquad (2.1)$$

where ρ_a is the density of the asthenosphere considered to be constant everywhere (3200 kg m^{-3}), α is the thermal expansion coefficient (K^{-1}), T_a is the temperature at the LAB and $T_m(z)$ is the temperature at depth z in the lithospheric mantle.

Although this approach has been successful in describing the first order thermal structure of different lithospheric mantle domains (i.e. oceanic and continental), it neglects compressibility and compositional effects. Since the relevant geophysical fields used in this thesis are only dependent on density contrasts, but not on absolute values, compressibility is a second-order effect (i.e. lateral pressure gradients are small). On the other hand, compositional changes within the lithospheric mantle can result in significant variations of its thermophysical properties. Therefore, the present assumption is valid only when

the chemical structure of the lithospheric mantle does not vary significantly through the modelled region.

2.2 GRAVITATIONAL FIELD

The Earth's gravitational field gives us information about the lateral density variations within the planet. Thus, although less precise than other geophysical data, it provides valuable indirect knowledge of the mass distribution at depths in which other, more accurate, geophysical methods are blind (i.e. seismics or soundings).

As a good approximation, the Earth can be described by an equipotential revolution ellipsoid. The gravitational field produced by this reference ellipsoid is called the normal or theoretical field. The real equipotential surface of the Earth coincident with the average level of the oceans is called the geoid. The gravity potential of the Earth can be adequately described using a global geopotential model, i.e. a spherical harmonic expansion, to degree and order N, plus a centrifugal term:

$$W(r,\phi,\lambda) = \frac{GM_T}{r}\left(\sum_{n=2}^{N}\left(\frac{a}{r}\right)^n \sum_{m=0}^{n}\left[\overline{C_{nm}}\cos(m\lambda) + \overline{S_{nm}}\sin(m\lambda)\right]\overline{P_{nm}}(\sin\phi)\right) \quad +$$

$$\frac{1}{2}\omega^2\left(x^2 + y^2\right) \qquad (2.2)$$

where G is the universal gravitational constant ($6.67*10^{-11}$ m^3 s^{-2} kg^{-1}), M_T the mass of the Earth, r, φ, λ, x and y the geocentrical coordinates of the observation point, $\overline{C_{nm}}$, $\overline{S_{nm}}$ a set of fully normalized coefficients, $\overline{P_{nm}}$ the fully normalized associated Legendre functions, and ω is the angular rotation velocity of the Earth. In this thesis, we have used the EGM96 geopotential model extended to degree and order 360 and referred to the WGS 84 Ellipsoid (Lemoine et al., 1998). A more recent model, GGM02, has been released from the Gravity Recovery and Climate Experiment (GRACE), but at regional scale differences are almost negligible (Tapley et al., 2005).

The gravity potential of the Earth, W, can be decomposed into two parts:

$$W = U + T \qquad (2.3)$$

where U is the normal or theoretical potential associated with the reference ellipsoid, and T is an anomalous potential. The partition of the Earth's gravity field into a normal and an anomalous part, simplifies the problem of its

determination: the ellipsoidal field is easier to handle from a mathematical point of view, and the deviations of the ellipsoidal field with respect to real field are so small that they can be considered linear (at a first order). Both, the gravity (free air and Bouguer) and the geoid anomalies, are referred to the normal field produced by the reference ellipsoid.

2.2.1 Gravity anomaly

The gravity anomaly (Δg) is the difference between the measured gravity over or reduced to the geoid, g, and the normal (theoretical) gravity in a point over the reference ellipsoid (projection of the measure point along a normal to the ellipsoid), γ. Both, the measured and the normal gravity, can be derived from the Earth and ellipsoidal potentials:

$$\begin{aligned} g &= \nabla W \\ \gamma &= \nabla U \end{aligned} \tag{2.4}$$

Due to its dependence on the square of the distance, gravity anomaly is mainly sensitive to lateral density variations at crustal depths. Directly observed gravity data contain the effects of latitude, Earth tides, instrumental drift, distance from the reference ellipsoid and masses between the actual topography and the reference ellipsoid. In order to obtain anomalies comparable over large areas, different corrections are applied: Earth tides, instrumental drift, latitude, free air and topography. When the first four corrections are applied to measured gravity data, we obtain the free air gravity anomaly (Δg_{FA}), which at short wavelengths correlates strongly with topography. The end-product of all gravity corrections is the Bouguer anomaly (Δg_B), which should correlate mainly with lateral variations of the density and thickness of the crust. Hence, Bouguer anomaly is obtained applying the correction for the gravitational attraction of topography to the free air anomaly. The primary objective of the complete Bouguer correction is to remove all non-geological components of the gravity anomalies enhancing subsurface mass variations.

The free air correction takes into account whether the measuring point is above or below the reference ellipsoid, considering the vertical gravity gradient. Strictly, free air correction must be done using the distance between the Earth's surface and the reference ellipsoid (ellipsoidal height). However, in general and for practical reasons, free air anomaly correction is applied using the distance between the Earth's surface and the geoid (elevation or orthometric height). Hence, rigorously, such free air corrections must be corrected by the separation between the reference ellipsoid and the geoid (i.e. the geoid anomaly). This is the

indirect effect over gravity and, in general, is of small magnitude and almost negligible for most purposes, due to the smoothness of the geoid (Li and Göetze, 2001).

Historically, the topography or complete Bouguer correction is composed of three parts: the Bouguer slab correction (Bullard A), which approximates the local topography (or bathymetry) by a slab of infinite lateral extent, constant density, and thickness equal to the elevation of the point with respect to the mean sea level; the curvature correction (Bullard B), which replaces the Bouguer slab by a spherical cap of the same thickness to a distance of 166.735 km; and the terrain correction (Bullard C), which consists of the effect of the surrounding topography above and below the elevation of the calculation point (Nowell, 1999). Terrain correction is always positive for land points, while offshore it can be either positive or negative, and is, by far, the most time-demanding and tedious task among the three parts of the topography correction. The topography correction removes the short wavelength features of free air anomalies associated with the relief. In general, we can consider that positive Bouguer anomaly values are related to thinned crust, while negative ones are indicative of a thick crust. This must only be considered as a rule of thumb, since lateral crustal density variations can lead to large Bouguer anomaly changes (e.g. sedimentary basins).

2.2.2 Geoid anomaly

The geoid is the equipotential surface of the Earth that coincides with the average sea level and contains, ideally, all the mass of the Earth. However, this is not a rigorous definition, since the average sea level is not completely equipotential (dynamic ocean processes), and, in addition, onshore topographical masses can lie above the geoid. The geoid anomaly is then the distance between the geoid surface and the reference ellipsoid model. The geoid anomaly, N, and the anomalous potential, T, of eq. 2.3, are related by the Bruns formula:

$$N = \frac{T}{\gamma} \tag{2.5}$$

In eq. 2.5 is assumed that the potential of the geoid and the reference ellipsoid are equal. In addition, the geoid anomaly, the gravity anomaly and the anomalous potential are related by the fundamental equation of the physical geodesy (Heiskanen and Moritz, 1967):

$$\Delta g = -\frac{\partial T}{\partial E} + N\frac{\partial \gamma}{\partial E} \tag{2.6}$$

where E is the elevation or orthometric height along the plumb line (positive upwards, negative towards the Earth's interior). Although eq. 2.6 has the form of a partial differential equation, it must be considered as a boundary condition, as the gravity anomaly, Δg, is only known over a surface (the geoid). If we assume that the mass distribution outside the geoid is null, T becomes an harmonic function and:

$$\nabla^2 T = 0 \tag{2.7}$$

Eq. 2.7, in conjunction with the boundary condition expressed by eq. 2.6**,** is a genuine partial differential equation. The knowledge of the anomalous potential using gravity measurements (eqs. 2.6 and 2.7) allows us to determine the geoid anomaly through eq. 2.5.

The spherical approximation considers the reference ellipsoid as a sphere and it is interesting for practical purposes. In the spherical approximation, eq. 2.6 has the following form:

$$\frac{\partial T}{\partial r} + 2\frac{T}{R_T} + \Delta g = 0 \tag{2.8}$$

where r is the radial distance and R_T is the radius of the Earth. Offshore, geoid variations can be determined straightforward via satellite altimetry. Onshore, the geoid anomaly must be determined by indirect methods. The Stokes formula gives us the geoid anomaly as a function of the gravity anomalies in the spherical approximation:

$$N = \frac{R_T}{4\pi g_0} \iint_{\sigma} \Delta g \; S(\psi) d\sigma \tag{2.9}$$

where ψ is the spherical distance between the calculation point and the mass distribution, g_0 is an average value of the gravity attraction over the surface of the Earth, dσ is the differential element of surface, and S(ψ) is the Stokes function, defined as:

$$S(\psi) = \frac{1}{\sin(\psi/2)} - 6\sin\left(\frac{\psi}{2}\right) + 1 - 5\cos(\psi) - 3\cos(\psi) L\left(\sin\left(\frac{\psi}{2}\right) + \sin^2\left(\frac{\psi}{2}\right)\right) \tag{2.10}$$

The surface integral of eq. 2.9 is extended to the whole surface of the Earth, and is valid under the following assumptions:

1) The mass within the reference ellipsoid is equal to the mass of the Earth.

2) The potential of the geoid and the reference ellipsoid are equal.

3) The centre of the reference ellipsoid is coincident with the centre of the Earth.

4) There are not masses outside the geoid (eq. 2.7).

5) Spherical approximation.

The assumption that no masses are present outside the geoid is critical. Over the continents, it is common that the geoid surface is located beneath topography, violating the aforementioned restriction. In such cases, topography outside the geoid must be removed by some procedure (e.g. Helmert condensation), taking into account the indirect effect that such procedure introduces in the geoid determination.

Geoid anomaly depends on the inverse of the distance to density anomalies, and is affected by lateral density variations located in a wide range of depths, from the core-mantle boundary up to crustal levels. In general, mass excess produces positive geoid anomalies and vice versa. Unfortunately, it is not possible to determine univocally the depth of the density anomaly, i.e. to decompose the potential field of the Earth into its causative sources (Bowin, 2000). However, global studies show that the geoid anomalies with wavelengths greater than 4000 km are produced by density contrast placed at sub-lithospheric levels (Bowin, 1983). Consequently, to study the lithospheric structure, we must retain only geoidal signatures with wavelengths smaller than 4000 km. The relation between the degree, n, and the associated wavelength of the spherical harmonics, λ, is (Strang van Hees, 2000):

$$\lambda = \frac{4\sqrt{\pi}R_T}{n+1} \tag{2.11}$$

According to eq. 2.11, for the degree 10 harmonic the associated wavelength is about 4100 km. Therefore, degrees n < 10 must be removed in order to keep the more likely "lithospheric" contribution to the geoid anomaly.

For a punctual mass, m_p we can obtain an equation that relates the gravity anomaly and the geoid anomaly in spherical coordinates. The anomalous potential produced by a punctual mass anomaly at a depth z is:

$$T = G\frac{m_p}{z} \tag{2.12}$$

The gravity anomaly produced by the same punctual mass anomaly reads:

$$\Delta g = G\frac{m_p}{z^2} \tag{2.13}$$

Combining eqs. 2.12 and 2.13 with eq. 2.5 we obtain the following expression for the depth at which the punctual mass anomaly is located:

$$z = \frac{N\gamma}{\Delta g} \tag{2.14}$$

According to eq. 2.14, a punctual mass anomaly that produces a gravity anomaly of 50 mGal, and a geoid anomaly of 1m, would be located at a depth of about 20 km.

2.3 THERMAL FIELD

Heat can be transferred in four different ways: conduction, advection convection, and radiation. Conduction of heat implies the transmission of the kinetic energy between adjacent atoms in the crystalline lattice or between neighbourhood molecules. The advection heat transfer occurs due to mass motion regardless of the source of that movement. This way of transferring heat takes place in geological processes like erosion/sedimentation, isostatic uplift, magmatic ascent or tectonic deformation. Convection is a special form of advection in which the motion is due specifically to the internal buoyancies of the material, and is important in liquids and gases. Radiation involves the direct transfer of heat by electromagnetic radiation.

Although convection cannot take place in rigid solids, over geological times the mantle appears to behave as a very high viscosity liquid and, therefore, slow convection is possible in the mantle. In fact, convection is the main heat transport mechanism in most of the mantle as well as the liquid outer core. The main characteristic of the lithosphere, considered as a thermal boundary layer, is the prevalence of conductive over convective heat transfer processes.

The mathematical expression of heat transfer processes within the Earth is the heat transport equation (e.g. Schubert et al., 2001):

$$\rho c_p \frac{\partial T}{\partial t} = \nabla\cdot(k\nabla T) + H - \rho c_p \vec{u}\cdot\nabla T \tag{2.15}$$

where, T is the temperature, t is the time, k is the thermal conductivity (W m^{-1} K^{-1}), ρ is the density, c_p is the specific heat at constant pressure (W kg^{-1} K^{-1}), $\vec{u}$ is the vector of velocity, and H is the radiogenic heat production per unit volume (W m^{-3}). The first term of the right hand side of eq. 2.15 corresponds to the

diffusion of heat by conduction, the second one reflects the presence of heat sources, and the third one is linked to the advective transfer of heat.

For the static modelling purposes of this thesis, we can assume steady state conditions, and disregard the advection term. Hence, we can rewrite eq. 2.15:

$$\nabla \cdot \left(k(\vec{x})\nabla T(\vec{x})\right) = -H(\vec{x}) \tag{2.16}$$

The term within parenthesis of the left hand side of eq. 2.16 is the negative heat flow, q.

The main contribution to the radiogenic heat production comes from the radioactive decay of isotopes U^{238}, Th^{232} and K^{40}, in relation to its relative abundance and decay rate. On average, the uranium and thorium contributions to heat production are larger than the potassium contribution. In general, granite has a more important internal heat generation than mafic igneous rocks, and the heat generation of undepleted mantle is very low. The distribution of heat production elements with depth is far from being well known and there are a wide variety of models proposed according to the different lithologies, ages or tectonic history of the rocks. In this thesis, and for the shake of simplicity, we have selected two simple models for the distribution of the heat production elements in the crust, constant and exponentially decreasing:

$$\begin{aligned} H(z) &= H_s \\ H(z) &= H_s \exp\left(-\frac{(z+E)}{h_r}\right) \end{aligned} \tag{2.17}$$

where H_s is the heat production at the surface of the Earth, h_r is the characteristic length scale of the heat production distribution, and z is the depth, which in contrast with E, is positive towards the Earth's interior. For the lithospheric mantle, and in the scope of the lithospheric modelling of this thesis, we can consider a negligible heat production.

The geotherms are temperature-depth profiles within the Earth. If we assume a constant heat flow in time and that no erosion/sedimentation is present, the profiles are called equilibrium geotherms (i.e. the temperature at any point is steady). The equilibrium geotherms can be calculated solving the 1D version of eq 2.16, which, for a constant thermal conductivity, reads:

$$-k\frac{d^2T(z)}{dz^2} = H(z) \tag{2.18}$$

The surface heat flow, SHF, measures the energy released from the Earth per unit area and per unit time. SHF measurements are expensive (in particular for continental areas) and, therefore, are scarcely distributed. In addition, SHF data are submitted to various perturbation processes like water circulation, faults, paleoclimate or data acquisition. In continents, the average SHF is about 60 mW/m^2, which is low in comparison to the average value for the oceans, ranging between 70-75 mW/m^2. SHF values tend to be higher in areas that have been tectonically active in the more recent past. Two sources contribute to SHF: the radiogenic heat produced mainly in the crust, and the heat flow from the underlying asthenosphere. The relative proportions of these contributions are not known very accurately, but they seem to be roughly comparable for continental areas. In oceanic areas, where the radiogenic heat production is considerably lower than in continents, the SHF is mainly correlated with the lithospheric thickness, i.e approximately inversely proportional to the square root of the sea floor age.

2.4 ISOSTASY

If we consider a flat-earth model, local isostasy implies that a series of rigid vertical columns (the lithosphere) float freely on an inviscid liquid (the asthenosphere) with the result that the pressure does not vary laterally below a certain level (the compensation level, z_{max}). This is the same as considering that the lithosphere does not support vertical shear stresses. Therefore, isostasy is achieved if:

$$\int_{LC} \Delta\rho(z)\, dz = 0 \tag{2.19}$$

where z is depth, $\Delta\rho(z)$ is the density contrast with respect to a given reference column, and LC indicates that the integration goes from the level of compensation to the top of the lithospheric column (topography). Local isostasy is an alternative statement of Archimedes' principle of hydrostatic equilibrium. The differences with respect to a spherical-earth model, which allows for the change in surface area with depth (e.g. Hager, 1983), are only relevant for very thick lithospheres. According to our calculations, for a 200-km-thick lithosphere the discrepancy between the spherical and flat-earth models is less than 5%.

In the context of local isostasy, elevation is a measure of the buoyancy of the lithospheric columns and can be expressed as (Lachenbruch and Morgan, 1990):

$$E = \frac{\rho_a - \rho_L}{\rho_a} \cdot L - L_0 \quad (E > 0) \tag{2.20a}$$

$$E = \frac{\rho_a}{\rho_a - \rho_w} \cdot \left(\frac{\rho_a - \rho_L}{\rho_a} \cdot L - L_0 \right) \quad (E < 0) \tag{2.20b}$$

where E is the elevation, L the total lithospheric thickness, ρ_a the density of the asthenosphere, ρ_L the average density of the lithosphere and L_0 is the depth of the free asthenospheric level, i.e. without any lithospheric load. E is positive above sea level and negative below it (**Fig. 2.1**). The value of L_0, which can be seen as a calibration constant, is calculated using eq. 2.20b with the parameters of an average mid-oceanic ridge lithospheric column (L_0=2320 m) according to Lachenbruch and Morgan (1990).

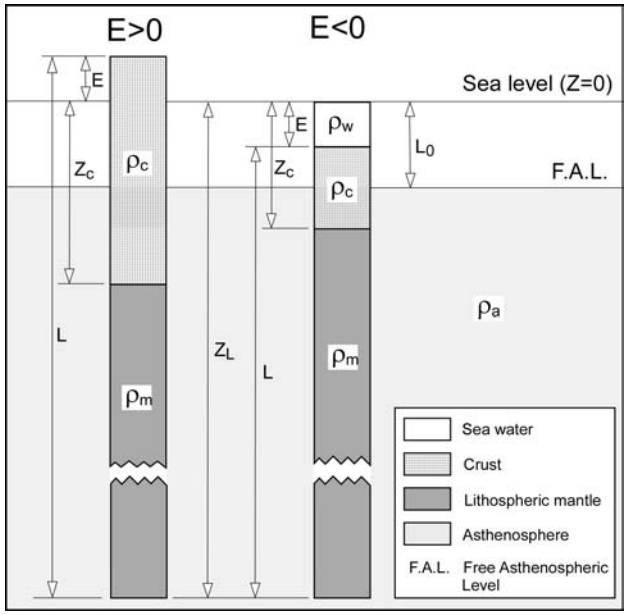

Fig. 2.1 *Notation for the lithospheric model used in Chapter 4. The model is composed of two layers, crust of density ρ_c and lithospheric mantle with density ρ_m, plus sea water and asthenosphere, with densities ρ_w and ρ_a, respectively. E is the elevation (E>0 topography, E<0 bathymetry), z_c, and z_L are the depths of the crust/mantle and lithosphere/asthenosphere boundaries, respectively, referred to the sea level. L is the total thickness of the lithosphere, and L_0 is the depth of the free asthenospheric level, i.e. without any lithospheric load.*

Local isostasy is a good approximation for long wavelength topographic features (Turcotte and Schubert, 1982; Watts, 2001). However, for short wavelengths, part of the load can be supported elastically resulting in a smoother

lithospheric deflection. The flexural response of a thin elastic plate is (e.g. Turcotte and Schubert, 1982):

$$q(x) = D\frac{d^4 w(x)}{dx^4} + N\frac{d^2 w(x)}{dx^2} + q_d(x)$$
$$D = \frac{E_y T_e^{\,3}}{12(1-\upsilon^2)} \qquad (2.21)$$

where D is the flexural rigidity, q the vertical load, q_d the restoring force, w the deflection, N the horizontal force per unit length, E_y the Young's modulus, ν the Poissons's ratio and T_e the elastic thickness of the thin plate. As an example, an elastic plate with T_e=10 km may support 90 % of the topography with wavelengths of up to 100 km (Cloetingh et al., 1992; Zeyen et al., 2005). Hence, to perform realistic local isostasy considerations, topography should be filtered in order to retain only its long wavelength part (i.e. not elastically supported by the lithosphere).

Chapter 3

THE GIBRALTAR ARC SYSTEM REGION: GEOLOGICAL AND GEOPHYSICAL CONTEXT

3. THE GIBRALTAR ARC SYSTEM REGION: GEOLOGICAL AND GEOPHYSICAL CONTEXT

3.1 GEOLOGICAL SETTING

East of the Azores triple junction, the limit between the Eurasian and the African plates in the Atlantic Ocean is an aseismic transform fault, which is nevertheless well defined by offsets of magnetic anomalies and bathymetric alignments. However, east of the Gorringe Bank, in the Atlantic-Mediterranean transition, the contact between the plates changes to a diffuse transpressive seismic plate boundary, comprising a wide band of active deformation (e.g. Meghraoui et al., 1996; Negredo et al., 2002; Jiménez-Munt and Negredo, 2003).

The Gibraltar Arc System region (GAS) comprises, in a general sense as stated in the introduction, several structural units, namely the Betic-Rif arcuate orogen, the inner Alboran extensional basin, the outer Guadalquivir and Rharb foreland basins, the frontal Gulf of Cadiz acretionary system, and the Atlas Mountains (Middle, High and Anti Atlas). The whole zone is affected by shallow and intermediate seismicity (Ramdani, 1998; Buforn and Coca, 2002), although some deep earthquakes of great magnitude have occurred near Granada (Buforn et al., 1991) (**Fig. 3.1**).

The Betic and Rif thrust belts consist of metamorphic rocks of the Internal Zones, a passive margin cover of the External Zones, Flysch Units, and both the foreland and intramontane Neogene Basins (**Fig. 3.1**). The Internal Zones are formed of Late Paleozoic to Triasic rocks that were piled up during Tertiary compression, followed by a pervasive extensional event started in the Early Miocene. The External Zones correspond to the cover sequences of the SW Iberian and NW Maghrebian paleomargins that were deformed above a highly arcuate thrust system. The Flysch Units comprise deep marine turbidites that were transported towards the west above an arcuate imbricate system of thrusts along the Gibraltar Arc. The Gibraltar Arc tectonic units are the result of the superposition of slow but long-living NW convergence of Africa towards Europe, and a much shorter but faster geodynamic process that produced the migration of the arc to the west. It is likely that the mechanism responsible for the westward migration is of deep nature (Iribarren et al., 2007, and references therein).

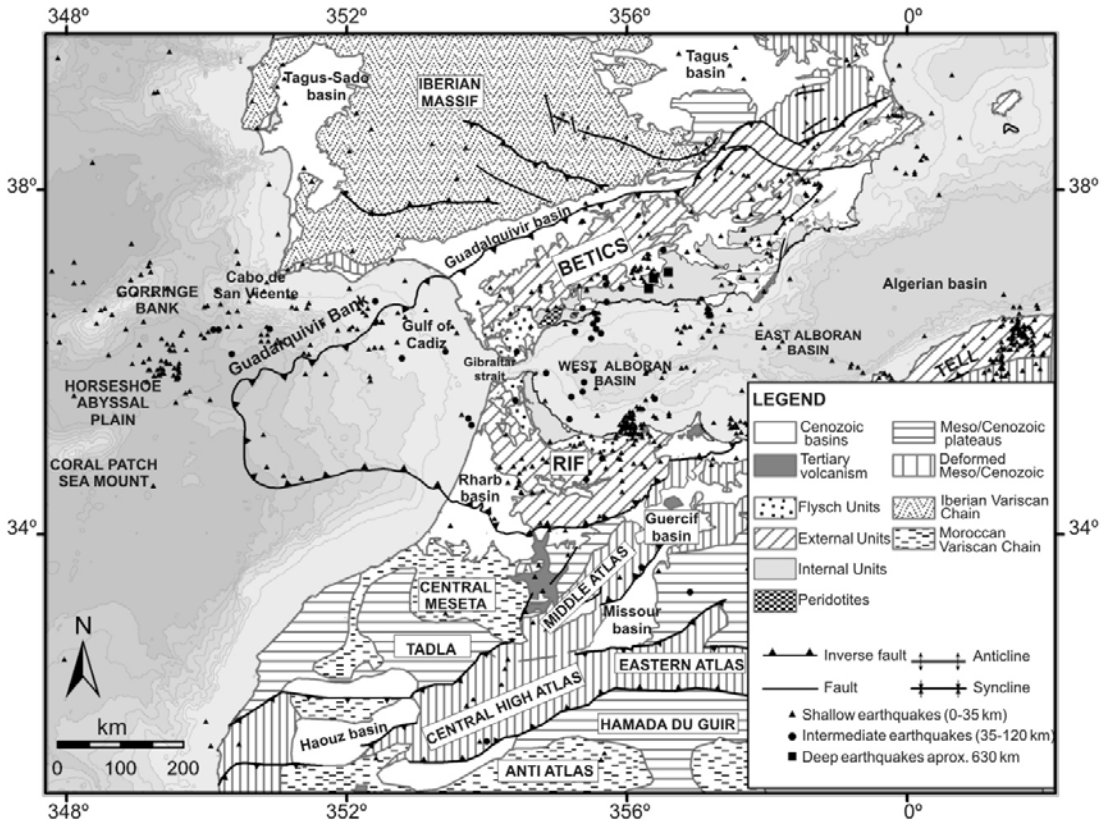

Fig. 3.1 *Geological map of the study area with epicenters of earthquakes of magnitude > 3.5 during 1961-2000 (AnSS catalogue http://quake.geo.berkeley.edu/anss/).*

The Alboran Basin is characterized by extensional tectonics and bounded by large extensional fault systems that follow the arcuate trend of the Gibraltar Arc. The sediment infill is marine in origin, and the basement consists of continental Paleozoic sediments that have been metamorphosed during the Alpine orogeny. East of 4 ºW broad areas of the top of the acoustic basement appear to be formed by volcanic rocks. The structure of the basin is the consequence of two successive stages of extensional and contractive tectonics. Late orogenic rifting and progressive exhumation of the Alboran domain took place from, at least, the early Miocene to the early Tortonian. The rifting initiated at the end of Oligocene and crustal stretching was accompanied by rapid tectonic exhumation of middle crustal rocks and advection of heat at relatively low pressure. The main phase of rifting ended in the latest Tortonian. After that, contractive tectonics disrupted the basin into subbasins, separated by emerged or submarine highs. This tectonic phase produced N-S shortening and considerable E-W elongation of the whole basin and the Betic-Rif orogen. Plio-Pleistocene tectonics was largely responsible for the present-day seafloor topography and location of the present-day coastline.

The early Miocene and late Serravallian to Tortonian alkaline and calc-alkaline volcanic rocks have resulted from the rifting process, while lamproites, shoshonitic lavas, and alkali basalts were erupted during the post-Tortonian compressional stage. Mainly shales, sandstones and marls compose the sedimentary column, late Aquitanian-Burdigalian to Recent in age. Volcanic and volcanoclastic levels intercalate throughout the middle and late Miocene sequences (Torne et al., 2000, and references therein).

The Guadalquivir Basin is the foreland basin of the central and western Betics. The basement composed by Paleozoic and Mesozoic rocks, dips SE beneath the Neogene sediments. The basin was formed by lithospheric flexure due to thrust loading and, probably, to an additional load produced by lithospheric mantle thickening (García-Castellanos et al., 2002). The basin is filled by six Miocene seismic stratigraphic depositional sequences spanning from late Langhian to late Messinian. These Miocene sequences are overlain by Plio-Quaternary sediments, which are prograding westwards along the axis of the basin. The southern border of the basin is filled by lateral diapirs of Triasic evaporites, which developed frontal imbricate wedges. These frontal imbricates involve late Serravallian to late Tortonian sediments (Berástegui et al., 1998; Fernàndez et al., 1998a). The Rharb Basin is the foreland basin of the Rif. Paleozoic Hercynian rocks and Mesozoic materials form its basement. Its southern flank is conditioned by Hercynian faults generating horsts and grabens filled with Miocene-Pliocene sequences, which are overlain by Quaternary sediments. The northern sector presents a Paleozoic basement with a Mesozoic cover that is flexed due to the emplacement of thrust loading coming from the Rif (Zohuiri et al., 2001).

The tectonic evolution of the Gulf of Cadiz region is related to the opening of the Central and North Atlantic and to the relative motion between Iberia and Africa. Continental break-up started at the central African margin in the Triassic and propagated to the north until middle-late Jurassic times. This produced seafloor spreading in the NW African margin and a transtensive tectonic regime between Africa and Iberia/Newfoundland. Iberia moved together with the African plate between latest Cretaceous and mid-Eocene, when it started to move as an independent plate, and a new plate boundary was formed in the Azores-Gibraltar fracture zone. The sense of motion between Africa and Iberia has remained essentially the same since that last time, producing contemporaneous transtension near the Azores and transpression in the Gulf of Cadiz. The structural units forming the Betics and the Rif chains have their

continuation beneath the Gulf of Cadiz. All these units are overlying a Hercynian basement that gently dips towards the East in the Gulf of Cadiz, and towards the south and north beneath the Betics and rhe Rif, respectively. One striking feature is the presence of large allochthonous masses with seismically chaotic reflections at the forefront of the Gibraltar Arc, called in many different ways as e.g. the "Giant Chaotic Body", "Allochthonous Unit" or "Olistostromic Complex". These chaotic Miocene masses can be divided into two units: an accretionary wedge located in the present Gulf of Cadiz continental slope formed by the imbrications of Triassic to upper Miocene sediments, and a submarine gravitational unit in the Horseshoe abyssal plain (Zeyen et al., 2005; Iribarren et al., 2007 and references therein).

The Atlas Mountains form an intracontinental mountain belt located in the foreland of the Rif-Tell interplate orogen of North Africa, extending for more than 2000 km in an SW-NE direction from Morocco into Algeria and Tunisia (**Fig. 3.1**). It is composed of folded and faulted Paleozoic, Mesozoic and Cenozoic rocks with summits that in its western part reach more than 4 km. The Atlas Mountains are the result of the tectonic inversion of a Mesozoic extensional basin, genetically related to the opening of the Atlantic and Tethys Ocean. From Cenozoic times to present, the chain has undergone compression associated with the NW convergence of Africa towards Europe. Shortening was achieved mainly by thick-skinned thrusting and folding, affecting the pre-Mesozoic basement and the Mesozoic-Cenozoic cover. The total shortening in the study region due to Cenozoic compression is 15-24 %. It is worth noting the presence of Triassic and Jurassic igneous rocks, as well as Tertiary and Quaternary alkaline volcanism (Ayarza et al., 2005; Teixell et al., 2005, and references therein)

A number of studies have been carried out in the area: seismic reflection/refraction profiles (e.g. Banda et al., 1993; Comas et al., 1997; Simancas et al., 2003), seismic tomography (e.g. Blanco and Spakman, 1993; Bijwaard et al., 1998; Calvert et al., 2000; Marone et al., 2004; Spakman and Wortel, 2004), gravity modelling (e.g. Torne et al., 2000; Gràcia et al., 2003) and heat flow (Polyak et al., 1996; Fernàndez et al., 1998b; Rimi et al., 1998). Despite these works, some aspects remain unclear, mainly the way in which is geometrically resolved the transition from an oceanic Jurassic lithosphere in the Atlantic domain to a Neogene oceanic lithosphere in the Algerian Basin. Furthermore, the origin and evolution of the inverted South Iberian and North African passive margins is still a matter of debate and there are several, even mutually exclusive, geodynamical models proposed, all of them based on

different geological and geophysical data: Neogene subduction associated with slab roll back (Frizon de Lamotte et al., 1991; Lonergan and White, 1997), active subduction (Gutscher et al., 2002), delamination (e.g. Seber et al., 1996a; Mezcua and Rueda, 1997; Calvert et al., 2000), convective removal (Platt and Vissers, 1989; Platt et al., 2003), slab break-off (Zeck, 1996; Wortel and Spakman, 2000) or slab roll-back and lithospheric tearing (Spakman and Wortel, 2004). Although most of these models are based on the present lithospheric structure beneath the study area, crustal geometry is well known only in certain areas of the region, while subcrustal images rely almost solely on seismic tomography works.

3.2 GEOPHYSICAL OBSERVABLES

Geophysical observables are magnitudes that can be measured or determined at the surface of the Earth, and offer us information about the petrophysical properties of the planet's interior. In the following, we show the elevation (E), geoid anomaly (ΔN), free air anomaly (Δg_{FA}), Bouguer anomaly (Δg_B) and surface heat flow (SHF) maps of the study area. Elevation, geoid anomaly and free air anomaly were obtained from global data base sets. In the case of Bouguer anomaly, since no global data base exists, we present a computer code (FA2BOUG) to calculate it in both land and marine areas using free air satellite-derived data as input. The program is applied, together with available measured gravity land data, to produce a complete Bouguer anomaly map of the GAS region. For the SHF, we have used a compilation of different authors. The geophysical data presented here are used as input data in the method of joint inversion of elevation and geoid anomaly presented in Chapter 4, and in the 3D forward model that will be introduced in Chapter 6.

3.2.1 Elevation

The elevation data, i.e. topography and bathymetry, come from the new release of ETOPO2 Global Data Base (V9.1) (Smith and Sandwell, 1994; Sandwell and Smith, 1997; Hastings and Dunbar, 1999) (**Fig. 3.2**). This database is a 1'x1' grid, which means roughly a point every 2 km. The vertical accuracy of these data is characterized by an RMS error of 18 m onshore and of 200 m offshore. Onshore, the Betic and Rif chains together form an arc parallel to the shoreline with short wavelength content. The elevation is locally higher than 3000 m and 2000 m in the Betic and Rif chains, respectively, although the mean elevation is 1000-1500 m for the Betics, and 500-1000 m for the Rif. In the north of the African continent, the Atlas Mountains trend NE-SW to E-W, with long

topographical wavelengths and a mean elevation of about 2000 m, although altitudes of >4000 m are locally reached. Offshore, in the Alboran Basin, the water depth increases towards the distal and eastern parts of the basin reaching depths >2000 m in the transition to the Algerian Basin. Located in the central part of the Alboran Basin, the Alboran Ridge is an elongated NE-SW bathymetric high, which is locally emerged. To the west, in the Atlantic Ocean, depths >4500 m are achieved in the Atlantic abyssal plains. The presence of contractive oceanic structures, which are 3000-4000 m elevated above the seafloor (Coral Patch, Gorringe Bank), is also noticeable. For the most part, the Iberian and North African Margins are steep, except for the western Alboran Basin and the Gulf of Cadiz, where the margin slope is smoother due to the large sediment accumulation and continental nature.

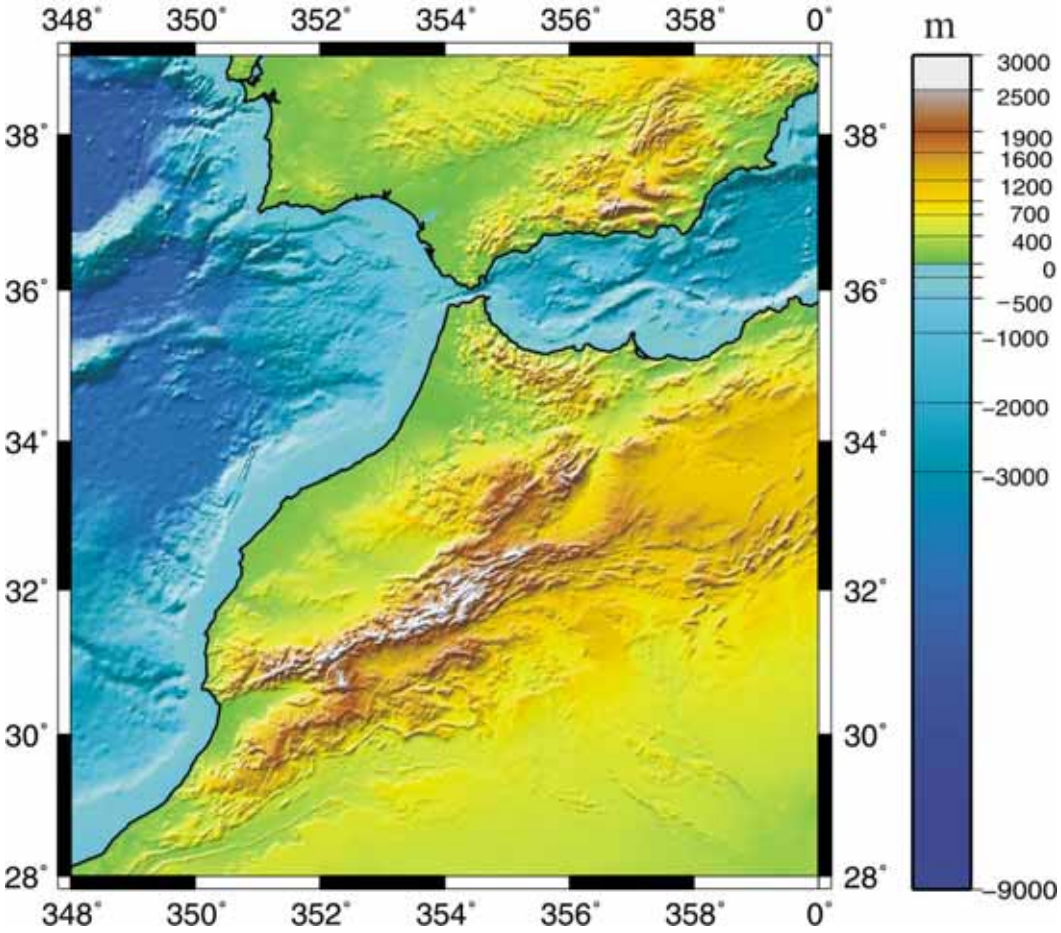

Fig. 3.2 *Elevation map from 1'x 1' ETOPO2 Global Data Base (V9.1) (Smith and Sandwell, 1994; Sandwell and Smith, 1997; Hastings and Dunbar, 1999).*

3.2.2 Geoid anomaly

Geoid anomaly data were taken from the Earth Global Model 96 (EGM96) spherical harmonic global model (Lemoine et al., 1998) (**Fig. 3.3**). The data has an RMS error of 36 cm. In order to eliminate the effect of sublithospheric sources of geoid undulations, we removed wavelengths >4000 km. Hence, according to eq. 2.11, we removed spherical harmonics of degrees 2-9.

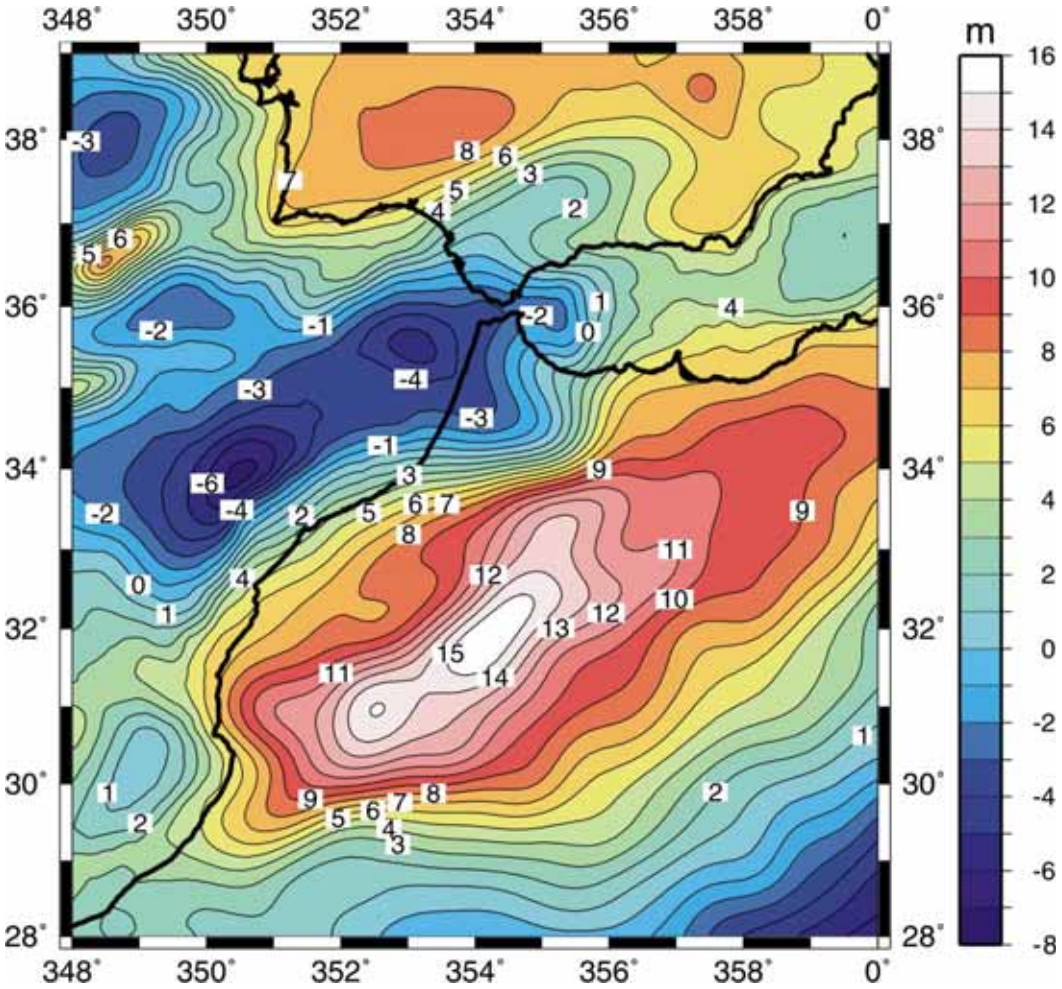

Fig. 3.3 *Geoid anomaly map from EGM96 Global Model (Lemoine et al., 1998). Long wavelengths (>4000 km) have been removed. Contour interval is 1 m.*

In general, geoid anomaly isolines in passive margins tend to follow the coastline, showing a decrease of about 5 m from the continent to the ocean. The most remarkable characteristics of the geoid anomaly map of the GAS region are, on the one hand, the strong minimum, NE-SW trending, in the Gulf of Cadiz (-5 m) and NW Moroccan Margin (-7 m) that extends reducing its amplitude to the

Guadalquivir, western Alboran and Rharb Basins, and the western parts of the Rif and Betic orogens. On the other hand, a NE-SW directed strong maximum (>15 m) is observed in the Atlas Mountains. The coupling between these maxima and minima geoid anomaly values produces a very steep lateral gradient amounting to 22 m over 450 km lateral distance. The geoid anomaly trend shows decreasing values towards the SE in the African Craton.

3.2.3 Free air anomaly

In **Fig. 3.4** a free air anomaly map of the GAS region is shown. Free air data come from the global satellite altimetry data compilation V16.1 model by Sandwell and Smith (1997). The resolution is 1'x 1' (approximately 2 x 2 km). The accuracy of the satellite-derived gravity anomaly is 4-7 mGal. Onshore, in Morocco, available data coming from Hildenbrand et al., (1988) were gridded to match the altimetric data prior to the grid merging.

In the Iberian Peninsula, positive Δg_{FA} are present in the Internal Betics (>60 mGal), in the Hercynian basement west of the Guadalquivir Basin (>80 mGal) and in the area of the Cabo de San Vicente (>100 mGal). The Guadalquivir Basin presents a NE-SW trending negative anomaly (<-60 mGal). Free air anomaly shows near zero values in the Alboran Basin except for the western part of the basin, where an N-S arcuate-shaped minimum (<-100 mGal) can be correlated with Neogene to Quaternary sediment accumulation (Torne et al., 2000). In the African continent, the Atlas Mountains shows positive free air anomaly values (> 140 mGal), while minimum values are present in the Rharb Basin (<-100 mGal), and the Tadla area (<-10 mGal). In the Atlantic domain, two conspicuous maxima can be found in the Gorringe bank (>350 mGal) and the Coral Patch Seamount (>220 mGal). The Guadalquivir Bank is also characterized by a narrow NE-SW maximum (>120 mGal). Negative free air values are located in the central Gulf of Cadiz (<-100 mGal) and to the west of the North African margin (<-160 mGal).

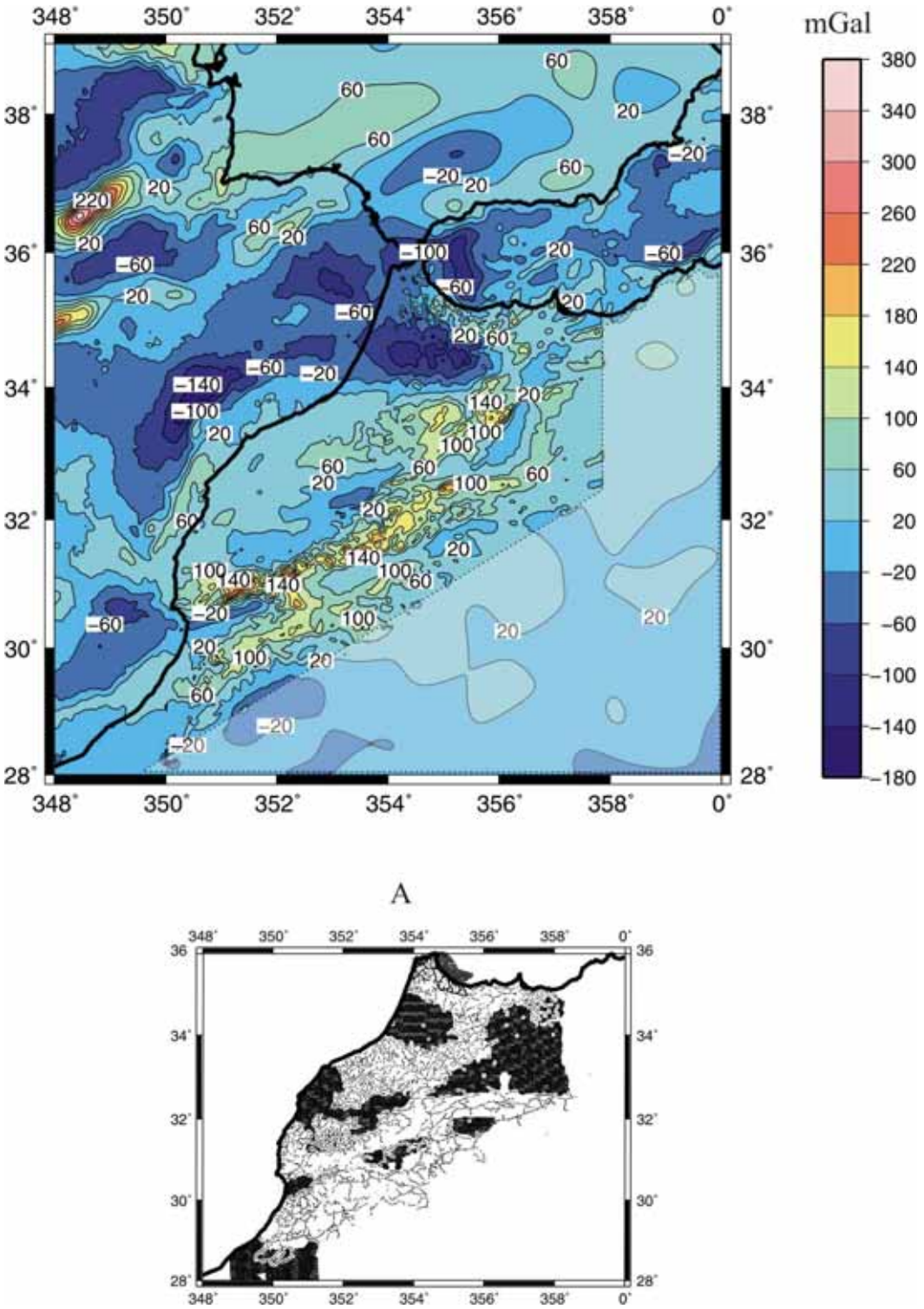

Fig. 3.4 *Free air anomaly map. Data offshore and in the shaded area in Africa, come from the 1'x 1' global satellite altimetry data compilation V16.1 model by Sandwell and Smith (1997). In Morocco, available data coming from Hildenbrand et al., (1988) (dots in inset A represent the gravity measurements) were gridded to match the altimetric data prior to the grid merging. Contours every 40 mGal.*

3.2.4 Bouguer anomaly

As stated in Chapter 2, Bouguer anomaly, Δg_B, is obtained applying Bouguer slab (Bullard A), curvature (Bullard B) and terrain (Bullard C) corrections to free air anomaly. Traditionally, terrain correction has been made manually using the method of Hammer (1939), which divides the surrounding area into compartments (cylindrical sectors) and compares their elevation with the elevation of the station. Since the early 60's, other techniques that take profit of increasing computer speed and the availability of Digital Elevation Models (DEM) have been developed for land terrain corrections. Numerical methods approximate in some way the exact solutions for the gravity attraction given by analytical expressions, e.g. Fast Fourier Transform, FFT, (Forsberg, 1985; Parker, 1996; Tsoulis, 2001) or Gaussian quadrature (Hwang et al., 2003). Analytical methods decompose the topography into a set of elementary bodies whose gravity effect is well known (Kane et al., 1962; Olivier and Simard, 1981; Blais and Ferland, 1984; Ketalaar, 1987; Cogbill, 1990; Lopez, 1990; Ma and Watts; 1993; Banerjee, 1998). One of the main limitations of the DEM-based techniques, which usually consider an average value over each cell of the model, is the omission of the near-meter effects, which can account for several mGals, depending on the roughness of the topography and the spatial resolution of the DEM (Leaman, 1998; Nowell, 1999). An alternative approach to gravity corrections including geodetic features such as a spherical free air correction or a non-geocentric coordinate system is that of Featherstone and Dentith (1997). The density used for the topography in the complete Bouguer correction is commonly a constant standard value of 2670 kg/m^3. However, the use of such a constant value instead of a variable density model can distort the resulting Bouguer anomaly (Flis et al., 1998).

Bouguer anomaly is more commonly used in onshore than in offshore investigations where mostly free air anomalies are used. However, its use may be worthwhile to avoid the bathymetric irregularities and to visualize sub-sea floor density effects. Fourier-based methods have been used to correct the effect of the water layer (Luis et al., 1998; Berndt, 2002). However, the zone closer to the station cannot be directly processed in the frequency domain due to convergence problems. Carbó et al. (2003) have applied a computer program based on the flat-topped prism approximation to determine marine Bouguer anomalies. Nevertheless, this program does not have a special treatment of the zone nearest to the station, does not take into account the curvature effect, and the topography correction is only extended to 22 km.

In this thesis, we have developed a FORTRAN 90 program (FA2BOUG), which calculates Bouguer anomalies for onshore and offshore points. FA2BOUG is mainly intended for regional grid-based computations. The format of the input files is particularly suitable for the use of publicly available global gridded Δg_{FA} and elevation data base sets (ftp://topex.ucsd.edu/pub; Sandwell and Smith, 1997). The program performs Bullard A, B and C corrections and distinguishes several zones depending on the horizontal distance (R) to the point where Bouguer anomaly is to be calculated and whether this calculation point is onshore or offshore. For offshore areas, FA2BOUG distinguishes three zones: inner zone ($R < \Delta x_i/2$; Δx_i being the grid step), intermediate zone ($R_i > R > \Delta x_i/2$), and distant zone ($R_d > R > R_i$), where R_i, R_d and Δx_i are input parameters (**Table 3.1**). For onshore areas, to exploit the availability of more detailed DEM (grid step $\Delta x_{det} < \Delta x_i$), the program offers the possibility to redefine the inner zone as ($R < \Delta x_{det}/2$), and add a new detailed intermediate zone to the calculation ($\Delta x_i/2 > R > \Delta x_{det}/2$). Each zone has its own grid step and calculation method (**Fig. 3.5**). FA2BOUG has been applied to the GAS region in order to produce the first Bouguer anomaly map of the whole region merging different data sets. Available land Bouguer anomaly data are used in the Iberian Peninsula (Mezcúa et al., 1996) and Morocco (Hildenbrand et al., 1988), while for the rest of the African region and offshore points Bouguer anomaly is calculated from free air satellite data.

Method

In the following section we describe how FA2BOUG performs the complete Bouguer correction. The topographic/bathymetric surface is divided into a set of square flat-topped prisms centred in each point of the DEM. The height of the prisms is the elevation, E, measured from sea level, and its horizontal dimensions are equal to the grid step. To avoid confusion, we will call the elevation at the calculation point h, in contrast to the elevation of the surrounding topography named E. Instead of the conventional approach using Bullard A, B and C corrections for computing Bouguer slab and terrain corrections, FA2BOUG computes the effect of the mass topography, i.e. the vertical gravitational attraction of each prism of the DEM whose distance from the calculation point is less than or equal to the limit of the distant zone, R_d. (**Fig. 3.5**). The calculations are performed assuming a flat Earth model and, therefore, the Bullard B correction is needed. The use of flat-topped prisms does not reproduce exactly the actual topography, and more refined analytical approaches such as slope-topped and –bottomed prisms (Smith, 2000) have been proposed.

However, these refined approaches increase considerably computational time without a significant improvement in accuracy, and, therefore, are not suitable for regional scale computations.

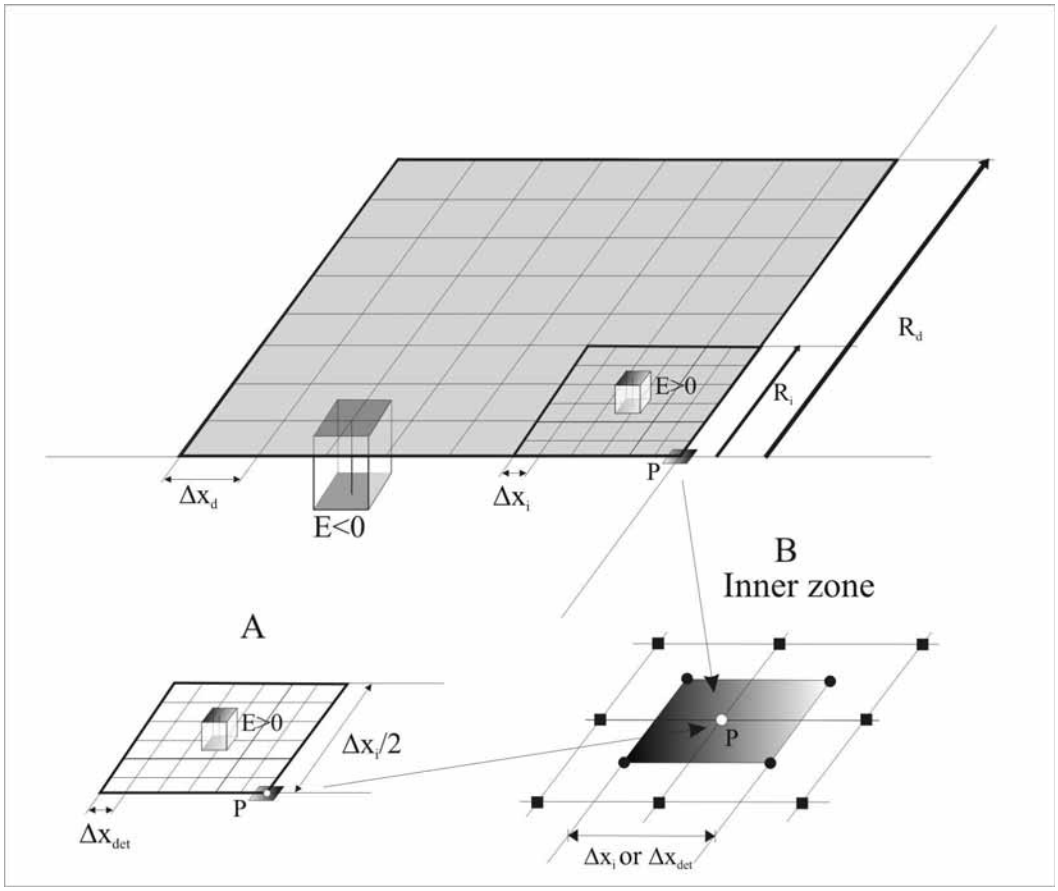

Fig. 3.5 *Different computational zones used by FA2BOUG according to the distance between topography and the calculation point (P), R: the distant zone ($R_d > R > R_i$) with a grid step of Δx_d, the intermediate zone ($R_i > R > \Delta x_i/2$) with a grid step of Δx_i. In order to exploit the availability of high resolution DEM (grid step $\Delta x_{det} < \Delta x_i$), FA2BOUG offers the possibility to work with an additional detailed intermediate zone: $\Delta x_i/2 > R > \Delta x_{det}/2$ (inlet A). In the distant, intermediate and detailed intermediate zones the topography is represented by a set of prisms centred in each node of the DEM. Inlet B shows the inner zone ($R < \Delta x_i/2$ or $\Delta x_{det}/2$, depending on whether the detailed intermediate zone is used in the calculation or not: see the text for further details). The elevation in each vertex defining the inner zone (black dots in inlet B) is linearly interpolated using the four nearest adjacent grid points, i.e.the three black squares and the calculation point, P (white dot in inlet B).*

The value for R_d has been usually set to 166.735 km (1.5º), which coincides with the outer limit of the Hayford-Bowie system (Hayford and Bowie,

1912). This particular value of R_d minimizes the difference between the effect of the spherical cap and the infinite horizontal Bouguer slab and, therefore, should be assumed as a standard distance for Bullard B correction (LaFehr, 1991). The vertical gravitational attraction produced by a right rectangular prism can be expressed analytically in Cartesian coordinates as (Nagy et al., 2000):

$$\Delta g_{FTP}(\rho) = G\rho \left\| x\ln(y+r) + y\ln(x+r) - z\arctan\left(\frac{xy}{zr}\right) \right\|_{x_1}^{x_2} \Bigg|_{y_1}^{y_2} \Bigg|_{z_1}^{z_2} \qquad (3.1)$$

$$r = \sqrt{x^2 + y^2 + z^2}$$

where G is the universal gravitational constant ($6.67*10^{-11}$ m^3 s^{-2} kg^{-1}) and ρ is the reduction density, whose value depends on the sign of elevation (i.e., onshore/offshore grid point):

$$\rho = \rho_c \quad if\ E > 0$$
$$\rho = (\rho_c - \rho_w) \quad if\ E < 0$$

Parameter	**Symbol**	**Value**
Distant zone grid step	Δx_d	4 km
Intermediate zone grid step	Δx_i	2 km
Detailed Intermediate zone grid step	Δx_{det}	0.1 km
Output Bouguer grid step	Δx_{Bg}	2 km
Crustal reduction density	ρ_c	2670 kg/m^3
Sea water reduction density	ρ_w	1030 kg/m^3
Limit of the intermediate zone	R_i	20 km
Limit of the distant zone	R_d	167 km

Table 3.1. *Input parameters for FA2BOUG.*

The Cartesian coordinates ($x_1<x_2$, $y_1<y_2$, z_1, z_2) define spatially the prism and are referred to a coordinate system with its origin located in the point where Bouguer correction is calculated. Onshore (h>0), the measurements are usually done at z_m=h, offshore (h<0) at z_m=0. With this definition the vertical limits of

the prism are $z_1=z_m$ and $z_2=|E-z_m|$, where the correct sign for each prism contribution is considered.

Bullard B correction takes into account the curvature of the Earth changing the infinite Bouguer slab by a spherical cap of the same thickness, a radius of 6731 km, and a width R_d. The first attempt to evaluate Bullard B correction was that of the tables presented by Swick (1942). More recently, LaFehr (1991) developed an exact formula for Bullard B correction. Concerning the computational efficiency, the exact formula for Bullard B correction (LaFehr, 1991) contains several trigonometric functions and a logarithm term, which considerably slows down the computation process. For that reason, in this work we prefer the approximation of Whitman (1991), which is accurate to 10^{-3} mGal for a slab of thickness up to 4 km. It represents a great simplification over the exact formula and can be interpreted physically in terms of fractions of Bullard A (slab) correction. According to this author, Bullard B correction, BB, can be expressed in terms of the elevation at the calculation point, h:

$$
\begin{aligned}
BB &= -2\pi G\rho_c h\left(\frac{\alpha}{2}-\frac{\eta}{2\alpha}-\eta\right) \quad if\ h>0 \\
BB &= -2\pi G(\rho_c-\rho_w)h\left(\frac{\alpha}{2}+\frac{\eta}{2\alpha}+\eta\right) \quad if\ h<0 \\
\alpha &= \frac{R_d}{R_T} \\
\eta &= \frac{h}{R_T+h}
\end{aligned}
\tag{3.2}
$$

where R_T is the radius of a spherical Earth. The first term in the parenthesis of eq. 3.2 accounts for the increased vertical attraction of the curved truncated Bouguer slab, i.e. the part of the spherical cap underlying the infinite slab, the second term is related to slab truncation with respect to the infinite Bouguer slab, and the third one expresses the decreased/increased Earth curvature with increasing/decreasing actual radius, R_T+E. The quantitative relevance of the three terms in eq. 3.2 decreases from left to right for slab thicknesses of up to 4.5 km (Whitman, 1991). As FA2BOUG does not subtract the Bouguer infinite slab (it calculates the gravitational influence of the topography only inside the Bullard radius, R_d), the second term of BB in eq. 3.2 is not taken into account.

FA2BOUG works with several computational domains that can be defined by the user according to the distance between topography and the calculation point, R: distant zone, intermediate zone and inner zone. For onshore calculation areas the program incorporates the possibility of adding a new detailed

intermediate zone to the calculation, in order to exploit the availability of detailed DEM (grid step $\Delta x_{det} < \Delta x_i$). In each zone a different calculation scheme is used (**Fig. 3.5**). To select appropriate values for the outer limit of the intermediate zone, we have performed several tests varying R_i between 10 and 40 km. The idea is to keep a compromise between the accuracy and the computation time. We calculate residuals between the Bouguer anomaly maps obtained using different R_i values. From R_i=10 km to R_i=20 km significant differences arise (>0.5 mGal), while maximum residual values are <0.1 mGal when Bouguer anomaly maps with R_i>20 km are compared (**Table 3.2**). Thus, to attain a correction accuracy of 0.1 mGal, a value of R_i equal to 20 km is enough. A similar distance is used as the starting point of the distant zone in previous works (Banerjee, 1998, Hwang et al., 2003).

R_i(km)	**Min**	**Max**	**Mean**	**Std. dev.**
20-10	-0.58	0.54	0.003	0.04
30-20	-0.07	0.06	$-5\ 10^{-4}$	0.006
40-30	-0.06	0.08	$5\ 10^{4}$	0.006

Table 3.2. *Residuals between the Bouguer anomalies calculated using different values for the outer limit of the intermediate zone, R_i. Minimum, maximum and mean values expressed in mGal.*

Distant zone ($R_d > R > R_i$) computation:

In the distant zone the grid step is Δx_d (**Table 3.1**). The expression presented for the attraction produced by a right rectangular prism (Eq. 3.1) can lead to numerical instabilities for far prisms (e.g. $x_1 >> x_2 - x_1$, where x_1 and x_2 are the Cartesian coordinates that define spatially the prism). For that reason, in this zone we consider the spherical harmonic expansion of the gravitational potential of a right rectangular prism, neglecting terms of the order $1/r^9$ or smaller (McMillan, 1958):

$$V_{SHE} = G\rho\Delta x\Delta y\Delta z\left[\frac{1}{r} + \frac{1}{24r^5}\left(V_1 + V_2 + V_3\right)\right] + o\left(\frac{1}{r^9}\right)$$

$$\begin{aligned}
V_1 &= \left(2\Delta x^2 - \Delta y^2 - \Delta z^2\right)x^2 \\
V_2 &= \left(2\Delta y^2 - \Delta x^2 - \Delta z^2\right)y^2 \\
V_3 &= \left(2\Delta z^2 - \Delta x^2 - \Delta y^2\right)z^2 \\
r &= \sqrt{x^2 + y^2 + z^2} \\
\Delta x &= x_2 - x_1 \\
\Delta y &= y_2 - y_1 \\
\Delta z &= z_2 - z_1 \\
x &= (x_1 + x_2)/2 \\
y &= (y_1 + y_2)/2 \\
z &= (z_1 + z_2)/2
\end{aligned} \qquad (3.3)$$

Hence, the vertical gravitational attraction is the vertical derivative of eq. 3.3:

$$\Delta g_{SHE} = -\frac{\partial V_{SHE}}{\partial z} = G\rho\Delta x\Delta y\Delta z\left[\frac{1}{r^2} + \frac{5}{24r^6}\left(V_1 + V_2 + V_3\left(1 - \frac{2r^2}{5z^2}\right)\right)\right]\frac{z}{r} + o\left(\frac{1}{r^{11}}\right) \quad (3.4)$$

In addition, the approximation by spherical harmonic expansion of eq. 3.4 reduces computing time without losing accuracy. The distant zone contribution to the Bullard A-C correction, Δg_D, is:

$$\Delta g_D = \sum_{Offshore\ prisms} \Delta g_{SHE}(\rho_c - \rho_w) + \sum_{Onshore\ prisms} \Delta g_{SHE}(\rho_c) \qquad (3.5)$$

Intermediate zone computation ($R_i > R > \Delta x_i/2$):

In the intermediate zone the grid step is Δx_i (**Table 3.1**). In this zone the gravitational attraction due to each prism is computed using eq. 3.1. The intermediate contribution, Δg_I, of the flat-toped prisms (FTP) is:

$$\Delta g_I = \sum_{Offshore\ prisms} \Delta g_{FTP}(\rho_c - \rho_w) + \sum_{Onshore\ prisms} \Delta g_{FTP}(\rho_c) \qquad (3.6)$$

For onshore areas, and due to the availability of high resolution DEM (SRTM www2.jpl.nasa.gov/srtm/, Farr et al., 2007), FA2BOUG offers the possibility of adding a new detailed intermediate zone to the calculation: $\Delta x_i/2 > R > \Delta x_{det}/2$, being $\Delta x_{det} (< \Delta x_i)$ the grid step of the detailed topography (**Table 3.1**). The gravitational attraction due to each prism is computed using eq. 3.1. The

contribution of this detailed intermediate zone to the complete Bouguer correction, Δg_{IDET}, is similar to eq. 3.6, but only referred to onshore prisms, where the detailed DEM is defined.

Inner zone computation ($R < \Delta x_i/2$ or $\Delta x_{det}/2$):

The inner zone consists of a Δx_i or Δx_{det}-sided square centred on the calculation point, depending whether the detailed intermediate zone is used in the calculation or not. The elevation in each vertex of the square is interpolated linearly using the three nearest adjacent grid points plus the calculation point (**Fig. 3.5**). The inner contribution to Bullard A-C correction is calculated in two steps. In the first step we compute the vertical attraction due to the inner flat-topped prism with lateral extension equal to the size of the inner zone and height equal to the elevation of the calculation point, h (x_1, y_1= $-\Delta x_i/2$ (or $-\Delta x_{det}/2$), x_2, y_2= $\Delta x_i/2$ (or $\Delta x_{det}/2$), z_1=0, z_2=h) as:

$$\begin{aligned} \Delta g_{IFTP} &= \Delta g_{FTP}(\rho_c) \quad if\ h \geq 0 \\ \Delta g_{IFTP} &= \Delta g_{FTP}(\rho_c - \rho_w) \quad if\ h < 0 \end{aligned} \tag{3.7}$$

In the second step we divide the inner zone into four quadrants with a constant slope upwards or downwards from its vertex to the calculation point, i.e. a quarter of a conic prism with its vertical axis through the calculation point (Lopez, 1990; Nowell, 1999). The vertical gravitational attraction produced by a quarter of a conic prism is:

$$\Delta g_{CP} = \frac{1}{4} 2\pi G\rho \int_0^{R_{CP}} dr' \int_0^{\Delta h \frac{r'}{R_{CP}}} dz \frac{zr'}{\left(r'^2 + z^2\right)^{\frac{3}{2}}} = \frac{\pi G\rho R_{CP}}{2\sqrt{R_{CP}^{\ 2} + \Delta h^2}} \left(\sqrt{R_{CP}^{\ 2} + \Delta h^2} - R_{CP} \right) \tag{3.8}$$

where R_{CP} is the radius of the conic prism, $r' = \sqrt{x^2 + y^2}$ and Δh=E-h is the difference of elevation between one vertex of the inner zone, E, and the calculation point, h, (**Fig. 3.6**). The inner zone contribution to the Bullard A-C correction, Δg_{IN}, is, therefore, equal to Δg_{IFTP} from eq. 3.7 plus an extra conic prism term whose value depends on the positive/negative elevation of the calculation point and the vertex of the inner zone (**Fig. 3.7 A1-A4**):

	h≥0	h<0
E≥0	$\Delta g_{CP}(\rho_c)$	$-\Delta g_{CP1}(\rho_c-\rho_w)-\Delta g_C(\rho_c-\rho_w)+\Delta g_{CP2}(\rho_c)$
E<0	$\Delta g_{CP1}(\rho_c)+\Delta g_C(\rho_c)+\Delta g_{CP2}(\rho_c-\rho_w)$	$-\Delta g_{CP}(\rho_c-\rho_w)$ if $\Delta h>0$ $\Delta g_{CP}(\rho_c-\rho_w)$ if $\Delta h<0$

$$\Delta g_{CP1} = -\Delta g_{CP}\frac{h}{\Delta h}$$

$$\Delta g_{CP2} = \frac{\pi G\rho}{2\Delta h}\left(-\frac{R_{CP}{}^2 E}{\sqrt{R_{CP}{}^2+\Delta h^2}} + \Delta h\sqrt{R_{CP}{}^2+h^2} + h\sqrt{R_{CP}{}^2+\Delta h^2}\right) \quad (3.9)$$

$$\Delta g_C = \frac{\pi G\rho}{2\Delta h}\left(R_{CP}E - \Delta h\sqrt{R_{CP}{}^2+h^2} - h\sqrt{R_{CP}{}^2+\Delta h^2}\right)$$

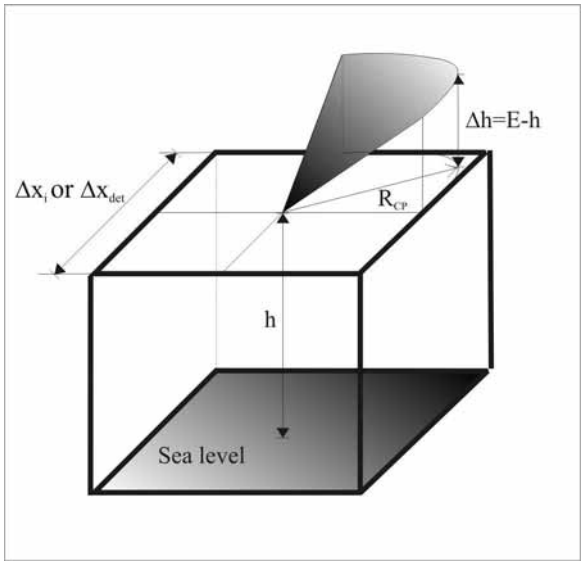

Fig. 3.6 *Inner zone ($R < \Delta x_i/2$ or $\Delta x_{det}/2$). The contribution to the topography correction (Bullard A-C) in the inner zone has two components. The first one is due to a flat-topped prism with square section (Δx_i or Δx_{det}-sided) and height equal to the elevation of the calculation point, h. For the second one, the inner zone is divided into four quadrants which dip continuously above or below the calculation point, i.e., a quarter of a conic prism with its vertical axis through the calculation point and height equal to the difference in elevation, $\Delta h=E-h$, where E is the elevation of the surrounding topography.*

The terms Δg_{CP1}, Δg_{CP2} and Δg_C of eq. 3.9 arise for calculation points near the coastline, where h and E have different signs (**Fig. 3.7, A2 and A4**). In that case, it is necessary to split the conic prism into three parts (**Fig. 3.7 B**). Δg_{CP1}, Δg_{CP2} represent the gravitational contribution of a quarter of a conic prism with height h and radius equal to the distance between the calculation point and the intersection between topography and sea level (R_{INT}), and a quarter of an annular sector of a conic prism ($R_{CP} > R > R_{INT}$) with height Δh, respectively. Δg_C is the contribution of a cylindrical sector ($R_{CP} > R > R_{INT}$) with height h, similar to the compartments used in the method of Hammer (1939). It must be pointed out that the quarters of the conic prism are discontinuous at his edges. However, for the most part the errors induced by this issue are small in the context of the accuracy requirements of this work.

At the limit between the intermediate and the distant zone, the prisms do not fill the whole space. The intermediate prisms go up to $R_i+\Delta x_i/2$ whereas the distant prisms start at $R_i+\Delta x_d/2$. In order to fill this space, R_{DZ}, the border prisms of the intermediate zone in eq. 3.6 are extended laterally by $R_{DZ}-(\Delta x_d+\Delta x_i)/2$ and are, therefore, not square except for the corner prisms. The value of R_{DZ} depends on the ratio $\Delta x_d/\Delta x_i$ and must be grater than or equal to $(\Delta x_d+\Delta x_i)/2$.

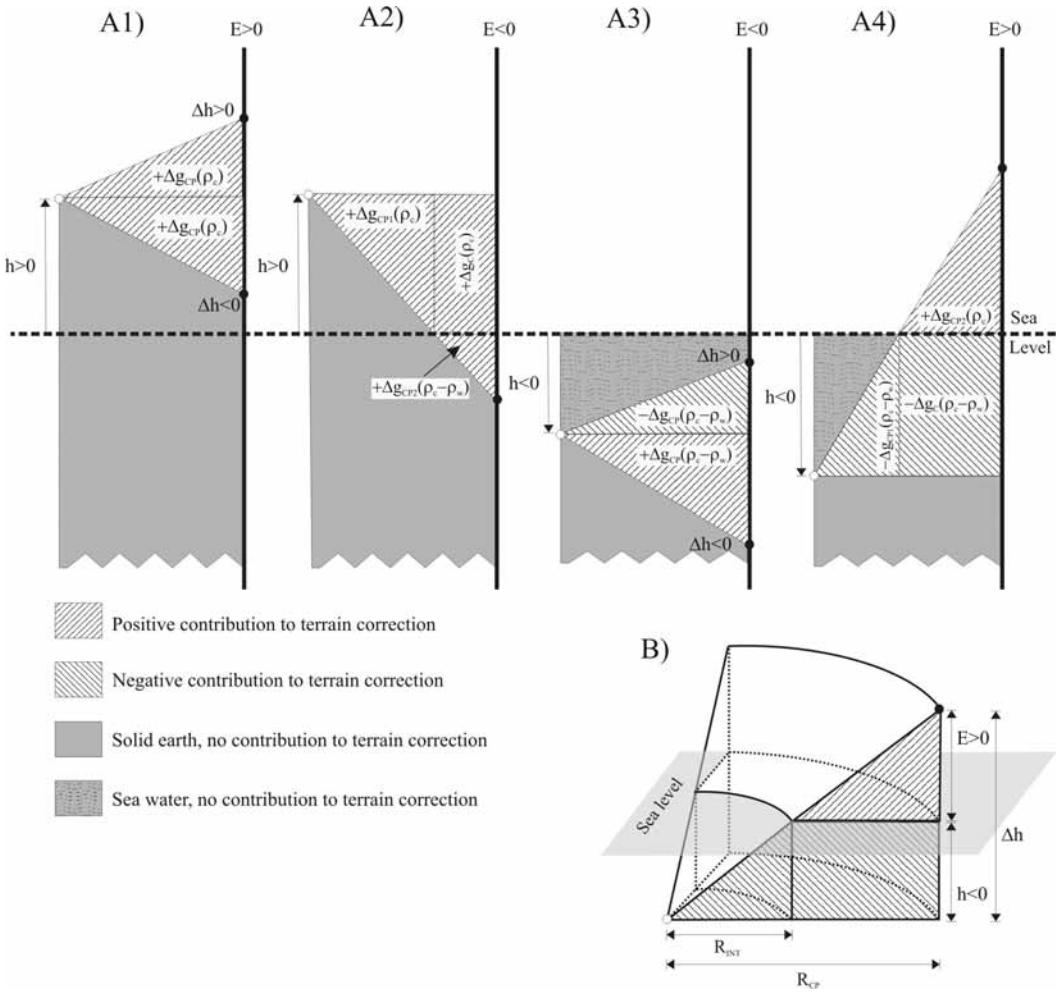

Fig. 3.7 *The terrain correction (Bullard C) in the inner zone, Δg_{CP}. Four cases (A1-A4) are possible depending on the sign of the elevation in the calculation point (white dot) and in the vertex of the inner zone (black dot). When the calculation point is near the coast line (A2 and A4) it is necessary to split each quarter of the inner zone into three parts, bearing in mind the distance between the calculation point and the intersection between the topography and the sea level, R_{INT} (B): a conic prism with height h and radius R_{INT} (Δg_{CP1}), an annular sector of a conic prism ($R_{CP} > R > R_{INT}$) with height Δh (Δg_{CP2}), and a cylindrical sector ($R_{CP} > R > R_{INT}$) with height h (Δg_C).*

The complete Bouguer correction is therefore applied to the free air anomaly in order to obtain the Bouguer anomaly using eq. 3.2 and eqs. 3.5-3.9:

$$\Delta g_B = \Delta g_{FA} + \Delta g_D + \Delta g_I + \Delta g_{IN} + BB \tag{3.10}$$

where Δg_{FA} is the free air anomaly, Δg_D is the contribution of the topography in the distant zone, Δg_I is the contribution of the topography in the intermediate zone, Δg_{IN} is the contribution of the topography in the inner zone, and BB is the Bullard B correction for the curvature of the Earth. For onshore

points, in some cases, the detailed intermediate zone, Δg_{IDET}, must be added to eq. 3.10.

Program description

FA2BOUG is a FORTRAN 90 code intended to obtain the Bouguer anomaly applying the topography correction (Bullard A-C) in a Cartesian free air grid. Therefore, it needs two input grid files, elevation and free air anomaly. It is also possible to start with slab-corrected Bouguer anomaly grid as input rather than a free air one. For onshore areas, new high resolution DEM are available for all continents (www2.jpl.nasa.gov/srtm/, Farr et al., 2007) and, therefore, the program can optionally read an extra file with the detailed topography of rugged zones.

FA2BOUG reads from the input file, *parameters.dat*, the variable *det* which indicates whether a detailed topography file onshore is expected (*det*=1) or not (*det*=0), the grid step for the intermediate and distant zones, Δx_i, Δx_d, the desired grid step for the output Bouguer anomaly grid, Δx_{Bg}, the reduction densities for the crust and the sea water, ρ_c, ρ_w, the number of points of the two regular grid files required (elevation and free air/slab-corrected Bouguer anomaly) in E-W and N-S directions, respectively, N x M, the limits of the intermediate and distant zones, R_i, R_d, the string variable land, which indicates if calculation must be done either for land and sea points (land=*'on'*) or only for sea points (land=*'off'*), and the variable Boug_slab, which indicates if the input gravity grid is Bouguer simple (Boug_slab=1) or free air anomaly (Boug_slab=0). If the detailed topography option is activated (*det*=1), the input file, *parameters.dat*, must contain also the following additional information: the number of points of the detailed topography grid file in E-W and N-S directions, respectively, N_{det} x M_{det}, and its grid step, Δx_{det}. The input elevation and free air ASCII files named *topo_cart.xyz* and *gravi_cart.xyz*, respectively, are expected to be in Cartesian coordinates, to have the grid step of the intermediate zone, Δx_i, and to cover a larger window than the desired output Bouguer anomaly grid. The last point is due to the fact that each calculation point needs to have grid points surrounding it at a distance of R_d at least. If necessary, an input detailed topography ASCII file named *topo_cart_det.xyz* can be provided. This file is expected to be in Cartesian coordinates and to have the grid step Δx_{det}. The limits of the spatial window of *topo_cart_det.xyz* must be at distance R_i of the limits defining the desired output Bouguer grid (**Fig. 3.8**). To perform a detailed calculation in a point using *topo_cart_det.xyz*, FA2BOUG needs to read the elevation in all grid points surrounding it at a distance of R_i. If any value is

missing, the program skips the calculation. Therefore, it is recommended to set nonnumeric values (NaN) in areas of relatively flat topography in order to reduce unnecessary computation time.

The expected format of elevation and free air input files is one column with data starting from the NW corner of the calculation area, which corresponds to (0,0) in the Cartesian reference system, and then going from West to East successively, ending at the SE corner, i.e. ((N-1) Δx_i, (M-1) Δx_i) in Cartesian coordinates. If the program reads a non numerical value (NaN) for the input gravity anomaly in a point, then it skips the calculation at this point. The output file, *Bouguer.xyz*, is expressed in Cartesian coordinates and covers a smaller area than the input files, ranging between (R_d, R_d) and ((N-1) Δx_i-R_d, (M-1) Δx_i-R_d), and has a grid step of Δx_{Bg} (**Fig. 3.8**). A similar output file containing the slab-corrected Bouguer anomaly, i.e. only Bullard A correction, is also produced (*Bouguer_slab.xyz*).

Global data base sets for elevation and free air anomaly (ftp://topex.ucsd.edu/pub, www2.jpl.nasa.gov/srtm/) are expressed in geographical coordinates. Thus, it is necessary to extract the data and to project them onto a Cartesian grid prior to start FA2BOUG calculation. This can be done using *FA2BOUG.job* script (for Linux), which prepare the input grids using Generic Mapping Tools (GMT, Wessel and Smith, 1998) software, and generates the input file *parameters.dat*. In addition, *FA2BOUG.job* plots the output Bouguer anomaly file (in postscript format) reading the file *lat_ex.dat*, which is generated by FA2BOUG and consists in one header with three fields: (N-1) Δx_i, (M-1) Δx_i and Δx_{Bg}. The format of the input files is the same that GMT uses when transforming grids into ASCII files.

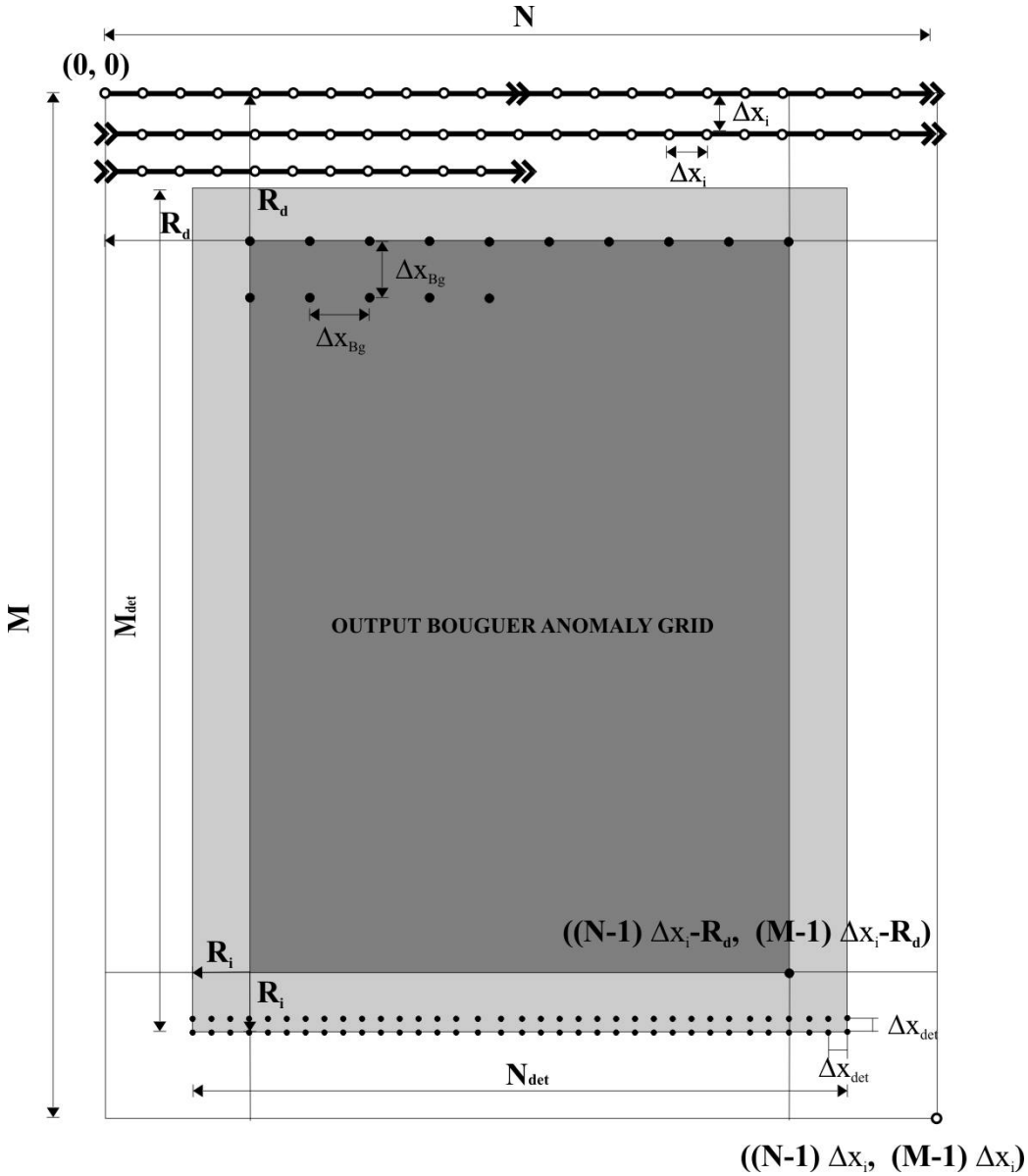

Fig. 3.8 *Scheme of the input and output files used by FA2BOUG. Two regular grid files (spacing Δx_i) of elevation and free air anomaly, in Cartesian coordinates, are required: topo_cart.xyz and gravi_cart.xyz, respectively. The expected format of these input files is one column with data starting at the NW corner (0, 0) and then going from West to East successively, ending at the SE corner, i.e. ((N-1) Δx_i, (M-1) Δx_i). The output file, bouguer.xyz, covers the smaller dark gray area ranging between (R_d, R_d) and ((N-1) Δx_i-R_d, (M-1) Δx_i-R_d) and has a grid step of Δx_{Bg}. Optionally, a detailed input topography ASCII file named topo_cart_det.xyz can be provided. This file is expected to be in Cartesian coordinates and to have the grid step Δx_{det}. The limits of the spatial window of topo_cart_det.xyz (light gray area) must be at a distance R_i of the limits defining the desired output Bouguer anomaly grid.*

Results: Bouguer anomaly map of the GAS region

With the aim of producing a complete Bouguer anomaly map of the GAS region, we have integrated several available gravity data sets. Onshore, in the Iberian Peninsula, Bouguer anomaly data come from the Spanish Instituto Geográfico Nacional. For these data, the Bouguer slab (Bullard A) and terrain (Bullard C) corrections were applied using a reduction density of 2670 kg/m^3 (Mezcua et al., 1996). In Morocco, available simple Bouguer anomaly data coming from Hildenbrand et al. (1988) were gridded to match the altimetric data before the terrain correction was applied. For the rugged topography in the Atlas Mountains we have calculated using a detailed topography grid (**Table 3.1**) extracted from SRTM data base (**Fig. 3.9**). The consequences of using SRTM instead the lower resolution ETOPO2 data base in rugged areas will be analysed later, in the Discussion section.

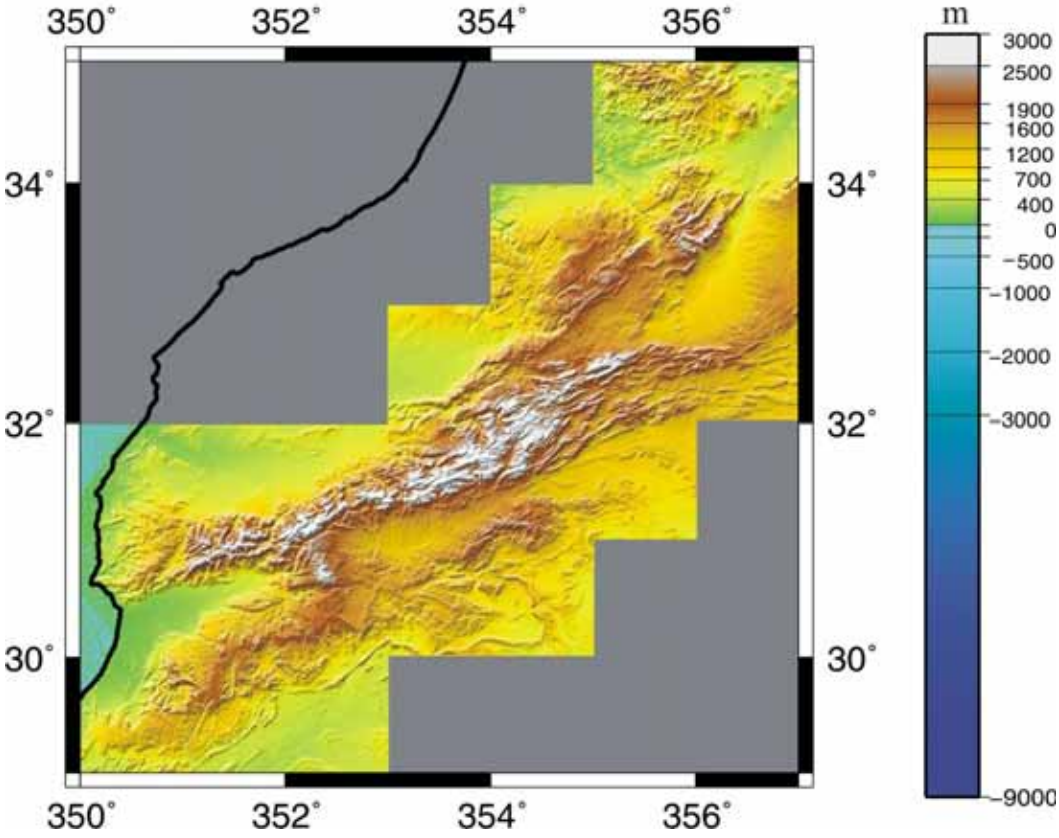

Fig. 3.9 *SRTM topography with a resolution of 3''x 3'' (about 90 m x 90 m) (Farr et al., 2007) used to compute the complete Bouguer correction in the Atlas Mountains.*

Offshore and in the rest of the African region Bouguer anomaly is calculated using FA2BOUG with the input parameters listed in **Table 3.1** and the

satellital free air anomaly data compilation by Sandwell and Smith (1997). As stated before, the use of a constant density for the topography instead of a variable density model can distort the resulting Bouguer anomaly (Flis et al., 1998). However, since a well-constrained regional density model of the study region is not yet available, we have preferred to use the standard constant value of 2670 kg/m^3 (**Table 3.1**). All the data are referred to the International Gravity Standardization Net of 1971 (IGSN71 gravity datum).

The resulting Bouguer anomaly map of the GAS zone is shown in **Fig. 3.10**. The minimum, maximum, mean and standard deviation values of the Bouguer anomalies are -159.43, 390.47, 19.04, 118.46, respectively. The western Atlantic oceanic domain is characterised by elevated anomaly values of 240-300 mGal, with a conspicuous maximum located in the Gorringe Bank (>360 mGal). A positive ENE-WSW trending maximum is also observed beneath the Guadalquivir Bank. In the Gulf of Cadiz, the accretionary wedge is depicted by a positive Bouguer anomaly with values ranging from -40 to 200 mGal from west to east. In the west Alboran Basin, near the Gibraltar Arc, we find an arcuate-shaped minimum (<-40 mGal), which can be correlated with Neogene sediment accumulation (Torne et al., 2000). In the central part of the basin, Bouguer anomaly reaches 40-120 mGal, increasing gradually eastwards (>160 mGal). The results obtained are coincident with earlier gravity studies in the Alboran Basin (Casas and Carbó, 1990 and references therein; Torne et al., 2000 and references therein). In the Iberian mainland, the most remarkable structure is an intensive Bouguer anomaly minimum ENE-WSW trending located beneath the Betics (<-120 mGal) caused by the combined effect of lateral variations in crustal thickness and low density sedimentary basins (Casas and Carbó, 1990). The 0 mGal isoline, which usually runs roughly parallel to the coastline, enters into the SW Iberian mainland perpendicular to the margin, along the Guadalquivir Basin, originating a noticeable positive anomaly in the area (>40 mGal).

In Africa, the background Bouguer anomaly is negative except for a narrow band located in the NW Atlantic Moroccan coast. Two conspicuous negative anomalies (<-120 mGal) are present in the African mainland: the first one located in the Rif and the Rharb Basin, and the second one, NE-SW trending, in the Atlas Mountains. The first negative anomaly trends nearly E-W, and affects more intensely the SE flank of the Rif. The negative anomaly in the Atlas is concentrated in the central High Atlas, decreasing moderately towards the Middle Atlas and the Anti Atlas. The eastern branch of the Atlas seems to lack a defined Bouguer anomaly signal.

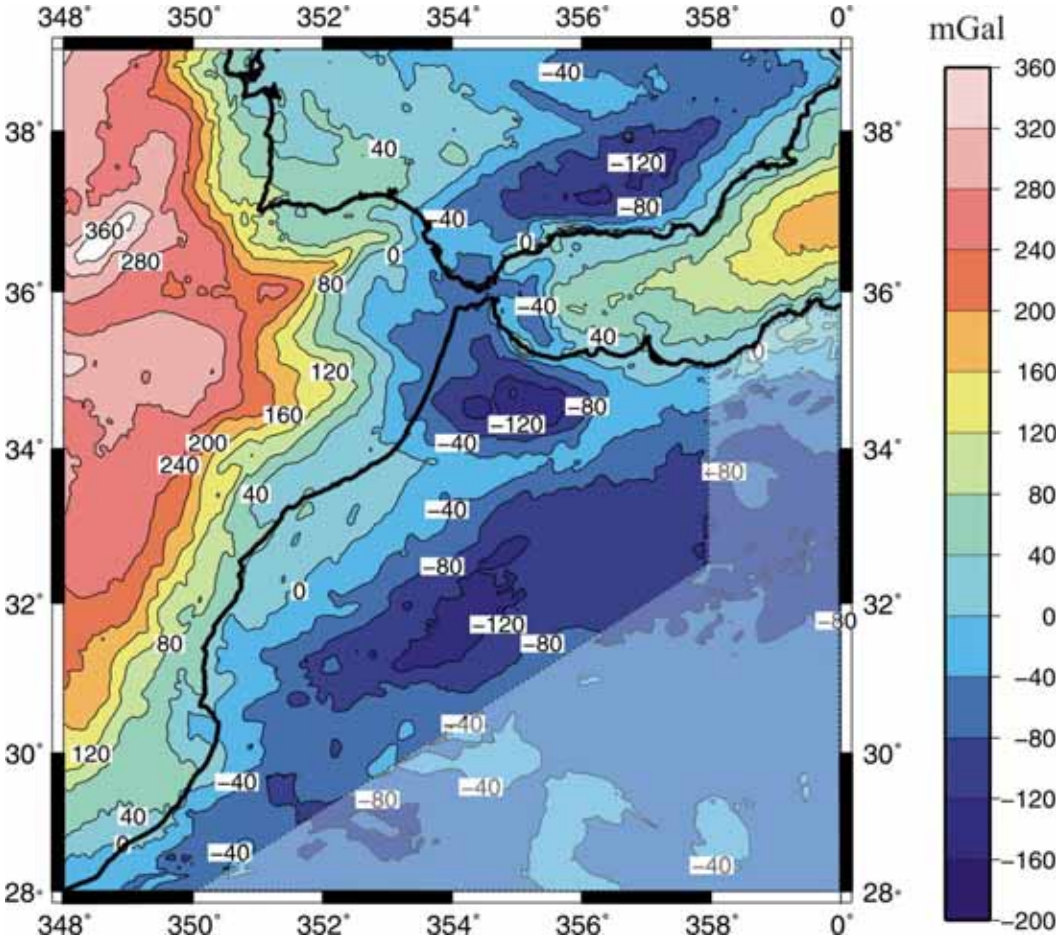

Fig. 3.10 *Bouguer anomaly map. Onshore, in the Iberian Peninsula and Morocco the Bouguer anomaly comes from Mezcua et al., (1996), and Hildenbrand et al., (1988), respectively (see details in the text). Offshore, and in the rest of the African region (shaded area,) Bouguer anomaly is calculated from the free air anomaly satellite data compilation by Sandwell and Smith (1997) using FA2BOUG (**Table 3.1**). Contour interval is 40 mGal.*

Discussion

In **Fig. 3.11** a map of the terrain (Bullard C) correction used to produce the Bouguer anomaly map of the study region is shown. Onshore, in Africa, the maximum (positive) corrections are present in elevated topography areas, particularly in the Atlas Mountains (up to 30 mGal), with the rest of the land characterized by a small terrain correction (<1mGal). Offshore, positive and negative Bullard C values can reach amplitudes higher than 20 mGal, and are widespread distributed. Those high offshore terrain correction values are coincident with the steeper bathymetric gradients, i.e. sea floor accidents (e.g.

Gorringe Bank, the Coral Patch Seamount) and some parts of the continental slope. Statistical analysis reveals that the average Bullard C correction value is 0.75 mGal with a standard deviation of 4 mGal, hence, 90 % of the values are comprised in the interval (-5.88, 7.28) mGal. The maximum correction is 43.7 mGal and the minimum -37.74 mGal (see histogram in **Fig. 3.11**).

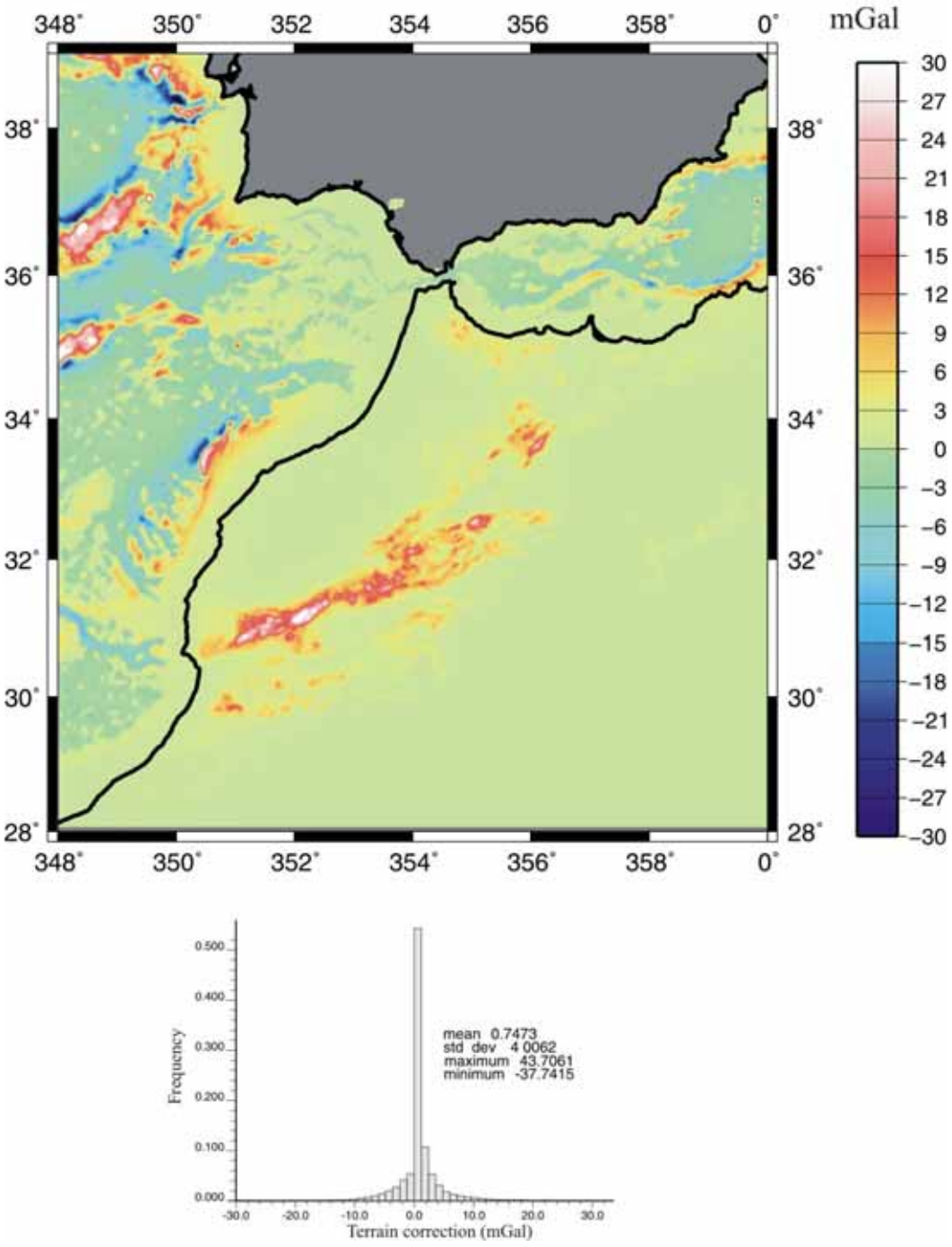

Fig. 3.11 *Map and histogram of the terrain (Bullard C) corrections obtained using FA2BOUG and the input parameters listed in* ***Table 3.1***.

The effect of the distant zone ($R_d > R > R_i$) in terrain (Bullard C) correction for R_i=20 km results in a long wavelength component, which is particularly important (> 10 mGal) in offshore areas with elevated bathymetric gradients, as can be seen in **Fig 3.12**. Therefore, not taking into account the topography beyond 20 km can lead to a considerable misfit in the terrain correction, especially in oceanic areas with rugged bathymetry.

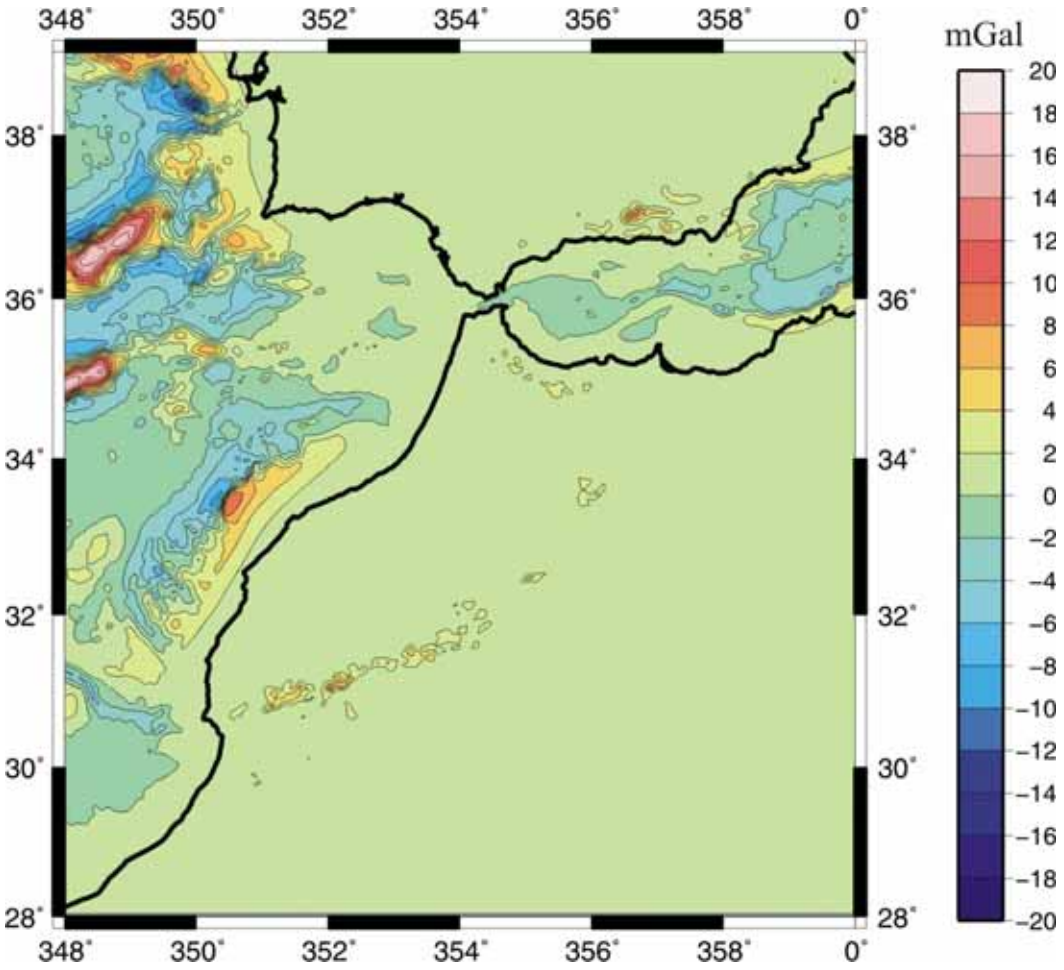

Fig. 3.12 *Map of the distant zone ($R_d > R > R_i$) contribution to terrain (Bullard C) correction using the input parameters listed in* ***Table 3.1****. Contours every 2 mGal.*

The contributions of the near zone are listed in **Table 3.3**. The first row corresponds to an inner zone $R < \Delta x_i/2$ using ETOPO2 elevation values, and stands for the whole study region. The second row corresponds to an inner zone $R < \Delta x_{det}/2$ using high resolution SRTM topography, and stands only for the Atlas Mountains (**Fig. 3.9**). The contribution of the inner zone in the first case ($R < \Delta x_i/2$) presents minimum and maximum values of -1.72 mGal and 3.44 mGal, respectively, with a mean value of 0.03 mGal and a standard deviation of 0.1

mGal (**Table 3.3**). In the second case ($R < \Delta x_{det}/2$), the contribution of the inner zone ranges between 0 mGal and 1.64 mGal, respectively, with a mean value of 0.08 mGal and a standard deviation of 0.14 mGal (**Table 3.3**). Therefore, the topography inner contribution must be taken into account to achieve a 1 mGal accuracy in the correction.

The effect of the curvature (Bullard B) correction is proportional to elevation and the density of reduction, as can be seen in eq. 3.2. As mentioned above, we do not include the term associated with the slab truncation in our curvature correction, since the infinite slab is not subtracted. The Bullard B corrections for the study area, without the slab truncation term, ranges from >4 mGal in the Atlantic abyssal plains to <-4 mGal in the most elevated parts of the Atlas Mountains (**Table 3.4**).

	Min	**Max**	**Mean**	**Std. dev.**
$R < \Delta x_i/2$	**-1.72**	**3.44**	**0.03**	**0.1**
$R < \Delta x_{det}/2$	**0**	**1.64**	**0.08**	**0.14**

Table 3.3. *Statistics for the inner zone contribution, $\Delta g_N - \Delta g_{IFTP}$, to terrain (Bullard C) correction. First row: ETOPO2 in the inner zone for the whole study region. Second row: high resolution SRTM data in the inner zone for the Atlas Mountains (**Fig. 3.9**). Minimum, maximum and mean values expressed in mGal.*

For some areas of rough topography the use of cell size of $\Delta x_i = 2$ km and, therefore an inner zone of 1 km, may result insufficient as short wavelength topography in the first km can induce large terrain corrections that would be underestimated. The release of new SRTM high-resolution DEM (www2.jpl.nasa.gov/srtm/, Farr et al., 2007) provides us with a powerful tool to overcome this difficulty, at least for land areas. To illustrate the importance of using an accurate DEM, we have selected a sub region of the western Atlas where terrain corrections are high (**Fig. 3.13 A**). In **Fig. 3.13 B** we show the terrain correction calculated using the SRTM topography in the intermediate ($R_i > R > \Delta x_i/2$), detailed intermediate ($\Delta x_i/2 > R > \Delta x_{det}/2$) and inner zones ($R < \Delta x_{det}/2$). The difference between this terrain correction and that calculated using ETOPO2 in the intermediate ($R_i > R > \Delta x_i/2$) and near zones ($R < \Delta x_i/2$) is shown in **Fig. 3.13 C**. In general, the use of the lower resolution DEM tends to

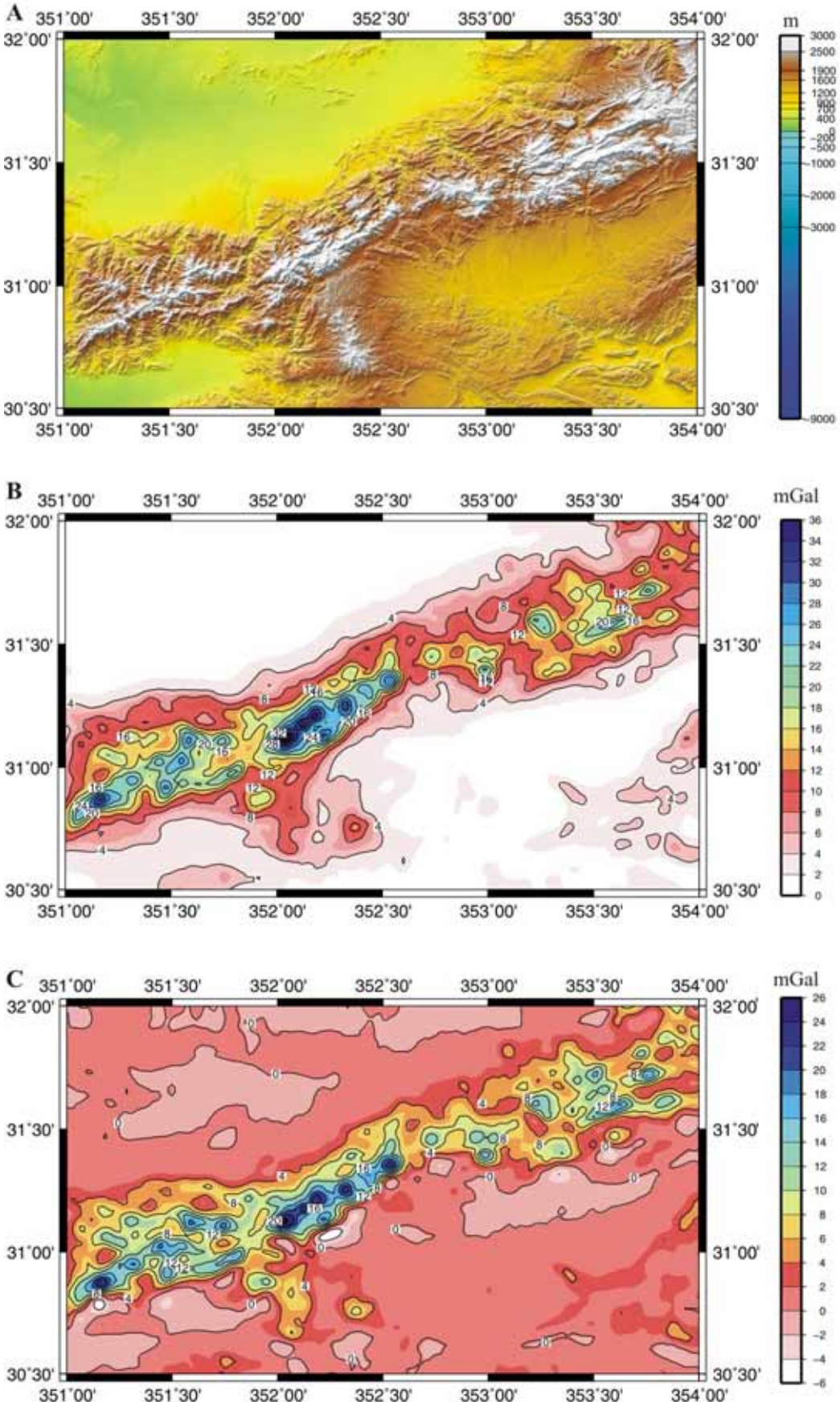

Fig. 3.13 (see next page)

Fig. 3.13 (previous page) *Comparison of terrain corrections (Bullard C) computed using different DEM.* ***A)*** *High resolution topography from SRTM (Farr et al., 2007) in a sub region of the Atlas Mountains.* ***B)*** *Terrain correction calculated using the SRTM topography in the intermediate ($R_i > R > \Delta x_i/2$), detailed intermediate ($\Delta x_i/2 > R > \Delta x_{det}/2$) and inner zones ($R < \Delta x_{det}/2$). Contours every 4 mGal.* ***C)*** *Difference between the terrain correction shown in B) and that calculated using instead ETOPO2 in the intermediate ($R_i > R > \Delta x_i/2$) and near zones ($R < \Delta x_i/2$). Contours every 4 mGal.*

underestimate the terrain correction, being this misfit higher for increasing terrain correction values (> 24 mGal locally). Therefore, the accuracy of the terrain correction will be strongly dependent on the resolution of the DEM used, at least for rugged topography areas.

	Min	**Max**	**Mean**	**Std. dev.**
BB	-4.51	4.4	0.02	1.74

Table 3.4. *Statistics for the curvature (Bullard B) correction without the slab truncation term. Minimum, maximum and mean values expressed in mGal.*

3.2.5 Surface heat flow

The SHF data used in this thesis come from different authors. In the Iberian Peninsula, we have used the data from Fernàndez et al., (1998), in the Alboran Basin from Polyak et al., (1996), in the Atlantic domain, near the Gorringe bank, from Verzhbitsky and Zolotarev (1989), and in North Africa, we have used the work of Rimi et al., (1998). In **Fig 3.14** we show a SHF map with the location of the available measurements. In the northern Gulf of Cadiz and Rharb Basin, the data present a wide scatter, mainly due to groundwater flow and hydrothermal activity, with average values of 70 mW/m^2. In the central and southern Gulf of Cadiz, SHF decreases to 40-50 mW/m^2 probably due to thrust stacking and rapid sedimentation. In the High Atlas and its southern slope, the few measurements cluster around 60 mW/m^2. The Rif is characterized by SHF values ranging 50-90 mW/m^2. In the east Alboran Basin, we find the highest SHF values (100-120 mW/m^2) probably due to Neogene extension. SHF increases towards the axial zone and eastwards, suggesting a hot lithosphere. In the SW

Iberian margin, a SHF relative maximum of 80 mW/m^2 centred in the Pyrite Belt is the better-constrained feature.

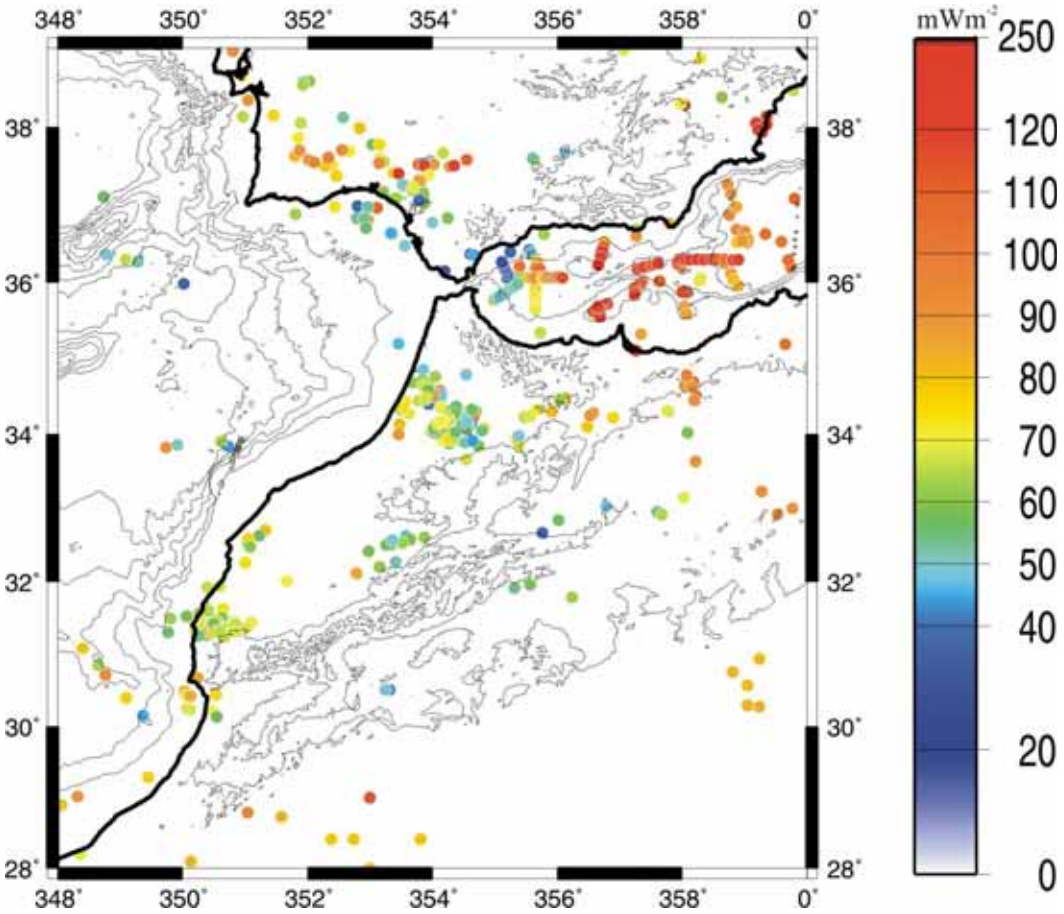

Fig. 3.14 *Surface heat flow data of the Gibraltar Arc System region. Data from Fernàndez et al., (1998), Polyak et al., (1996), Verzhbitsky and Zolotarev (1989), and Rimi et al., (1998).*

Chapter 4

JOINT INVERSION OF GEOID AND ELEVATION: 1D APPROACH

4. JOINT INVERSION OF GEOID AND ELEVATION: 1D APPROACH

4.1 INTRODUCTION

Elevation and geoid anomaly data have been widely used in different geophysical studies in the last years. Studies of geoid/topography ratio and admittance (its equivalent in the frequency domain) have been performed to investigate the depth and mechanism of isostatic compensation in oceanic plateaus and swells (e.g. Sandwell and Renking, 1988; Sandwell and MacKenzie, 1989; Wessel, 1993; Grevemeyer, 1999; Cserepes et al., 2000; Heller and Marquart, 2002). Other works have been focused on the viscous mantle flow associated with thermal convection and induced dynamic topography (e.g. Hager et al., 1985; Le Stunff and Ricard, 1995; Kiefer and Kellogg, 1998; Panasyuk and Hager, 2000). Furthermore, both geophysical observables have been employed to study the crustal thickness of other solid planets of the Solar System where, in contrast to the case of the Earth, no other geophysical data are available (e. g. Simons et al., 1994; Moore and Schubert, 1997; Sandwell et al., 1997; Wieczorek and Zuber, 2004). On the other hand, the coupling between elevation and thermal field in the context of isostasy has been used to study the continental deformation in convergent orogens (Sandiford and Powell, 1990; Zhou and Sandiford, 1992), and the lithospheric gravitational potential energy as a source of intraplate stress and associated deformation at both global and tectonic plate scales (Coblentz et al., 1994).

In this chapter, we present a straightforward method to automatically determine the crustal and lithospheric thickness using elevation and geoid anomaly data coupled with the temperature and density distributions under the following conditions: thermal equilibrium, local isostatic compensation of the lithosphere, and one-dimensionality. In this case, elevation reflects the average density of the lithosphere, whereas geoid anomaly is related to variations in the vertical dipole moment of the density. As a further constraint, we integrate the temperature distribution under steady state conditions considering radioactive heat production in the crust but neglecting it in the mantle. In our approach, we consider a four-layered model composed of crust and lithospheric mantle plus sea water (ρ_w =1030 kg/m^3) and asthenosphere (**Fig. 2.1**). For the crustal density, we assume a positive linear vertical gradient simulating the usual density increase

with depth due to pressure and mineralogical changes (e.g. upper vs. lower continental crust), while for the lithospheric mantle a temperature dependent density is considered, resulting in a negative linear gradient.

In the first part of the chapter, we present the theoretical aspects of our method. Then, we consider a synthetic model in the elevation-geoid space to analyse the dependence of the derived lithospheric structure on both observables. Estimates of the influence of root-mean-square (RMS) error in elevation and geoid anomaly are also considered. Finally, we investigate the effect of thermal parameters on the resulting lithospheric structure. In the second part, we apply our technique to the GAS region to provide a first approach to image the crustal and lithospheric thicknesses, and we compare them with previous works, particularly with seismic reflection/refraction and tomography. The study area has been the target of several geophysical studies (e.g. Banda et al., 1993; Torne et al., 2000; González-Fernández et al., 2001; Teixell et al., 2003; Zeyen et al., 2005) and is, therefore, a suitable candidate to test our method.

4.2 METHOD

If local isostasy holds and the wavelength of lateral density variations is large enough with respect to their depth, the geoid anomaly, N, is proportional to the dipolar moment of the vertical anomalous density distribution beneath the observation point for a flat-earth model (Ockendon and Turcotte, 1977; Haxby and Turcotte, 1978; Turcotte and Schubert, 1982; Doin et al., 1996; Strang van Hees, 2000). Then,

$$N = -\frac{2\pi G}{g} \int_{LC} z \cdot \rho(z)\, dz + N_0 \tag{4.1}$$

where G is the universal gravitational constant ($m^3\ s^{-2}\ kg^{-1}$), $\Delta\rho$ the density contrast and g is the terrestrial gravitational acceleration over the Earth's surface ($m\ s^{-2}$). The integration constant N_0 plays the role of a reference level, and is needed to adjust the zero level of the geoid anomalies.

The depths of the base of the crust and the lithosphere are related with elevation under local isostasy according to (Fullea et al., 2006):

$$z_c = \frac{\rho_a L_0 + E \cdot \left(\overline{\rho_c} - \rho_w\right) + z_L \cdot \left(\overline{\rho_m} - \rho_a\right)}{\overline{\rho_m} - \overline{\rho_c}} \tag{4.2}$$

where z_c is the depth of the crust-mantle boundary (Moho), z_L is the depth of the lithosphere-asthenosphere boundary (LAB), and $\overline{\rho_c}$ and $\overline{\rho_m}$ are the average densities of the crust and lithospheric mantle, respectively. All the depths are referred to the mean sea level and are positive downwards, whereas E is defined positive upwards (**Fig. 2.1**).

For the lithospheric mantle density, ρ_m, we consider a linear dependence on temperature based on Parsons and Sclater, (1977). Therefore:

$$\rho_m(z) = \rho_a\left(1 + \alpha\left[T_a - T_m(z)\right]\right) \tag{4.3}$$

where α is the linear coefficient of thermal expansion (K^{-1}), T_a is the temperature at the LAB, and $T_m(z)$ is the temperature at depth z in the lithosphere.

The temperature distribution within the crust with fixed temperature, T_s, at the surface of the Earth, and fixed heat flow, q_m, at the base of the crust is obtained solving eq. 2.18:

$$T^c(z) = T_s + \frac{q_m}{k_c}(z+E) + \frac{H_s}{2k_c}\left(E^2 - z^2 + 2z_c\left[z+E\right]\right) \tag{4.4a}$$

$$T^e(z) = T_s + \frac{q_m}{k_c}(z+E) + \frac{H_s h^2{}_r}{k_c}\left(1 - \exp\left(-\frac{(z+E)}{h_r}\right)\right) \tag{4.4b}$$

where k_c is the thermal conductivity of the crust, H_s is the crustal surface heat production, and h_r is the characteristic length scale of the heat production distribution. T^c and T^e are the temperature profiles using constant and exponentially decreasing heat productions throughout the crust (eq. 2.17).

The temperature at the crust-mantle boundary, T_{mh}, is calculated stating z = z_c in eq. 4.4, thus:

$$T_{mh} = T_s + \frac{q_m}{k_c}(z_c + E) + \frac{f}{k_c} \tag{4.5}$$

where f=f_c for a constant heat production, and f=f_e for an exponentially decreasing heat production, and

$$\begin{aligned} f_c &= H_s \frac{(E+z_c)^2}{2} \\ f_e &= H_s h_r^2\left(1 - \exp\left(-\frac{(z_c+E)}{h_r}\right)\right) \end{aligned} \tag{4.6}$$

For the lithospheric mantle, we can consider a negligible heat production and, therefore, a linear temperature profile (Lachenbruch and Morgan, 1990). This means that the heat flow is constant within the lithospheric mantle and equal to:

$$q_m = k_m \frac{T_a - T_{mh}}{z_L - z_c} \tag{4.7}$$

where k_m is the thermal conductivity of the lithospheric mantle. We can introduce eq. 4.7 into eq. 4.5 to obtain the temperature at the base of the crust as a function of E, z_c, z_L, and other thermal parameters:

$$T_{mh}(E, z_c, z_L) = \frac{(z_L - z_c)\theta + \delta}{z_c \Delta k + z_L k_c + E k_m} \tag{4.8}$$

where

$$\theta = \left(k_c T_s + f\right)$$

$$\delta = k_m T_a (z_c + E)$$

$$\Delta k = k_m - k_c$$

The average value of the lithospheric mantle density, $\overline{\rho_m}$, can be determined by integrating eq. 4.3 between z_c and z_L :

$$\overline{\rho_m} = \frac{1}{z_L - z_c} \int_{z_c}^{z_L} \rho_m(z) dz = \rho_a \left(1 + \frac{\alpha}{2}\left[T_a - T_{mh}\right]\right) \tag{4.9}$$

The generalized isostasy equation including the thermal field is obtained combining eq. 4.9 and eq. 4.8 with eq. 4.2:

$$z_L^{\,2}(T_a k_c - \theta) + z_L \left(z_c \left(T_a (k_m - 2k_c) + 2\theta\right) - \delta + T_a E k_m - \frac{2k_c}{\rho_a \alpha}\left[(\rho_a - \overline{\rho_c}) z_c + \eta\right]\right)$$

$$+ \left(z_c \left[\delta - T_a (z_c \Delta k + E k_m) - z_c \theta\right] - \frac{2}{\rho_a \alpha}\left[(z_c \Delta k + E k_m)(\eta + (\rho_a - \overline{\rho_c}) z_c)\right]\right) = 0 \tag{4.10}$$

where

$$\eta = -\left(\rho_a L_0 + E(\overline{\rho_c} - \rho_w)\right)$$

and only the real solutions of equation 4.10 are meaningful.

The geoid anomaly from eq. 4.1 for a four-layered lithospheric model in which the density of the crust varies linearly with depth, and the density of the lithosphere mantle does with temperature is:

$$N = -\frac{\pi G}{g}\left[\begin{array}{l}\rho_w E^2 + \frac{2\beta}{3}\left(z_c^3 - \left|E^3\right|\right) + \left(\beta E + \rho_c{}^T\right)\left(z_c^2 - E^2\right) + \left(z_{\max}^2 - z_c^2\right)\rho_a + \\ \rho_a \alpha \frac{T_a - T_{mh}}{3}\left[\left(z_L - z_c\right)\left(z_L + 2z_c\right)\right]\end{array}\right] + N_0$$

(4.11)

where

$$\beta = \frac{\rho_c{}^B - \rho_c{}^T}{z_c + E}$$

z_{max} is the depth of the compensation level, and $\rho_c{}^T$ and $\rho_c{}^B$ are the densities of the top and the bottom of the crustal layer. Since we use absolute densities, we need to determine the integration constant, N_0, to tie the zero level of the geoid anomalies (see Appendix A). The joint resolution of equations 4.10 and 4.11 allows us to calculate the average lithospheric mantle density, $\overline{\rho_m}$, as well as the depths of the Moho, z_c, and LAB, z_L, which simultaneously fit the elevation and the geoid anomaly under local isostasy. To obtain the aforementioned lithospheric variables, constant values of N_0, the average crustal density and its gradient, β, must be assumed. Owing to the non-linearity of the system of equations formed by 4.10 and 4.11, we adopt an iterative scheme to obtain the lithospheric structure with the following steps:

1) Estimate initial values for z_c and z_L assuming a constant density for the crust and lithospheric mantle, and a given value for N_0 (i.e. using equations A2 and A3 from Appendix A).

2) Use the initial value of z_c to calculate the depth of the LAB, z_L, which fits local isostasy coupled with thermal field using eq. 4.10.

3) Calculate the temperature at the Moho, T_{mh}, as a function of z_c and z_L from the previous step using eq. 4.8.

4) Calculate the geoid anomaly with eq. 4.11 using the lithospheric variables, z_c, z_L and T_{mh} from the previous steps.

5) Subtract the calculated and observed geoid anomalies to obtain a residual geoid anomaly. Depending on the sign of the residual, the initial value of

z_c is increased or decreased, and steps 2) to 5) are repeated until the residual geoid anomaly becomes smaller than a predefined value.

4.3 SENSITIVITY OF THE METHOD

To perform a sensitivity test of our algorithm we introduce the elevation-geoid space (E-N thereafter). E-N diagrams are contoured surfaces of the calculated lithospheric variables (i.e. the Moho and LAB depths, and the mean lithospheric mantle density) plotted as a function of elevation and geoid anomaly. We consider two different heat production models in which heat sources are constantly distributed throughout the crust or exponentially decreasing with depth, respectively (eq.2.17). The heat production parameters have been selected in such a way that for a 30 km thick crust the integrated crustal heat production is the same in both models. **Table 4.1** summarizes the parameters used in the sensitivity test.

Parameter	**Symbol**	**Value**
Density at the top of the crust	ρ_c^T	2640 kg/m^3
Density at the bottom of the crust	ρ_c^B	2920 kg/m^3
Lithospheric mantle density	ρ_m	ρ_a [1-α (T- T_a)] kg/m^3
Asthenosphere density	ρ_a	3200 kg/m^3
Sea water density	ρ_w	1030 kg/m^3
Compensation level depth	z_{max}	300 km
Moho depth of the reference column	z_{cREF}	31.4 km
LAB depth of the reference column	z_{LREF}	150.8 km
Linear coefficient of thermal expansion	α	3.5 10^{-5} K^{-1}
Crustal surface heat production	H_s	
*Constant		1.25 10^{-6} Wm^{-3}
*Exponentially decreasing		2.5 10^{-6} exp (-(z+E)/15000) Wm^{-3}
Crustal thermal conductivity	k_c	2.5 W m^{-1} K^{-1}
Mantle thermal conductivity	k_m	3.2 W m^{-1} K^{-1}
Surface temperature	T_s	0ºC
Temperature at the LAB	T_a	1350 ºC

Table 4.1. *Parameters used in the inversion of elevation and geoid anomaly.*

A key parameter in the joint inversion of elevation and geoid data is the reference level for geoid anomalies, N_0, which depends on the particular configuration of the lithospheric column considered as reference. The range of meaningful solutions in the E-N space will vary depending on the configuration of the considered reference lithospheric column. Two conditions must be fulfilled: a) the existence of the lithospheric mantle layer, i.e. $z_L > z_c$; and b) the existence of the crust layer i.e. $|E| < z_c$ if $E<0$ (Appendix A).

In the present test, elevation varies in the range of -5200 to +2200 m, whereas the geoid anomaly varies in the range of -8 m to 15 m covering a wide variety of regions. In the figures presenting the results (**Figs. 4.1 and 4.2**), hatched areas represent the combination of E and N values for which the aforementioned conditions are not satisfied and, hence, no solution exists for a given reference lithospheric column (**Table 4.1**).

The left-hand diagrams in **Fig. 4.1 (A, B, C)** correspond to models with constant crustal heat production distribution, whereas right-hand diagrams (**Fig. 4.1 D, E and F**) correspond to models with an exponentially decreasing crustal heat production. The rows from top to bottom correspond to depth to Moho, depth to LAB, and average lithosphere mantle density, respectively. Regardless of the heat production model considered, three features can be observed in **Fig. 4.1**: i) an increase in elevation (E) keeping the geoid height (N) constant implies a thicker crust and lithosphere and, conversely, an increase in N maintaining E constant implies a crustal and lithospheric thinning; ii) for the same differences in N or E, variations in the crustal and lithospheric thickness are larger in emerged areas ($E>0$) than in submerged regions ($E<0$), which would imply, theoretically, a higher dispersion of E and N values over oceans than over continents for similar variations of crustal or lithospheric thicknesses; and iii) the crustal thickness influences mainly the elevation, especially for $E>0$, whereas the lithospheric mantle thickness has also a strong influence on the geoid anomaly variations, particularly for $E<0$.

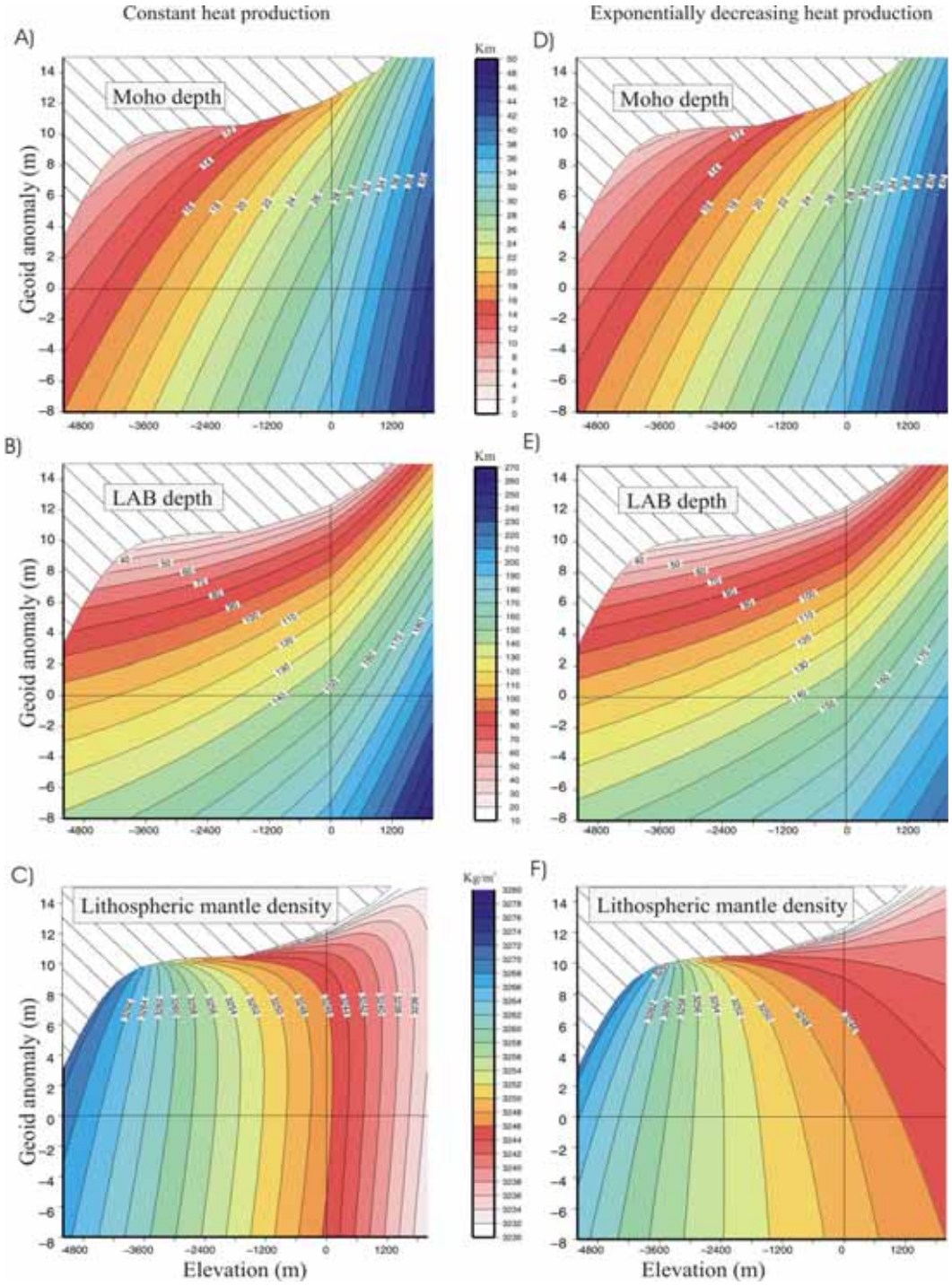

Fig. 4.1 *Elevation-geoid diagrams (E-N). For the crust, a constant density of 2780 kg/m^3 is assumed, whereas in the lithospheric mantle a temperature dependent density is considered.* ***A, B and C*** *correspond to constant heat production in the crust, and* ***D, E and F*** *are associated with an exponentially decreasing heat production model (**Table 4.1**). Hatched areas in the upper left corner represent the combination of E and N values for which no solution is found, for the given reference lithospheric column.* ***A, D)*** *Moho depth. Isolines every 2 km.* ***B, E)*** *LAB depth. Contour interval is 10 km.* ***C, F)*** *Mean lithospheric mantle density. Isolines every 2 kg/m^3.*

As regards the radiogenic heat production model (constant or exponential decrease), the resulting Moho depth does not show major differences with respect to the constant heat production model (**Figs. 4.1 A and D**). In the case of LAB depth, differences are only apparent for E>0, especially for negative geoid anomaly values, where the constant heat production model predicts a thicker lithosphere and is more sensitive to E and N variations (**Fig 4.1 B and E**). The E-N diagrams for the mean lithospheric mantle density are shown in **Figs. 4.1 C and F**. Since $\overline{\rho_m}$ is inversely proportional to the temperature at the Moho, T_{mh}, these diagrams can be regarded as an inverse E-N plot of T_{mh}. The differences between the constant and exponentially decreasing heat production models are striking for E>0. In this area, $\overline{\rho_m}$ (T_{mh}) variations are nearly independent of the geoid anomaly for the constant heat production model (**Fig. 4.1 C**), whereas for the exponential model, $\overline{\rho_m}$ (T_{mh}) shows smooth changes with E and N except for elevated N values near the "forbidden" region of the E-N diagram, where the geoid anomaly is noticeably influenced by the hot and less dense lithosphere (**Fig. 4.1 F**). For E<0, in the two heat production models, $\overline{\rho_m}$ (T_{mh}) variations are strongly controlled by the bathymetry. Higher densities/lower Moho temperatures correspond to deeper bathymetries.

We estimated the sensitivity of our calculations for the Moho (Δz_c) and LAB (Δz_L) depths induced by the typical RMS error of elevation and geoid anomaly databases. The vertical accuracy of elevation data from ETOPO2 Global Data Base (Smith and Sandwell, 1994; Sandwell and Smith, 1997; Hastings and Dunbar, 1999) is characterized by an RMS error of 18 m onshore and of 200 m offshore. Geoid anomaly data from the EGM96 spherical harmonic global model (Lemoine et al., 1998) have a RMS error of 36 cm. For each point we considered the RMS errors of the input elevation and geoid anomaly data, and calculated the change (uncertainty) induced in both the Moho and LAB depths associated to such errors. In general, the strongest uncertainties arise for high N values in a narrow band near the "forbidden" region (**Fig. 4.2**). With respect to the crust, for E>0, Δz_c is (0.5-2) km, the larger uncertainties being restricted to high N values (**Fig 4.2 A**). For E<0 the uncertainties in z_c range from 2 km to 4 km, with the maximum values located near the "forbidden" region (**Fig. 4.2 A**). The uncertainty in the lithospheric thickness for E>0 is smaller than 10 km almost everywhere except for high N values (**Fig. 4.2 B**). For E<0, Δz_L is between 6 km and 15 km except for high N values (**Fig. 4.2 B**). The higher magnitude of both

Δz_c and Δz_L for E<0 is due to the fact that the RMS for bathymetry is typically one order of magnitude larger than RMS error for topography.

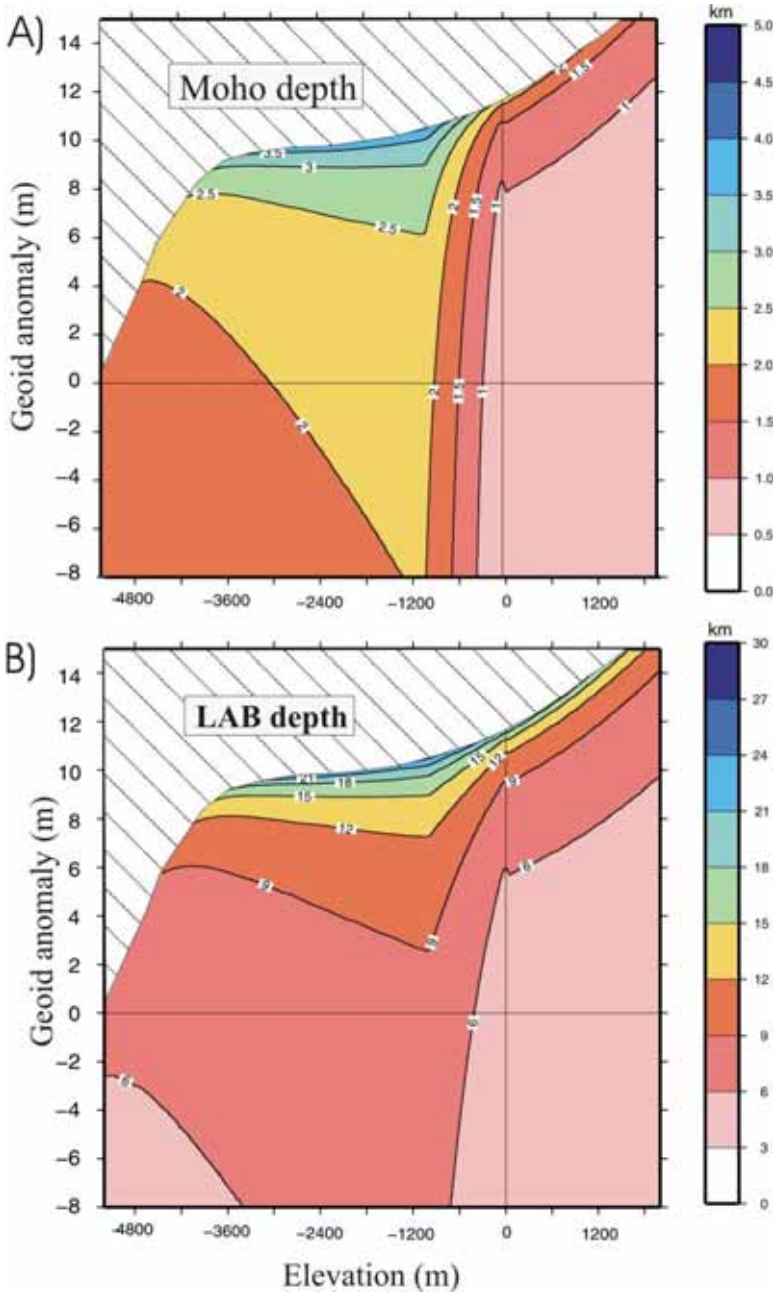

Fig. 4.2 *Elevation-Geoid diagrams for the estimated uncertainty in the Moho (Δz_c) and LAB (Δz_L) depths induced by RMS errors of elevation and geoid anomaly data, considering an exponentially decreasing heat production model in the crust (**Table 4.1**). Hatched areas in the upper left corner represent the combination of E and N values for which no solution is found, for the given reference lithospheric column. **A)** Moho depth uncertainty. Isolines every 0.5 km. **B)** LAB depth uncertainty. Contour interval is 3 km.*

As stated above, the reference level for the geoid anomaly, N_0, depends on the reference lithospheric column selected. In general, the thicker the reference column the deeper the Moho and LAB depths obtained. If we vary by ±1 km the crustal thickness of the reference column (which implies a lithospheric thickness change of ±9 km due to the isostasy constraint, eq. 4.10), N_0 changes roughly by ±1.5 m. Such variation in the reference level affects the resulting lithospheric structure in different ways, depending on the elevation and geoid anomaly values (i.e. the position in the E-N diagram). For instance, if E= -4 km and N=-5 m, z_c varies by ±1 km and z_L by ±10 km, whereas for E= 1.5 km and N=10 m, z_c varies by ±1.5 km and z_L by ±15 km (**Fig. 4.3**), which indicates that near the "forbidden" region the influence of N_0 variations is more important.

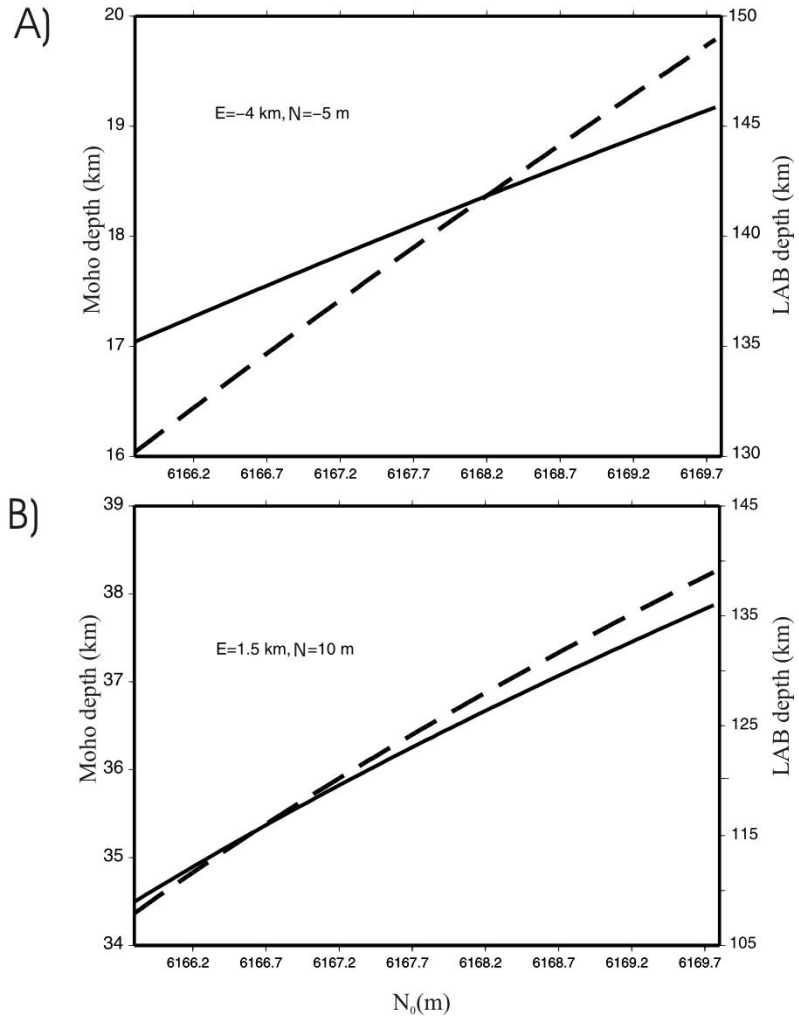

Fig. 4.3 *Variation of the Moho (solid line, z_c) and LAB (dashed line, z_L) depths in relation to a varying reference level for geoid anomalies, N_0.* ***A)*** *Lithospheric column with E= -4 km, N= -5 m.* ***B)*** *Lithospheric column with E= 1.5 km, N= 10 m.*

Finally, we assessed the effect of varying some of the thermal parameters on the results obtained. The tests were performed for a lithospheric column with elevation and geoid anomaly equal to zero, and an exponentially decreasing distribution of heat sources in the crust. The thermal parameters were varied within geologically meaningful ranges. Afonso et al. (2005) suggest that the coefficient of thermal expansion, α, may vary from about $3 \cdot 10^{-5}$ K^{-1} for an Archaean lithosphere to $3.8 \cdot 10^{-5}$ K^{-1} for a Phanerozoic continental and oceanic lithosphere. Consequently, we vary the coefficient of thermal expansion in the range of $[3\text{-}4] \cdot 10^{-5}$ K^{-1}. For the crustal surface heat production, H_s, and crustal and lithospheric mantle thermal conductivities, k_c and k_m, we tested values between $[1\text{-}3] \cdot 10^{-6}$ W m^{-3}; [2-3] W m^{-1} K^{-1}; and [2.8-3.4] W m^{-1} K^{-1}, respectively (Fernàndez et al., 1998b; Torne et al., 2000; Fernàndez et al., 2004; Zeyen et al., 2005). The resulting lithospheric thickness is mostly affected by α (~12 km) and, to a lesser extent, by H_s and k_c (6-8 km). We observed that the LAB depth decreases almost linearly with increasing α and k_c, and decreasing H_s values. In addition, we found that the Moho depth is not much affected (~1km) by variations of any of the thermal parameters considered, and that changes in k_m have no relevant consequences on either z_c or z_L.

4.4 MODELLING RESULTS

The method based on the joint inversion of elevation and geoid anomaly data has been applied to the GAS region with several initial considerations. For the lithospheric mantle, a temperature-dependent density was considered according to equations 4.3 and 4.9. In the crust, an exponentially decreasing distribution of heat sources was assumed. The maximum compensation level, z_{max}, was set to 300 km. The rest of the model parameters are presented in **Table 4.1**. As discussed by Fullea et al. (2006), the use of a uniform crustal density leads to local misfits in the model that can be related to lithological changes (large sediment accumulations, changes in crustal domains, etc.). Thus, we assume an average crustal density of 2780 kg/m^3 in the study area except for four sub regions, where the average crustal density was redefined: 2820 kg/m^3 in the SW Variscan crust of the Iberian Peninsula (Fernàndez et al., 2004), 2830 kg/m^3 in the NW Moroccan margin (Contrucci et al., 2004), 2670 kg/m^3 in the central Alboran Basin and 2700 kg/m^3 in the eastern Alboran Basin (Polyak et al., 1996, Torne et al., 2000) (**Fig 4.4**).

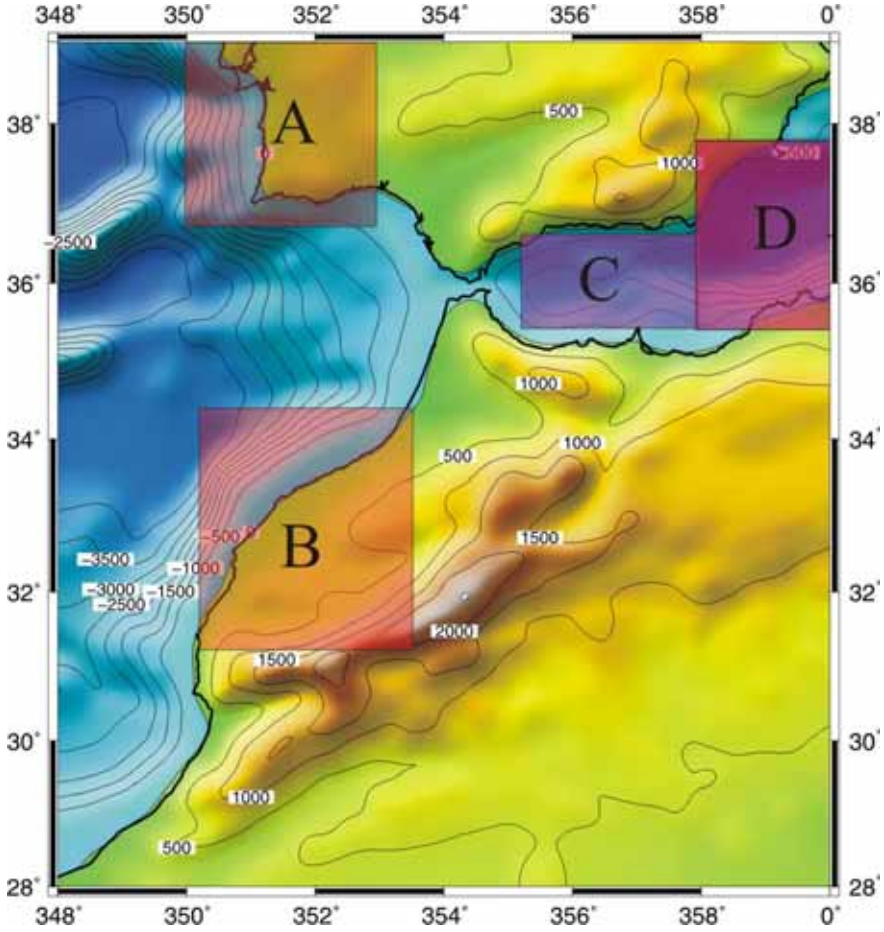

Fig. 4.4 *Elevation map from ETOPO2 Global Data Base filtered applying a low-pass filter to eliminate short wavelengths (<100 km). Contours every 500 m. Shaded boxes indicate areas where the average crustal density used in the model (**Table 4.1**) was redefined: A: 2820 kg/m^3 in the SW Variscan crust of the Iberian Peninsula; B: 2830 kg/m^3 in the NW Moroccan margin; C: 2670 kg/m^3 in the central Alboran Basin; D: 2700 kg/m^3 in the eastern Alboran Basin.*

It is clear that short wavelengths are partly supported by the rigidity of the lithosphere. In most parts of the area, the rigidity seems to be relatively small, corresponding to an elastic plate of a thickness of up to 10 km (e.g. Cloetingh et al., 1992; Garcia-Castellanos et al., 2002; Zeyen et al., 2005). Such a plate may support a significant part of the topography with wavelengths of up to 100 km. Therefore, we applied a low-pass filter to elevation data to eliminate the short wavelengths (<100 km) that would produce unrealistic effects in our model.

4.4.1 Crust

The crustal structure calculated from elevation, geoid anomaly and thermal field, is shown in **Fig. 4.5 A**. The depth to the crust-mantle boundary, z_c

is less than 16 km in the easternmost part of the Alboran Basin, towards the Algerian Basin. Beneath the central Alboran Basin, the Moho is rather flat (20-18) km, while near the Gibraltar Arc, z_c is about 32 km. The Betics are characterized by a crustal thickness of 34-36 km, shallowing abruptly southwards, towards the Alboran Basin. The crustal thickness in the SW Iberian Peninsula is about 28-30 km. In northern Africa, the Rif and Atlas Mountains are underlain by a thick crust, with Moho depths of >36 km and >38 km, respectively. The crust-mantle boundary shallows towards the Moroccan margin, where z_c is ~26 km, and towards the African Craton, where z_c is 34 km, with smooth lateral variations. In the Atlantic domain, the Moho depth is 12-16 km in the abyssal plains and 26-32 km in the Gulf of Cadiz region.

Seismic refraction surveys carried out along the southern Iberian margin indicate that the crust thins from ~38 km beneath the central Betics (Banda and Ansorge, 1980; Banda et al., 1993) to 22-25 km under the south-Iberian coast, and <15 km in the centre of the Alboran Basin (Hatzfeld, 1976; Banda and Ansorge, 1980). Other works based on gravity modelling (Torne et al., 1992) and seismic interpretation and backstripping analysis along profiles (Watts et al., 1993) propose a slightly thicker crust of 17-20 km in the central Alboran Basin. A 3D gravity modelling study focused in the Alboran Basin suggests a 30-32 km thick crust beneath the Gibraltar Arc, thinning to less than 12 km in the easternmost part of the Alboran Basin, with a relatively constant Moho depth of about 18 km in the central part of the basin (Torne et al., 2000). Medialdea et al., (1986) obtained a similar value of about 30 km for the crustal thickness in the Gibraltar Arc. Our results coincide with these studies in the Gibraltar Arc but show a deeper Moho in the central and eastern parts of the Alboran Basin.

Below the Rif, the crust reaches a maximum thickness of 40 km according to Giese and Jacobshagen (1992), although other works suggest ~36 km based on gravity, elevation, heat flow and seismic data (Torne et al., 2000), which is in line with our results. In the Atlas, tectonic shortening is moderate and poorly correlated with topography, suggesting that the crustal root beneath the Atlas Mountains is not deep enough to isostatically support the high topography. In that context a thin, hot, low density lithosphere has been invoked in order to achieve full isostatic compensation (Seber et al., 2001; Teixell et al., 2003; Frizon de Lamotte et al., 2004; Teixell et al., 2005; Zeyen et al., 2005). Available seismic data indicate a maximum crustal thickness of (38-39) km beneath the most elevated parts of the Atlas (Makris et al., 1985; Wigger et al., 1992), which is in agreement with our results. Recent wide-angle reflection and refraction seismic

data along a NW-SE profile from the oceanic Jurassic crust to the NW Moroccan continental margin show that the Moho deepens from 15 km beneath the oceanic crust to 35 km under the African continent (Contrucci et al., 2004). Our results are in agreement with this work in the oceanic Jurassic domain, although we obtain a thinner crust beneath the Moroccan continental crust.

The IBERSEIS deep seismic profile indicates that the crustal thickness varies from 30 to 35 km in the SW Iberian Peninsula, near the Gulf of Cadiz (Simancas et al., 2003). A work based on the reinterpretation of seismic refraction/wide-angle reflection profiles indicates a remarkable crustal thinning from 30 km under the Iberia mainland to less than 15 km offshore, in the Horseshoe Abyssal Plain, over a horizontal distance of 120 km (González-Fernández et al., 2001). The same authors propose a Moho depth of 22-30 km under the Gulf of Cadiz. Recent 2D integrated lithospheric modelling suggests a maximum crustal thickness of about 30 km under the SW Iberian Margin (Fernàndez et al., 2004). Our results are consistent with earlier works in the eastern part of the Gulf of Cadiz but show a slightly thicker crust in its central part.

4.4.2 Lithospheric mantle

Fig. 4.5 B shows the results for the thickness of the lithosphere. The most striking feature is the NE-SW trend of the LAB relief, which depicts two elongated areas with a relatively thin lithosphere separated by a region of thick lithosphere. The lithospheric thinning affects the SW Iberian Peninsula (~95 km) and the Coral-Patch regions, as well as the Atlas Mountains and the eastern Alboran Basin (80-90 km). On the other hand, the thick lithosphere is located beneath the Gulf of Cadiz and the Rharb Basin (>160 km). This thickening continues along a NE-SW strip and affects the western Betics and the NW Atlantic margin of Morocco (130-140 km). Towards the SE, beneath the African Craton, the lithosphere thickens steadily to depths of more than 180 km.

Studies on the deep lithospheric structure and the LAB depth of the Atlantic-Mediterranean transition region are relatively scarce. According to Torne et al. (2000), the lithosphere thins from 140 km in the Gibraltar Arc, Betics and Rif to < 45 km in the easternmost part of the Alboran Basin. A noticeably thickened lithosphere of 160-190 km is imaged beneath the Gulf of Cadiz in a recent work that integrates surface heat flow, elevation, gravity and geoid data along a NW-SE transect running from the SW Iberian Peninsula to the African Craton (Zeyen et al., 2005). These authors also report a pronounced lithospheric

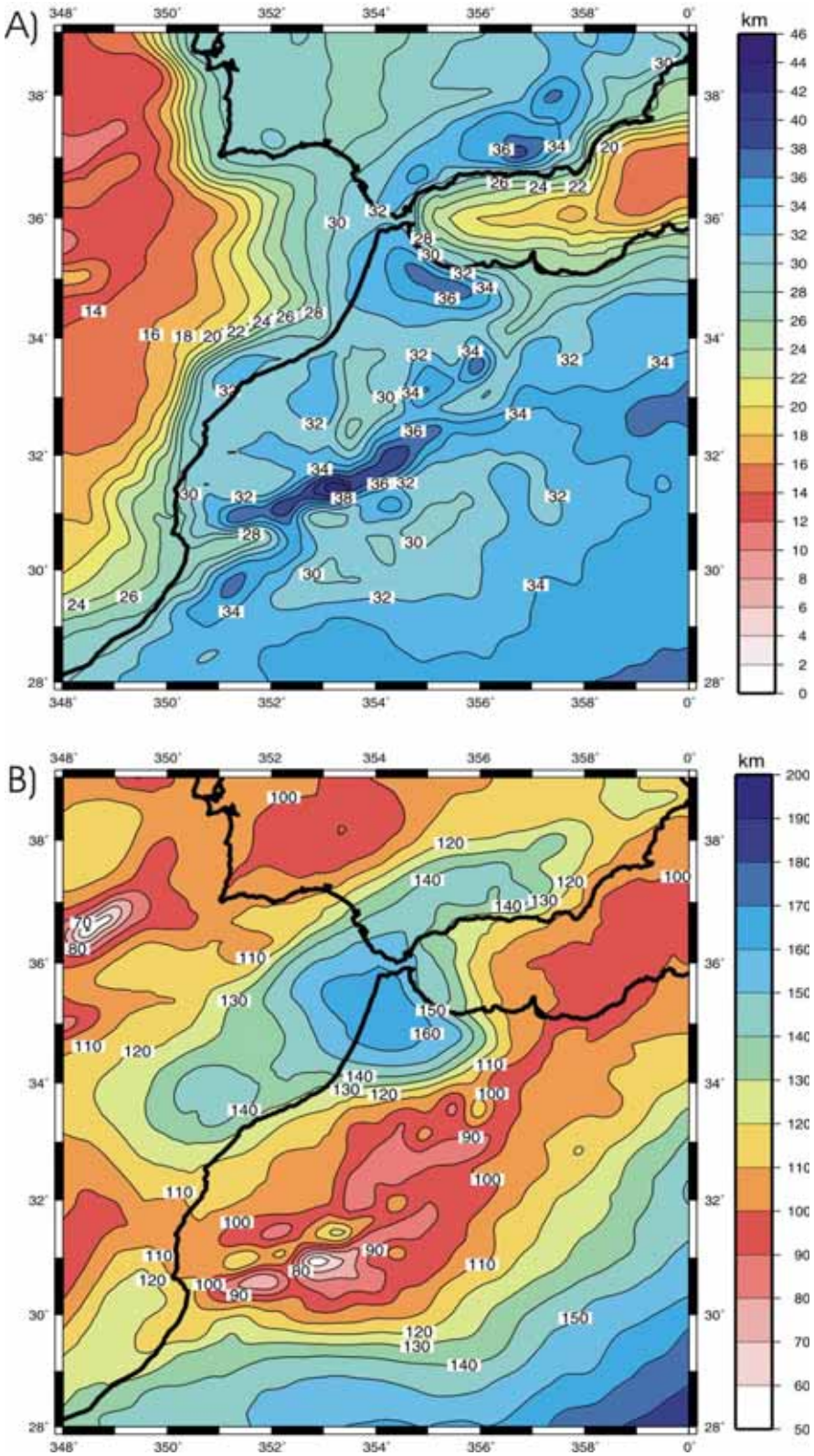

Fig. 4.5 *Lithospheric structure derived from elevation and geoid anomaly data. For the crust, a constant average density of 2780 kg/m^3 is assumed in the study area except for the four shaded areas shown in* ***Fig. 4.4****. For the lithospheric mantle a temperature-dependent density is considered (****Table 4.1****).* ***A)*** *Map of the Moho depths. Isolines every 2 km.* ***B)*** *Depth of the LAB. Contour interval is 10 km.*

thinning towards the Atlas up to 70 km, and a 180-km-thick lithosphere beneath the African Precambrian Craton confirmed by Teixell et al. (2005) and Missenard et al., (2006). Other works based on global thermal and geochemical studies suggest a lithospheric thickness of 140-200 km for Proterozoic cratonic areas such as the African Craton, which is compatible with these results (Artemieva and Mooney, 2001; Poudjom Djomani et al., 2001).

Torne et al., (1995) present two lithospheric profiles across the SW Iberian margin constrained by elevation, SHF, gravity and geoid anomalies, resulting in a 110 km-thick lithosphere beneath the south Iberian Massif, and a lithospheric thickness of 120 km in the Tagus abyssal plain. However, other authors find a lower value of the lithospheric thickness in the SW Iberian Peninsula of 95 km invoking a deep mass deficit in order to make high Bouguer anomaly values compatible with moderate elevation and geoid anomaly values in the area (Fernàndez et al., 2004). Southwestwards these authors propose a LAB depth of 125 km beneath the 150 My old African oceanic lithosphere, (Fernàndez et al., 2004).

From a comparison of our results with those obtained from earlier studies, we infer that the main features and trends are in good agreement. Major discrepancies arise when comparing our results with global tomography anomalies that show a lithospheric slab beneath the Gibraltar Arc region down to 500-600 km (e.g. Spakman and Wortel, 2004), and in the Alboran Basin, where our results suggest a LAB about 35 km deeper than proposed by Torne et al. (2000).

4.5 DISCUSSION

4.5.1 Assumptions and discrepancies with previous studies

The method presented to calculate the crust and the lithosphere thickness from elevation and geoid anomaly data, incorporating a simplified thermal model, is based on three main assumptions: i) the thermal regime of the lithosphere is in steady-state; ii) the lithosphere is not able to support shear stresses, which implies that elevation is locally compensated; and iii) the model consists of two layers with linear density gradients (crust and lithospheric mantle) and two layers with constant densities (water and asthenosphere).

The assumption of thermal steady-state is particularly valid in old tectonothermal provinces, however, regions deformed during the Mesozoic extension and/or the Alpine orogeny, are probably affected by transient

perturbations in the temperature distribution. Therefore, the results of our model must be interpreted as average physical conditions necessary to produce the required density distribution rather than the actual thermal boundaries. Transient temperature distribution in the lithospheric mantle would produce a displacement of the isotherms with the result that steady-state thermal modelling overestimates the actual lithospheric thickness in regions of recent lithospheric thinning and underestimates it where the lithosphere is thickened. Therefore, the lithospheric thickness variations presented here must be considered as a lower limit.

For some areas of the model, undesirable short wavelengths are present in the calculated lithospheric thickness, e.g. the Atlas **(Fig. 4.5 B)**. The original elevation and geoid anomaly datasets have different resolutions and were subsequently filtered with distinct pass-bands. In consequence, the pair of elevation and geoid values to be inverted in a given lithospheric column could show small departures from the actual values. As this could be the reason of the high frequency content in the calculated lithospheric thickness, we have tested several different filters for both elevation and geoid anomaly. The results do not show a relationship between the filter used and the high frequency content. Thus, we conclude that this adverse effect is inherent to the 1D approach, at least for zones with large lateral changes.

The model of density distribution assumed within the crust and the lithospheric mantle can introduce changes in the modelling results. An earlier work on the lithospheric structure of the study region using elevation and geoid anomaly data was performed assuming constant densities for the crust and the lithospheric mantle of 2780 kg/m^3 and 3245 kg/m^3, respectively (Fullea et al., 2006). The effect of introducing the thermal field and a linear density gradient in the crust into the model leads to different variations in crustal and lithospheric thicknesses. In the crust, for $E<0$ we observe an increment of the Moho depth ranging from 10% to 40%, while for $E>0$ the crustal thickness increases moderately or even decreases (-5% to +10%). In the case of the lithospheric thickness, the changes are less important, spanning from -5 % to +5 % for most of the study area.

Our results in the eastern Alboran Basin considerably exceed the crustal and lithospheric thickness values proposed by other works, which do not use geoid anomaly as a constraint (Hatzfeld, 1976; Hatzfeld, 1978; Torne and Banda, 1992; Polyak et al., 1996; Fernàndez et al., 1998b; Torne et al., 2000). According to our model, fitting the lithospheric thickness values proposed by Torne et al. (2000) would require a higher geoid anomaly in the area. On the other hand, the

crust in the central and eastern Alboran Basin is characterized by low average P-wave velocities of about 6.1 km/s (Hatzfeld, 1978), which are probably related to the lack of a high density lower crust (Galindo-Zaldivar et al., 1997). The uppermost mantle also shows anomalously low P-wave velocities beneath the central and eastern Alboran Basin, ranging from 7.6 to 7.8 km/s (Hatzfeld, 1978). To explain this feature, the presence of a layer beneath the crust with a density of 3200 kg/m^3 and a thickness of 10-15 km has been suggested (Hatzfeld, 1976; Torne and Banda, 1992; Galindo-Zaldivar et al., 1997). Other authors invoke the presence of asthenospheric material at subcrustal levels based on backstripping (Docherty and Banda, 1995), shear wave attenuation and 3D gravity modelling (Seber et al., 1996a). This low velocity layer is underlain by a high velocity mantle according to seismic tomography (Seber et al., 1996b; Gurría and Mezcua et al., 2000). The presence of this anomalous hot mantle layer at subcrustal depths has important consequences for the isostatic balance and geoid anomaly in the context of our method. To introduce this constraint, we have considered a different model for the central and eastern Alboran Basin composed of three layers: a crust with a density of 2680 kg/m^3, an anomalous lithospheric mantle with a density of 3200 kg/m^3 (Hatzfeld, 1976; Torne and Banda, 1992; Galindo-Zaldivar et al., 1997) and a standard lithospheric mantle with a density of 3300 kg/m^3 (Torne and Banda, 1992). We fixed a depth of 18 km for the Moho and a thickness of 12 km for the anomalous lithospheric mantle layer (from 18 km to 30 km depth) (**Fig. 4.6**). We find that the presence of the anomalous low-density mantle at subcrustal depths reduces the LAB depth to about 65 km, making the prominent lithospheric thinning compatible with the observed bathymetry and geoid anomaly values.

In the Gulf of Cadiz, deep seismic near-vertical reflection and refraction/wide-angle reflection data indicate a thinner crust in comparison with our results. The reason for this misfit is related to the presence of a thick sedimentary cover (~8 km-thick) in the centre of the Gulf (González-Fernández et al., 2001; Iribarren et al., 2007). One of the limitations of the presented method is to consider a unique crustal layer, which cannot take into account the presence of sediment accumulations. We will further discuss this issue in Chapter 6, in the context of a full 3D modelling.

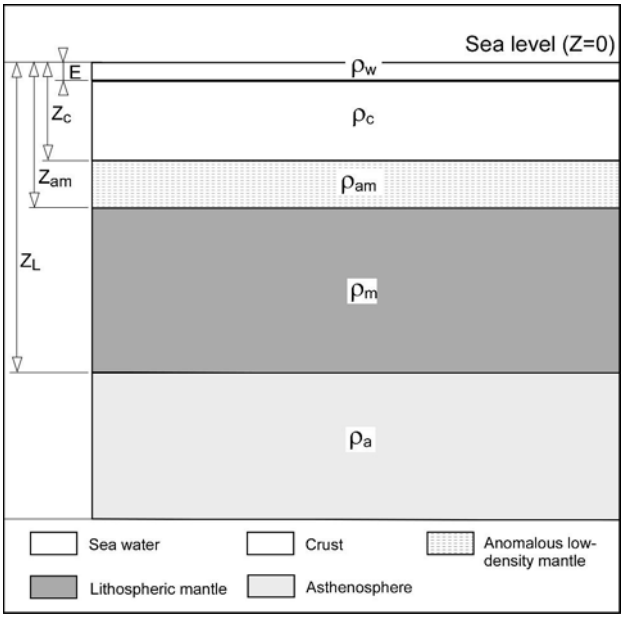

Fig. 4.6 *Sketch of the alternative lithospheric model for the central and eastern Alboran Basin composed of three layers: crust of average density ρ_c=2680 kg/m^3, anomalous lithospheric mantle with density ρ_{am}=3200 kg/m^3 (Hatzfeld, 1976; Torne and Banda, 1992; Galindo-Zaldivar et al., 1997), and a standard lithospheric mantle with density ρ_c=3300 kg/m^3 (Torne and Banda, 1992). The depth of the base of the layers referred to the sea level is, for the crust z_c=18 km, for the anomalous mantle z_{am}=30 km and for the standard lithospheric mantle z_L=65 km. The average bathymetry is E=-1 km. The densities for the sea water and asthenosphere are ρ_w=1030 kg/m^3 and ρ_a=3200 kg/m^3, respectively.*

4.5.2 Comparison with seismic tomography

The comparison of our results with seismic tomography studies shows interesting aspects. One of the first tomographic studies of the P-wave velocity in the study area using both regional and teleseismic data is that of Blanco and Spakman (1991). They image low velocity beneath the Middle Atlas, and high velocity in the Gulf of Cadiz and Gibraltar Arc, between 50 and 100 km depth. The same authors depict a strong positive NE-SW trending anomaly from 200 to 700 km depth beneath the Betics and the Alboran Basin (Blanco and Spakman, 1991). Other global tomography studies coincide in the high P-velocity anomaly beneath the Betics and the western Alboran Basin from 200 to 600 km depth (Bijwaard and Spakman, 2000; Spakman and Wortel, 2004). Calvert et al., (2000) performed a local, regional and teleseismic tomography inversion in the study area. They observed low P-wave velocities in the Middle Atlas and eastern Alboran Basin between 60 and 100 km depth. From 100 to 200 km depth, these

authors obtain high P-wave velocities beneath the Betics, the Gibraltar Arc and, partially, in the NW Moroccan margin, while the Gulf of Cadiz does not show any significant anomaly. Seber et al., (1996b) integrated teleseismic P-wave travel times to study the Atlas and Rif mountains. These authors obtain high velocities for the eastern Rif and the Meseta area, and low velocities beneath the Atlas, the Gibraltar Arc and the Gulf of Cadiz, between 35 and 150 km depth. From 150 to 350 km depth, they observe a strong high velocity anomaly beneath the eastern Rif and the Alboran Basin, low velocities in the Rharb Basin and Gulf of Cadiz, and no significant perturbations along the Atlas (Seber et al., 1996b). A local and regional tomography study carried out in the Alboran Basin and the Betics indicates low P-wave velocities in the Alboran Basin within the depth range of 40-60 km, and normal mantle velocity for depths <40 km (Gurría and Mezcua, 2000). Marone et al., (2004) presented a regional S-velocity inversion combined with the fit of the waveforms of S and Rayleigh wave trains, resolving the Eurasia-Africa plate boundary. Their results do not show any significant signature at depths up to 200 km in the Gulf of Cadiz, Rharb and Alboran Basins, Rif, Betics or Atlas Mountains. However, they observe high S-wave velocity beneath the central and eastern Alboran Basin at a depth between 250 and 500 km.

Our results suggest that both the crust and the lithosphere thicken below the Gibraltar Arc, Betics and Rif Mountains, which is in line with the high P-wave velocities obtained by tomography results (Blanco and Spakman, 1993; Bijwaard and Spakman, 2000; Calvert et al., 2000; Spakman and Wortel, 2004). The lithospheric thinning beneath the Atlas and the Alboran Basin has also been imaged by tomography inversion as a low velocity layer between about 40 and 100 km depth (Blanco and Spakman, 1991; Seber et al., 1996b; Calvert et al, 2000; Gurría and Mezcua, 2000). According to our results, however, the lithospheric thickening affects also the Rharb Basin and the Gulf of Cadiz, and, to a lesser extent, the NW margin of Morocco (**Fig. 4.5 B**). This result is particularly interesting given the poor resolution of tomography models in the Gulf of Cadiz and NW Moroccan margin due to an inconvenient distribution of stations and events.

One thing that the aforementioned tomography studies seem to have in common is the P-wave anomaly that depicts a lithospheric slab from about 200 to 600 km (with the required caution concerning its continuity) located in a region comprising the Gibraltar Arc, the Alboran Basin, the Betics and the Rif (Blanco and Spakman, 1993; Bijwaard and Spakman, 2000; Calvert et al., 2000; Spakman

and Wortel, 2004). Despite we are fitting simultaneously elevation and geoid anomaly data, such a slab is not depicted in our model since we are assuming a constant density everywhere beneath the compensation level (300 km depth) and a four-layer model with simple density-depth variations. In this particular region characterized by deep (>300 km) and narrow (~200 km) structures, the combination of geoid and elevation data under the assumptions of local isostasy and 1D approach has some restrictions. Furthermore, matching seismic velocity and density anomalies down to 660 km depth is a hot issue that requires a deep knowledge on the equations of state governing mineral assemblages submitted to high temperatures and pressures. More detailed modelling requires transient thermal state and 3D calculations, which was beyond the aims of the simple method presented in this chapter.

Chapter 5

3D LITHOSPHERIC NUMERICAL MODELLING: GEO3Dmod

5. 3D LITHOSPHERIC NUMERICAL MODELLING: GEO3Dmod

5.1 INTRODUCTION

In this chapter we present a computer program that allows for interactive 3D lithospheric forward modelling integrating SHF, elevation, and gravity and geoid anomalies. The program consists of two modules. The first one (GEO3Dmod) resolves the direct problem, i.e. given a lithospheric model (a set of layers with different properties), calculates the associated geophysical observables. The second one (GEO3Dmod_INTF) is a graphical interface designed to visualize and modify the lithospheric structure according to the differences between calculated and measured geophysical observables (**Fig. 5.1**). The 1D four-layered model composed of crust, lithospheric mantle, asthenosphere and sea water presented in Chapter 4 is a useful initial model. The code is written in FORTRAN 90, uses the graphical libraries PGPLOT (http://www.astro.caltech.edu/~tjp/pgplot/) and is available for both Linux and Windows platforms. The algorithm determines the 3D thermal and density structure of the lithosphere and, though it does not give a unique solution, allows us to reduce the number of possible solutions due to the use of different geophysical data sets.

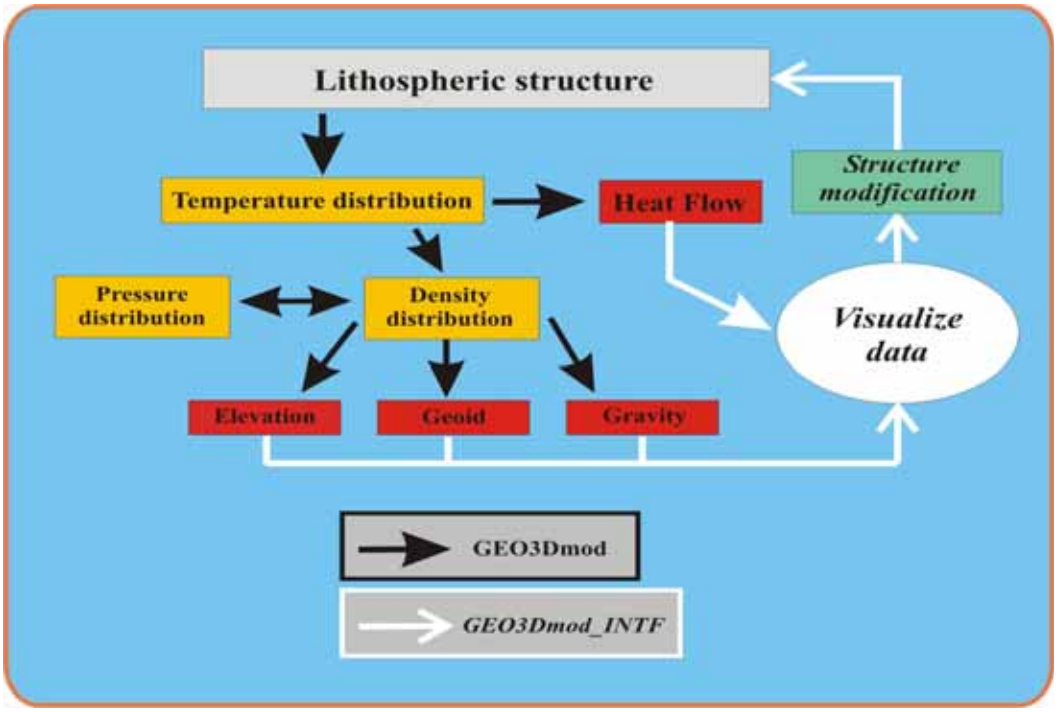

Fig. 5.1 *Flow-chart of the 3D lithospheric modelling program GEO3Dmod.*

5.2 GEO3Dmod

This module is a 3D forward modelling algorithm to calculate the thermal, pressure, and density distributions for a given lithospheric model. Then, it calculates elevation assuming local isostasy, geoid, free air and Bouguer anomalies, and SHF. GEO3Dmod allows for working with several layers (bodies) with different physical properties: density, thermal expansion coefficient, pressure coefficient, volumetric heat production, and thermal conductivity. Each layer is defined between two successive limit surfaces, which are defined in the whole model space.

5.2.1 Thermal field

GEO3Dmod uses a Finite Difference (FD) scheme to solve the steady state 3D thermal equation in a rectangular prism representing the lithosphere. The following vector equation must be solved:

$$\nabla \cdot \left(k(\vec{x})\nabla T(\vec{x})\right) = -H(\vec{x}) \tag{5.1}$$

where k is the thermal conductivity tensor (W m^{-1} K^{-1}), T is the temperature and H is the radiogenic heat production per unit volume (W m^{-3}). The boundary conditions are: fixed temperature at the top (T_s) and the bottom of the lithosphere (T_a), and no heat flow perpendicular to vertical boundaries (i.e. the four XZ and YZ planes). The asthenosphere is assumed to be at constant temperature, T_a. In the framework of the finite difference scheme, we discretize our model in a 3D grid with N_x, N_y and N_z nodes in the X, Y and Z-axis, respectively, being the grid steps Δx, Δy and Δz (**Fig. 5.2**). Hence, the physical variables T, K and H are defined in each node (T_{ijk}=T(x,y,z)), and we can rewrite eq. 5.1 in its discretized form for each node and its nearest neighbours :

$$\begin{aligned}
&\frac{1}{2\Delta x^2}\left((k_{i+1jk}+k_{ijk})T_{i+1jk}+(k_{ijk}+k_{i-1jk})T_{i-1jk}-(k_{i+1jk}+2k_{ijk}+k_{i-1jk})T_{ijk}\right)\\
&+\frac{1}{2\Delta y^2}\left((k_{ij+1k}+k_{ijk})T_{ij+1k}+(k_{ijk}+k_{ij-1k})T_{ij-1k}-(k_{ij+1k}+2k_{ijk}+k_{ij-1k})T_{ijk}\right)\\
&+\frac{1}{2\Delta z^2}\left((k_{ijk+1}+k_{ijk})T_{ijk+1}+(k_{ijk}+k_{ijk-1})T_{ijk-1}-(k_{ijk+1}+2k_{ijk}+k_{ijk-1})T_{ijk}\right)=-H_{ijk}
\end{aligned} \tag{5.2}$$

where *i* goes from 2 to N_x-1, *j* from 2 to N_y-1, and *k* from 2 to N_z-1. The nodes pertain always to a certain layer, i.e. the borders of the different layers are located between the nodes.

The boundary conditions in the FD grid implying null lateral heat flow are equivalent to consider the following values for the thermal conductivity in the vertical limits of the grid (i.e., i=1, i=N_x, j=1,and j= N_y):

$$
\begin{aligned}
k_{1jk} &= -k_{2jk} \\
k_{Nxjk} &= -k_{Nx-1jk} \\
k_{i1k} &= -k_{i2k} \\
k_{iNyk} &= -k_{iNy-1k}
\end{aligned}
\tag{5.3}
$$

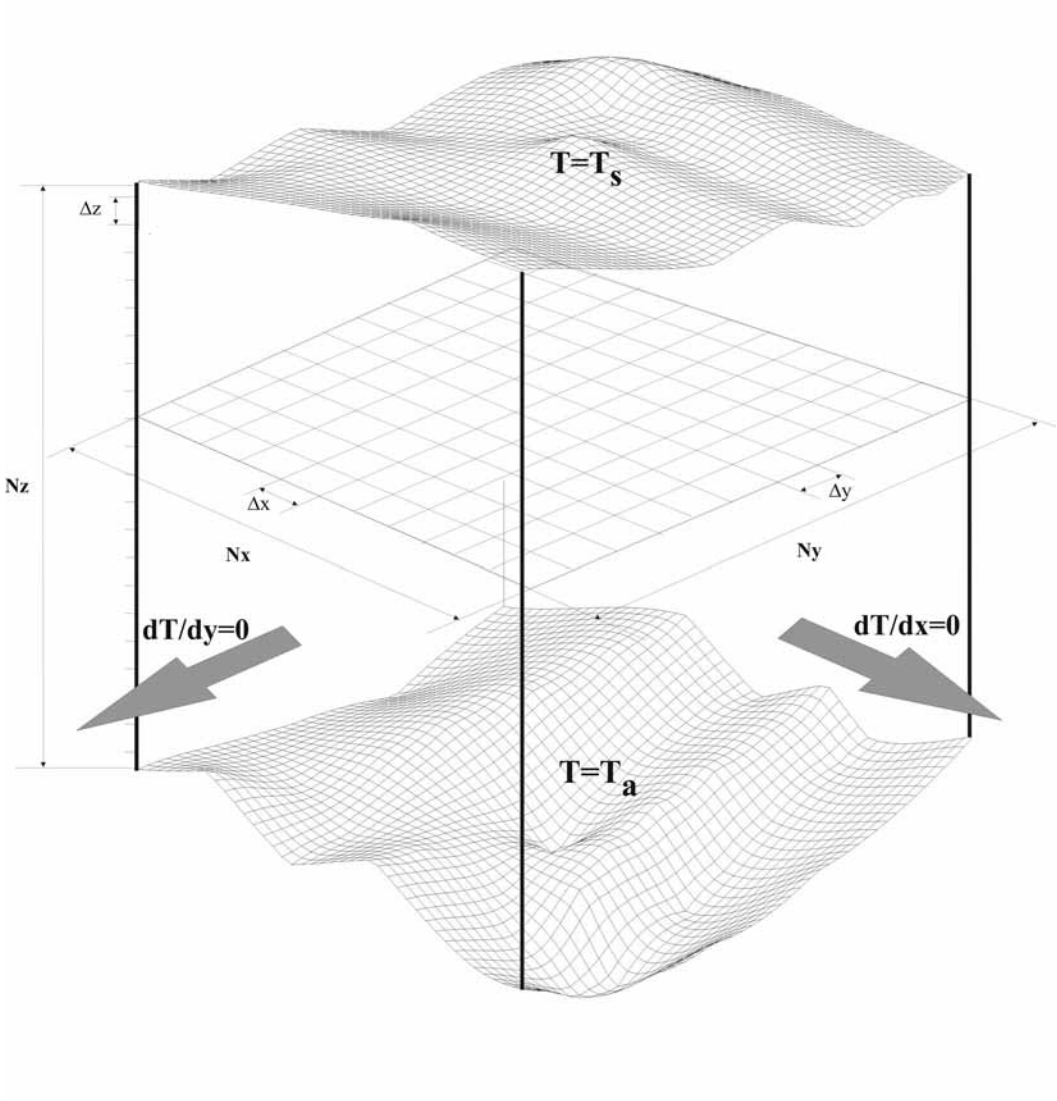

Fig. 5.2 *Scheme showing the main parameters of the FD grid as well as the boundary conditions used by GEO3Dmod to solve the 3D steady-state thermal equation.*

For the nodes with neighbours over the topography and the lithosphere-asthenosphere boundary (LAB), the system of eq. 5.2 must be modified in order to consider the fixed temperature at both surfaces, T_s and T_a, respectively. This is equivalent to change the heat production term corresponding to the nodes with neighbours over the topography of the model, (at fixed temperature, T_s) in the X, Y or Z direction:

$$\begin{aligned} H_{ijk} &= H_{ijk} - \frac{T_s}{2\Delta x}\left(k_{ijk} \pm k_{i\pm 1\,jk}\right) \\ H_{ijk} &= H_{ijk} - \frac{T_s}{2\Delta y}\left(k_{ijk} \pm k_{ij\pm 1k}\right) \\ H_{ijk} &= H_{ijk} - \frac{T_s}{2\Delta z}\left(k_{ijk} + k_{ijk+1}\right) \end{aligned} \tag{5.4}$$

In eq. 5.4, the first line corresponds to nodes with neighbours over the topography in the X direction, the second line in the Y direction, and the third line in the Z direction. The ± signs in the first two lines of eq. 5.2 corresponds to a neighbour over the topography for increasing (+) or decreasing (-) X or Y values. In the Z direction, a neighbour over the topography can only be found, obviously, for increasing Z values.

Analogously, for the nodes in contact with the LAB at fixed temperature T_a, the heat production term reads:

$$\begin{aligned} H_{ijk} &= H_{ijk} - \frac{T_a}{2\Delta x}\left(k_{ijk} \pm k_{i\pm 1\,jk}\right) \\ H_{ijk} &= H_{ijk} - \frac{T_a}{2\Delta y}\left(k_{ijk} \pm k_{ij\pm 1k}\right) \\ H_{ijk} &= H_{ijk} - \frac{T_a}{2\Delta z}\left(k_{ijk} - k_{ijk-1}\right) \end{aligned} \tag{5.5}$$

The expressions of eqs. 5.2 to 5.5, for all grid nodes, form a linear system of equations, being H the vector of independent terms and T the vector of unknowns. The coefficient matrix is symmetric (if the grid steps are constant) and band-structured, i.e. with nonzero elements only in the main diagonal and three diagonals above and below the main diagonal. For numerical reasons, it is more convenient to assign one number (node number, n) to each node instead of three (*ijk*) referred to its XYZ position. Thus, we numerate each node starting in the X direction, then in the Y, and finally in the Z direction. The relation between the node number and the *ijk* indexes is:

$$n = (k-1)N_x N_y + (j-1)N_x + i \tag{5.6}$$

Most of the elements of the matrix are zero and, therefore it is not necessary to store them in memory. Thus, we define a matrix with NTOT=N_xxN_yxN_z rows and four columns, the first one containing the main diagonal, and the other three the rest of the diagonals above the main diagonal (the diagonals below the main diagonal are not necessary since the original matrix is symmetric). The system of equations can now be rewritten as:

$$
\begin{aligned}
&B(NTOT\times 4)\,T(NTOT) = H(NTOT)\\
&B(n,1) = -\left(\frac{k_{n+1}+2k_n+k_{n-1}}{\Delta x^2}+\frac{k_{n+Nx}+2k_n+k_{n-Nx}}{\Delta y^2}+\frac{k_{n+NxNy}+2k_n+k_{n-NxNy}}{\Delta z^2}\right)\\
&B(n,2) = \frac{k_{n+1}+k_n}{\Delta x^2}\\
&B(n,3) = \frac{k_{n+Nx}+k_n}{\Delta y^2}\\
&B(n,4) = \frac{k_{n+NxNy}+k_n}{\Delta z^2}
\end{aligned}
\qquad (5.7)
$$

To solve the linear system of eq. 5.7 we have selected a least square iterative scheme.

5.2.2 Pressure, density and elevation

Once the thermal field has been resolved, GEO3Dmod calculates the pressure within the model region and the density distribution. The density of the different bodies is given by:

$$\rho = \rho_0\left(1-\alpha T+\beta P\right)) \qquad (5.8)$$

where T is in ºC, P in Pa, ρ_0 is the reference density at T=P=0, α is the thermal expansion coefficient [K^{-1}] and β the pressure coefficient [Pa^{-1}] (for those bodies with a constant density both coefficients are equal to zero). In the case of the lithospheric mantle, the reference temperature and density are usually taken at the LAB (eq. 2.1). Hence, to keep the consistency with eq. 5.8, we must redefine the reference density and volumetric expansion coefficient for the lithospheric mantle:

$$
\begin{aligned}
&\rho_0 = \rho_a\left(1+\alpha T_a\right)\\
&\alpha' = \frac{\alpha}{1+\alpha T_a}\\
&\rho_m = \rho_0\left(1-\alpha' T+\beta P\right))
\end{aligned}
\qquad (5.9)
$$

In general, the density depends on pressure (eq. 5.8), but the pressure depends also on density:

$$P(z) = \int_E^z g\rho(z')dz' \tag{5.10}$$

To solve this coupling, we proceed in the following way. Let us assume that the density at a certain depth, z_0, is known, $\rho(z_0)$. As a first estimate, we consider the following expression for the pressure at a depth $z > z_0$ (z and z_0 belonging to the same layer):

$$P(z) = P(z_0) + \rho(z_0) \cdot g \cdot (z - z_0) \tag{5.11}$$

Eq. 5.11 is formally equivalent to assume that the density in eq 5.10 is constant. However, the density changes with the pressure (eq 5.8) and, therefore, the increase in pressure from z_0 to z is:

$$\begin{aligned} &\Delta P = \int_{z_0}^z \rho(z')gdz' = \int_{z_0}^z \rho_0\left(1+\alpha\Delta T+\beta(P(z_0)+\rho(z_0)g\cdot(z'-z_0))\right)gdz' = \\ &g\rho(z_0)\cdot(z-z_0)\left(1+\frac{g\rho_0\beta(z-z_0)}{2}\right) \end{aligned} \tag{5.12}$$

In the next step, the program calculates the actual elevation of the model in each column according to local isostasy (eq. 2.20). An equivalent formulation of eq. 2.20 considering the thickness of the layers, Δz, and its average density, ρ^{av}, is:

$$\begin{aligned} &E = L - L_0 - \frac{1}{\rho_a}\sum_{bodies}\rho^{av}{}_i\Delta z_i \quad \text{if } E > 0 \\ &E = \frac{\rho_a}{\rho_a - \rho_w}\left(L - L_0 - \frac{1}{\rho_a}\sum_{bodies}\rho^{av}{}_i\Delta z_i\right) \quad \text{if } E < 0 \end{aligned} \tag{5.13}$$

where the summation is carried out over all layers present in the lithospheric column.

5.2.3 Gravity and geoid anomalies

Once the density distribution is known, GEO3Dmod calculates the gravity and geoid anomalies. The program considers a number of right rectangular flat-topped prisms centred in each node of the FD grid. Gravity anomalies depend upon the inverse of the square of the distance to mass anomalies, whereas geoid anomalies diminish only inversely proportional to the distance (**Fig. 5.3**). Each lithospheric column is decomposed into different vertical prisms according to the number of existing layers (**Fig. 5.4**). For each prism, a linear density gradient is

considered. The gravity and geoid anomalies in every surface point of the model are calculated adding the effect of all individual prisms. In contrast with thermal calculation, where Δz determines the resolution, the program considers the real vertical dimensions of the prisms to evaluate the potential fields (i.e., the vertical limits of the prisms do not have to be necessarily a multiple of Δz).

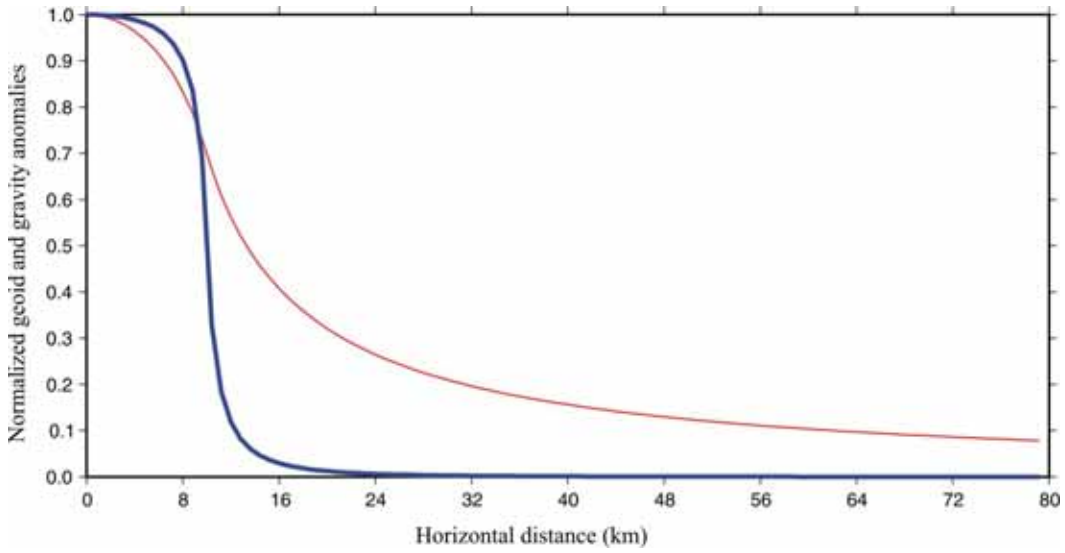

Fig. 5.3 *Gravity (blue) and geoid anomaly (red) produced by a right flat-topped prism of 20 km x20 km, a height of 2 km, and a density of 2670 kg/m^3. The horizontal distances are referred to the centre of the prism.*

The vertical gravitational attraction produced by a right rectangular prism whose density varies linearly with depth can be expressed analytically in Cartesian coordinates as (Gallardo-Delgado et al., 2003):

$$\Delta g_{FTP}(\rho) = G(\rho_0 + \gamma z_0)\left\| x\ln(y+r) + y\ln(x+r) - z\arctan\left(\frac{xy}{zr}\right)\right\|_{x_1}^{x_2}\Bigg|_{y_1}^{y_2}\Bigg|_{z_1}^{z_2} +$$

$$G\gamma\left\| -xy\ln(r+z) - \frac{z^2}{2}\arctan\left(\frac{xy}{zr}\right) + \frac{x^2}{2}\arctan\left(\frac{yz}{xr}\right) + \frac{y^2}{2}\arctan\left(\frac{xz}{yr}\right)\right\|_{x_1}^{x_2}\Bigg|_{y_1}^{y_2}\Bigg|_{z_1}^{z_2} \qquad (5.14)$$

$$r = \sqrt{x^2 + y^2 + z^2}$$

$$\rho(z) = \rho_0 + \gamma z$$

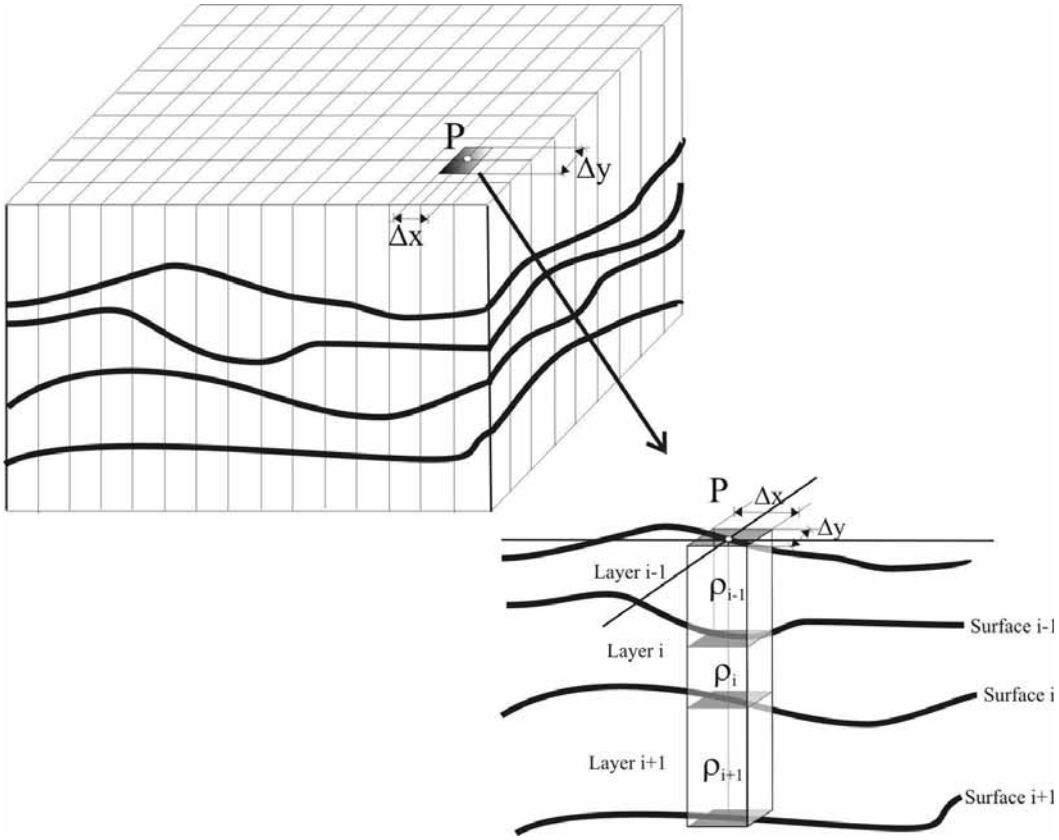

Fig. 5.4 *Decomposition of the lithospheric columns into several vertical prisms centred on the grid nodes (according to the number of layers defined) performed by GEO3Dmod to calculate elevation, geoid and gravity anomalies.*

The first term on the right-hand side of eq 5.14 is equivalent to the contribution of a constant density prism (e.g. Nagy et al., 2000). The second term, the one multiplied by γ, is related to the density gradient. The formula for the geoid anomaly contains also a constant density and a gradient term (Zeyen, personal communication):

$$\Delta N_{FTP}(\rho)=\frac{G(\rho_0+\gamma z_0)}{g}\left\|\begin{array}{l} xy\,\ln(z+r)+yz\,\ln(x+r)+xz\,\ln(y+r)-\frac{z^2}{2}\arctan\left(\frac{xy}{zr}\right) \\ -\frac{x^2}{2}\arctan\left(\frac{yz}{xr}\right)-\frac{y^2}{2}\arctan\left(\frac{xz}{yr}\right) \end{array}\right\|_{x_1}^{x_2}\Bigg|_{y_1}^{y_2}\Bigg|_{z_1}^{z_2}+$$

$$\frac{G\gamma}{3g}\left\|xyr+\frac{y}{2}\left(y^2+3z^2\right)\ln(x+r)+\frac{x}{2}\left(x^2+3z^2\right)\ln(y+r)-z^3\arctan\left(\frac{xy}{zr}\right)\right\|_{x_1}^{x_2}\Bigg|_{y_1}^{y_2}\Bigg|_{z_1}^{z_2}$$

(5.15)

The Cartesian coordinates ($x_1<x_2$, $y_1<y_2$, z_1, z_2) define spatially the prism and are referred to a coordinate system with its origin located at the point where the gravity/geoid anomaly is calculated. To improve the computational efficiency of both eq 5.14 and 5.15 by reducing the number of calls to the time-demanding ATAN (arctan) intrinsic function, we make use of the relation:

$$\arctan(x) + \arctan(y) = \arctan\left(\frac{x+y}{1-xy}\right) \pm \pi \qquad (5.16)$$

To avoid undesired border effects produced by the density contrasts at the physical limits of the model, the columns located at the edges are extended 10^6 km. For the gravity, the average of the calculated anomalies is fitted to the average of the data, since we are dealing with relative anomalies. In the case of the geoid anomaly, due to its slower decay (~1/r) small perturbations of local isostasy at the borders can lead to a regional, long wavelength, component in the calculated anomaly. Therefore, to remove such regional component, it is also necessary to subtract the plane that best fits (lest square sense) the calculated geoid.

5.2.4 Program description

A general scheme of the files and folders used by GEO3Dmod is shown in the upper panel of **Fig. 5.5.** GEO3Dmod performs the calculation using a Cartesian coordinate system with its origin located in the SE corner of the model. The program reads from the input file *GEO3Dmod.info* the horizontal dimensions of the model, L_x(km), L_y(km), the maximum topography of the modelled region, E_{max}(km), the number of nodes in the X, Y and Z-axis, N_x, N_y, N_z, the vertical grid step, Δz(km), the variable *topo*, which indicates whether the program must calculate using an input filtered topography (*topo*=0) or not (*topo*=1), the variable *temp_calc*, which indicates if the thermal calculation must be done (*temp_calc*=1) or not (*temp_calc*=0), and the fixed temperature at the top and the bottom of the lithosphere, T_s and T_a, respectively. A list of typical values for the input parameters is shown in **Table 5.1**. Obviously, the calculation time will increase for an increasing number of nodes. On the other hand, the number of nodes must be large enough to assure the desired accuracy. Several tests indicated that a number of nodes greater than the values listed in **Table 5.1** will increase computation time without a significant increase in resolution. One of the most time-demanding task is the resolution of the thermal problem which, under certain circumstances (i.e., no changes in the LAB since the last modelling step), can be avoided by setting *temp_calc=0*.

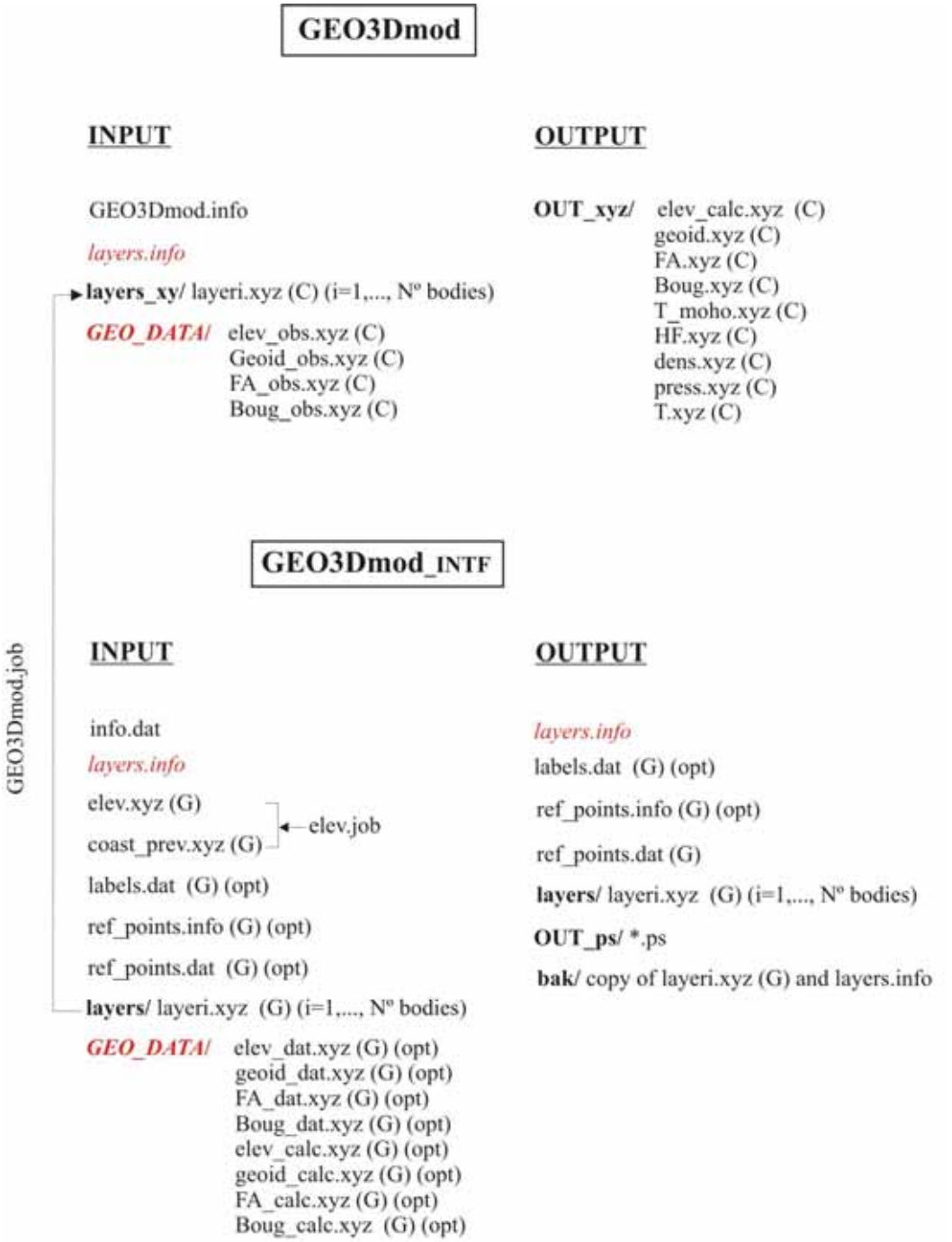

Fig. 5.5 *Scheme of the different input/output **folders** (in bold, followed by /) and files involved in GEO3Dmod (upper panel) and GEO3Dmod_INTF (lower panel). Files and folders in red italics are shared by both GEO3Dmod and GEO3Dmod_INTF. After the name of the files, (C) means that the file is in Cartesian coordinates, whereas (G) indicates geographical coordinates. Files followed by (opt) are optional. See the text for further details.*

GEO3Dmod reads the number of defined layers (bodies) and its properties in the file *layers.info* (**Fig. 5.5 upper panel**). Each row designs a layer and contains the following information: number of the layer, name/brief description, density, thermal expansion coefficient, thermal conductivity, volumetric heat production and pressure coefficient for the density. An example file is shown in **Fig. 5.6**. A negative density value indicates that the reference density is taken at the LAB rather than at the topography, and that rescaling of eq. 5.9 must be applied. Each layer defined in *layers.info* must have associated an ASCII file in the folder **layers_xy** named *layer*i*.xyz*, where i is the number of the layer defined in *layers.info*. The file *layer*i*.xyz* represents the interface between the i^{th} and the $(i+1)^{th}$ layer (**Fig. 5.7**). The first layer is assumed to have the topography as the upper limit. The expected format for the layer files consists of three columns with data starting from the NW corner of the calculation area, which corresponds to (0,0) in the Cartesian reference system, and then going from West to East successively, ending at the SE corner. The first two columns contain the x and y coordinates, respectively, and the third one the depth of the i^{th} layer at every column of the FD grid. The presence of asthenospheric material with constant density (ρ_a=3200 kg/m^3) beneath the last layer is implicitly assumed.

Parameter	Symbol	Value
Number of nodes in the X-direction	N_x	51
Number of nodes in the Y-direction	N_y	51
Number of nodes in the Z-direction	N_z	126
Vertical grid step	Δz	2 km
Surface temperature	T_s	0ºC
Temperature at the LAB	T_a	1350 ºC

Table 5.1. *Typical input parameters for GEO3Dmod for a model of 1200x1200x250 km.*

The program requires also as input files the observed geoid, *geoid_obs.xyz*, free air anomaly, *FA_obs.xyz*, and Bouguer anomaly, *Boug_obs.xyz*. These files must be located in the folder **GEO_DATA** and are expected to have the same format as the layer files (**Fig. 5.5 upper panel**).

The output files are placed in the folder **OUT_xyz**. The calculated elevation (*elev_calc.xyz*), geoid anomaly (*geoid.xyz*), free air anomaly (*FA.xyz*), Bouguer anomaly (*Boug.xyz*), temperature at the Moho (*T_moho.xyz*) and SHF (*HF.xyz*) files follow the same NW to SE corner order as the layer files. The density, pressure and temperature files (*dens.xyz, pres.xyz, T.xyz*) contain the corresponding values at every node, stored by columns from the NW to the SE corner (**Fig. 5.5 upper panel**).

Since global database sets for elevation, free air and geoid anomalies (***ftp://topex.ucsd.edu/pub***) are expressed in geographical coordinates, it is necessary to extract the data and to project them onto a Cartesian grid prior to start GEO3Dmod calculation. This can be done using the *GEO3Dmod.job* script (for Linux), which prepares the input grids using Generic Mapping Tools software (GMT, Wessel and Smith, 1998), and generates the input file *GEO3Dmod.info* (**Fig. 5.5**). Complementary, *GEO3Dmod.job* plots the output files in postscript format (either calculated or residual values). The Format of the input files is the same as that used by GMT when transforming grids into ASCII files.

```
'BODY NUMBER          | DENSITY | ALPHA | THERMAL CONDUCTIVITY | HEAT PRODUCTION RATE | PRESSURE COEFFICIENT'
 1 sedi_alboran         2400.    0.0          2.0                0.10E-05               0.00E+00
 2 sedi_rharb_guadal    2200.    0.0          2.0                0.10E-05               5.0E-2
 3 sedi_g_cadiz         2400.    0.000E+00    2.3                0.10E-05               3.0E-2
 4 transitional_crust   2800.    0.000E+00    2.1                0.20E-06               0.00E+00
 5 upper_crust          2700.    0.000E+00    2.5                0.10E-05               0.00E+00
 6 lower_crust          2920.    0.000E+00    2.1                0.20E-06               0.00E+00
 7 lith_mant           -3200.    0.350E-04    3.2                0.00E+00               0.00E+00
```

Fig. 5.6 *Example of the input file layers.info. Each row designs a body and contains the following information: number of the layer (body), name/brief description, density, thermal expansion coefficient, thermal conductivity, volumetric heat production and pressure coefficient for the density.*

5.3 GEO3Dmod_INTF

GEO3Dmod_INTF is a graphical interface designed to visualize the results of the forward modelling performed with GEO3Dmod and to modify interactively the geometry and properties of the layers. It makes use of the

FORTRAN graphical libraries PGPLOT, which are available for both Linux and Windows platforms (http://www.astro.caltech.edu/~tjp/pgplot/).

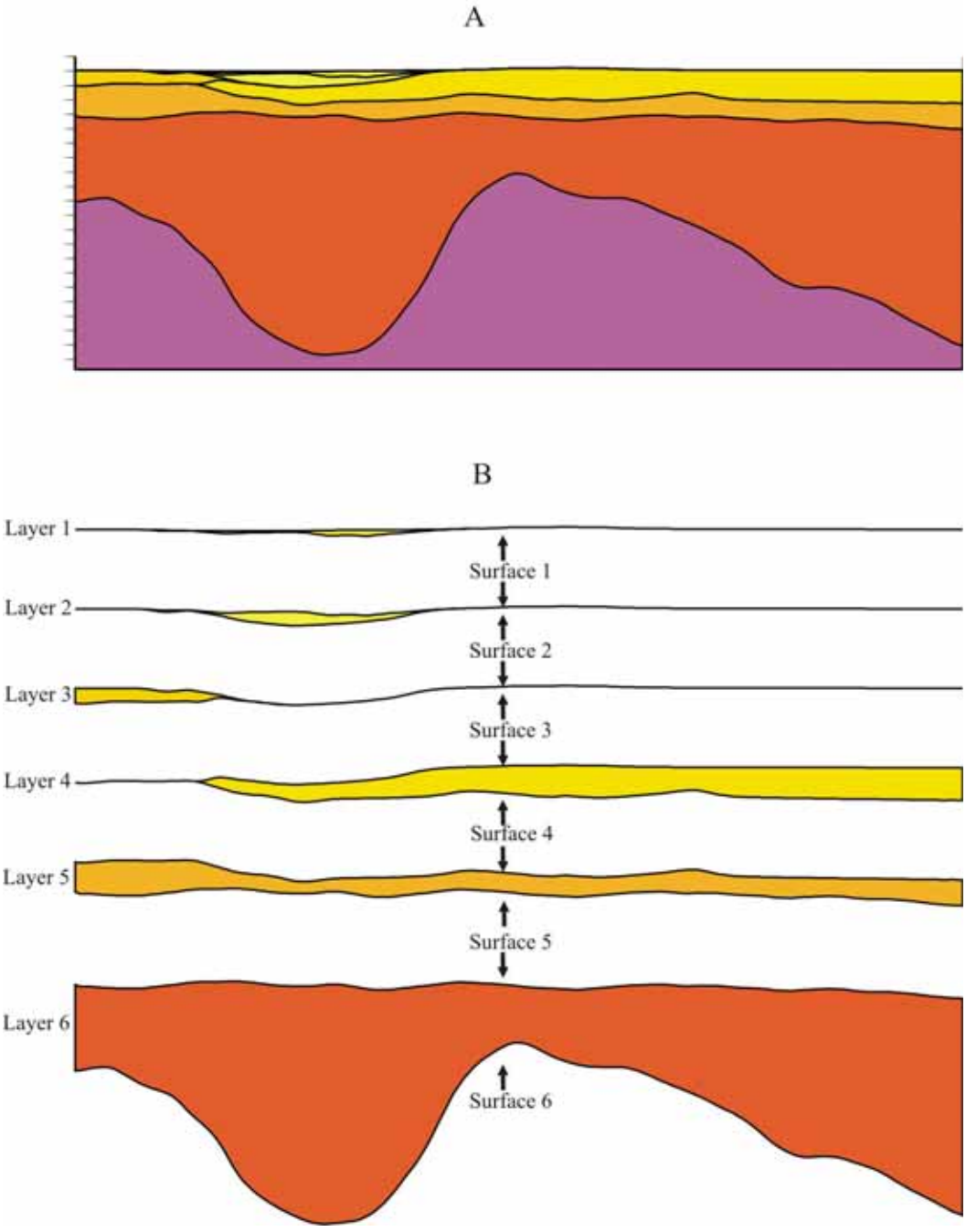

Fig. 5.7 *A lithospheric model in GEO3Dmod is composed by a number of layers (bodies), with different physical properties, defined by an upper and a lower sub-horizontal surface extended over the whole model.* ***A)*** *Cross section of a lithospheric model. The colour scale indicates different densities.* ***B)*** *The same lithospheric model of the upper panel has been split. Each layer (with a different colour) is defined by two consecutive surfaces. For instance, Layer 3 is defined by its upper limit, surface 2, and its lower limit, surface 3. Moreover, surface 3 is the lower limit for layer 3, and the upper limit for layer 4.*

The program allows for working with several layers with different physical properties: density, thermal expansion coefficient, pressure coefficient, volumetric heat production and thermal conductivity. Each layer is defined between two successive limit surfaces, extended in X and Y directions across the whole model space. A particular layer may be missing in certain part of the model if the two surfaces defining it share the same depth. The files containing the surfaces are expected to be in geographical coordinates. The surfaces are hierarchically ordered, i.e. surface *i* cannot be deeper than surface *i+1* at a given x, y position and vice versa (**Fig. 5.7**).

Changes in the geometry of the lithospheric model are done by modifying the boundary surfaces that define the layers in successive vertical cross sections (profiles). The program performs a linear interpolation along and across the modified profiles in order to reconstruct the surface, considering the hierarchy between the different surfaces. The four-layered model composed of crust, lithospheric mantle, asthenosphere and sea water presented in Chapter 4 can be readily used as initial or preliminary model.

5.3.1 Main functions of GEO3Dmod_INTF

The options of GEO3Dmod_INTF can be classified in three groups: visualization, modification and additional data. The main window of the program is divided into two parts: on the right, a topographic map of the study area is shown; on the left part of the window, the number of layers (bodies) defined as well as a menu with the different available options is presented (**Fig. 5.8**). When an option is selected, the program displays a new input window (if necessary), performs the action, and finally returns to the main window.

Visualization options

The program offers two possibilities to visualize the 3D geometry of the lithospheric model: vertical cross sections and 2D map views. With the option *EXTRACT PROFILE (p)*, the user selects through the mouse the two extreme points defining a vertical profile. Then, the program plots in a new window the lithospheric profile with the different layers defined. In the upper part of the window, the program displays the calculated geophysical observables (elevation, geoid anomaly, free air anomaly and Bouguer anomaly) along the cross section (**Fig. 5.9**).

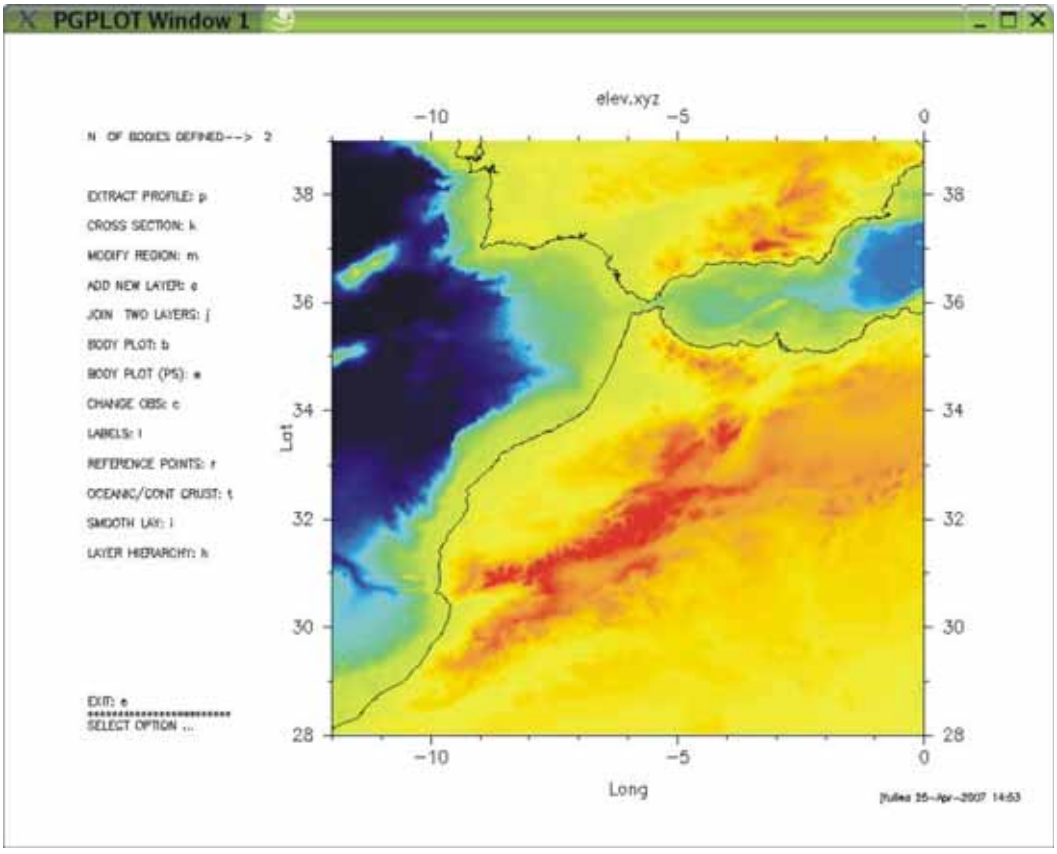

Fig. 5.8 *Main window of GEO3Dmod_INTF with an elevation map of the study area and a list with all available options as well as the number of bodies defined on its left side.*

The user can perform a quick 2D calculation of the geoid, free air and Bouguer anomalies, and 1D elevation, by means of the option *CROSS SECTION (k)* (**Fig. 5.10**). The possibilities to change between the lithospheric and crustal scales as well as Post Script output are also available for both *CROSS SECTION* and *EXTRACT PROFILE* options. The option *BODY PLOT* allows the user to obtain a map of the thickness of any selected layer either as a new window *(b)* or a post script file *(s)* (**Fig. 5.11**). The 2D view of the main window (elevation, initially) can be changed to any of the different geophysical observables (either calculated or residual) using the option *CHANGE OBS (c)* (**Fig. 5.12**).

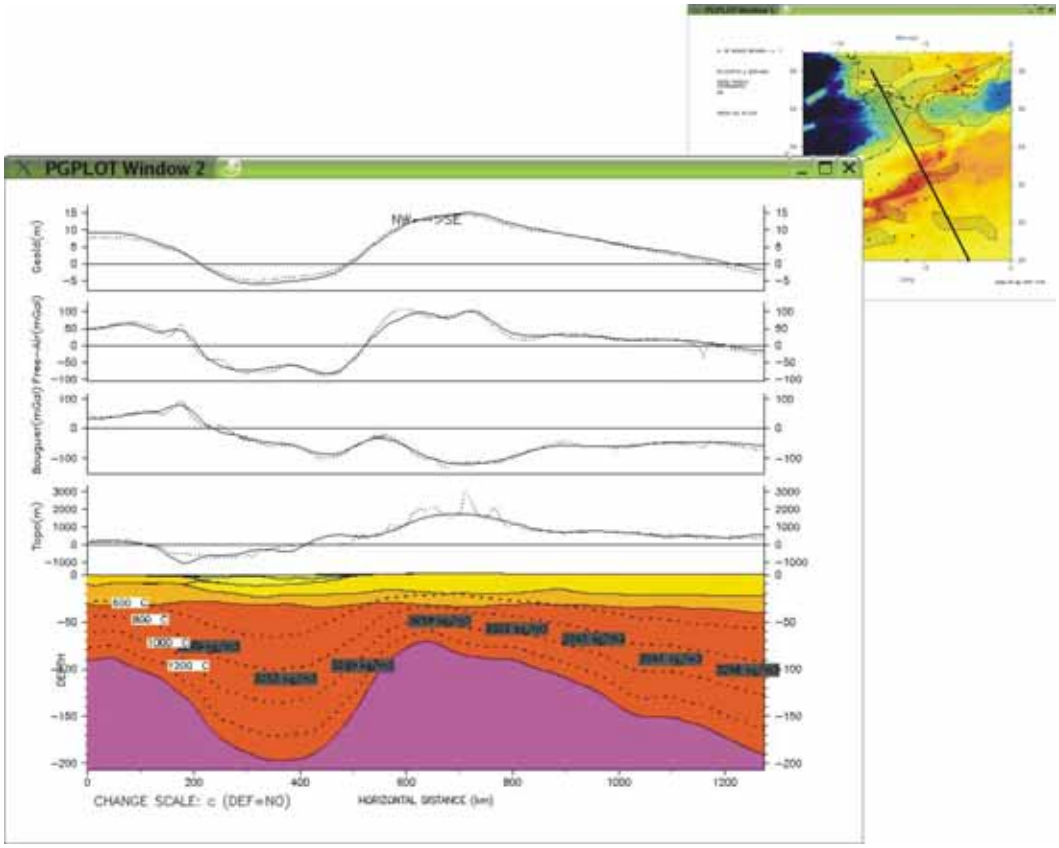

Fig. 5.9 *Vertical profile obtained using the option EXTRACT PROFILE (p). Solid lines represent the geophysical observables calculated by GEO3Dmod. Dashed lines indicate observed values. The lower panel represents the lithospheric model with isotherms and average lithospheric mantle densities if appropriate.*

Modification options

The lithospheric geometry is changed by modifying the boundary surfaces that define the layers in successive vertical profiles. This is done using the option *MODIFY REGION (m)*. First, the surface that is going to be changed must be selected. To do so, a mouse click in any point of the model in the main window will display a new window with a column containing all the available layers (**Fig. 5.13**). If two or more surfaces have the same depth (i.e. the associated layers do not exist in that point of the model) only the upper and the lower surfaces of the group will be available to be selected. Depending on the structure to be modified, E-W or N-S vertical profiles will be more appropriate. At this step, the program offers two possibilities: working with a fixed number of equidistant profiles (n, n>0) or selecting each profile by clicking with the mouse (n=0). Finally, it is necessary to specify if the *glue* option is either *on* or *off*. If the *glue* option is *on*, the program reads the present model geometry and keeps this information for

further modifications: if two or more surfaces coincide and one of them changes its depth, the other surfaces are forced to the same change. This is useful to avoid undesirable effects like the involuntary creation of a layer in some region of the model. The next step is to select the sub region of the model that the user wants to modify. It is highly recommendable to choose an area bigger than the zone that is actually to be modified to avoid border effects. Once the surface and the sub region have been selected, the program opens a new window with the first vertical profile to be modified. The surface selected for modification will appear as a dashed line (**Fig. 5.14**). Each profile must be saved or skipped for the following 3D reconstruction of the surface. GEO3Dmod_INTF performs a linear interpolation along each modified profile. Afterwards, another linear interpolation (perpendicular) between the saved profiles is done in order to reconstruct the surface in the sub region previously selected. Hence, the user works with 2D data, whereas the program builds the final 3D structure. The smoothness obtained in the modified surface will depend on the number of profiles saved during the modification process.

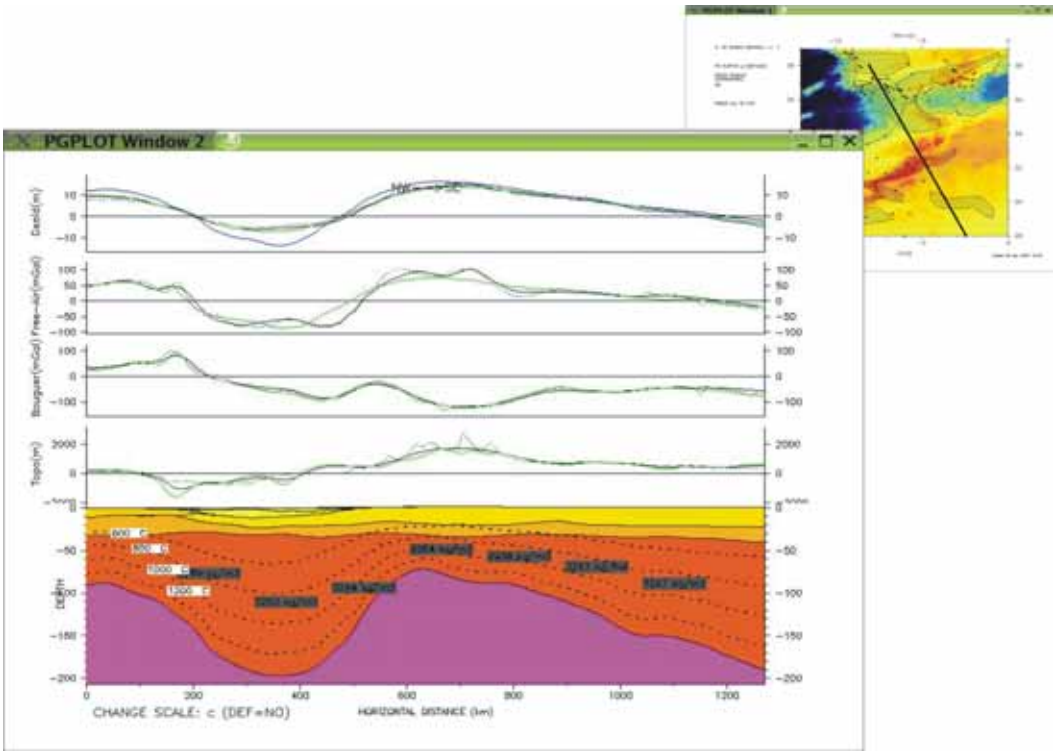

Fig. 5.10 *Vertical profile obtained using the option CROSS SECTION (k). Solid black lines represent the geophysical observables calculated by GEO3Dmod. Dashed lines indicate observed values. Solid green lines stand for 2D calculation performed by GEO3Dmod_INTF. The solid blue line in the upper panel is the geoid anomaly in the 1D approximation (eqs. 4.1 and 4.11).The lower panel represents the lithospheric model with isotherms and average lithospheric mantle densities if appropriate.*

The option *ADD NEW LAYER (a)* allows the user to introduce a new layer, i.e. a new body. The spatial distribution of the new layer is selected by a number of closed polygons defined with the mouse over a map view of the model. The new layer will be created inside the polygons. Outside, its thickness will be null, i.e. the new surface, i, will have the same depth of surface *i-1* or *i+1*. The selection of surface *i-1* or *i+1* as reference for the new surface *i* is a matter of modelling convenience, and is done by a mouse click in a window which contains all the available layers similar to **Fig. 5.13**. The next step is to define the properties of the new layer in a different window (**Fig. 5.15**). A special version of *ADD NEW LAYER* is the option *OCEANIC/CONT CRUST (t)*, designed for the first modelling stages. In general, the user starts with a simple model composed by a uniform crust and the lithospheric mantle. This option allows the user to transform the uniform crust into an upper and lower crust in continental areas (keeping local isostasy), and to define zones (using polygons over a map view) with a transitional/oceanic crust. The program offers also the possibility to join two consecutive surfaces inside/outside the area that is defined by one or more polygons by means of the option *JOIN TWO LAYERS (j)*. This option may be used to eliminate a layer or parts of a layer.

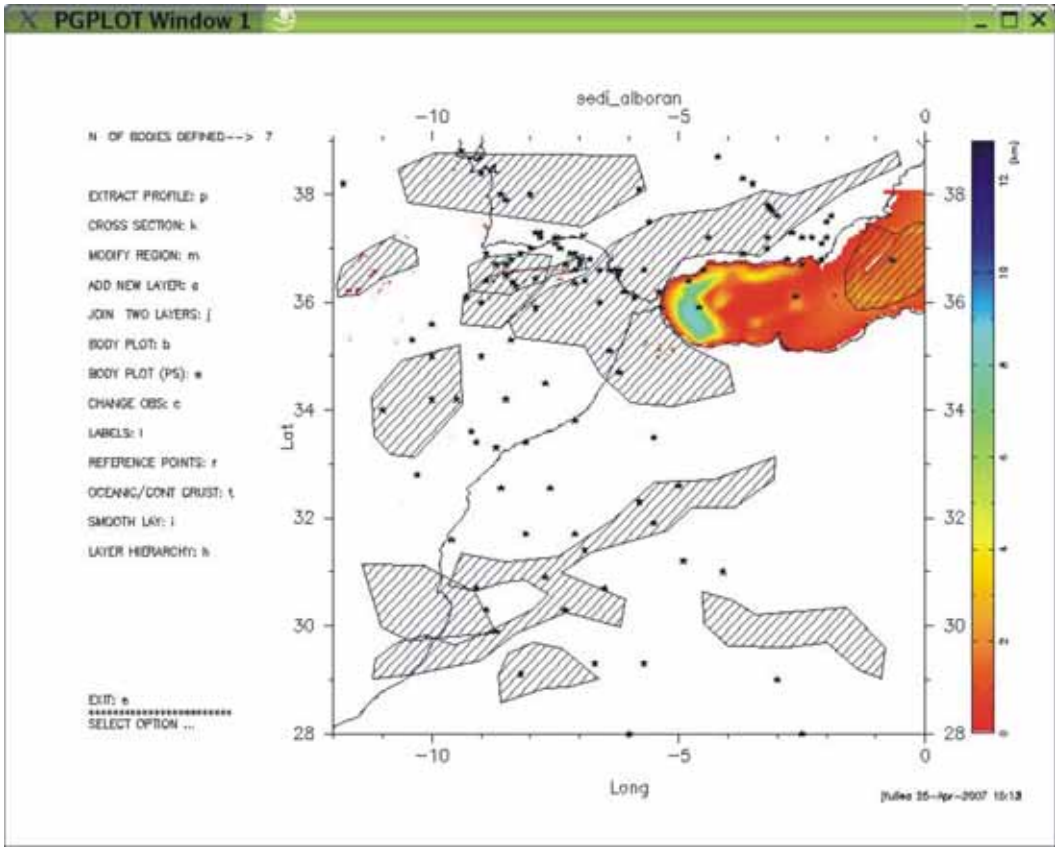

Fig. 5.11 *Example of layer thickness plotted with GEO3Dmod_INTF (coloured polygon). The hashed polygons correspond to reference polygons (see text).*

Sometimes, undesired effects can occur in the modelling process. The next options try to help to correct such problems. The option *LAYER HIERARCHY (h)* checks for the proper order between two surfaces, and corrects if necessary. Another available option is *SMOOTH LAY (i),* which smoothes a selected surface. This option may be helpful in cases when the successive modifications introduce roughness in the geometry of the bodies.

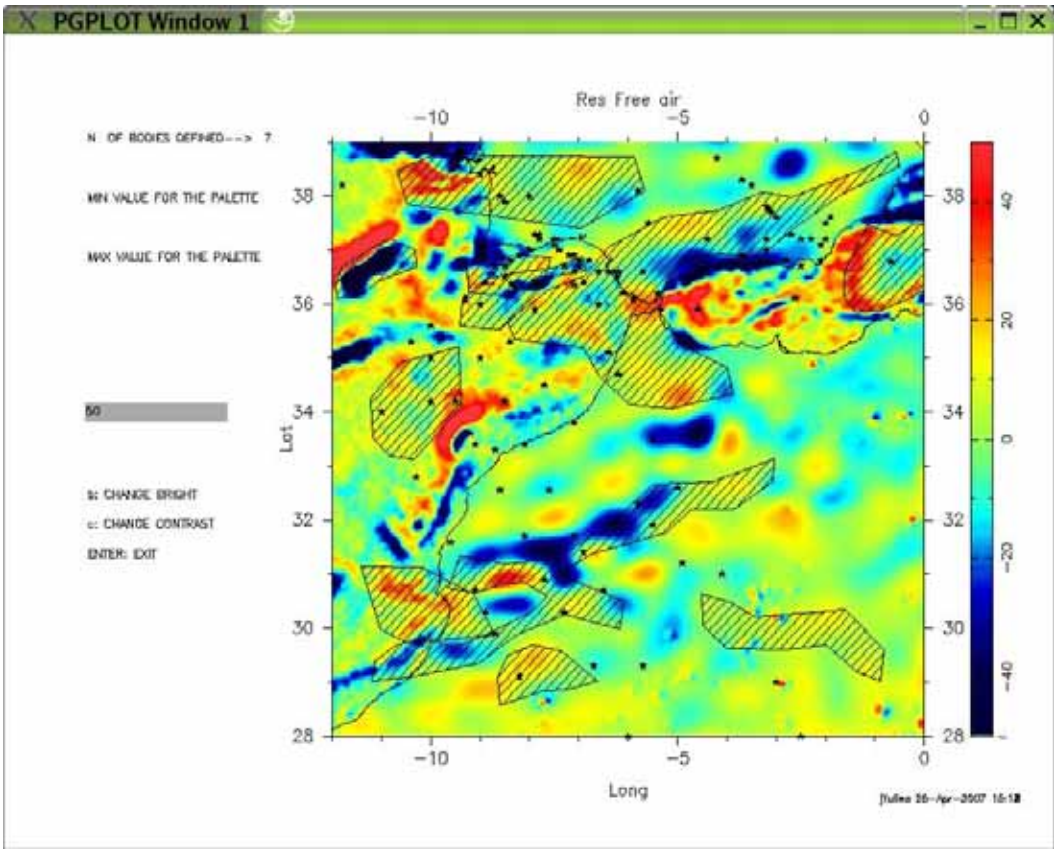

Fig. 5.12 *The 2D view of the main window (elevation, initially) can be changed to any of the different geophysical observables (either calculated or residual) using the option CHANGE OBS (c). The limits, brightness and contrast of the palette can also be modified.*

Additional data options

To facilitate the modelling process, GEO3Dmod_INTF presents two additional options. The option *LABELS (l)* let the user introduce labels (i.e. text strings located at a point characterized by its latitude, longitude and depth) containing previous geophysical data to be used as constraints in the lithospheric modelling. First, a mouse click at any point of the model in the main window

selects the geographical coordinates. Subsequently, the text strings are introduced in a new window with a column containing all the available layers. The labels are written in the file *labels.dat*. The labels are projected within a certain bandwidth onto the vertical profiles displayed when using the option *MODIFY REGION* (**Fig. 5.16**).

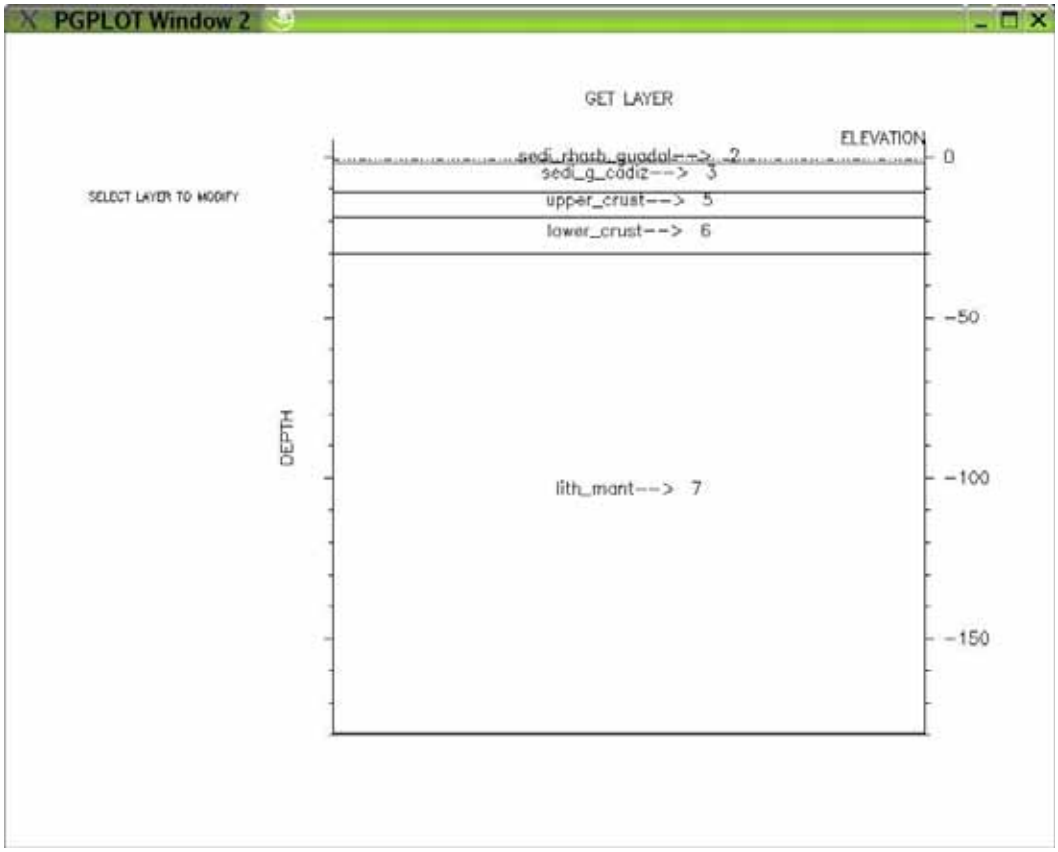

Fig. 5.13 *Window displayed by GEO3Dmod_INTF containing a column with all available bodies at one point of the model.*

Another option offered by the program is *REFERENCE POINTS (r)*. It allows the user to define interactively a number of reference polygons (i.e. areas over a map view of the model) by their geographical coordinates in the main window. The aim of this option is twofold. First, it may be helpful to identify areas of the model corresponding to their geophysical signature (calculated/observed geophysical observables, residuals, geometry of the bodies). The polygons defined by the reference points are displayed on all maps containing the geophysical observables or the different layers when using the options CHANGE *OBS*, and *BODY PLOT*, respectively. Second, the intersections between the vertical profiles displayed by the option MODIFY *REGION* and the

polygons defined by the reference points are projected onto the vertical profiles (**Fig. 5.17**). Therefore, *REFERENCE POINTS* can also be used to mark structures, over the plain view maps, which are going to be next modified via *MODIFY REGION* option. The information concerning the reference points is stored in the files *ref_points.info* and *ref_points.dat*.

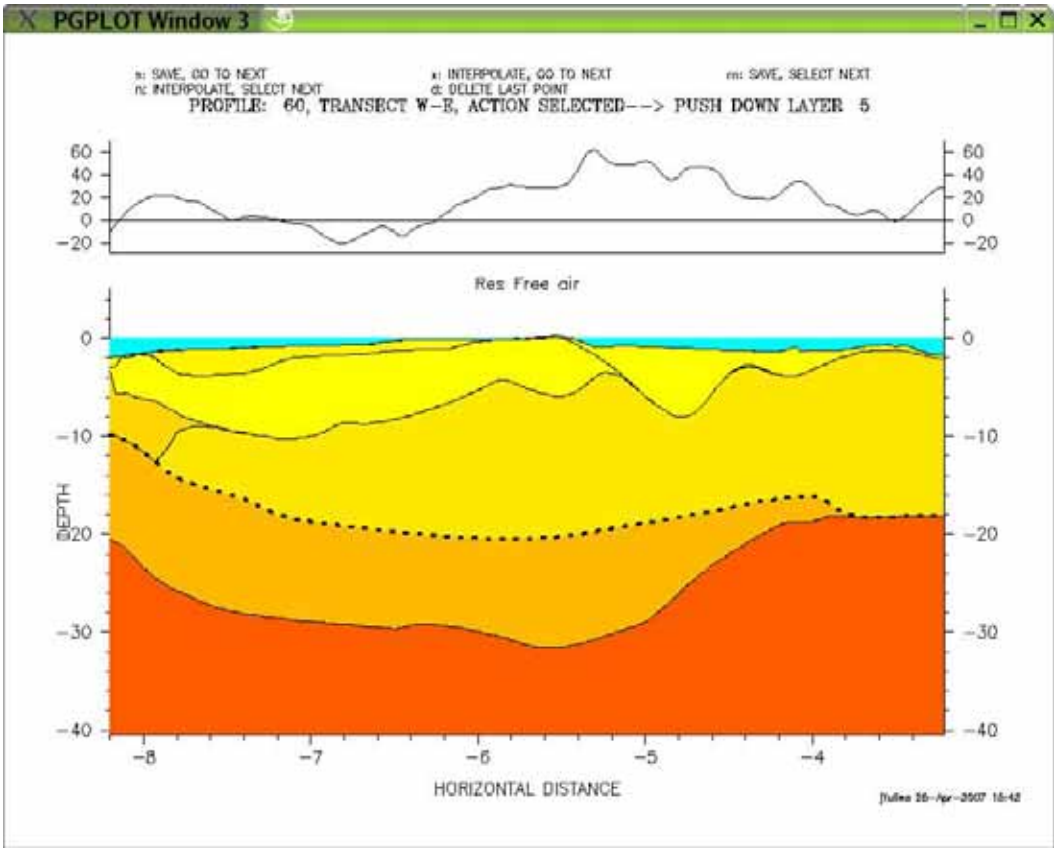

Fig. 5.14 *Vertical profiles displayed when using the option MODIFY REGION (m). The upper panel represents a profile of the geophysical observable selected with CHANGE OBS (c) in the main window. The lower panel corresponds to the lithospheric model, with the layer selected for modification as a dashed line.*

5.3.2 Program description

A general scheme of the files and folders used by GEO3Dmod_INTF is shown in the lower panel of **Fig. 5.5**. GEO3Dmod_INTF works in geographical coordinates. The program reads from the input file *info.dat* the minimum and maximum geographical coordinates that define the study area, *lon_min, lon_max, lat_min, lat_max*, and the grid step in decimal degrees, *p_m*. Files with the elevation, *elev.xyz*, and the geographical coordinates of the coastline of the

model, *coast_prev.xy*, are also necessary. The expected format of *elev.xyz* consists of three columns, longitude, latitude, and elevation (km), starting from the NW corner of the calculation area and then going from West to East successively, ending at the SE corner. Both input files can be generated using the script *elev.job* (for Linux).

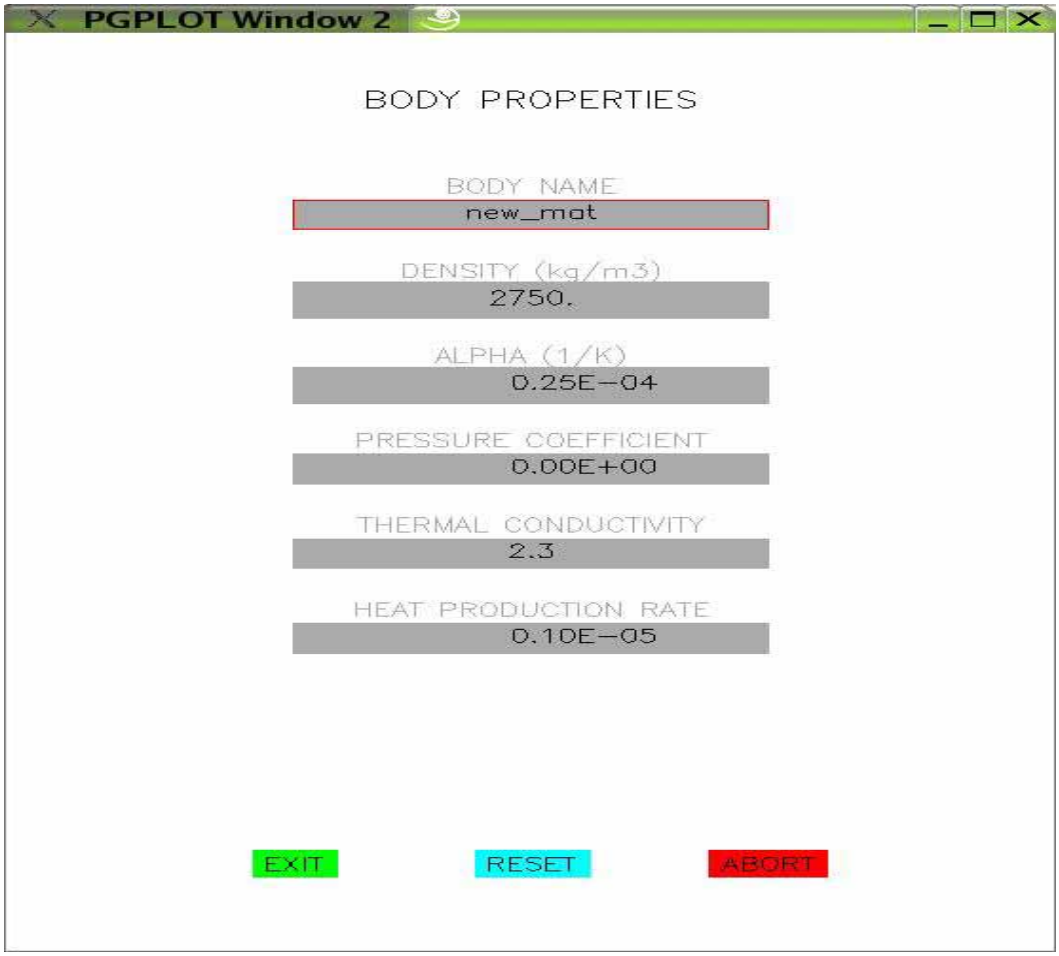

Fig. 5.15 *Window displayed when using the option ADD NEW LAYER (a) to define the properties of a new layer (body).*

Optionally, the program reads the labels in the file *labels.dat* with the format: longitude, latitude, depth (km), and text string. The files concerning reference points, *ref_points.info, ref_points.dat*, are also optional. The file *ref_points.info* must have one register for each reference polygon with its number of vertices. The file *ref_points.dat* must have the geographical coordinates of all the polygons listed in the same order as *ref_points.info* (**Fig. 5.5 lower panel**).

The files with the calculated and observed geophysical observables, if present, must be placed in the folder **GEO_DATA**. The calculated/observed elevation (*elevation_calc.xyz, elevation_dat.xyz*), geoid anomaly *(geoid_calc.xyz/geoid_dat.xyz*), free air anomaly (*FA_calc.xyz/FA_dat.xyz*), Bouguer anomaly (*Boug_cal.xyz/Boug_dat.xyz*) and temperature at the Moho (*T_moho.xyz*) files, follow the same NW to SE corner order as the elevation file (**Fig. 5.5 lower panel**).

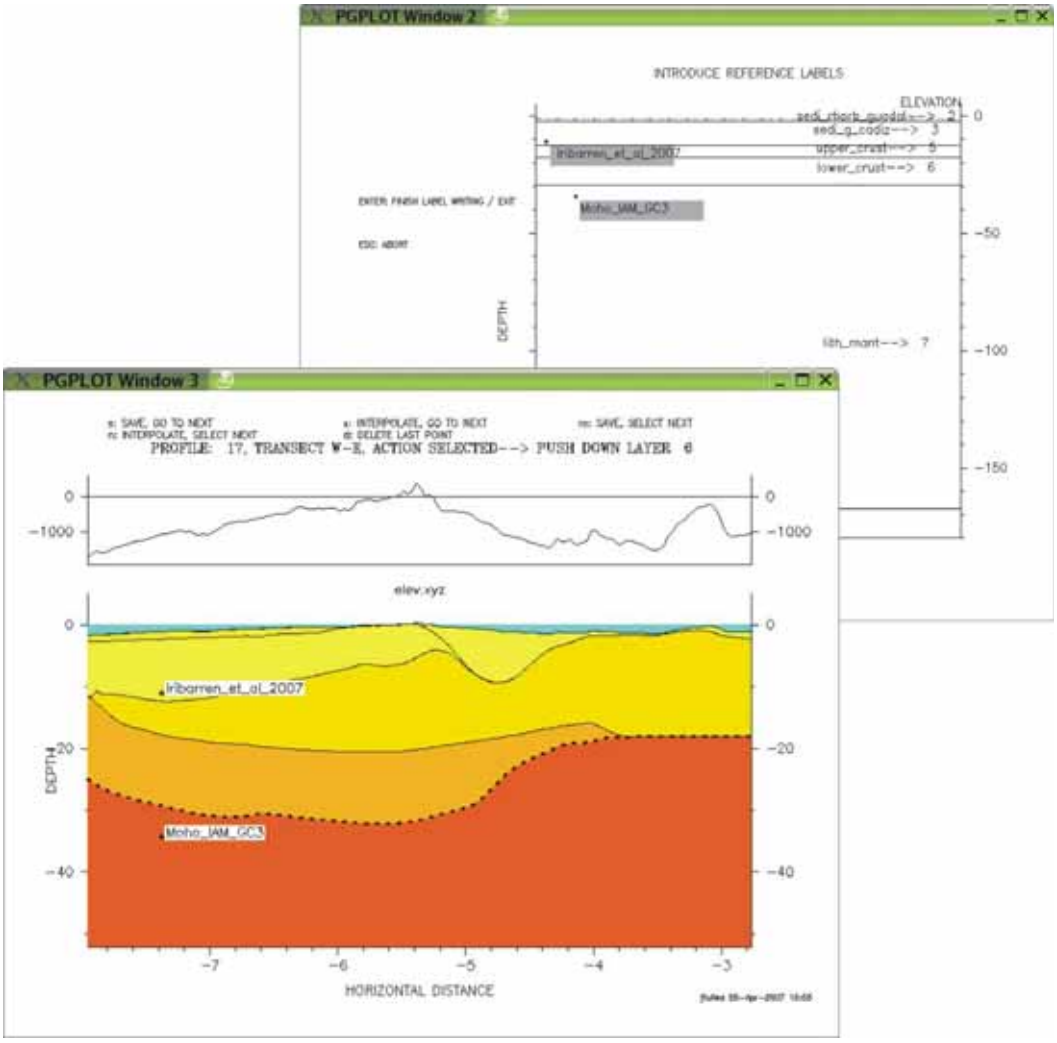

Fig. 5.16 *The option LABELS (l) allows the user to introduce labels (i.e. a text string located at a point characterized by its latitude, longitude and depth) containing previous geophysical data to be used as modelling constraints. The text strings are introduced in a window with a column containing all the available bodies (upper panel). The labels are projected within a certain bandwidth in the vertical profiles displayed by the option MODIFY REGION (lower panel).*

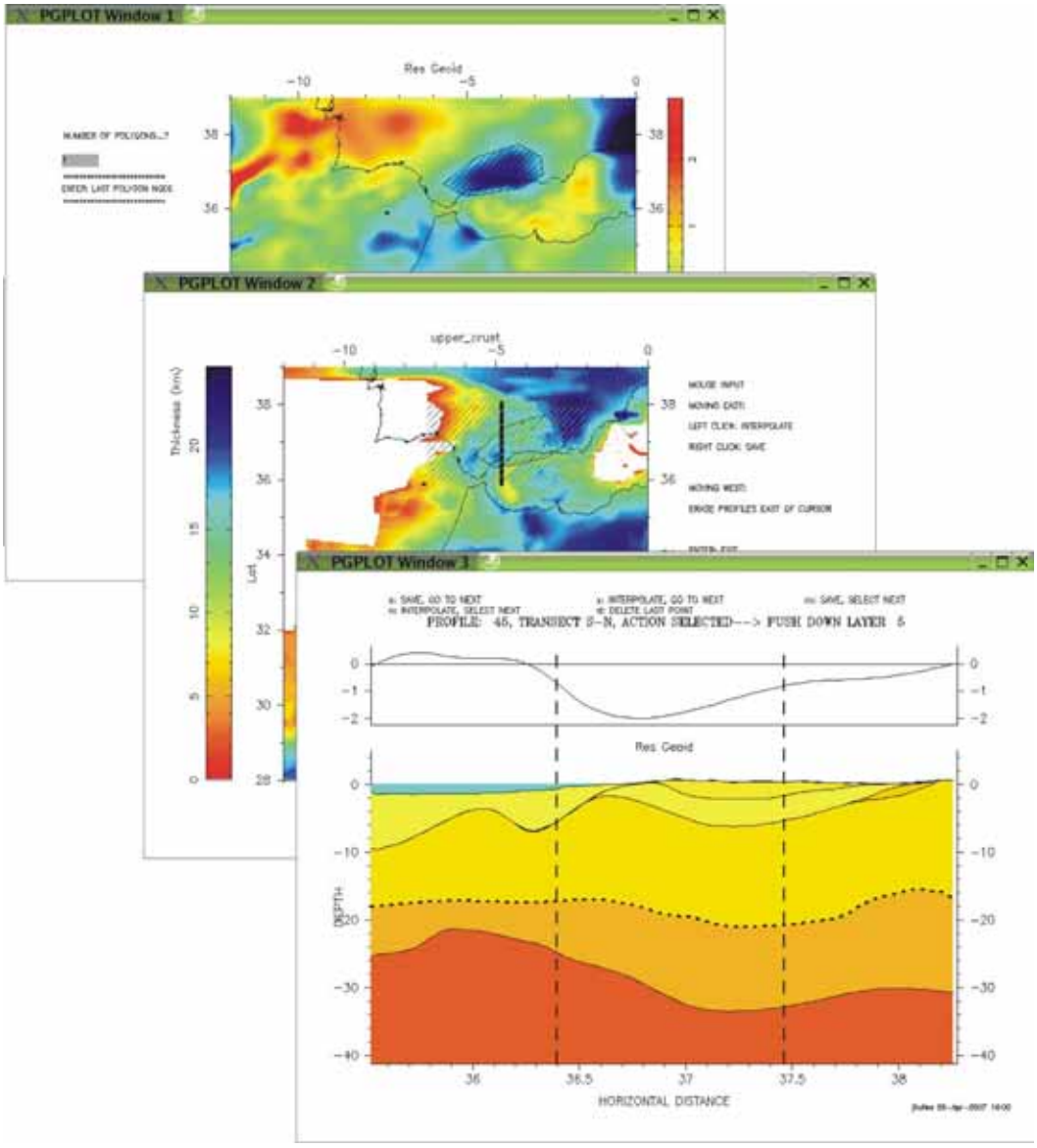

Fig. 5.17 *The option REFERENCE POINTS (r) allows the user to define interactively a number of reference polygons by its geographical coordinates in the main window (upper panel). The intersections between the vertical profiles displayed by the option MODIFY REGION and the polygons defined by the reference points (middle panel) are projected in the vertical profiles (lower panel).*

The program reads the number of layers defined and their properties in the same file that is used by the forward module (GEO3Dmod): *layers.info*. Every layer defined in *layers.info* must be associated with an ASCII file in the folder **layers** named *layer*i.*xyz*, where i is the number of the layer defined in *layers.info* (**Fig. 5.5 lower panel**). The expected format for the layer files is the same as that for the elevation and geophysical observables files. The script *GEO3Dmod.job* (for Linux) transforms the geographical layer files (in folder **layers**) into the

Cartesian layer files (in folder **layers_xy**) required by GEO3Dmod to calculate the geophysical observables (**Fig. 5.5**). For each run of GEO3Dmod_INTF, the layer files (*layer*i*.xyz and layers.info*) of the last run are saved in the folder **bak**. Some options produce output Post Script files (map views of the bodies, vertical profiles), which are put in the folder **OUT_ps**.

5.4 SYNTHETIC MODELS: 1D, 2D AND 3D CALCULATIONS

In the following, we will compare the differences between 1D, 2D and 3D calculations. When working in 1D, one assumes that the lithospheric structures extend infinitely in both x and y directions for each point of the mesh, although the structure can vary laterally. A typical case of the 1D approach is the concept of local isostasy (eqs. 2.7 and 5.13). In the case of the gravity anomalies, this means that the topography and the rest of density contrasts within the lithosphere are computed as infinite slabs, i.e. their vertical attraction depends only on the thickness and the density contrasts. The latter implies, assuming local isostasy, a null free air anomaly and the following expression for the Bouguer anomaly:

$$\begin{aligned} &\Delta g_B = -2\pi G\rho E \\ &\rho = \rho_{cRED} \quad IF\ E > 0 \\ &\rho = \left(\rho_{cRED} - \rho_w\right) \quad IF\ E < 0 \end{aligned} \tag{5.17}$$

For the geoid anomaly, the 1D approximation was presented in Chapter 4 of this thesis (eqs. 4.1 and 4.11).

The most popular potential field interpretation technique is the 2D approach. It assumes that the geological bodies extend to infinity perpendicular to the modelled cross section, and simplifies the calculation and the model parameterisation. The 2D calculation can be done by either considering polygonal bodies (e.g. Talwani et al., 1959; Chapman et al., 1979; Ayala et al., 1996) or using a real 3D geometry (e.g. a set of right rectangular prisms) extended homogenously and infinitely along one horizontal axis. GEO3Dmod_INTF uses the second approach to perform 2D calculations. However, the 2D approach is only suitable when the wavelengths of geological structures, and their geophysical signatures, do not vary considerably across-strike to the modelled transect. In other cases, a 3D approach must be used.

To test our program we have used a number of four-layered models composed of crust, lithospheric mantle, sea water and asthenosphere (**Table 5.2 and Table 5.3**).

Parameter	Symbol	Reference	Topography	Bathymetry
Elevation	E	0 km	2 km	-4 km
Crustal density	ρ_c	2780 kg/m^3	2780 kg/m^3	2780 kg/m^3
Lithospheric mantle density	ρ_m	3245 kg/m^3	3245 kg/m^3	3245 kg/m^3
Sea water density	ρ_c	1030 kg/m^3	1030 kg/m^3	1030 kg/m^3
Asthenosphere density	ρ_a	3200 kg/m^3	3200 kg/m^3	3200 kg/m^3
Moho depth	z_c	30 km	42 km	15 km
LAB depth	z_m	145 km	145 km	145 km

Table 5.2. *Parameters used in the synthetic models with constant layer densities.*

5.4.1 Comparison between 3D and 1D approaches

As a benchmark, it would be desirable to recover the 1D value for long wavelength topography in the case of gravimetric and geoid anomalies. To test this issue, we have considered two synthetic models: a vertical block with 2 km of topography and a 4 km-deep basin filled with sea water (**Fig 5.18**). In both cases, we assume local isostasy and, therefore, the corresponding crustal thickening/thinning necessary to compensate the topography/bathymetry is calculated using eq. 2.7 (**Table 5.2**). We have varied the horizontal extension of the synthetic models in the x and y directions (i.e. its wavelength) in order to compare the 1D and 3D approaches. In **Fig. 5.19 A and B** we represent the quotient between the 3D and the 1D geoid anomaly values as a function of the width of the topography anomaly for both synthetic models. We observe a rapid increase of the quotient for short wavelengths tending to an asymptotic behaviour for long wavelengths.

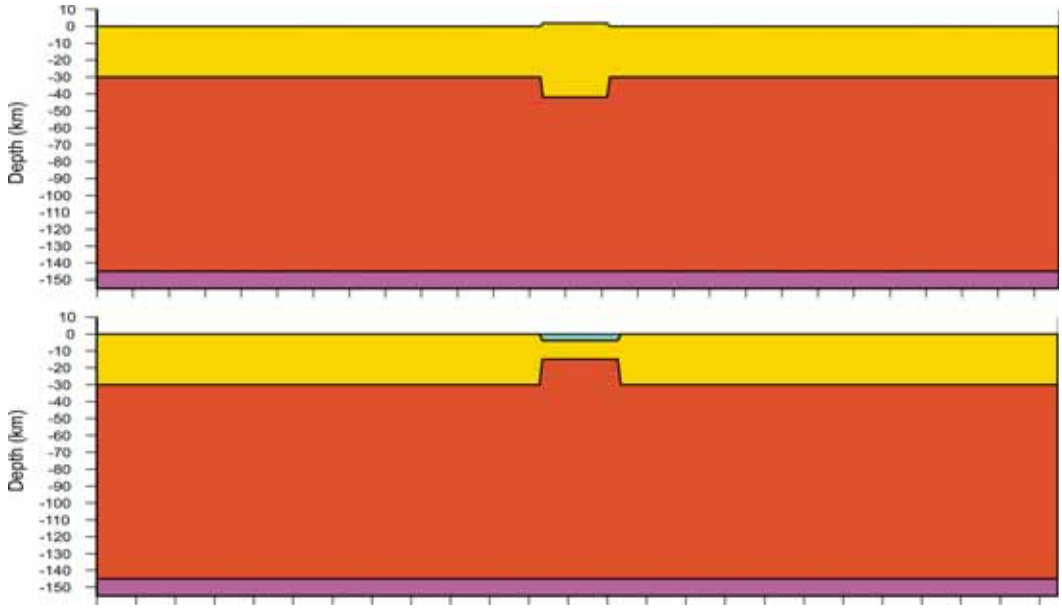

Fig 5.18 *Synthetic models used to test GEO3Dmod. Upper panel: vertical block with 2 km of topography. Lower panel: 4 km-thick crustal hole filled with sea water. In both cases local isostasy in the crust is assumed (**Table 5.2**).The width of the topography has been varied between 0 and 2000 km (both in x and y directions) to evaluate the 3D/1D ratio as shown in **Fig. 5.19**.*

For the positive topography, a wavelength of about 350 km is necessary for the 3D value to reach 90% of the 1D value (**Fig. 5.19 A**). This wavelength is reduced to about 220 km in the case of the negative elevation (**Fig. 5.19 B**). In the 1D approach, the geoid anomaly is proportional to the dipolar moment of the vertical anomalous density distribution beneath the observation point (eq. 4.1).

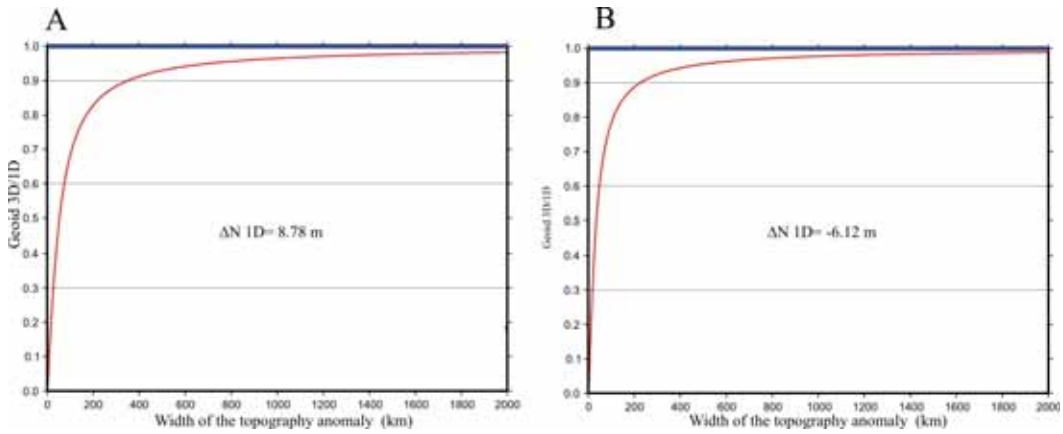

Fig. 5.19 *Ratio between the 3D and the 1D geoid anomaly values as a function of the width of the topography anomaly for the synthetic models shown in **Fig. 5.18**. **A)** Positive topography. **B)** Negative topography.*

In our case, the mass dipole is constituted by the topography/bathymetry and the crust-mantle density contrast, and its length is 37 km for E=2 km and 20.5 km for E= -4 km. In both cases, the wavelength necessary to achieve 90% of the 1D value is about 10 times the length of the mass dipole. Thus, the 1D approach is more appropriate as the ratio between the topography wavelength and the dipole length increases.

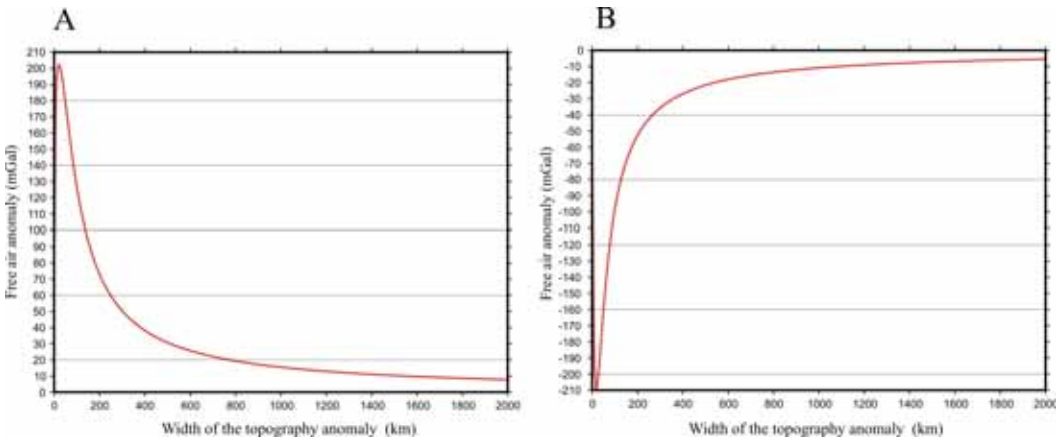

Fig. 5.20 *Free air anomaly as a function of the width of the topography anomaly for the synthetic models shown in* ***Fig. 5.18****. **A)** Positive topography. **B)** Negative topography.*

For the gravimetric anomalies, as mentioned above, the 1D approach implies a null free air anomaly, i.e. the contribution of the topography is exactly cancelled with that due to the density contrast at depth (e.g. Moho). However, in the 3D approach this is not true. In **Fig. 5.20 A and B** we can see the free air anomaly value for both synthetic models. As in the case of the geoid anomaly, the 3D value tends to zero rapidly for short wavelengths and asymptotically for long wavelengths, for both E=2 km and E= -4 km. For the positive topography, the free air anomaly starts with positive values and goes to zero (**Fig. 5.20 A**), while conversely for E= -4 km, it goes from negative values to zero (**Fig. 5.20 B**). Therefore, in both cases for the short wavelengths, the effect of the topography/bathymetry predominates over the deeper crust-mantle density contrast. For E=2 km a wavelength of about 800 km is required to reduce the free air anomaly to 20 mGal (**Fig. 5.20 A**), while for E= -4 km a wavelength of 550 km is needed in order to increase the anomaly to -20 mGal (**Fig. 5.20 B**).

To further illustrate the contrast between the 1D and the 3D approach, we have calculated in 3D with GEO3Dmod the geophysical observables associated with the lithospheric model obtained by 1D inversion of elevation and geoid

anomaly data using the methodology presented in Chapter 4 (**Fig. 4.5 A and B**). The model consists of four layers, crust and lithospheric mantle plus sea water and asthenosphere. For the crustal density, a linear gradient is assumed, while for the lithospheric mantle a temperature dependent density is considered (**Table 4.1**). The differences between the calculated and measured geophysical observables for the four-layered lithospheric model are shown in **Fig. 5.21 (A-D)**.

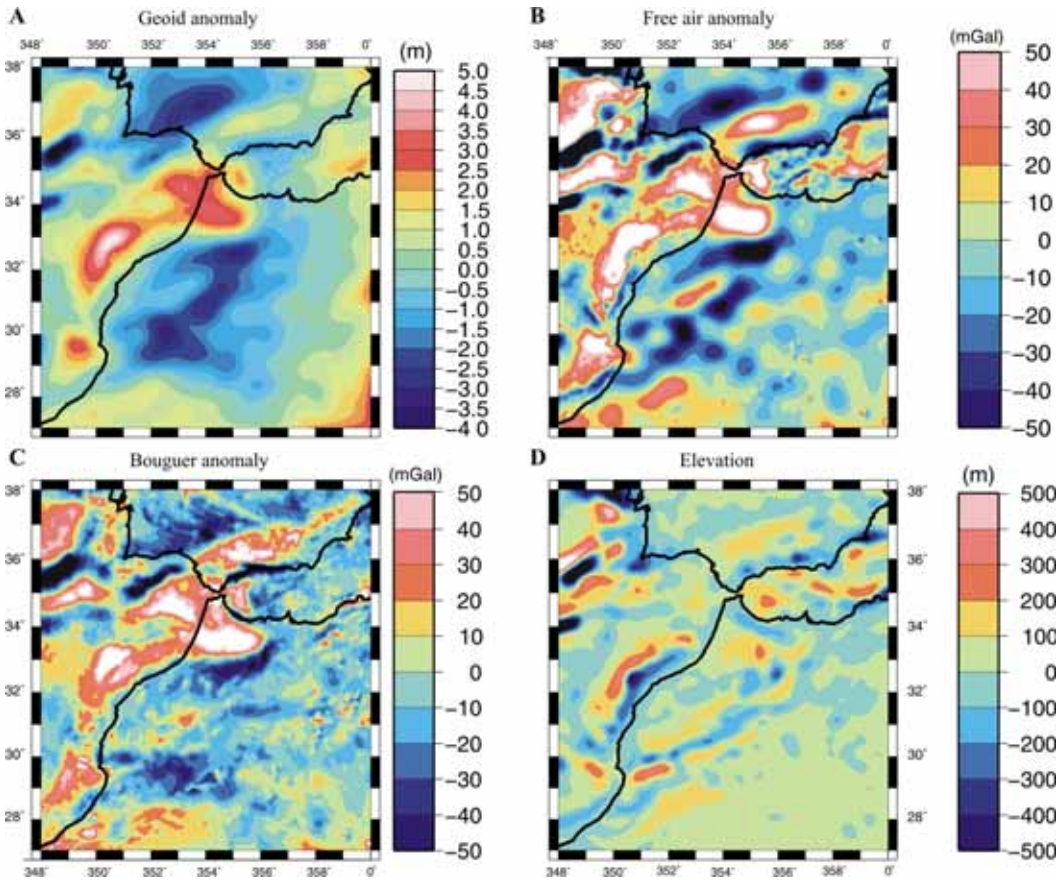

Fig. 5.21 *Residual geophysical observables (calculated minus observed. Calculations have been performed in 3D using the 1D crustal and lithospheric structure obtained by inversion of elevation and geoid anomaly (**Table 4.1**). **A)** Geoid anomaly. **B)** Free air anomaly. **C)** Bouguer anomaly. **D)** Elevation.*

Positive residuals in the Bouguer, free air and geoid anomalies indicate mass excess, whereas positive residual elevation implies a mass deficit in the lithospheric model. As expected, the calculated elevation is in good agreement with the actual topography, particularly for zones with smooth lateral variations, where the 1D and the 3D temperature distributions are similar (and, therefore, the lithospheric mantle density) (**Fig. 5.21 D**). Another source of the misfits in the

elevation is the different resolution of the 1D and the 3D model (i.e. the grid step of the 3D model is larger). The gravity anomaly residuals show elevated high frequency content compared with that of the geoid anomaly (**Fig. 5.21 A-C**). This suggests that the crustal misfits of our model can be mainly constrained by gravity anomalies, and that geoid anomaly is more sensitive to the long wavelength LAB depth variations. The long wavelength positive residuals in free air, Bouguer and geoid anomalies (i.e. the mass excesses) are present in areas where the 1D model predicts a thick lithosphere and vice versa. In the context of local isostasy, these misfits imply that the lateral variations of the lithospheric model obtained by 1D inversion of elevation and geoid anomaly are underestimated.

5.4.2 Comparison between 3D and 2D approaches

In the 2D approach it is assumed that the geological bodies extend infinitely perpendicular to a modelled profile. To test the validity of the 2D approach we have followed two steps. In the first step, we have considered an isometric block of topography, E=2 km, isostatically compensated using the parameters listed in **Table 5.2.** In **Fig. 5.22 A and B** we show a panel with the 2D and 3D calculated free air, Bouguer and geoid anomalies for two wavelengths, 100 km and 600 km. For a 100 km wavelength, the differences between 2D and 3D are conspicuous (**Fig. 5.22 A**), particularly for Bouguer anomaly (~100 mGal) and geoid anomaly (~2 m). As expected, when the topography wavelength is increased to 600 km, the 2D-3D differences are strongly reduced (**Fig. 5.22 B**). In the second test we considered a rectangular topography/bathymetry, E=2 km, E= -4 km, isostatically compensated using the parameters listed in **Table 5.2**, with horizontal wavelengths of 1000 km and 100 km in the x and y axis, respectively (**Fig. 5.23**). We have calculated two cross sections in the x and y-axis for both structures. As expected, the 2D approach is valid when we cut the synthetic structure across its short dimension (y direction) (**Fig. 5.23 A and C**). In the cross section along the long direction, however, the differences between 2D and 3D calculations are obvious (**Fig. 5.23 B and D**). This is to illustrate the importance of choosing the right direction (perpendicular to the strike of the body) when performing 2D modelling. We also observe that the 2D-3D differences are larger for the positive topography case (E=2 km). This is due to its longer mass dipole separation in comparison with the bathymetric case (E= -4 km).

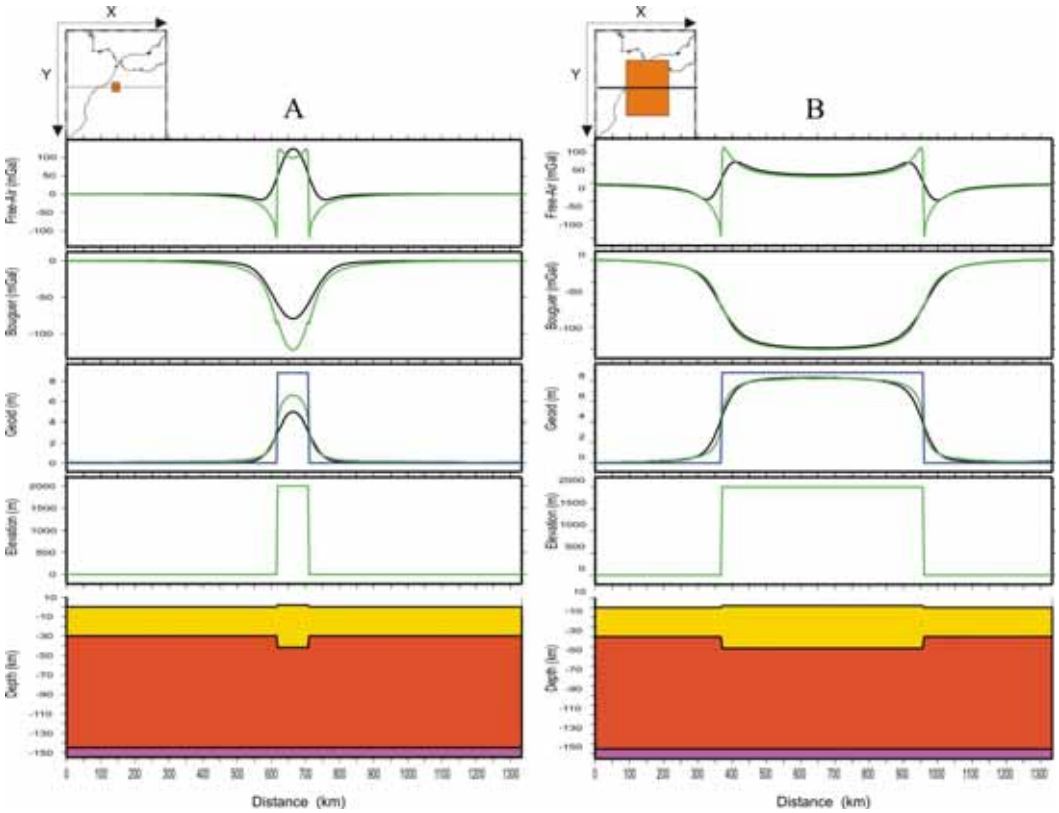

Fig. 5.22 *Comparison between 2D and 3D approaches for different topography wavelengths. The synthetic model consists of a vertical isometric block of positive topography isostatically compensated at the crust (**Table 5.2**). Black solid lines represent the 3D approach performed by GEO3Dmod, whereas green solid lines are the 2D values calculated using the CROSS SECTION (k) option of GEO3Dmod_INTF. The blue solid line in the geoid panel is the 1D value for the geoid anomaly (eqs. 4.1 and 4.11). **A)** Topography wavelength equal to 100 km. **B)** Topography wavelength equal to 600 km. The maps at the top of the profiles represent a plain view of the topography.*

Fig. 5.23 (see next page) *Two rectangular synthetic models with horizontal wavelengths of 1000 km and 100 km in the x and y axis, respectively, calculated along two different profiles. The model is assumed to be in local isostasy for both the positive and the negative topography (**Table 5.2**). Black solid lines represent the 3D approach performed by GEO3Dmod, whereas green solid lines are the 2D values calculated using the CROSS SECTION (k) option of GEO3Dmod_INTF. The blue solid line in the geoid panel is the 1D geoid anomaly (eqs. 4.1 and 4.11). **A)** and **C)** vertical cross section across the short dimension. **B)** and **D)** vertical cross section across the long dimension. The maps at the top of the profiles represent a plain view of the topography.*

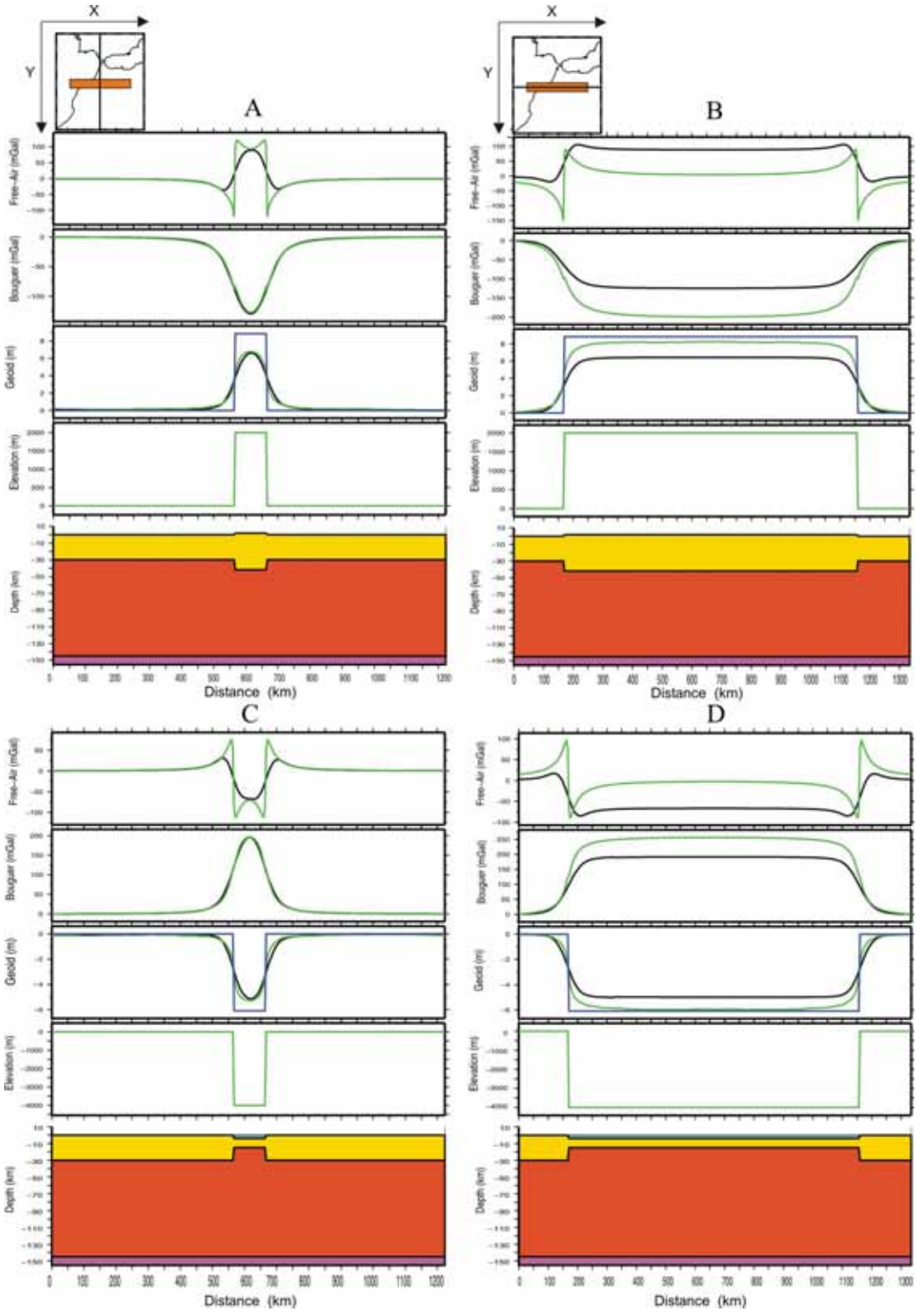

Fig. 5.23 (see previous page)

5.4.3 The thermal field. Over/under compensated lithosphere

Up to now, we have assumed a constant density for the lithospheric mantle. However, for most cases, a temperature-dependent density is a more suitable approximation (eq. 2.1). In this case, the local isostasy condition is expressed by eq. 4.10, and the heat transport equation (eq. 5.1) must be solved in order to obtain the temperature at the Moho. GEO3Dmod allows for the use of bodies with a linear density gradient. In the case of the lithospheric mantle, the latter implies that the density contrasts are higher at the Moho than at the LAB (eq 2.1). To test this issue, we have used the isometric isostatically compensated block of topography (E=2 km) of the last sections, but now with a temperature-dependent lithospheric mantle density (**Table 5.3**).

Parameter	**Symbol**	**Flat LAB (1)**	**Flat LAB (2)**	**Under comp.**	**Over comp.**
Elevation	E	2 km	2 km	2 km	2 km
Crustal density	ρ_c	2780 kg/m^3	2780 kg/m^3	2780 kg/m^3	2780 kg/m^3
Average lithopheric mantle density	ρ_m	3241 kg/m^3	3237 kg/m^3	3232.2 kg/m^3	3237 kg/m^3
Sea water density	ρ_c	1030 kg/m^3	1030 kg/m^3	1030 kg/m^3	1030 kg/m^3
Asthenosphere density	ρ_a	3200 kg/m^3	3200 kg/m^3	3200 kg/m^3	3200 kg/m^3
Moho depth	z_c	40.5 km	39.5 km	35.1 km	43 km
LAB depth	z_m	138.5 km	137.5 km	90 km	180 km
Temperature at the Moho	T_{mh}	617.9 ºC	696.9 ºC	774.2 ºC	685.6 ºC
Surface Heat flow	SHF	61.4 mW/m^2	62.7 mW/m^2	70.7 mW/m^2	60.6 mW/m^2
Heat production	H_s	2.5 10^{-6} exp (-(z+E)/15) Wm^{-3}	1.10^{-6} Wm^{-3}	1.10^{-6} Wm^{-3}	1.10^{-6} Wm^{-3}

Table 5.3. *Parameters used in the synthetic models with a temperature dependent lithospheric mantle density. (1) Flat LAB model with an exponentially decreasing heat production in the crust. (2) Flat LAB model for a constant heat production in the crust. For all models the reference crustal thickness is 30 km, and the heat production in the mantle is assumed to be null.*

The wavelength of the synthetic topography has been selected large enough to avoid 2D-3D differences. The heat production model used, constant or exponentially decreasing (eq. 2.17), affects the temperature distribution, mainly at crustal levels. The exponentially decreasing model (**Fig. 5.24 A**) leads to a cooler crust in comparison with the constant model (**Fig. 5.24 B**) and, therefore, to a higher average lithospheric mantle density (**Table 5.3**). This density difference does not have a significant effect on both free air and Bouguer anomalies, although the geoid anomaly is about 1.5 m lower for the exponentially decreasing model due to the stronger negative density contrast at the Moho (**Figs. 5.24 A and B**).

In all the synthetic models that we have considered in the previous sections, isostatic compensation of the topography is achieved only within the crustal layer (i.e. flat LAB). Nevertheless, the isostatic balance commonly involves the whole lithosphere. With the aim of investigating the effect of the lateral variations in the LAB depth, we have performed an additional test. For the same isometric block of topography, E=2 km, we have distinguished two synthetic models: one with crustal overcompensation (i.e. lithospheric thickening) (**Fig. 5.24 C**) and the other one with crustal undercompensation (i.e. lithospheric thinning) (**Fig. 5.24 D**). The condition of local isostasy changes the Moho depth by about ±4 km with respect to the case of a flat LAB (**Table 5.3**). For the overcompensated topography, the temperature at the Moho (and, hence, the average lithospheric mantle density) and SHF are little changed with respect to the flat LAB model. Conversely, the temperature at the Moho and SHF are noticeably increased for the undercompensated model. The increase of the temperature at the Moho implies a decrease of the average lithospheric mantle density (**Table 5.3**). As can be seen in **Fig. 5.24 C and D**, the lithospheric thickening is associated with a decrease of the free air (-15 mGal), Bouguer (-30 mGal) and geoid anomalies (-3.7 m) with respect to the flat LAB model. Conversely, the undercompensated lithosphere leads to an increment of the free air (+10 mGal), Bouguer (+10 mGal) and geoid anomalies (+2.8 m) with respect to the flat LAB model, being this change is smaller than in the case of the overcompensated model. The reason of that difference is the following: in these simple models, the gravity and geoid anomalies are governed by the crust-mantle and lithosphere-asthenosphere density contrasts. Due to its higher magnitude and lower depth, the crust-mantle density contrast is dominant over the lithosphere-asthenosphere density contrast (**Table 5.3**). For the overcompensated model (**Fig. 5.24 C**), the crust thickens (i.e. mass defect) with no change in the crust-mantle density contrast with respect to the flat LAB model (**Table 5.3**). In contrast, for

the undercompensated model (**Fig. 5.24 D**) the crust thins (i.e. mass excess), but the crust-mantle density contrast is decreased with respect to the flat LAB model (**Table 5.3**). In addition, the lithosphere-asthenosphere density contrast (with an effect opposite to that of the crust-mantle contrast) in the overcompensated model is smaller than that of the undercompensated model.

Fig. 5.24 (see next pages) *Synthetic positive topography model with a temperature dependent lithospheric mantle density, assuming local isostasy (**Table 5.3**). The wavelength is 600 km. **A**) Model with flat LAB and an exponentially decreasing crustal heat production. **B**) Model with flat LAB and a constant heat production in the crust. **C**) Over compensated model (lithospheric thickening) with a constant heat production in the crust. **D**) Under compensated model (lithospheric thinning) with a constant heat production in the crust. The maps at the top of the profiles represent a plain view of the topography.*

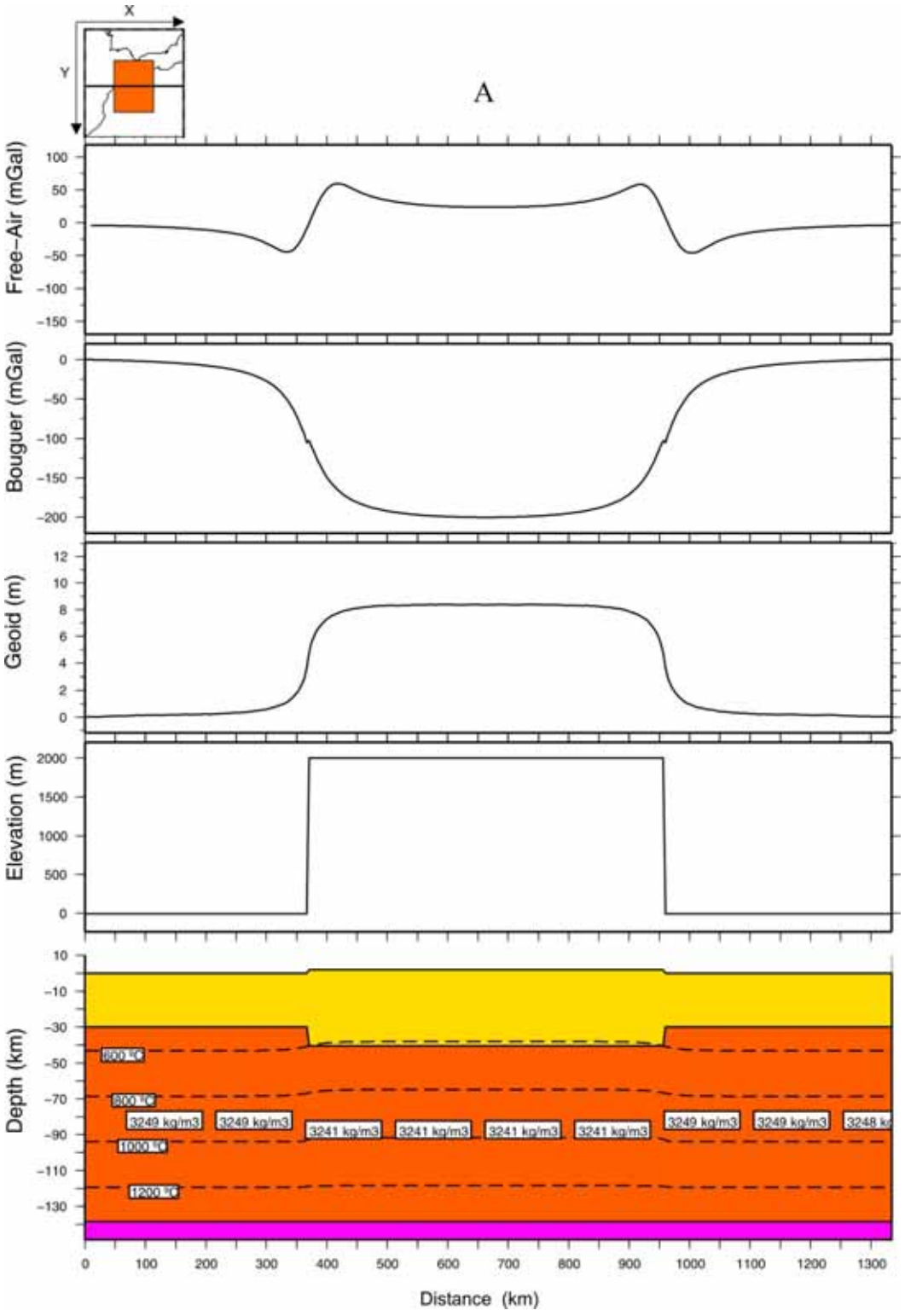

Fig. 5.24 A (see pag. 115).

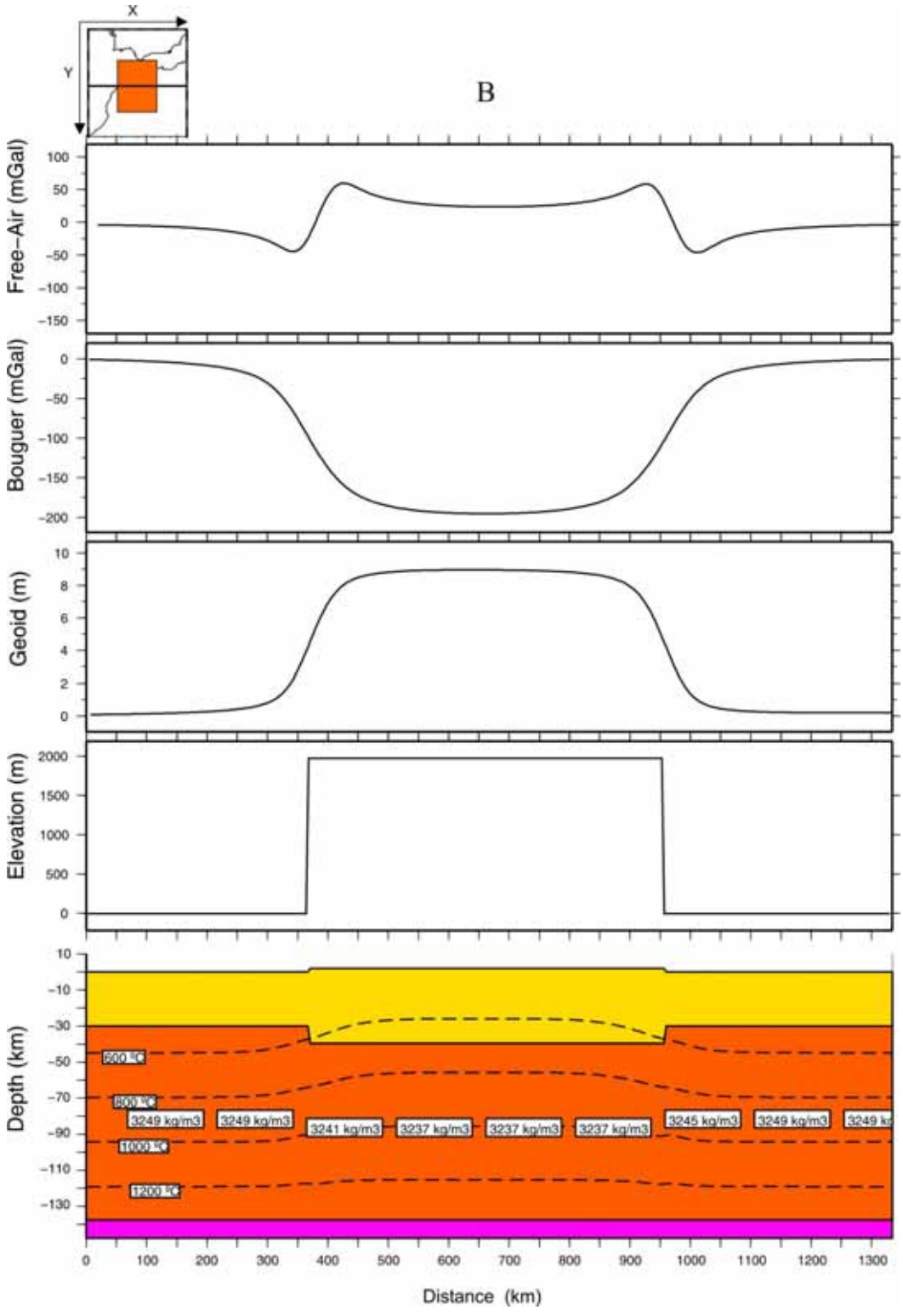

Fig. 5.24 B (see pag. 115)

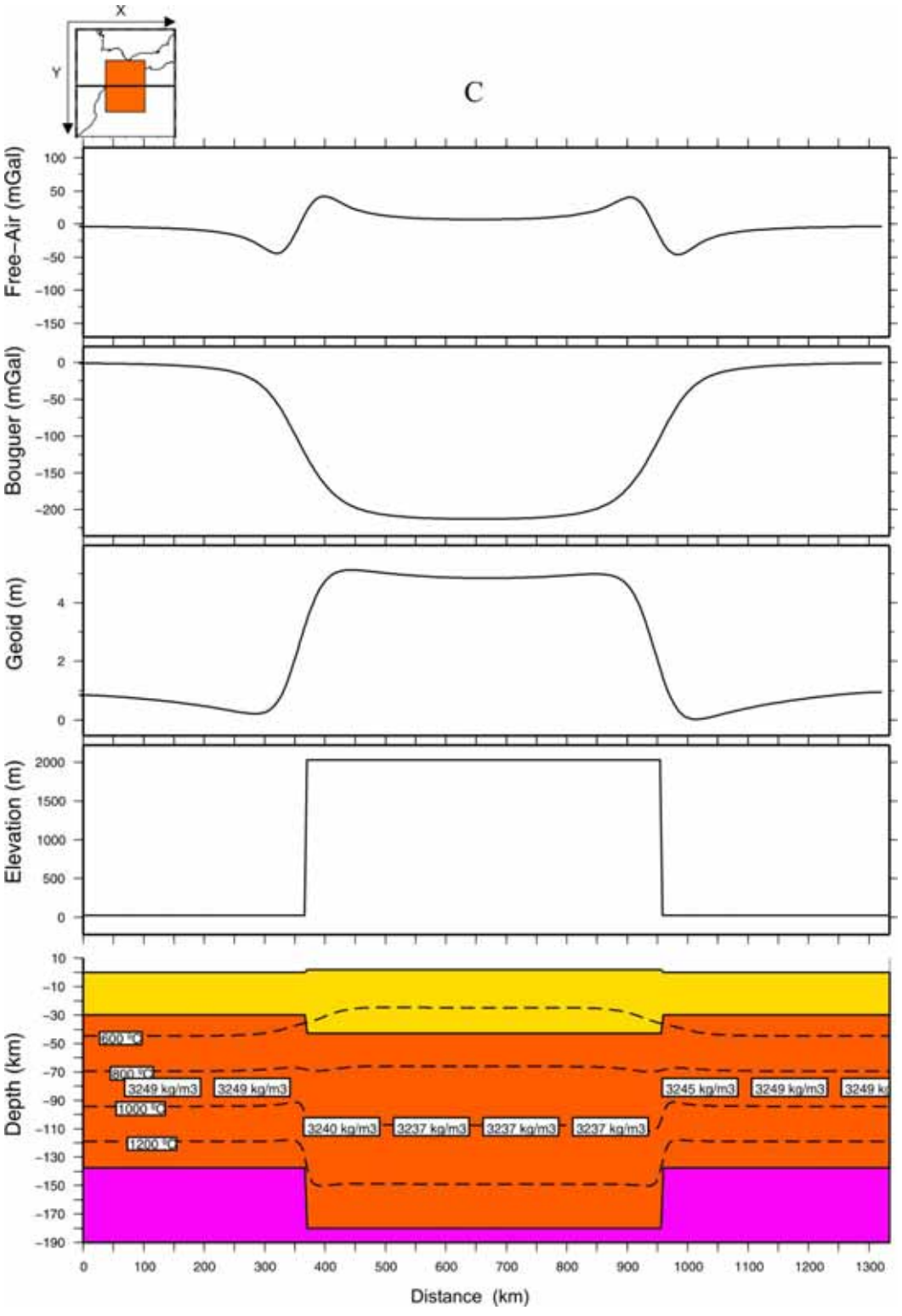

Fig. 5.24 C (see pag. 115).

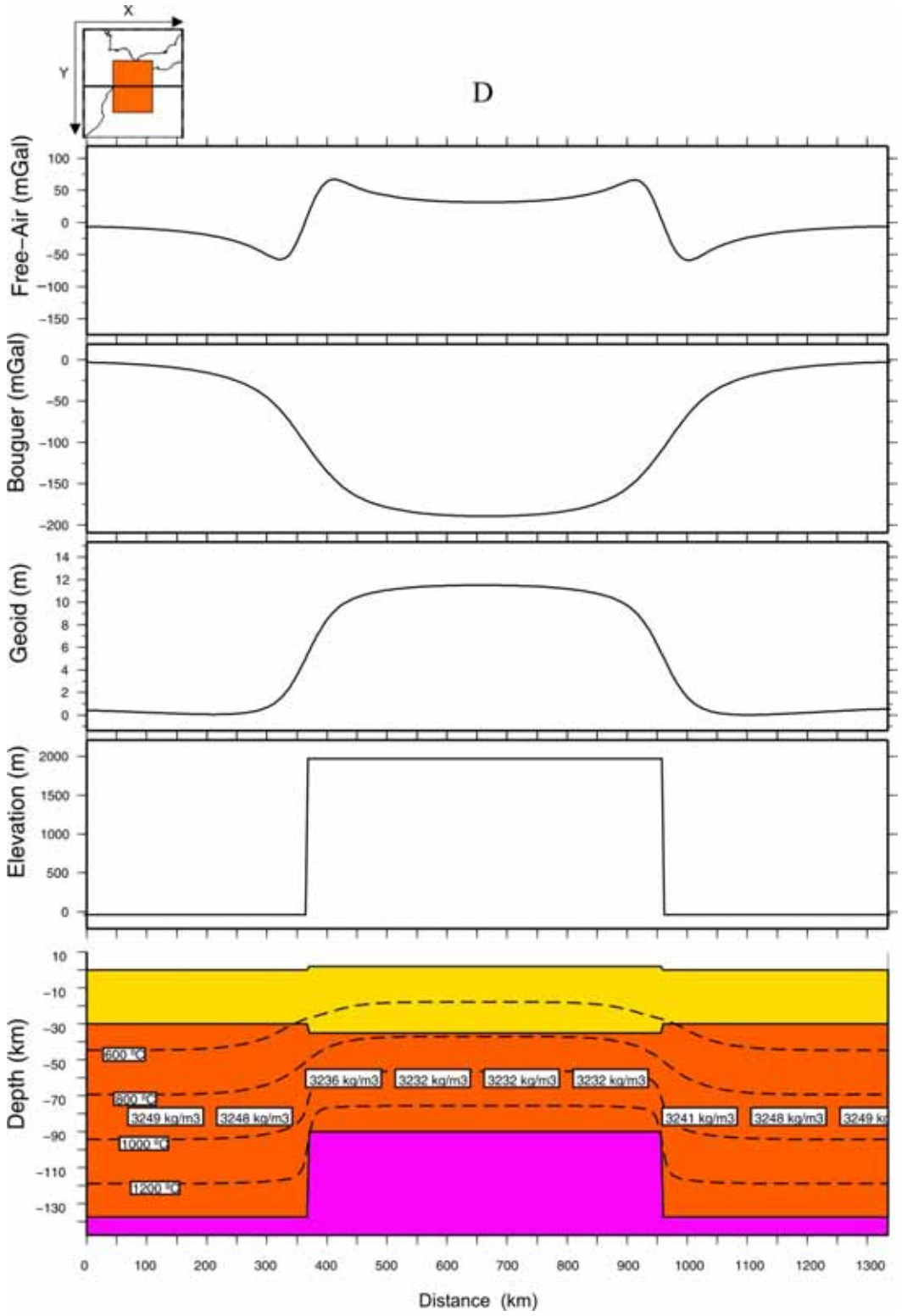

Fig. 5.24 D (see pag. 115)

Chapter 6

APPLICATION OF GEO3Dmod TO THE GIBRALTAR ARC SYSTEM REGION

6. APPLICATION OF GEO3Dmod TO THE GIBRALTAR ARC SYSTEM

6.1 INTRODUCTION

In this chapter, we apply the modelling computer program presented in Chapter 5 (GEO3Dmod) to the Gibraltar Arc System region (GAS). Our aim is, thus, to perform a 3D lithospheric regional model of the study area integrating gravity and geoid anomalies, elevation and surface heat flow (Chapter 3). The crustal structure has been constrained using seismic a-priori information wherever reliable data were available. In the present 3D model, eight different layers have been distinguished according to their physical properties. The geometry of the layers is shown in depth maps of the different surfaces that compose the model and several cross sections. We compare our results with previous works, especially with the four-layered 1D model obtained by inverting elevation and geoid anomaly, which has been used as the starting point for the modelling (Chapter 4). Finally, we discuss the main lithospheric structures obtained in the context of the different geodynamic models proposed to explain the origin and evolution of the GAS region.

6.2 DESCRIPTION OF THE 3D MODEL

The crustal structure in the GAS region is far from being well described by a unique laterally homogeneous layer, due to the presence of deep basins with sediment infill, crusts of different nature and composition, and peridotitic bodies. For that reason, in the 3D model, eight different layers have been considered according to their density, thermal conductivity, heat production, and thermal expansion coefficient (**Table 6.1**).

Layer	Density (kg/m^3)	Heat production (W/m^3)	Thermal conductivity (W/m K)
Peridotites	3100	0	3.2
Neogene and Quaternary Sediments of Alboran *(NQSA)*	2350	2 10^{-6}	2
Upper Sediments *(US)*	2200	1 10^{-6}	2
Accretionary Prism Sediments *(AWS)*	2400	1 10^{-6}	2.3
Intermediate Crust *(IC)*	2800	1 10^{-6}	2.1
Upper-Middle Crust *(UMC)*	2700	1.5 10^{-6}	2.5
Lower Crust *(LC)*	2920	0.2 10^{-6}	2.1
Lithospheric mantle	3200*[1-3.5 10^{-5} (T-1350 ºC)]	0	3.2

Table 6.1. *Properties of the different bodies used in the 3D model.*

6.2.1 Sediments

Three types of sediments are used in our 3D model. In the Alboran Basin we have used an isopach map of the Neogene and Quaternary sediments, constructed using a depth conversion function that combines stack velocities with measured depths in wells (Soto et al., 1996; Torne et al., 2000). Concerning the density, Torne et al. (2000) propose a value of 2400 kg/m^3. In this work, we have used a slightly lower value in order to achieve a better fit of geoid and Bouguer anomalies (**Table 6.1**). The maximum sediment accumulations are located in the west Alboran Basin in an arc-shaped depocentre (>8 km) near the Gibraltar Strait, which thins progressively towards the west up to approximately 3ºW. At the centre of the Alboran basin the sedimentary cover has a thickness of less than 1km that is further reduced around the volcanic edifices (**Fig. 6.1**). In the following, we will refer to the Neogene and Quaternary Sediments of Alboran as NQSA.

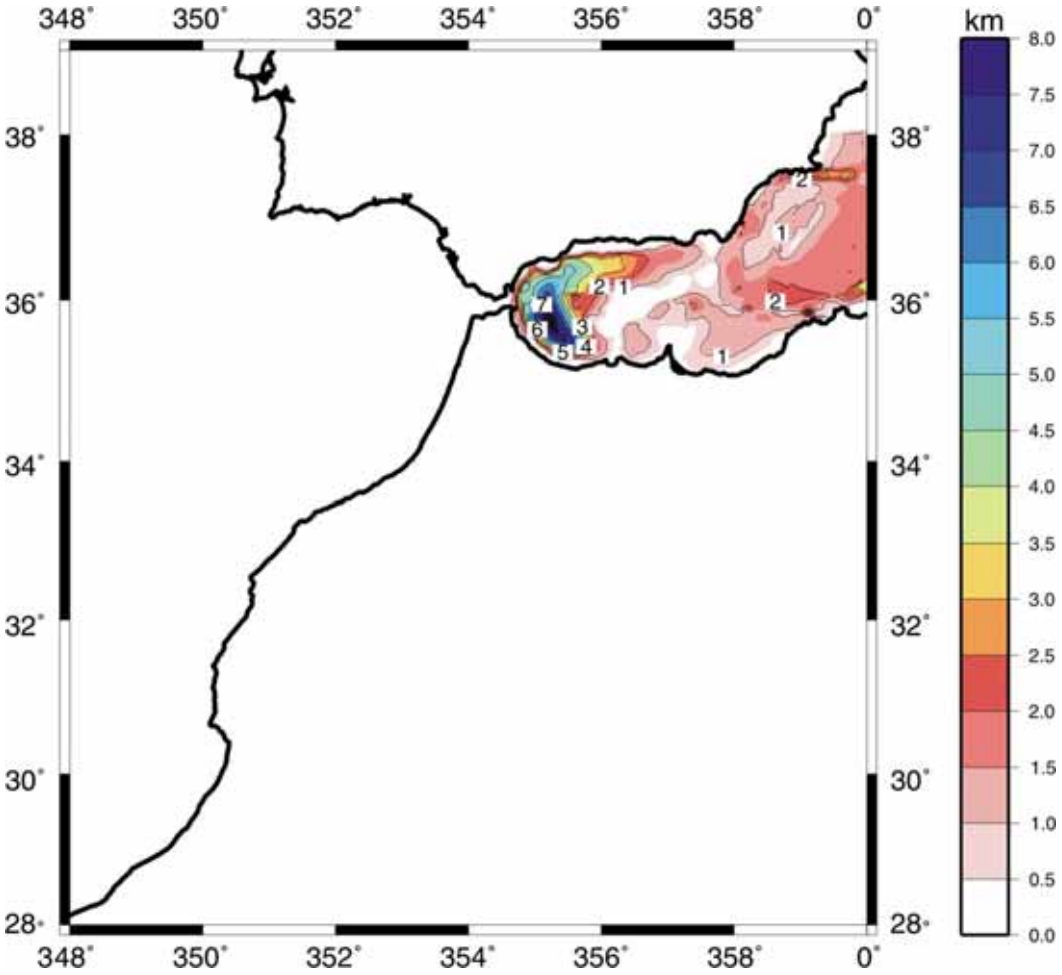

Fig. 6.1 *Thickness map of the Neogene and Quaternary Sediments of the Alboran Basin (NQSA) used in the 3D model. For the petro-physical properties of the NQSA layer, see* ***Table 6.1****. Isolines every 500 m.*

In the Atlantic oceanic domain and in some continental areas in Africa and the Iberian Peninsula, we have distinguished two adjacent sedimentary layers according to their density. For the upper layer we have chosen an average density of 2200 kg/m^3 (Gutscher et al., 2002; Contrucci et al., 2004; Zeyen et al., 2005). This sedimentary layer is present in almost the entire Atlantic oceanic domain as well as the Rharb and Guadalquivir Basins. In the continental area, the Miocene and Plio-Quaternary sediments have been modelled following geological maps. In the oceanic area, we have started with a 1 km-thick layer of sediments beneath the sea floor that was modified during the modelling process. For the most part, the thickness of this upper, unconsolidated sedimentary layer is comprised between 1 and 1.5 km, excepting some areas located near the North African continental shelf, the Gulf of Cadiz and the Rharb Basin, where it can reach >4 km (González et al., 1998; Litto et al., 2001; Gràcia et al., 2003) (**Fig. 6.2**). The

lower layer of sediments is denser than the former one, and an average density value of 2400 kg/m^3 has been used (Gutscher et al., 2002; Zeyen et al., 2005). In general it coincides with the accretionary wedge formed by the imbrication of Triassic to upper Miocene sediments, including also sediments of different ages with a similar density. Its thickness can reach more than 8 km in the Gulf of Cadiz and the Gibraltar Strait (González-Fernández et al., 2001; Medialdea et al., 2004; Iribarren et al., 2007) (**Fig. 6.3**). In the following, we will refer to these sedimentary layers as Upper Sediments (US), and Accretionary Wedge Sediments (AWS), respectively.

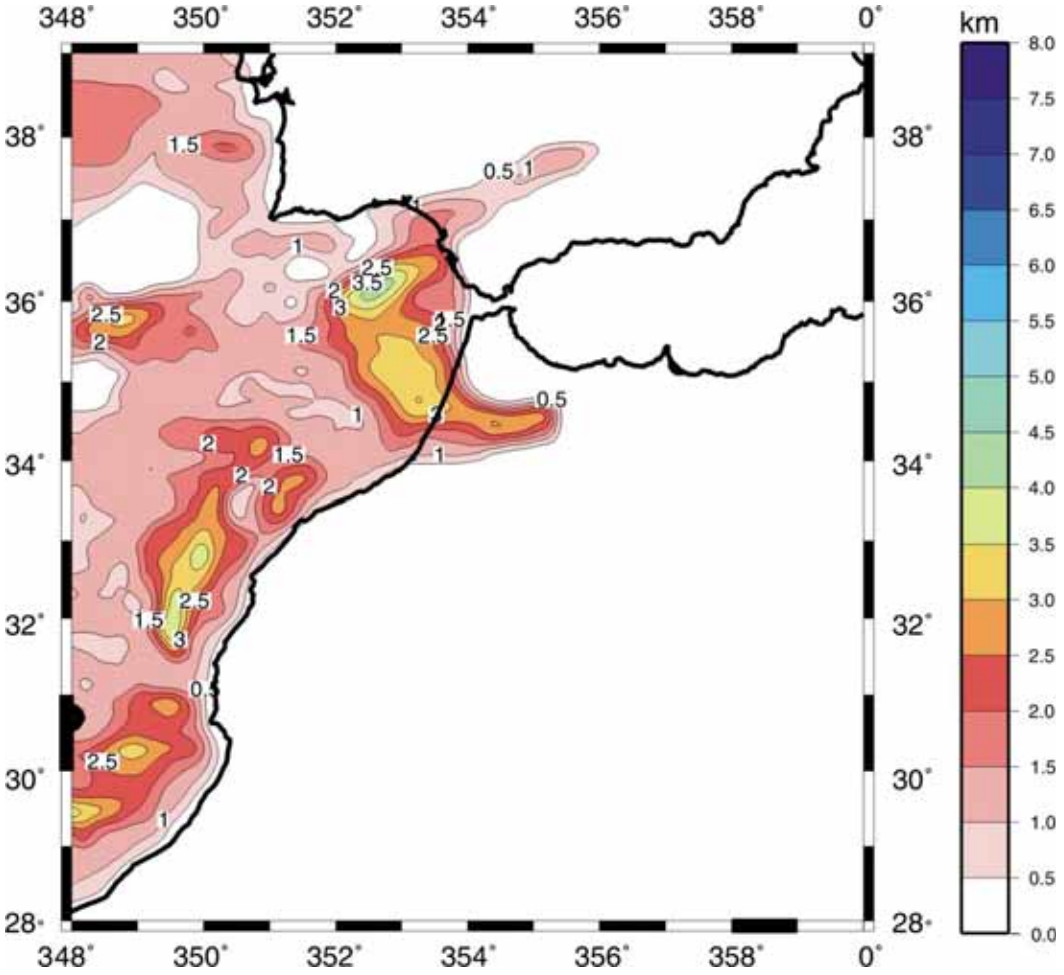

Fig. 6.2 *Thickness map of the modelled Upper Sediments (US) used in the 3D model. For the petro-physical properties of the US layer, see* ***Table 6.1****. Isolines every 500 m.*

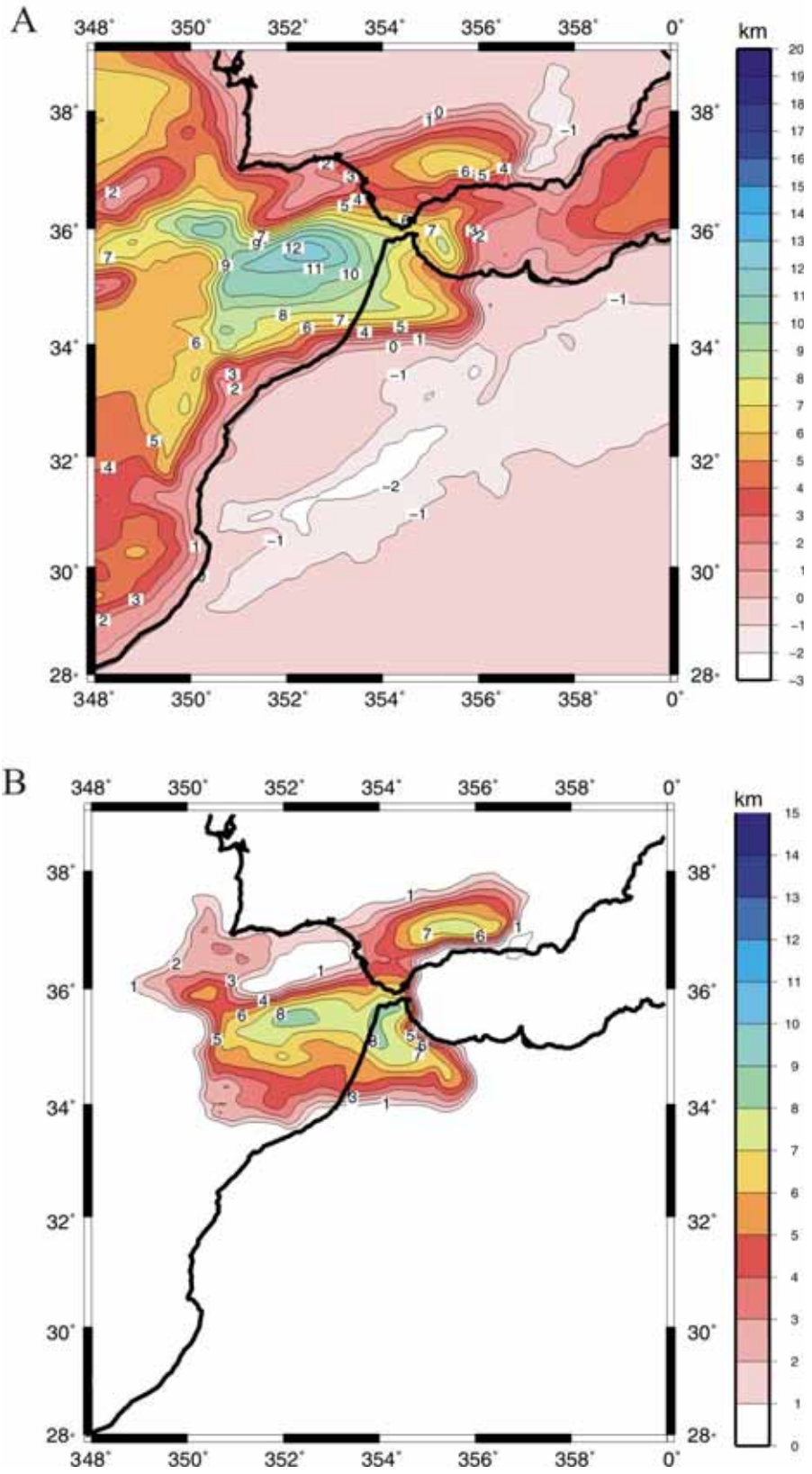

Fig. 6.3 ***A)*** *Depth of the base of the Accretionary Wedge Sediments (AWS) used in the 3D model. Negative depths indicate values above sea level.* ***B)*** *Thickness map of the AWS. For the petro-physical propertie of the AWS layer, see* ***Table 6.1****. Isolines every 1 km. Note that the layer is defined in the Betic-Gibraltar-Rif domain.*

6.2.2 Crust

In the following, we describe the layers defined for the crust (**Figs. 6.4, 6.5, 6.6 and 6.7**). As an initial model for the Moho depth, we have used the model inferred by 1D inversion of elevation and geoid anomaly presented in Chapter 4, which was already constrained with previous studies, particularly with seismic data (**Fig. 4.5 A**). For the most part of the model, we have divided the crystalline crust into two layers: an Upper-Middle Crust (UMC) with an average density of 2700 kg/m^3, and a Lower Crust (LC) with a density of 2920 kg/m^3. We have obtained the initial UMC and LC subdividing into two equal parts the crustal layer of the 1D model, maintaining the isostatic balance. For some areas, however, we have integrated an Intermediate Crust (IC) with average properties between the upper-middle and lower crust (**Table 6.1**), which can replace the upper-middle crust (SW Iberian Peninsula) or the whole crust, playing the role of a transitional crust (east Alboran Basin) (**Figs. 6.4, 6.5 and 6.7**). The presence of intra-crustal mantle-lithosphere bodies (peridotites) in the Betic-Rif orogen as suggested by gravimetric modelling (Torne et al., 1992) and seismic refraction/wide-angle reflection (Barranco et al., 1990, Banda et al., 1992), introduces in our model an undesirable long wavelength effect in the residual geoid anomaly (i.e. difference between calculated and observed). Therefore, and although we are interested in a regional scale model, we have introduced a high-density crustal layer (**Table 6.1**) located in two small areas in both the Betics and the Rif, in order to avoid this misfit (**Fig. 6.6**).

Fig. 6.4 (pag. 129) ***A)*** *Depth of the base of the Intermediate Crust (IC) used in the 3D model. Negative depths indicate values above the sea level.* ***B)*** *Thickness map of the IC. For the petro-physical properties of the IC layer, see* ***Table 6.1****. Isolines every 1 km. Note that this layer is only defined in the SW Iberian Massif and the oceanic domains of the Atlantic and the Mediterranean Seas.*

Fig. 6.5 (pag. 130) *Depth of the base of the Upper-Middle Crust (UMC) used in the 3D model, for further details see the text. For the petro-physical properties of the UMC layer, see* ***Table 6.1****. Isolines every 2 km.*

Fig. 6.6 (pag. 130) *Thickness map of the Peridotites used in the 3D model, for further details see the text. For the petro-physical properties, see* ***Table 6.1****. Isolines every 500 m.*

Fig. 6.7 (pag. 131) *Depth of the base of the Lower Crust (LC), coincident with the Moho. For the petro-physical properties of the LC layer, see* ***Table 6.1****. Isolines every 2 km.*

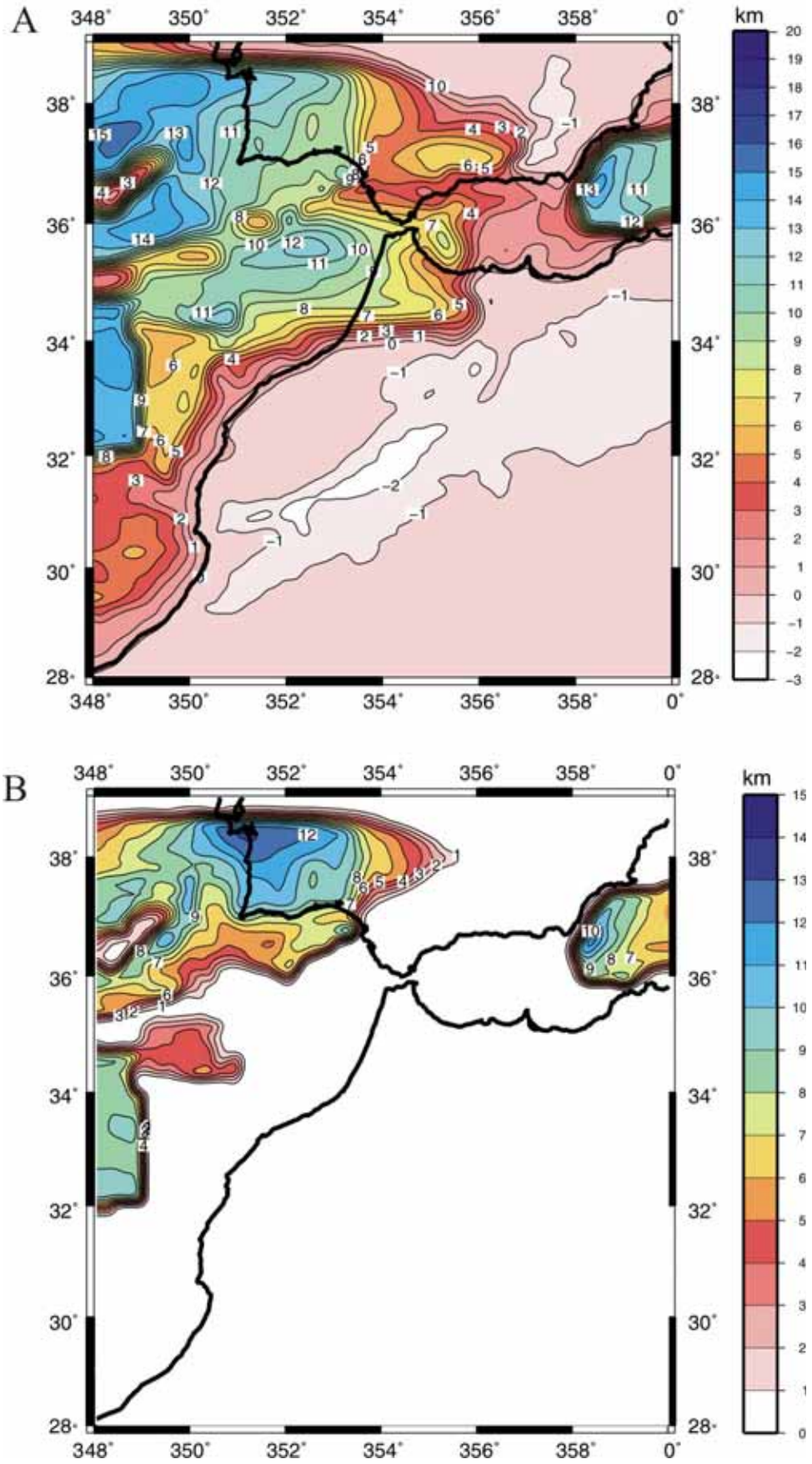

Fig. 6.4 (see page 128)

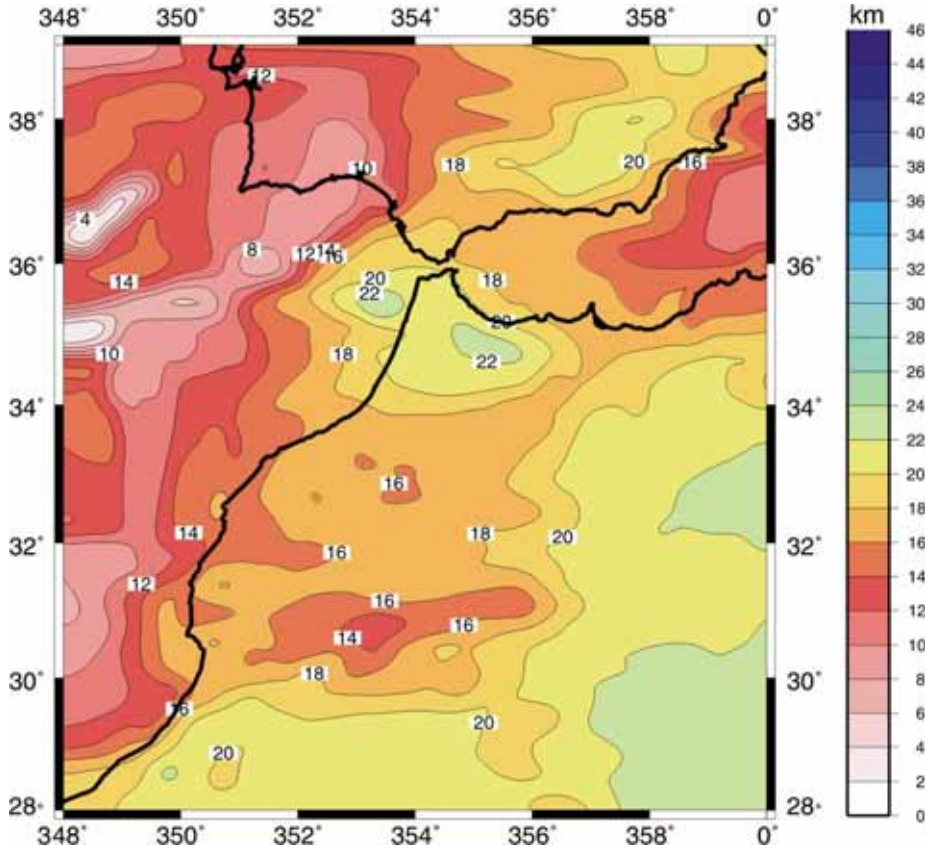

Fig. 6.5 (see page 128)

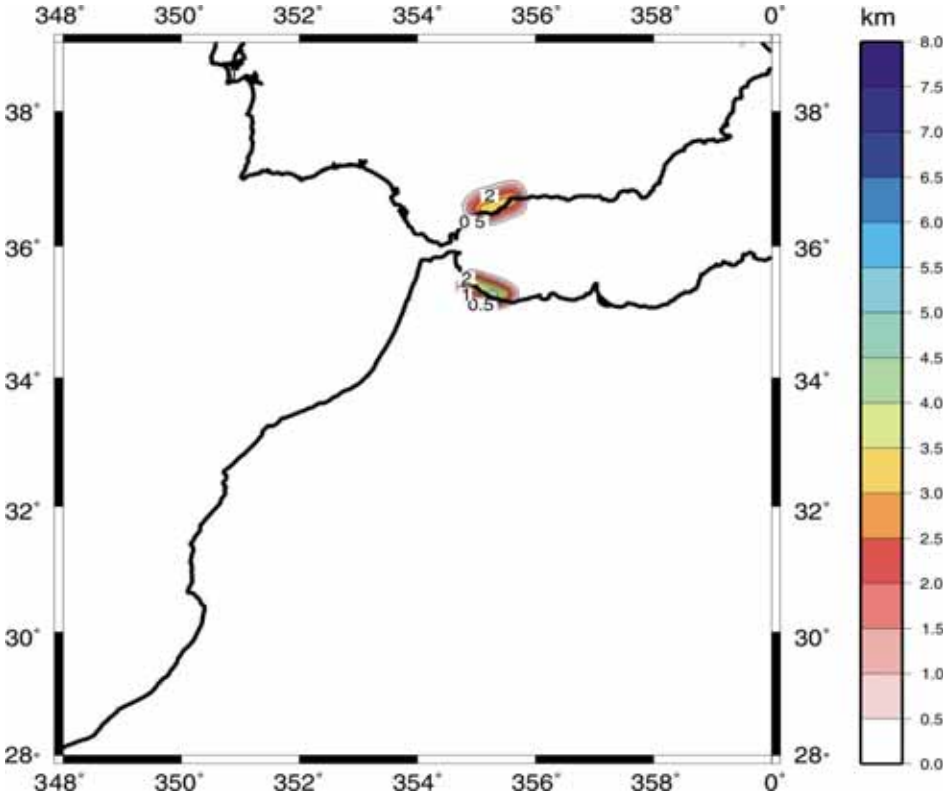

Fig. 6.6 (see page 128)

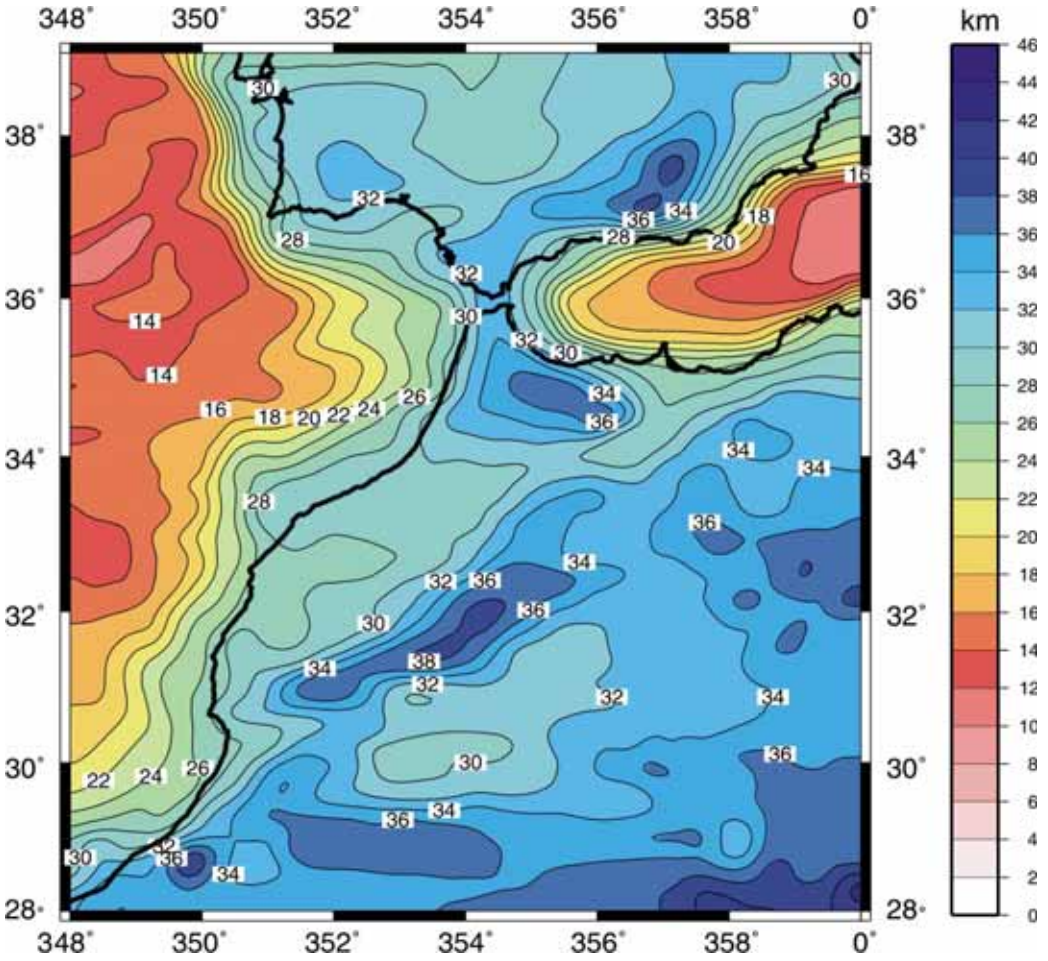

Fig. 6.7 (see page 128)

6.2.2 Lithospheric mantle

For the lithospheric mantle, we have assumed a temperature-dependent density (eq. 2.1). As initial model we have used the LAB obtained by 1D inversion of elevation and geoid anomaly in Chapter 4 (**Fig. 4.5 B**), where the unrealistic short wavelengths under the Atlas Mountains have been removed (**Fig. 6.8**).

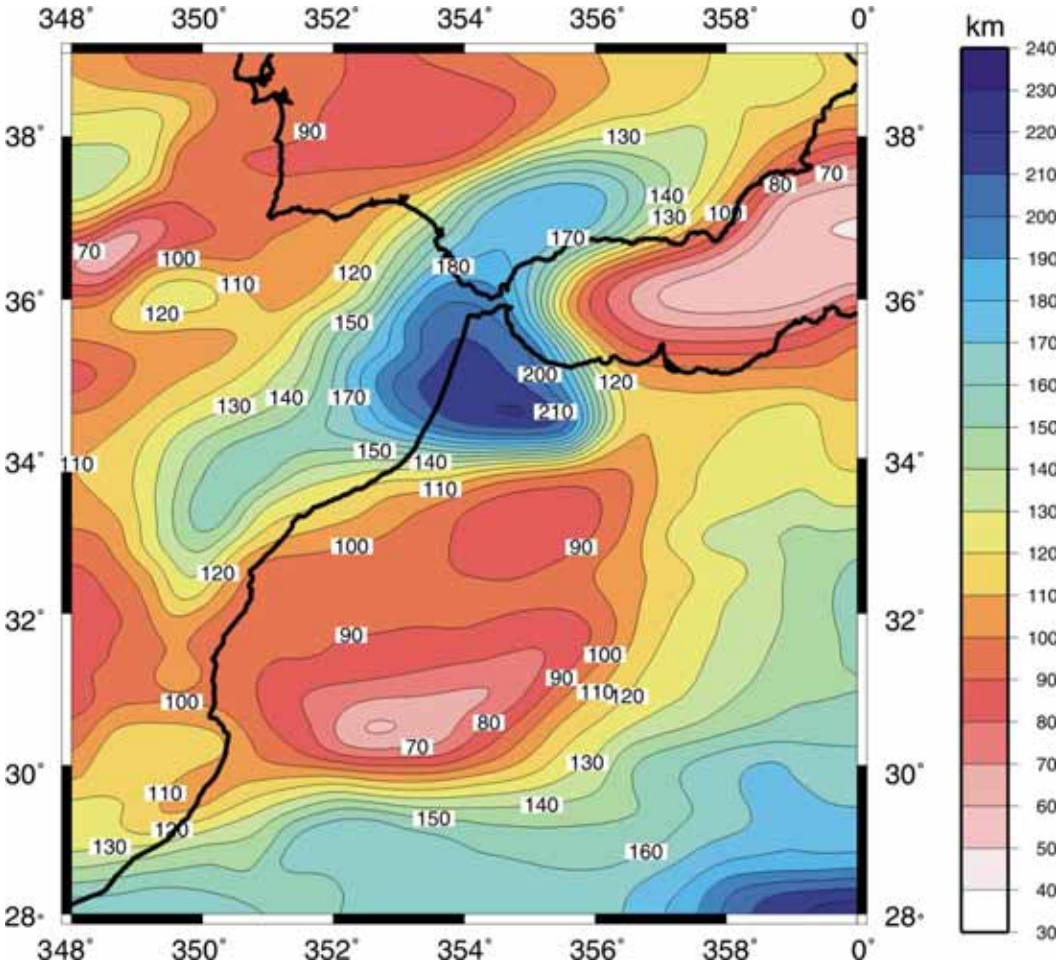

Fig. 6.8 *Depth of the lithosphere-asthenosphere-boundary (LAB). For the petro-physical properties of the lithospheric mantle, see* ***Table 6.1****. Isolines every 30 km.*

6.3 MODELLING RESULTS

The methodology used by GEO3Dmod to calculate the temperature distribution as well as the different geophysical observables was already explained in Chapter 5. For the 3D model, we have avoided using free air anomaly due to its high dependence on near surface short wavelength features that are less important in a regional study.

The measured geophysical observables, elevation (**Fig. 3.2**), Bouguer anomaly (**Fig. 3.10**), geoid anomaly (**Fig. 3.3**) and surface heat flow (**Fig. 3.14**), have been described and analysed in Chapter 3. In order to compare the calculated and measured Bouguer anomaly, geoid anomaly, elevation and surface heat flow (SHF), we show the residual values in **Fig. 6.9**. The 3D model is the best-fitting model after many runs, where the initial geometry was modified in a

trial and error process. The main anomalies were satisfactorily reproduced. The fit is achieved for the dominant long wavelength part of the geophysical observables. Local features that are out of the scope of this study affect the shorter wavelength part of the residuals, particularly the elevation. The short wavelength misfits are attributed to the gross geometry adopted for the sediments and/or the top of the basement. The main misfit is located in the Alboran Basin, where the calculated geoid anomaly is about 1-3.5 m higher than the observed one. We will examine this issue later, in the discussion.

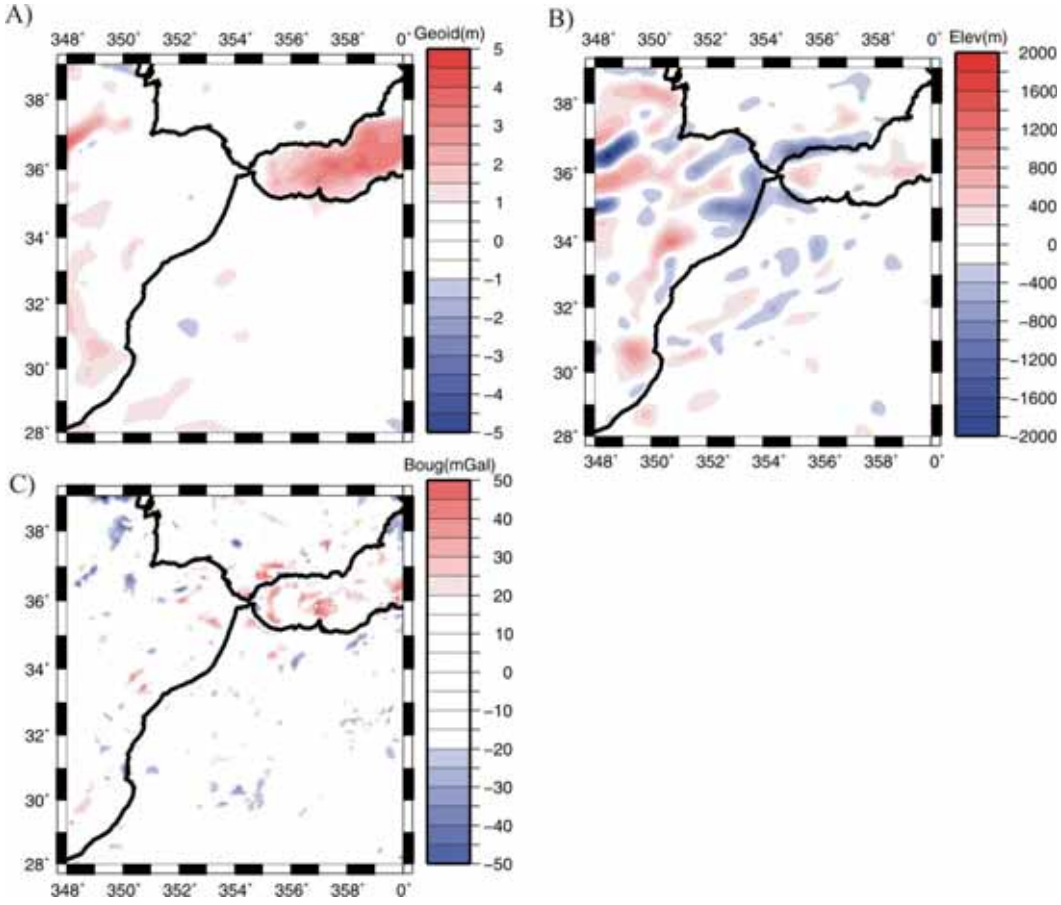

Fig. 6.9 *Residual values (calculated-measured) obtained for the 3D model.* ***A)*** *Geoid anomaly.* ***B)*** *Elevation.* ***C)*** *Bouguer anomaly.*

6.3.1 Lithospheric profiles

A number of lithospheric cross sections have been modelled in this area following a 2D approach integrating gravity and geoid anomalies, elevation and surface heat flow (Teixell et al., 2005; Zeyen et al., 2005; Missenard et al., 2006). These published cross-sections represent a good tie points to benchmark our

results. In the following, we illustrate the lithospheric structure modelled along six profiles across the study region (**Fig. 6.10**). Some of these profiles were selected to be coincident with the aforementioned 2D studies in order to compare the inferred lithospheric structures. Earthquakes hypocenters with magnitude >3.5 (AnSS catalogue http://quake.geo.berkeley.edu/anss/) are projected onto profiles from a stripe of 25 km width each side of the profiles as a complementary information that can help to understand the complexity of the study area. Our intention, however, is not to provide a rigorous analysis of seismicity, which is out of the scope of this work. Crustal thickness is constrained at some locations by seismic data (Gonzalez et al., 1998; Gonzalez et al., 2001; Contrucci et al., 2004). These constraints are plotted as green rhombus in the profiles (**Figs. 6.11 A-F**).

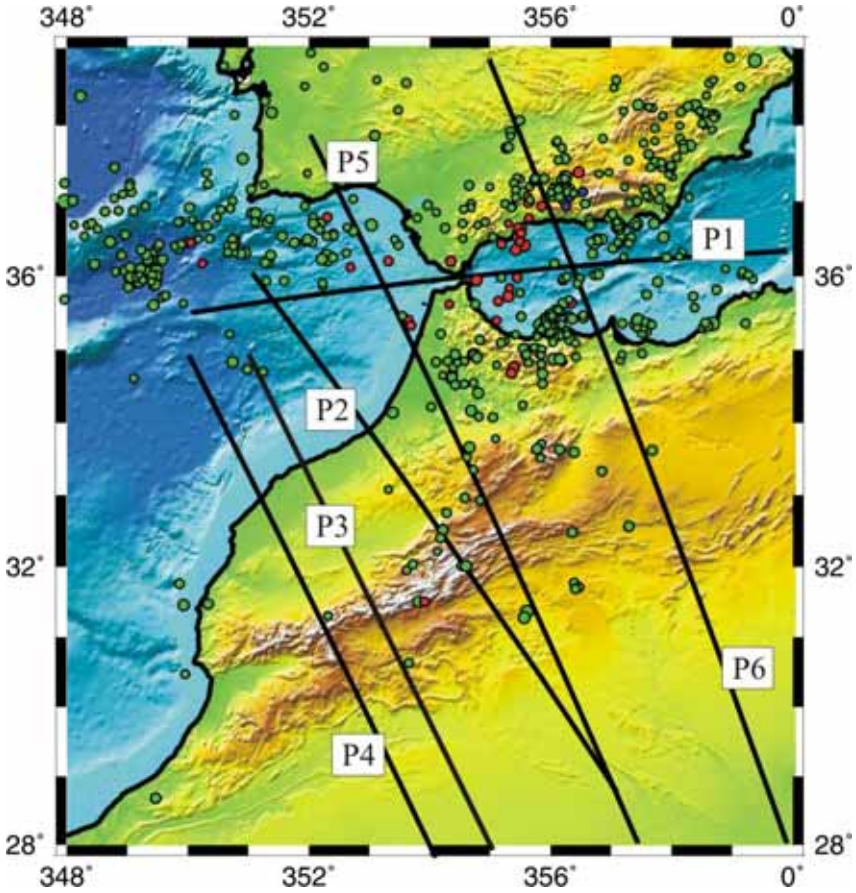

Fig. 6.10 *Location of lithospheric profiles P1-P6 across the 3D model (see the text). Earthquakes epicentres with magnitude >3.5 are also plotted. Blue circles correspond to hypocenters with depth >300 km and <700 km, red ones to depths between 40 km and 300 km, and green ones to depths < 40 km (AnSS catalogue http://quake.geo.berkeley.edu/anss/). The lithospheric cross sections are shown in* ***Figs 6.11 A-F****.*

Profile P1 runs E-W and, starting in the Atlantic oceanic domain, crosses the Gulf of Cadiz, the Gibraltar Strait and the Alboran Basin, ending in the transition from the Alboran to the Algerian Basin (**Fig. 6.10**). The model results are in good agreement with the observed data except for the too strong geoid anomaly calculated in the Alboran Basin (**Fig. 6.11 A**). In the Atlantic Ocean, the crust is 9 km thick, and is covered by > 4 km of water and 1 km of unconsolidated sediments (US). Beneath the Gulf of Cadiz, the Moho depth ranges from 20 to 30 km, with a 7-14 km-thick upper-middle crust (UMC). The thickness of the unconsolidated sediments (US) is increased up to 2 km, and a large body (~8 km thick), formed mainly by the imbrication of Triassic to upper Miocene sediments (AWS), is present beneath the Gulf of Cadiz. To the east, in the Alboran Basin, we first cross a conspicuous depocentre of Neogene and Quaternary sediments (NQSA) near the Gibraltar Strait (>8 km). The lower crust (LC) disappears in the central Alboran Basin, leading to a thinned continental-nature crust with a thin NQSA cover and a Moho depth of 18-14 km. Towards the east, we have modelled a transitional crust (IC) with average properties between the continental and the oceanic crust (**Table 6.1**), which thins to <12 km in the transition to the oceanic crust of the Algerian Basin. The lithosphere starts with normal thickness beneath the Atlantic oceanic domain (100-110 km) and thickens to ~ 200 km under the Gibraltar Strait. In the Alboran Basin, the lithosphere thins steeply reaching a LAB depth of 50 km in its eastern part (**Fig. 6.11 A**). Analogue results for the LAB depth were obtained integrating elevation, heat flow and gravity anomaly by Torne et al. (2000).

Profiles P2, P3 and P4 run NW to SE from the Atlantic domain across the NW Moroccan continental margin. Profile P2 starts in the Gulf of Cadiz and crosses the northern High Atlas near the contact with the Middle Atlas, running parallel to Profile II in Teixell et al. (2005). Profile P3 crosses the central High Atlas, the Anti Atlas, and is coincident with profile 3 in Missenard et al. (2006), and similar to profile I in Teixell et al. (2005). Profile P4 crosses the western termination of the central High Atlas, the Anti Atlas, and coincides with profile 2 in Missenard et al. (2006). Profiles P2, P3 and P4 end in the NW Sahara (**Fig. 6.10**).

The calculated geophysical observables are in good agreement with observed data (**Figs. 6.11 B, C and D**). The Moho depth rises from about 15 km in the Atlantic oceanic domain to about 28 km in the Meseta. Along the central High Atlas the Moho depth varies from 34-36 km in its western and mid parts (**Figs. 6.11 C and D**) to 38-40 km in the transition to the Middle Atlas (**Fig. 6.11**

B). Towards the Sahara Craton the crustal thickness is 35-40 km (**Figs. 6.11 B, C and D**). Concerning the lithospheric thickness, the profiles show a relatively thick lithosphere beneath the NW Moroccan oceanic margin (150-170 km) that thins beneath the central High Atlas and thickens again towards the NW Sahara (160-220 km). In the central High Atlas the LAB depth ranges from 90-80 km, thinning to <70 km south-westwards, in the Anti Atlas (**Figs. 6.11 B, C and D).** In **Figs. 6.11 B, C and D** we have plotted the Moho and LAB depths (thick solid lines), as well as the calculated SHF, of the coincident 2D models, superposed to our lithospheric structure. In the case of **Fig. 6.11 C,** we have also projected the Moho and LAB depths of profile I in Teixell et al. (2005) (dotted lines). This profile, although not coincident, has a similar trend to profile P3. Our results coincide with Teixell et al. (2005) in the lithospheric thickness derived for the Meseta and central High Atlas, where they model the minimum LAB depth beneath the orogen (**Figs. 6.11 B and C)**. However, we find that the most prominent thinning takes place underneath the Anti Atlas, as proposed by Missenard et al. (2006). These authors circumscribe the lithospheric thinning to a narrow band centred in the Anti Atlas with a relatively thick lithosphere in the adjacent High Atlas (~130 km), in contrast with our 3D model (**Figs. 6.11 C and D**). Despite these differences, the two models fit satisfactorily the geophysical observables. This is because Missenard et al. (2005) are modelling a thick crust and using a relatively high constant heat production parameter in the upper crust (2.5 μWm^{-3}), which tends to reduce the average lithospheric mantle density. Furthermore, these authors use a higher average crustal density (2835 kg/m^3) in comparison to ours (2810 kg/m^3). The elevated crustal heat production also affects the SHF calculated by Missenard et al. (2005), which is 10-18 mW/m^2 higher than the predicted by our 3D model. Teixell et al., (2005) use in its 2D transects a heat production parameter for the crust similar to ours. However, they use a higher average crustal density (2840 kg/m^3), and propose a thicker crust and lithosphere in the Meseta and Anti Atlas (**Figs. 6.11 B and C**). The two models achieve a good fit of the geophysical observables. The main difference stands for the calculated SHF, which is 10-25 mW/m^2 lower than the predicted by our 3D model.

Profile P5 runs parallel to the lithospheric transect of Zeyen et al. (2005), i.e. NNW-SSE, starting in the SW Variscan Iberian Massif, crossing the Gulf of Cadiz, the Rif foreland, the Middle and High Atlas, and ending in the Sahara Craton (**Fig 6.10**). The calculated geophysical observables are in good agreement with observed data except for some local misfits (**Fig. 6.11 E).** In the SW Iberian Peninsula, the Moho depth is about 32 km, with a 12 km-thick intermediate crust

(IC) replacing the less dense upper-middle crust (UMC) used in the rest of the continental areas of the model. Beneath the Gulf of Cadiz the crust is thinned, the IC disappears and instead the upper-middle crust (UMC) is present. A thick cover (~8 km) formed mainly by the imbrications of Triassic to upper Miocene sediments (AWS) and about 2 km of unconsolidated sediments (US), overlies the basement in the Gulf of Cadiz. The Moho depth is 32-34 km under the Rharb Basin, deepening to >36 km beneath the contact between the central High Atlas and the Middle Atlas. Towards the Sahara Craton the crustal thickness ranges between 35 and 40 km (**Fig. 6.11 E)**.

In **Fig. 6.11 E**, we have plotted the Moho and LAB depths (thick solid lines), as well as the calculated SHF, of the lithospheric transect of Zeyen et al. (2005), superposed to our lithospheric structure. The LAB topography exhibits notable lateral variations along the profile. A prominent lithospheric thickening (>210 km) is imaged by our 3D model under the eastern Gulf of Cadiz, the Rharb Basin and the Rif. Farther to the SE, the lithosphere thins to <90 km in the Middle Atlas. Towards the Sahara Craton the lithosphere thickens gently up to 190 km. The differences of the LAB depth with respect to the model by Zeyen et al. (2005) are <10 km, excepting the Gulf of Cadiz and Rharb Basin, where our model is ~25 km thicker, and the northern central High Atlas, where our model is about 20 km thinner. The value of the average crustal density used by Zeyen et al. (2005) is higher than ours, particularly in the Gulf of Cadiz, where the difference is about 50 kg/m^3. Another important difference is the layer of Neogene and Quaternary sediments in the Rharb Basin, which in the work of Zeyen et al. (2005) is >5 km thick, has a density of 2000 kg/m^3, and is underlain by thrusted and stacked sediments of different ages down to a depth of 8 km with a density of 2400 kg/m^3. In our 3D model the layer of unconsolidated sediment (US) is denser (2200 kg/m^3) and thinner (~2-3 km), and is underlain by a 6-km-thick layer of consolidated sediments (2400 kg/m^3). The differences in the calculated SHF are < 10 mW/m^2, excepting the SW Iberian Massif (10-15 mW/m^2), where Zeyen et al. (2005) are using a relatively high upper crustal heat production (2.5 μWm^{-3}) (**Fig. 6.11 E**).

Profile P6 runs NNW-SSE, starts in the Iberian Massif, crosses the Betics, the central Alboran Basin, the eastern High Atlas, and ends in the Sahara Craton (**Fig. 6.10**). The Moho depth is >34 km beneath the Betics. The basement is covered by a layer formed mainly by the imbrications of Triassic to upper Miocene sediments (AWS) of ~4 km thick (**Fig. 6.11 F**). In the central Alboran Basin the lower crust is lacking, and the crust is formed only by a 16-18-km-thick

upper-middle crust (UMC). In the African mainland we found again the lower crust layer (LC) and a Moho depth between 35 and 40 km, with >36 km beneath the eastern High Atlas (**Fig. 6.11 F**). The LAB depth starts with normal values in the Iberian Massif (100 km), thickens to >170 km in the Betics, and thins to 70 km in the central Alboran Basin. Farther to the SE, the LAB depth increases to 230 km in the Sahara Craton (**Fig. 6.11 F**).

Fig. 6.11 A-F. **(Pags. 139-144)** *Lithospheric profiles across the 3D model. For their location, see* ***Fig. 6.10****. Earthquake hypocenters with magnitude >3.5 are projected onto profiles from a stripe of 25 km width each side of the profiles (AnSS catalogue http://quake.geo.berkeley.edu/anss/). Average lithospheric mantle density and isotherms of 600 ºC, 800ºC, 1000ºC and 1200 ºC (thin dashed lines) are also plotted. From top to bottom: surface heat flow (blue line: our model, black lines, if present: previous 2D models, red points: measured data with error bars), Bouguer anomaly, geoid anomaly, elevation (dashed lines: measured data, continuous lines: model effect), blow up of the crustal structure, lithospheric structure. The green rhombus represents seismic a priori information. The numbers indicate the different bodies used in the 3D model (****Table 6.1****). 1: Neogene and Quaternary Sediments in the Alboran Basin (NQSA), 2: Unconsolidated Sedimentary (US), 3: Accretionary Wedge Sediments (AWS), 4: Intermediate crust (IC), 5: Upper-Middle Crust (UMC), 6: Lower crust (LC), 7: Lithospheric mantle. In the crustal and lithospheric structure of B, C, D and E, the thick black lines (solid and doted) corresponds to the crustal and lithospheric geometry derived in previous 2D models (see the text for further details).*

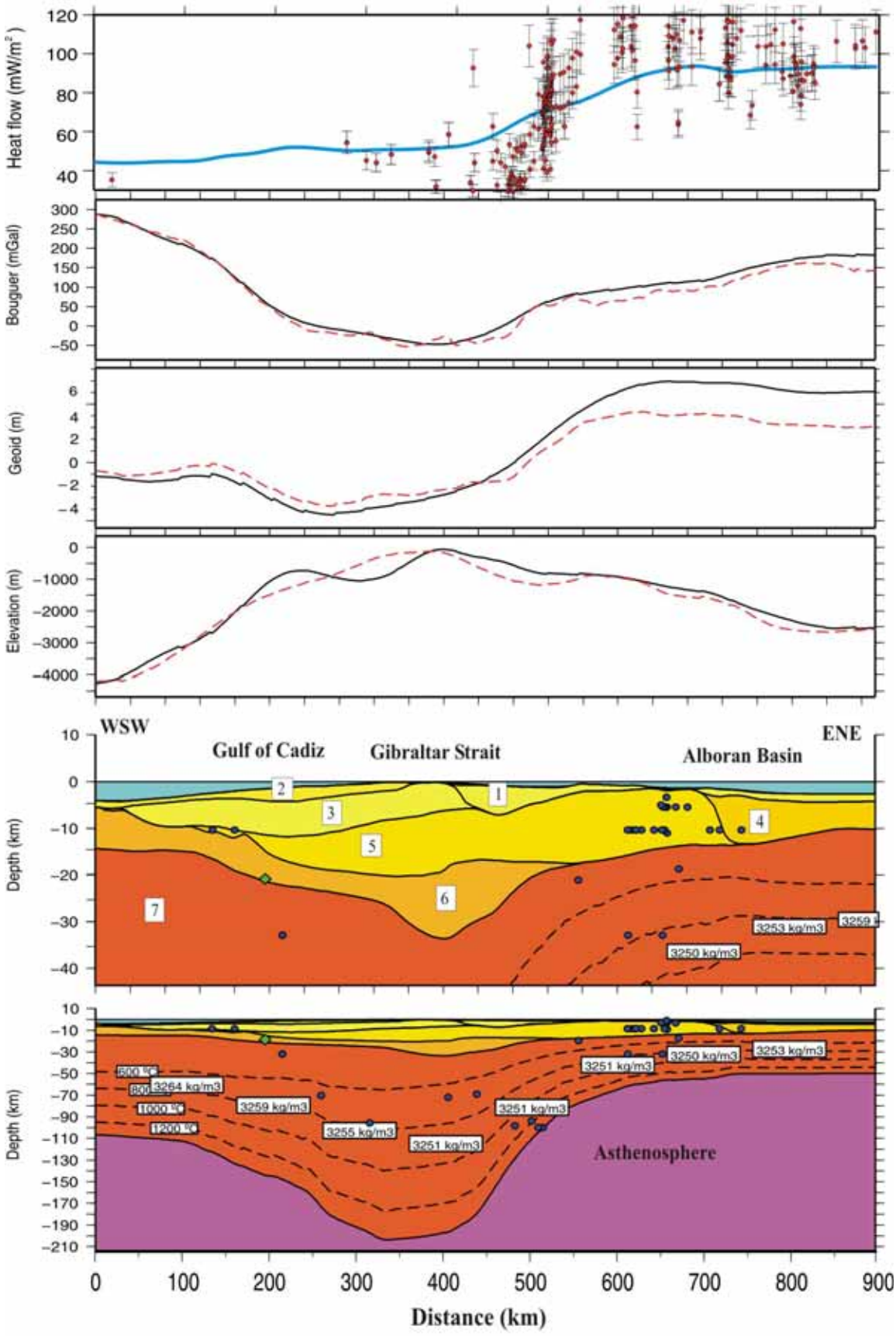

Fig. 6.11 A) Profile P1 (see pag. 138)

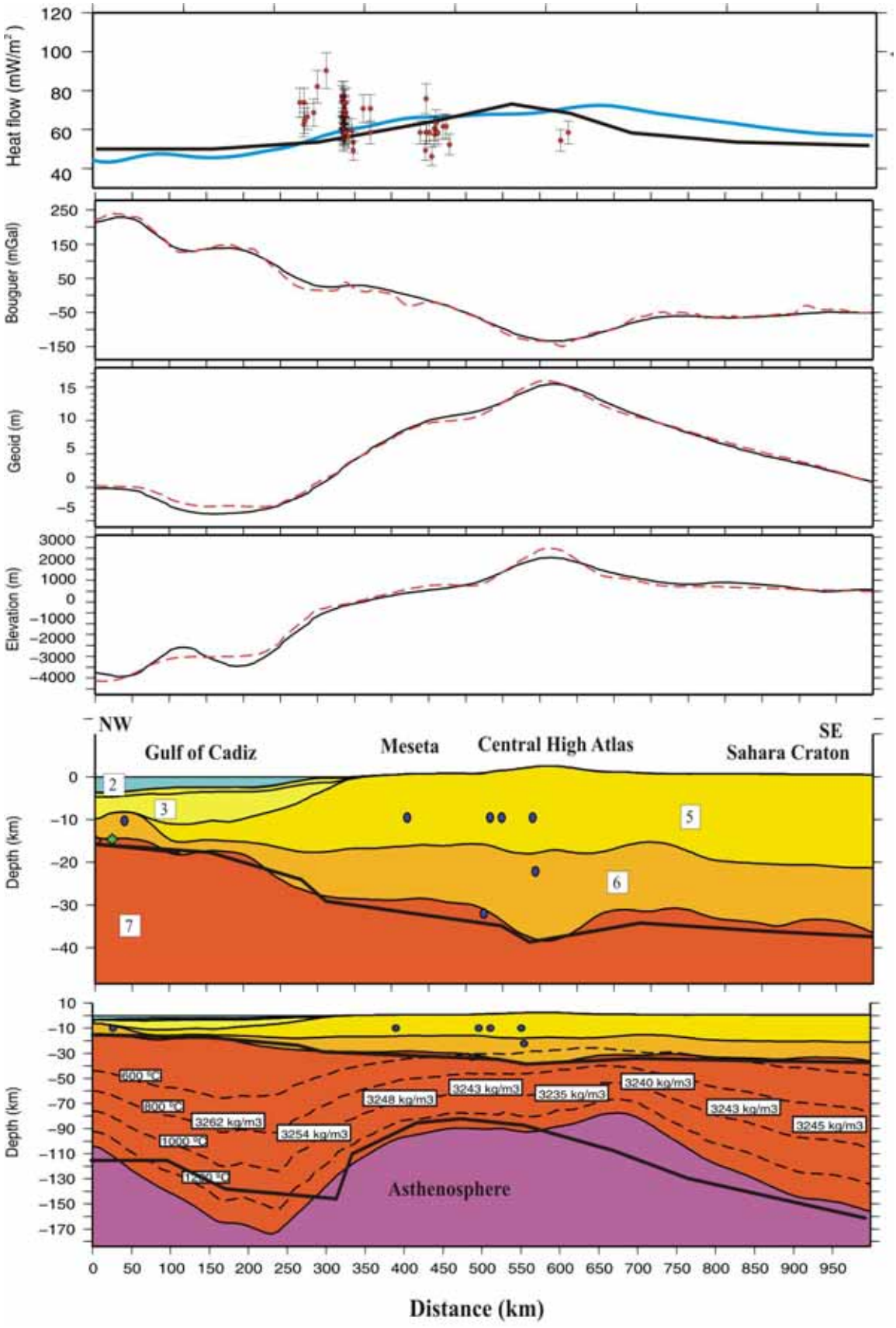

Fig. 6.11 B) Profile P2 (see pag. 138)

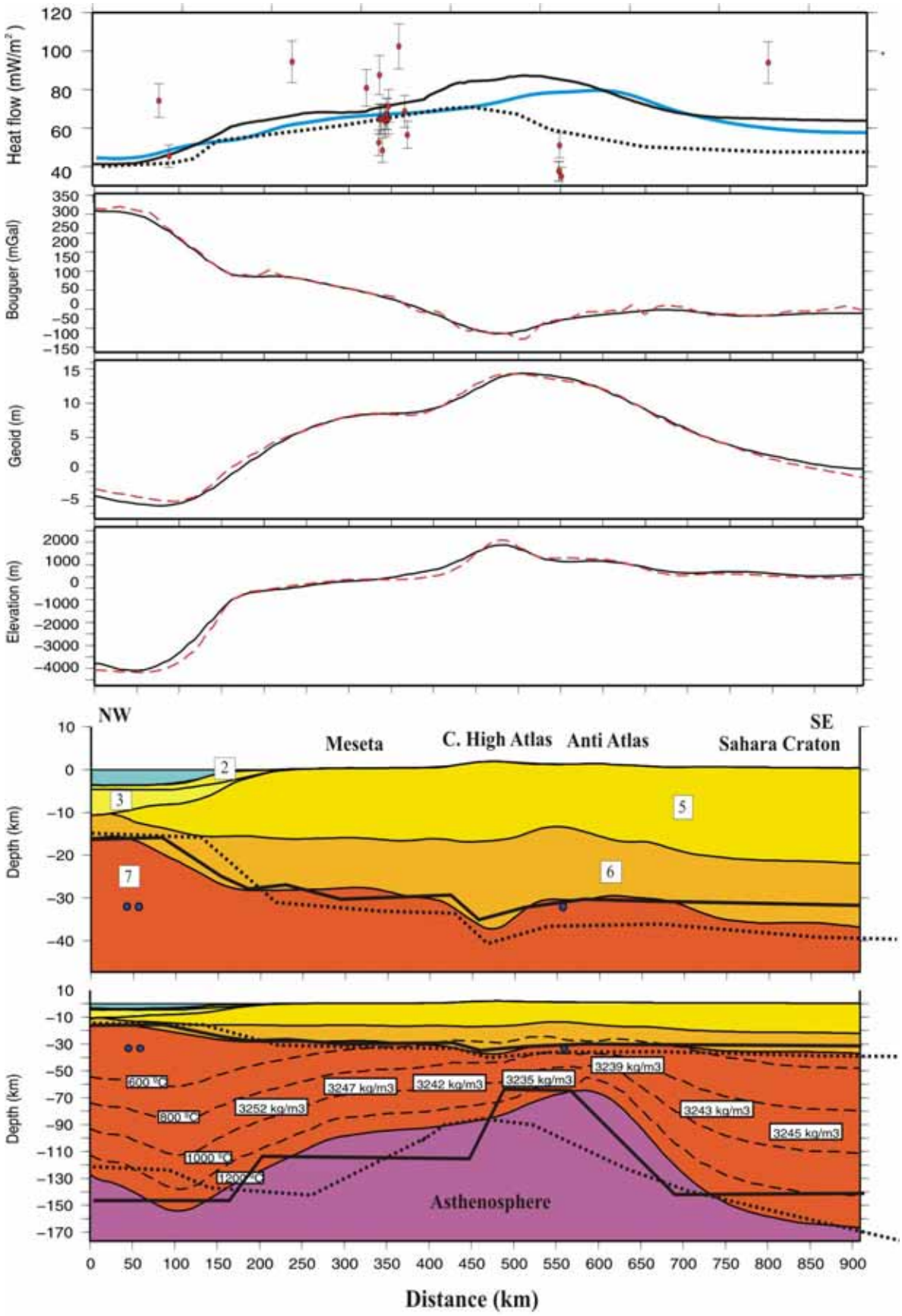

Fig. 6.11 C) Profile P3 (see pag. 138)

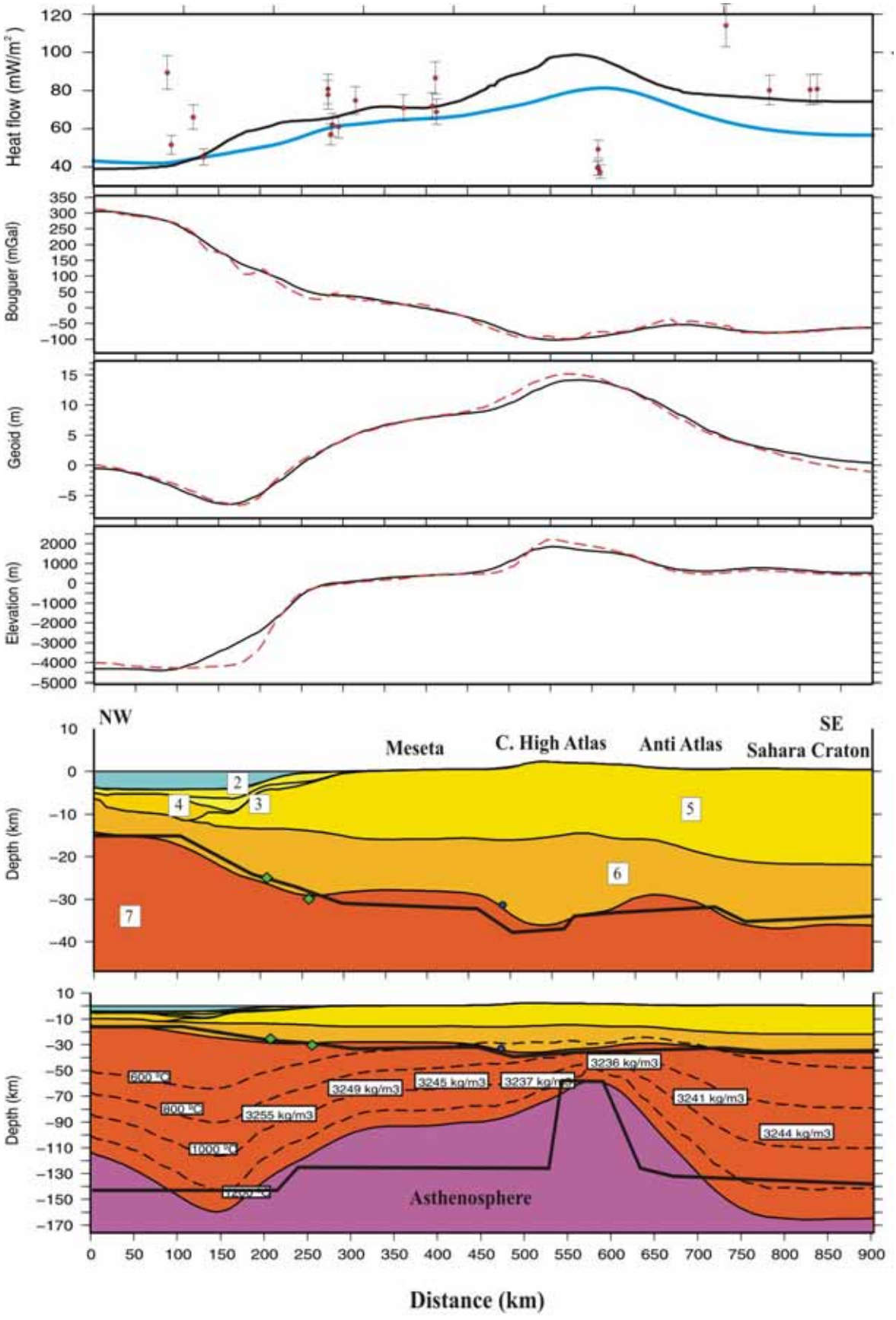

Fig. 6.11 D) Profile P4 (see pag. 138)

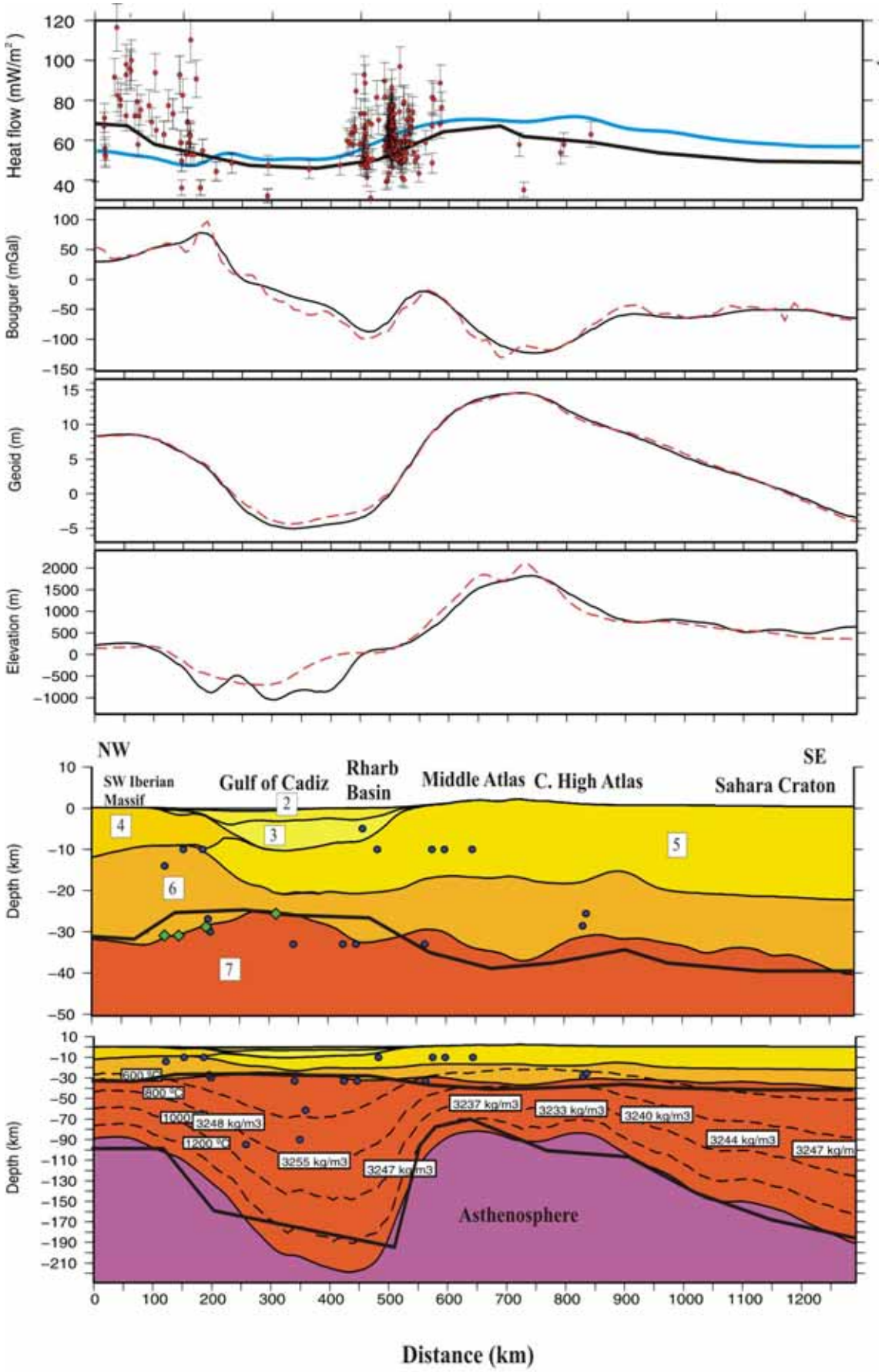

Fig. 6.11 E) Profile P5(see pag. 138)

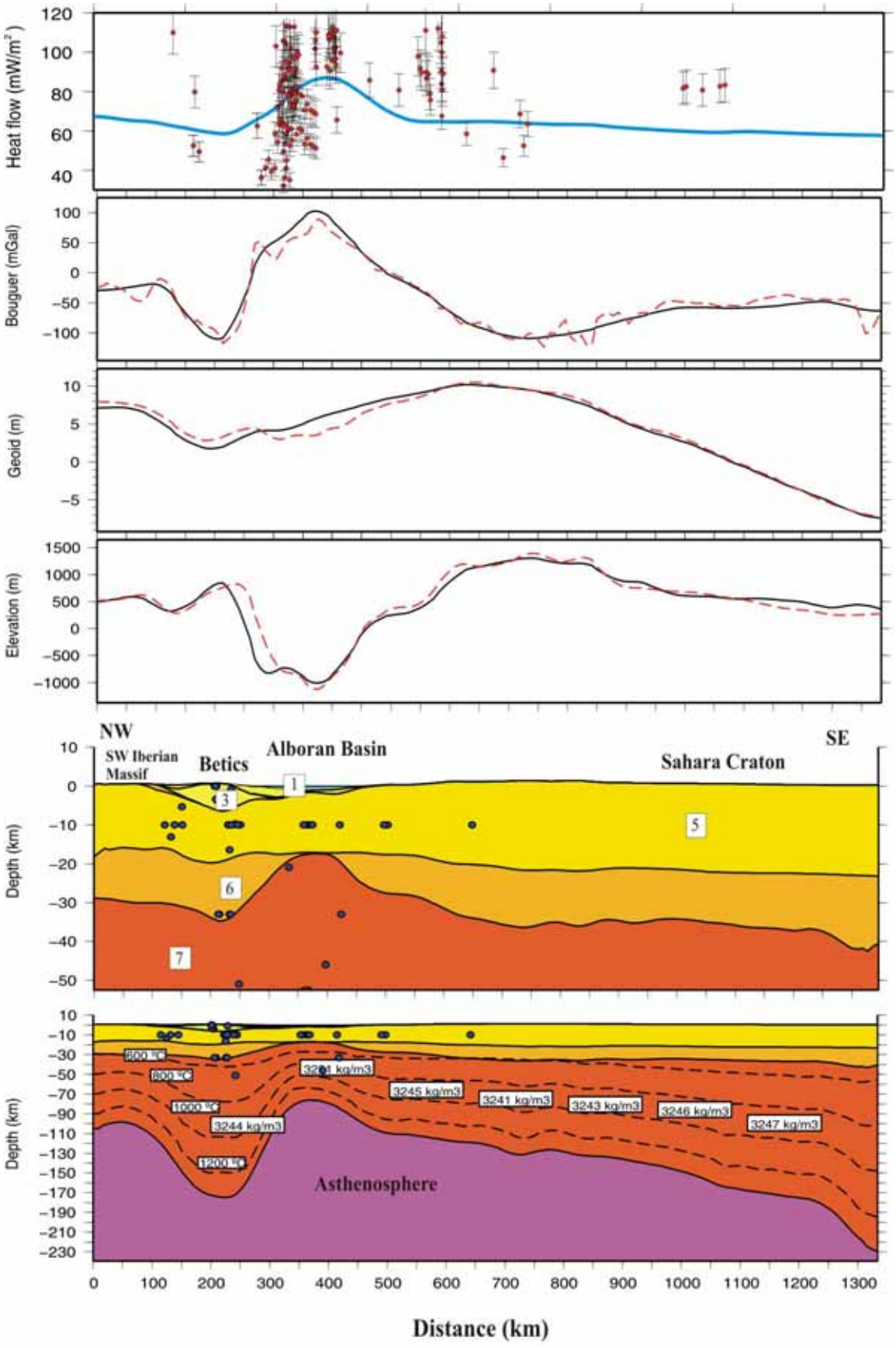

Fig. 6.11 F) Profile P6 (see pag. 138)

The whole Atlas Mountains seem to be affected by lithospheric thinning, but this feature is more conspicuous in its southern part, the Anti Atlas Variscan domain, and its northern part, the Middle Atlas. Furthermore, the eastern branch of the Atlas does not seem to be much affected by the lithospheric thinning. The strongest lithospheric thickness gradients are present in the north, south and east limits of the thick lithosphere imaged beneath the Gulf of Cadiz, the Betics and the Rif. These regions coincide with the contact between the Iberian Variscan Massif and the Betic chain in the north, the contact between the Middle Atlas and the external Rif domain to the south, and the contact between the Betic-Rif orogen and the Alboran Basin to the east (**Fig. 6.12**).

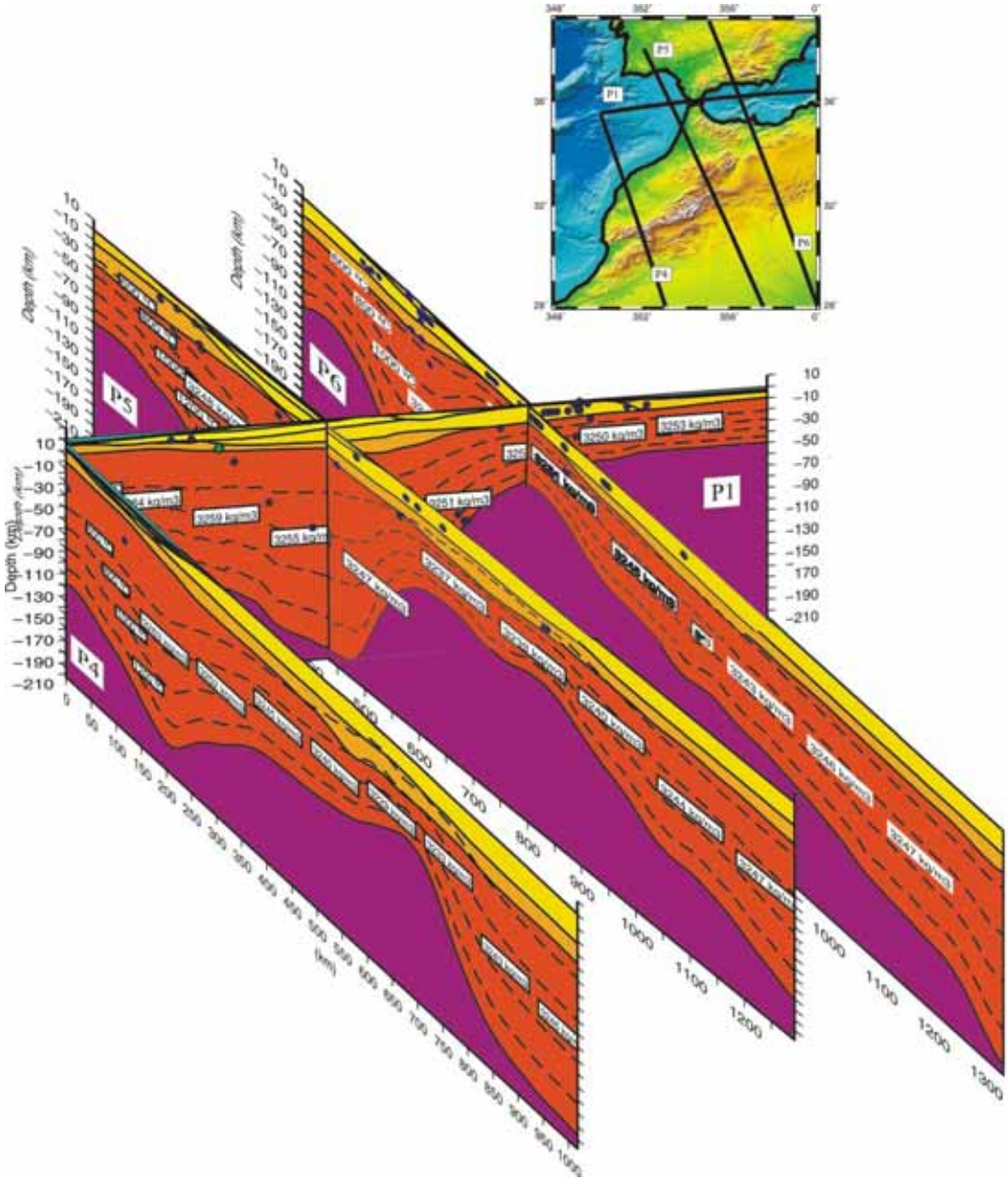

Fig. 6.12 *Perspective view of profiles P1, P4, P5 and P6.*

The comparison between our 3D model and previous 2D studies, illustrates about how important the precise knowledge of the composition and geometry of the crust is. Although all models depict the main issues (i.e. the lithospheric thinning in the Atlas Mountains and the lithospheric thickening beneath the Gulf of Cadiz and the NW Moroccan margin), **Figs. 6.11 B, C, D and E** show how relatively different lithospheric structures are able to show a good fit to observed data. The main differences between these alternative models rely on the thickness and density of the crust used in the modelling, as well as the predicted SHF. Unfortunately, for the most part of our study area (particularly for Africa) reliable geophysical data are scarce. Therefore, more accurate seismic and SHF data are required to obtain a better constraint of the lithospheric structure.

Concerning the earthquakes hypocentres, in the crust we observe that they cluster in the first 15 km. However, some hypocentres are also present in the lower crust, showing different rheological behaviour and how the sismogenic zone changes its depth laterally (**Figs. 6.11 A, B, E and F**). In the lithospheric mantle, the intermediate seismicity (30-100 km depth) coincides with the areas of lithospheric thickening, where the lithosphere is cooler and, hence, more brittle (**Figs. 6.11 A, E and F**). A more accurate study about the seismicity and stress orientation in the crust of the Betic-Rif-Alboran region has been recently presented by Fernández-Ibáñez, (2007) and Fernández-Ibáñez et al., (2007). According to these authors, 85% of the earthquakes occur at depths <15 km, whereas only 12% are located in the mantle.

6.3.2 Moho temperature and surface heat flow

The temperature distribution is essentially controlled by two factors: the crustal heat production and the crustal and lithospheric thickness. The temperature at the Moho tends to be high when the crust is thick (as the amount of heat producing elements increases and the temperature augments with depth) and the LAB depth shallows. In **Fig. 6.13 A,** a map of the calculated Moho temperature is shown. Moho temperatures above 480 ºC characterize the continental areas of Iberia and Africa. The temperatures at the Moho are lower in marine areas, particularly where a low heat production transitional crust has been used in the 3D model: <200 ºC in the oceanic crust of the Atlantic abyssal plains, and <340 °C in the thinned continental crust of the eastern Alboran Basin. In Africa, the highest temperatures are located beneath the relatively thick crust of the central High Atlas (760-830 ºC), the Middle Atlas (690-760 ºC), and the Anti Atlas (830-900 ºC), where, in addition, a conspicuous lithospheric thinning is imaged by the 3D model (**Fig. 6.7 and 6.8**). In the Rif, where the crustal

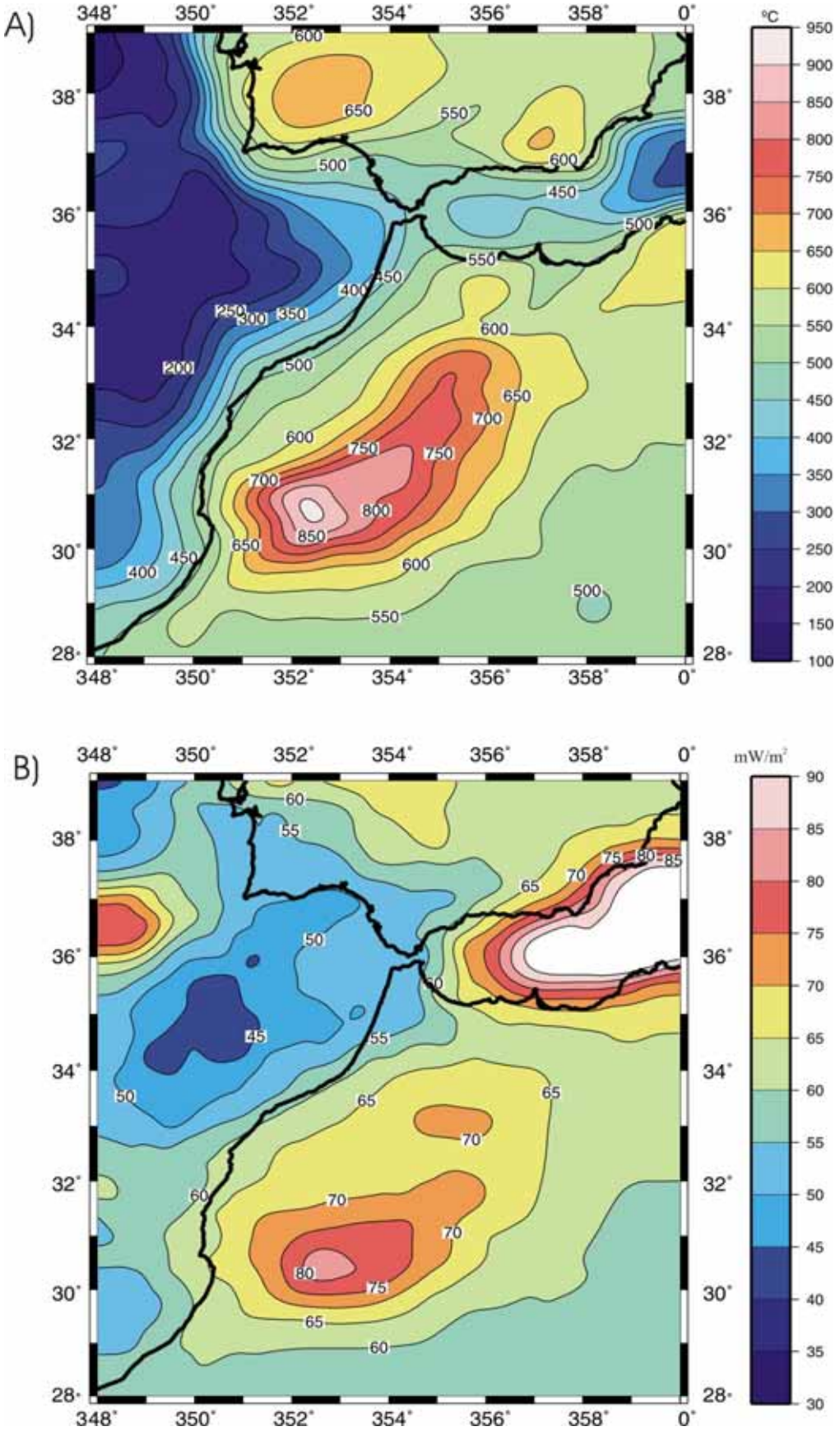

Fig. 6.13 *Thermal field obtained in the 3D model.* ***A)*** *Temperature at the Moho, isotherms every 50 ºC.* ***B)*** *Surface heat flow, isolines every 5 mW/m*^{2}.

thickness is similar to that of the Atlas, the temperatures are lower (550-620 ºC) owing to the deep LAB depth in the area (**Fig. 6.7 and. 6.8**). In Iberia, we found two moderated maxima for the Moho temperature in the SW Variscan Massif and the Internal Betics (<690 ºC). The first one is related to the lithospheric thinning, while the second one is likely due to the thick crust present beneath the Internal Betics (**Fig. 6.7 and. 6.8**). Fernández-Ibáñez, (2007) has calculated the temperature distribution and lithospheric structure of the Gibraltar Arc using elevation and SHF as input data in a 1D approach. The temperature at the Moho calculated by this author is similar to ours in the eastern Alboran Basin, SW Iberian Massif and Rif. However, for the Internal Betics and the northern Mediterranean margin of Africa, he obtains temperatures at the Moho which are 100-200 ºC higher than our results (**Fig. 6.13 A**). This is due to the lithospheric thickness that this author uses in his 1D approach, which is strongly dependent on the SHF, and up to 40 km thinner than our model in some areas (**Fig. 6.8**).

The surface heat flow (SHF) map of the study area is dominated by the influence of the lithospheric thickness and the crustal heat production (**Fig. 6.13 B**). In the African continent, the lowest SHF is located in the Rif (50-65 mW/m^2) and towards the Sahara Craton (<60 mW/m^2), where a thick lithosphere is imaged by our 3D model (**Fig. 6.8**). On the contrary, SHF values are larger in the High Atlas (65-80 mW/m^2), the Middle Atlas (65-70 mW/m^2), and the Anti Atlas (>80 mW/m^2), in line with the lithospheric thinning modelled in this work (**Fig. 6.8**). Offshore, the differences in the SHF are extreme. The lowest SHF values are present in the abyssal plains of the Atlantic oceanic domain (<45 mW/m^2), while the most elevated values characterize the thinned continental crust of the central and eastern Alboran Basin (>90 mW/m^2), where the thinnest lithosphere of the 3D model is present (**Fig. 6.8**). The Iberian mainland presents SHF values ranging from 50 to 65 mW/m^2. Although the temperature at the Moho presents a local maximum in the SW Iberian Variscan Massif (**Fig. 6.13 A**), the calculated SHF is moderated due to the low heat production assigned to the intermediate crust layer (IC) that replaces the less dense upper-middle crust (UMC) in this area (**Fig. 6.11 E**). In general, the calculated SHF values are compatible (bearing in mind the wide scatter and elevated uncertainties inherent to SHF measurements) with the observed values (**Fig. 3.14**). The most remarkable misfit is present in the SW Iberian Massif, where the relative SHF maximum of 80 mW/m^2 is likely to be related to the Pyrite Belt, which is a local feature out of the scope of the present regional scale study. Other authors have obtained values up to 60 mW/m^2 in this area using elevated heat productions in the upper crust (2-3.5 μWm^{-3}) in a 2D modelling profile (Fernàndez et al., 2004)

6.4 DISCUSSION

6.4.1 Comparison between the 1D and the 3D models

The comparison between the structures obtained in the 3D, and the 1D-inversion models, shows major discrepancies in the Gulf of Cadiz, Alboran Basin, SW Iberian Massif, and the NW Moroccan continental margin (**Fig. 6.14 A**). The 3D model indicates that the crust in the Gulf of Cadiz is thinner than previously imaged by inverting elevation and geoid anomaly. Seismic data suggests that the Moho depth is situated between 22 and 30 km in the Gulf of Cadiz (González-Fernández et al., 2001), in agreement with the results inferred by the 3D model. Several workers have reported the presence of a conspicuous sediment accumulation in the centre of the Gulf of Cadiz (González-Fernández et al., 2001; Medialdea et al., 2004; Iribarren et al., 2007). The lithospheric model obtained using elevation and geoid anomaly presented in Chapter 4 does not take into account the presence of sediments and, instead, assumes a unique crustal layer. Therefore, the 1D inversion method of Chapter 4 tends to overestimate the crustal thickness in order to compensate the mass deficit induced by the sediments.

In the Alboran Basin, the 3D model shows a Moho depth of ~18 km in its central part and <12 km in its easternmost extreme, i.e. 2-4 km thinner than the 1D model (**Fig. 6.14 A**). This result is in agreement with a 3D gravity, elevation and SHF modelling study focused in the Alboran Basin (Torne et al., 2000), and with the recent reprocessing and reinterpretation of the ESCI-Alb 2b and 2c seismic lines (Booth-Rea et al., 2007). The crust in the central and eastern Alboran Basin is characterized by low average P-wave velocities of about 6.1 km s^{-1} (Hatzfeld, 1978), which are probably related to the lack of a high density lower crust (Galindo-Zaldivar et al., 1997). To satisfy this requirement, we have removed the lower crust layer in the 3D model (**Fig. 6.11 A**). Farther to the east, the crustal thinning points to the transition from a thinned continental crust in the Alboran Basin to the oceanic crust of the Algerian Basin. For the eastern Alboran Basin we have used a transitional crust (IC) with average properties between the upper-middle and lower crust (**Table 6.1**) (**Fig. 6.11 A**).

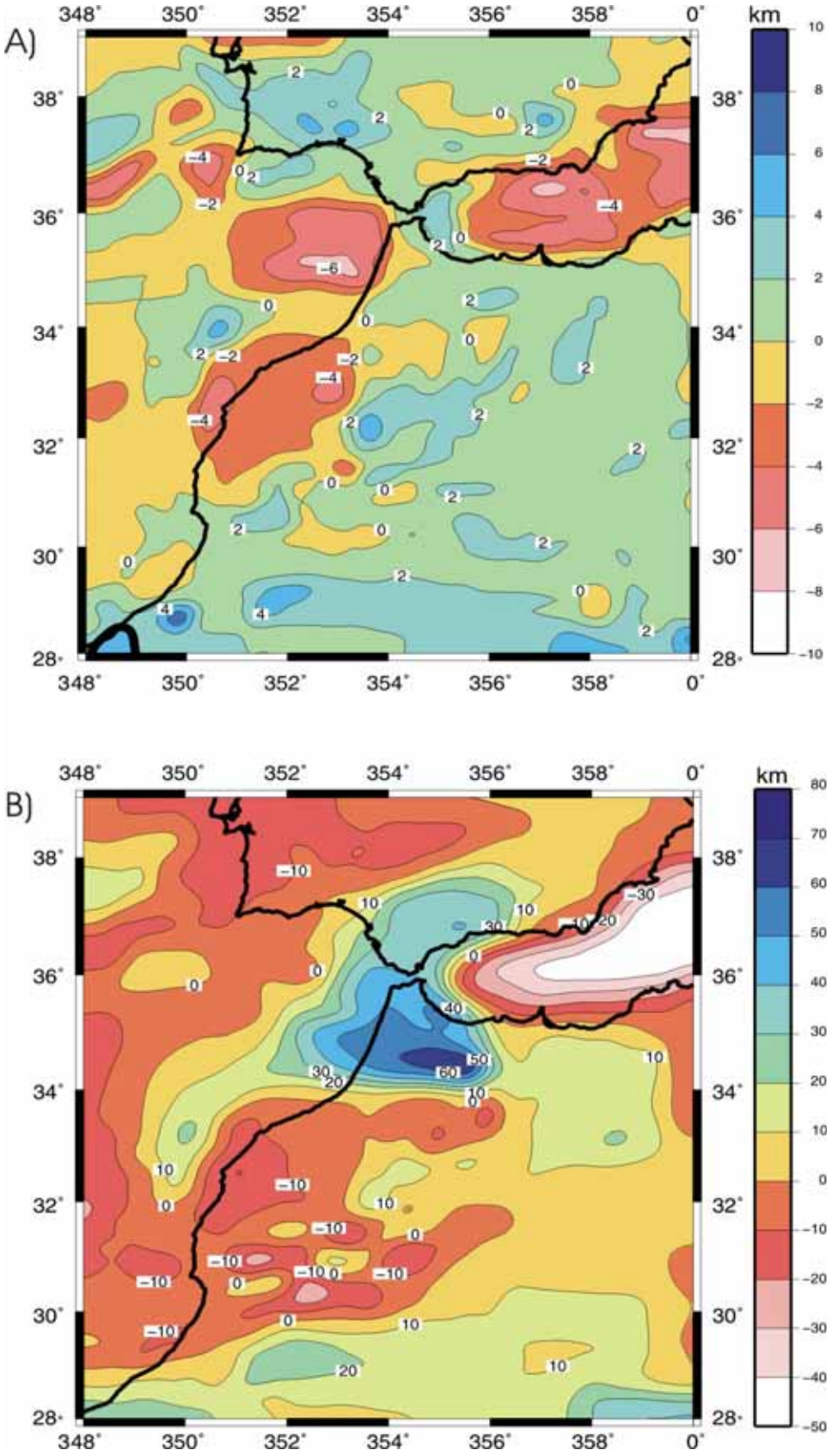

Fig. 6.14 *Differences between the 3D model and the 1D inversion model obtained using elevation and geoid anomaly (see Chapter 4).* ***A)*** *Differences in the Moho depth.* ***B)*** *Differences in the lithosphere-asthenosphere-boundary.*

In the SW Iberian Peninsula, the Moho is 2-4 km deeper in the 3D model with respect to the 1D model and the 2D lithospheric profile integrating elevation, geoid, gravity and SHF of Fernàndez et al., (2004) (**Fig. 6.14 A**). This increase of the Moho depth coincides with the thickening of the lower crust proposed by González et al. (1998) based on refraction/wide-angle reflection data. The upper-middle crust layer has been replaced by a denser layer (2800 kg/m^3) in the Iberian Massif (limiting with the Guadalquivir Basin to the east) according to the increment of P-wave seismic velocities reported in the area (González et al., 1998) (**Fig. 6.11 E**).

The crustal thickness is about 28 km beneath the onshore part of the NW Moroccan margin according to the 3D model (**Fig. 6.7**). This is 2-4 km thinner than inferred from the 1D model (**Fig. 6.14 A**). The first seismic study carried out in this area showed that the Moho depth is about 30 km in the continental area beneath the Meseta (Makris et al., 1985). However, more recent wide-angle reflection and refraction seismic data in a NW-SE profile from the oceanic Jurassic crust to the NW Moroccan continental margin show the presence of a high-density crustal layer ranging from 30 km to 35 km depth in the short emerged part of the profile (Contrucci et al., 2004). The nature and lateral extent of this anomalous layer remains unclear. Due to these uncertainties and, for the shake of simplicity, we have preferred to avoid including such a body and situate the Moho depth at about 30 km.

For the lithospheric mantle, the major differences between the 3D and the 1D model are located in Rharb Basin, Gibraltar Strait, Betics, and Gulf of Cadiz, where the lithosphere inferred in the 3D model is thicker (up to 50 km) than the 1D inversion model (**Fig. 6.14 B**). On the contrary, the 3D model results in a thinner lithosphere beneath the Atlas, SW Iberian Peninsula, and the Alboran Basin. As expected, the amplitude differences in the LAB depth inferred from the 3D model are stronger in comparison with the 1D model, since the 1D approach tends to smooth long-wavelength LAB undulations. However, the 1D model can also introduce short wavelength artifacts that have been removed in the 3D model (e.g. beneath the Atlas Mountains).

In the Alboran Basin the predicted geoid anomaly, according to our 3D model, is about 1-3.5 m higher than the observed value (**Fig. 6.9 A**). Assuming that the density and thickness of the crust are well constrained, we have tried an alternative model for the Alboran Basin modifying the lithospheric thickness. To reduce the mass excess responsible for the excessive geoid anomaly, for a fixed crustal thickness and density, it is necessary to diminish the lithospheric

thickness. Several tests performed have suggested us that it is not possible to fit simultaneously the elevation and the geoid anomaly in the Alboran Basin. For instance, in **Fig. 6.15** we show a cross section of what can be considered as the other end-member model, in which we have fitted the geoid anomaly by thinning the lithosphere by approximately 10 km. The lithospheric thinning reduces the geoid anomaly but increases the elevation in the central and eastern Alboran Basin by about 300 m. One of the main assumptions of our 3D model is that the density of the asthenosphere is constant everywhere. However, active flow in the sublithospheric mantle related to either sinking slabs or mantle plumes can modify the density of the asthenosphere and, consequently, the derived geoid anomaly. With respect to elevation, if we assume that at temperatures above those corresponding to the LAB the rocks are not able to support noticeable static vertical forces, then taking the compensation level at the base of the lithosphere is a good approach. The central and eastern Alboran Basin are characterized by low P-wave velocities according to seismic tomography studies (Blanco and Spakman, 1993; Bijwaard and Spakman, 2000; Calvert et al., 2000; Spakman and Wortel, 2004). Although the relation between low P-wave velocities and low densities is not straightforward, we could presume that low sublithospheric densities are diminishing the geoid anomaly signal, in line with tomography images. Another assumption is that of thermal steady state. The effects of non-stationary processes or even compositional changes could induce further lateral inhomogeneities in the lithospheric mantle out of the scope of our model.

Fig. 6.15 (next page) *Alternative model for the Alboran Basin changing the lithospheric thickness (see text for further details). Top panel, from left to right, residual values (calculated-observed) of: Bouguer anomaly, geoid anomaly, and elevation. Lower panel: surface heat flow (black line: our model, red points: measured data with error bars) Bouguer anomaly, geoid anomaly, elevation (dashed lines: measured data, continuous lines: model effect), and lithospheric structure along the profile depicted in the top panel. It can be seen that geoid anomaly fits, but the calculated elevation is about 300 m higher than the actual bathymetry.*

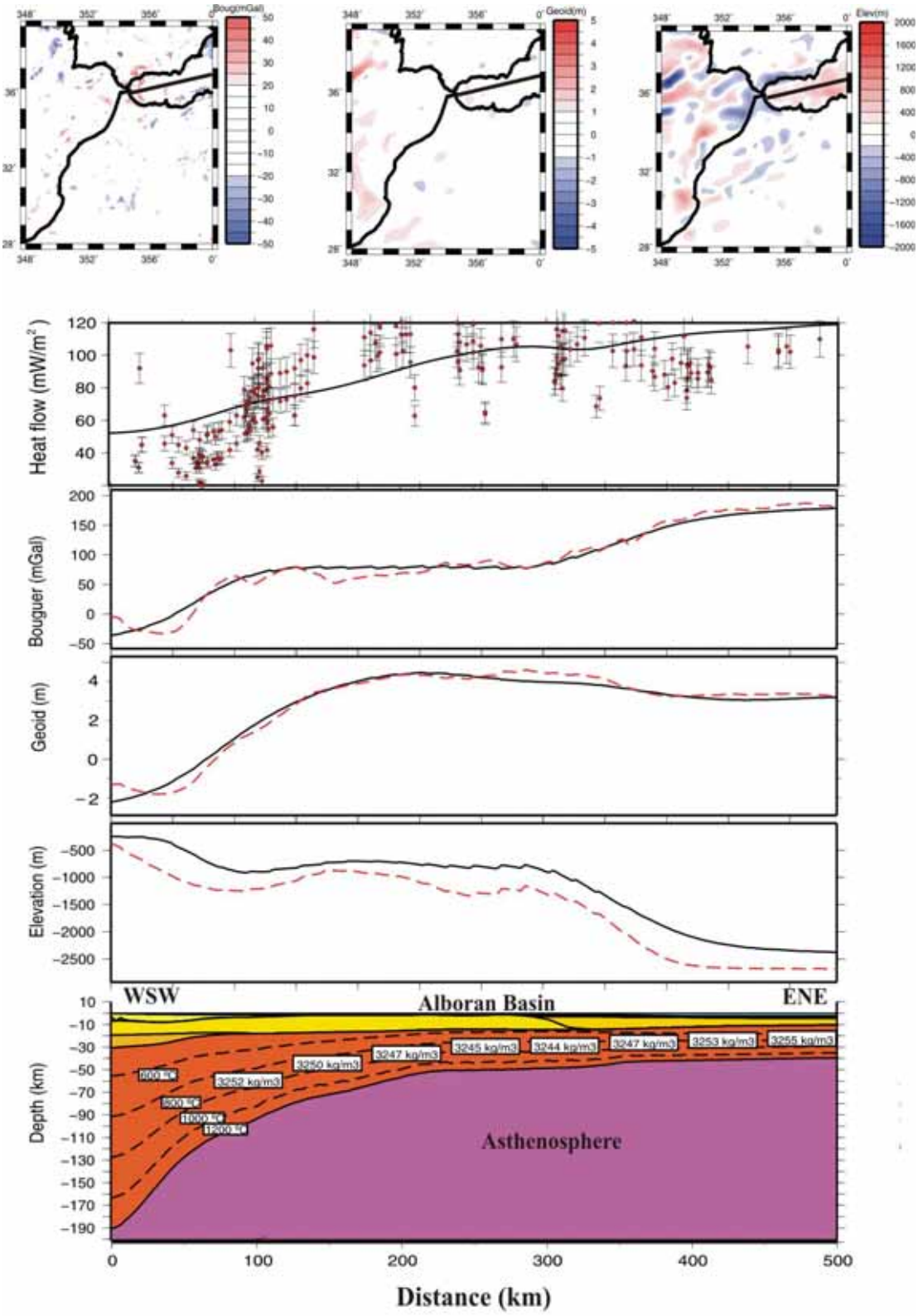

.

Fig. 6.15 (see previous page)

6.4.2 Sensitivity analysis

The 3D lithospheric structure presented here is our preferred model after several tests following a trial-and-error approach. The most outstanding result is the strong variation of the lithospheric thickness. This variation is mainly controlled by elevation and geoid anomaly, since these two observables are sensitive to density variations at deep levels. To illustrate the sensitivity of the different observables, we have performed the following test: we have reduced the amplitude of the LAB topography by 30% to make it smoother. At the same time, we have allowed for variations in the Moho depth by ±10 % (< 4 km), which is the poorest resolution in seismic experiments, trying to keep the fitting with geophysical observables. To do this, we have selected two areas where the lithospheric thickness is extreme. In the Gulf of Cadiz, Rharb Basin, Betics and

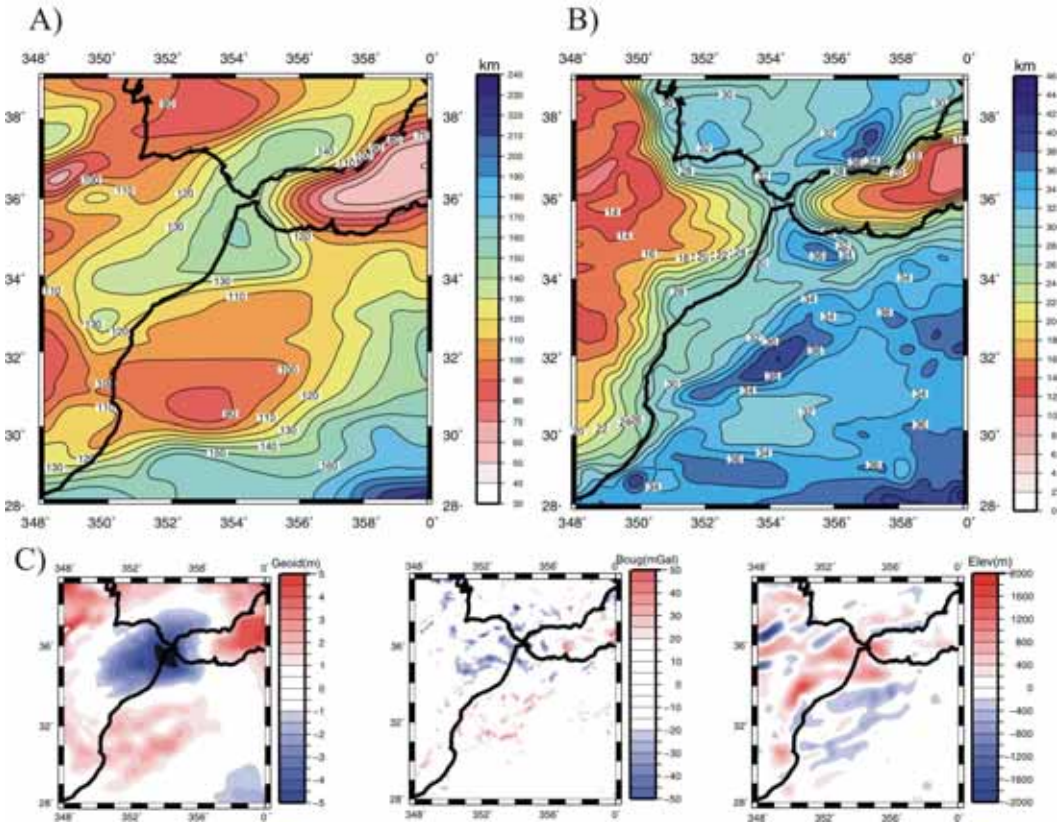

Fig. 6.16 *Alternative model changing the LAB and Moho depths to test the sensitivity of the geophysical observables (see text for further details).* ***A)*** *Modified LAB depth (±30 %). Isolines every 30 km.* ***B)*** *Modified Moho depth (±10 %). Isolines every 2 km.* ***C)*** *From left to right: residual values (calculated-observed) of geoid anomaly, Bouguer anomaly and elevation.*

Rif, the lithospheric thickness has been reduced, while in the Atlas Mountains we have increased the LAB depth (**Fig. 6.16 A**). To compensate these lithospheric thickness variations, we have reduced the Moho depth in the first area and increased it in the second one (**Fig. 6.16 B**). As can be seen in **Fig. 6.16 C**, the amplitude of the geoid anomaly in the first area is too small, and becomes too large beneath the Atlas Mountains. The same pattern is observed in the shorter-wavelength residual Bouguer anomalies. This model also poorly explains elevation. Therefore, we conclude that the large LAB topography variations shown in our 3D model (**Fig. 6.8**) are necessary to explain the observed geophysical data, if we assume that the crustal structure is relatively well constrained up to a resolution of ±10 %.

6.4.3 Crustal structure: isostatic analysis

Gravity anomalies, due to their dependence on the square of the distance, are mainly sensitive to lateral density variations at crustal depths. In general, we can consider that positive Bouguer anomaly values are related to thin crust, while negative ones are indicative of a thick crust. The reason of this is that the complete Bouguer correction removes the effect of the topography but does nothing about the compensation masses. The isostatic residual anomaly (IRA) is calculated removing the gravimetric effect of the isostatic compensation masses assuming an isostatic compensation model (usually at a crustal scale), i.e. applying an isostatic correction to the Bouguer anomaly. The IRA should be null for a perfect isostatic balance, i.e. if the topographic masses were exactly cancelled by the compensation masses. Deviations of this reference value give us information about the density structure. In **Fig. 6.17**, we show an IRA map of the study area. To compute it, we have assumed an Airy-Heiskanen local compensation model, where elevation is compensated at the crust-mantle boundary, with the following parameters: density of the topography equal to 2670 kg/m^3, density contrast at the Moho equal to 450 kg/m^3, and a normal crustal thickness of 30 km. The contribution of the compensation masses has been calculated over a distance of 167 km around each point in a 2 km x 2 km grid, and then subtracted from the Bouguer anomaly shown in **Fig. 3.10**. In the Atlantic domain, strong positive residuals coincide with the most prominent bathymetric accidents: Gorringe, Coral Patch and Guadalquivir Bank. In Africa, the Sahara Craton shows near zero residual values suggesting that topography is mainly compensated at crustal levels. Interesting issues are the strong negative residual values in the Betics, the Rif, the western Alboran Basin, the Rharb Basin, the Gulf of Cadiz and NW Moroccan margin, and the positive residuals in the

SW Iberian Massif, the Atlas Mountains and the central and eastern Alboran Basin.

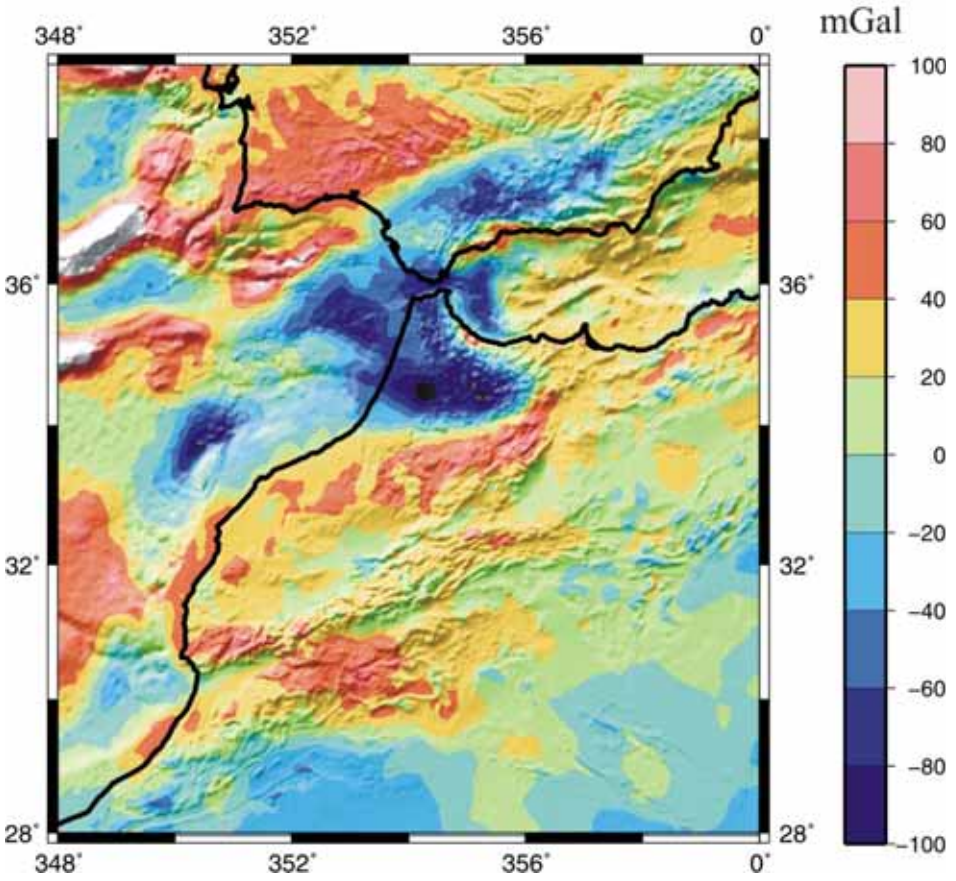

Fig. 6.17 *Isostatic residual anomaly (IRA) map of the study region computed applying an isostatic correction to the Bouguer anomaly of* ***Fig. 3.10****, assuming an Airy-Heiskanen local compensation model. The following parameters were used: density of the topography equal to 2670 kg/m^3, density contrast at the Moho equal to 450 kg/m^3, and a normal crustal thickness of 30 km. In background: elevation shaded relief.*

To the west, in the Atlantic oceanic domain, the Moho depth is situated between 14 and 16 km (**Fig. 6.7**). This thinned transitional crust is consistent with the high positive Bouguer anomaly values shown in **Fig. 3.10**. On the other hand, low, even negative, Bouguer anomaly values are present beneath the Gulf of Cadiz (**Fig. 3.10**), where the crust is of continental character and 22-30 km thick (**Fig. 6.7**). In the Alboran Basin, the Moho depth varies from 30-32 km in the Gibraltar Strait to less than 12 km in the easternmost part of the basin, with a rather flat Moho situated at 18 km depth in its central part (**Fig. 6.7**). The Bouguer anomaly follows this crustal pattern, increasing gradually from west to east, reaching values of >160 mGal in the easternmost Alboran Basin (**Fig. 3.10**). The positive residual values in the central and eastern Alboran Basin suggest an

excess of mass at crustal levels or an extra crustal thinning with repect to the isostatic compensation model (**Fig. 6.17**). The reason for this apparent misfit in the isostatic balance can be explained if we consider that the compensation is achieved at lithospheric levels. An extremely thin lithosphere (40-60 km thick) has been proposed by several authors in the central and eastern Alboran Basin (e.g. Torne et al., 2000). The elevated SHF (**Fig. 3.14**), the low P-wave velocities imaged in seismic tomography (Blanco and Spakman, 1993; Bijwaard and Spakman, 2000; Calvert et al., 2000; Spakman and Wortel, 2004), and the results of our 3D model (**Fig. 6.8**) confirm this issue. The presence of asthenospheric material at such shallow depth, which has been invoked based on backstripping analysis (Docherty and Banda, 1995) and shear wave attenuation coupled with 3D gravity modelling (Seber et al., 1996a), would compensate the mass excess in the Alboran crust related to extra crustal thinning.

In Africa, two Bouguer anomaly minima of the same amplitude (-120 mGal) are present: the first one, nearly E-W oriented, comprising the Rharb Basin and Rif chain, and the second one, NE-SW trending, below the Atlas (**Fig. 3.10**). The similarity in the amplitude of both Bouguer anomaly minima beneath the orogens is somewhat surprising, since the Rif's average topography is of 500-1000 m, while in the Atlas it is about 2000 m (**Fig. 3.2**). Furthermore, the differences in the crustal thickness between the Rif and the Atlas are < 2 km (**Fig. 6.7**). The IRA shows positive values in the Atlas, particularly for the Middle and Anti Atlas (**Fig. 6.17**). As pointed out by Ayarza et al. (2005), the crustal root beneath the Atlas is not thick enough as to isostatically support the elevated topography. Hence, Bouguer anomaly in the Atlas is not as negative as would be expected according to the topography, and isostatic compensation must be accomplished at a lithospheric scale. According to our 3D modelling, the lithosphere seems to be relatively thin beneath the Atlas (**Fig. 6.8**). This hot, less dense and thin lithosphere could explain how the relatively high topography in the Atlas is supported in the absence of a significantly thick crustal root, as suggested by several authors (Frizon de Lamotte et al., 2004, Ayarza et al., 2005, Teixel et al., 2005; Zeyen et al., 2005, Missenard et al., 2006).

Concerning the western Alboran Basin, the Rharb Basin, the Gulf of Cadiz and NW Moroccan margin, part of the negative residual anomaly values (**Fig. 6.17**) can be related to the remarkable sediment accumulations present in these areas (Torne at al., 2000; Medialdea et al., 2004; Iribarren et al., 2007). On the other hand, the aforementioned zones, as well as the Betics and the Rif orogens, are characterized by a thick lithosphere, according to geophysical

modelling (Torne at al., 2000; Zeyen et al., 2005, Fullea et al., 2007), and our 3D model (**Fig. 6.8**), suggesting that compensation is achieved at a lithospheric scale.

The SW Iberian Massif is characterized by a positive Bouguer anomaly (**Fig. 3.10**) and IRA values (**Fig. 6.17**). According to seismic data and integrated geophysical modelling, the crust in this area shows a thick middle crust (up to 17 km) in comparison with the upper crust layer (<8 km) (González-Fernández et al., 2001; Fernàndez et al., 2004). In our 3D model, the upper-middle crust (UMC) is substituted by the denser intermediate crust (IC) (**Table 6.1**), and the lower crust (LC) is relatively thick (**Fig. 6.11 E**). The use of a higher average crustal density would reduce the density contrast in the Airy-Heiskanen isostasy model and, therefore, increase the calculated Moho depth. Furthermore, either a moderate lithospheric thinning or a lithospheric mantle mass deficit due to depletion have been proposed in order to fit the high Bouguer anomaly with the moderate topography and geoid anomaly values (Fernàndez et al., 2004), in line with the relatively thin lithosphere depicted in our 3D modelling (**Fig. 6.8**). Hence, part of the positive residual anomaly in the SW Iberian Massif may be due to the underestimation of the average crustal density in the isostatic compensation model.

6.4.4 Geodynamic models

The lithospheric thickening beneath the Gibraltar Arc and the adjacent thinning in the Alboran Basin have given rise to a variety of geodynamic models related to convective removal and orogenic collapse (e.g. Dewey, 1988; Platt and Vissers, 1989; Platt et al., 2003), mantle delamination (e.g. Seber et al., 1996a; Mezcua and Rueda, 1997; Calvert et al., 2000), slab roll back (Frizon de Lamotte et al., 1991; Lonergan and White, 1997), active subduction (Gutscher et al., 2002), slab break-off (Zeck, 1996; Wortel and Spakman, 2000) or slab roll-back and lithospheric tearing (Spakman and Wortel, 2004) (**Fig. 6.18**). All the aforementioned models include, in a variety of ways, the sinking of a cold and dense lithosphere, and the presence of low P-wave velocity/hot and less dense or even asthenospheric material beneath the Alboran Basin. Most of these geodynamic models, however, do not include the lithospheric thinning beneath the Atlas Mountains as a key parameter to explain the evolution of the GAS region.

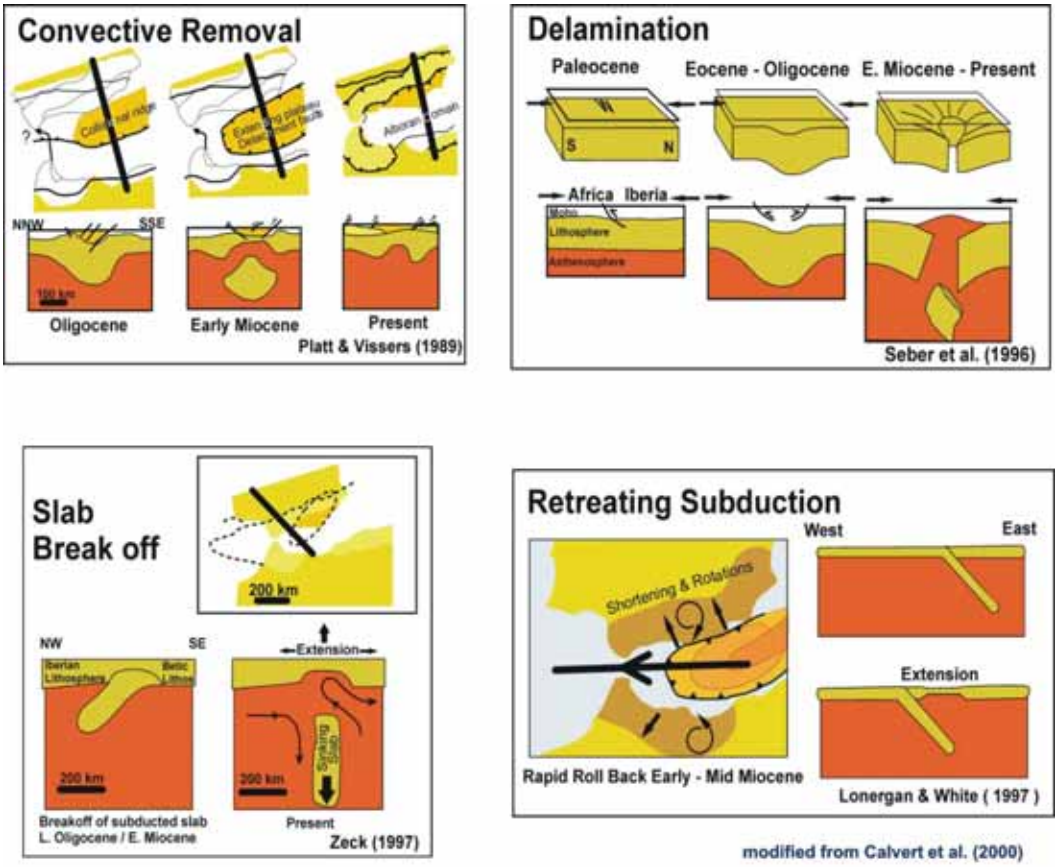

Fig. 6.18 *Scheme of some of the different geodynamic models proposed to explain the origin and evolution of the study area. Modified from Calvert et al. (2000).*

Although the lithospheric thinning induced by mantle upwelling beneath the Atlas Mountains seems to be a well established feature (e.g. Ramdani, 1998, Anguita and Hernán, 2000; Teixell et al., 2005, Missenard et al., 2006), its origin is still a mater of debate. Essentially, there are two groups of theories proposed depending on the relation considered between the mantle upwelling and the Eurasia-Africa plate boundary dynamics. For some authors, the lithospheric thinning along the Atlas and its continuation towards the East Alboran Basin would be caused by lateral asthenospheric flow related to the Eurasia-Africa plate boundary, induced either by slab tear and roll-back (Spakman and Wortel, 2004; Teixell et al., 2005), or lithospheric delamination (Ramdani et al., 1998). On the other hand, the lithospheric thinning in the Atlas may be also explained by thermal erosion produced by some kind of upwelling mechanism independent of the Eurasia-Africa plate limit (Anguita and Hernán, 2000; Zeyen et al., 2005; Missenard et al., 2006). A number of authors have highlighted the connection between the Canary Islands volcanism and the Neogene and Quaternary volcanism existing in the Atlas Mountains, and have proposed the existence of an

elongated sublithospheric magma reservoir extending over the whole region (see Anguita and Hernán, 2000 and references therein). Such a reservoir would be a remnant of an old and deep mantle plume, the volcanism being channelled by the fracturing inherited from the Triassic and Jurassic extension. Other works suggests a baby-plume like mechanism similar to that affecting the French Massif Central (Granet et al., 1995) and the Eifel in Germany (Ritter et al., 2001) on the basis of the elongated shape and relatively reduced area affected by the plume. The aforementioned plumes would be part of a hot sublithospheric mantle reservoir system extending from the Canary Islands to Central Europe (Hoernle et al., 1995).

In spite of the simplifying assumptions, the obtained 3D image depicts the main lateral variation in the crust and lithosphere over the GAS region. An interesting result of the presented work is the difference between Moho and LAB topographies. Our results indicate that both the crust and the lithosphere thicken below the Gibraltar Strait, Betics and Rif Mountains, which is in agreement with the velocity anomalies imaged by tomography studies (Blanco and Spakman, 1993; Bijwaard and Spakman, 2000; Calvert et al., 2000; Spakman and Wortel, 2004). However, the thick lithosphere seems to continue further to the SW encompassing the entire NW margin of Morocco, the Rharb Basin and the Gulf of Cadiz, without an apparent counterpart in the crust (**Figs. 6.7 and 6.8**). To the SE of this lithospheric thickening, there is a marked lithospheric thinning beneath the Atlas Mountains focused in the Middle and Anti Atlas, i.e. oblique trending with respect to the tectonic branch of the orogen in the High Atlas. In that region the relief is due to the intracontinental deformation that partially accommodates the compressive regime between Africa and Iberia during the late Eocene and Quaternary. The central and eastern parts of the Alboran Basin also show an extremely thin lithosphere. However, the lithosphere shows relatively thick values (110-120 km) between the thinned lithosphere in the Middle Atlas and the Alboran Basin, respectively (**Fig. 6.8**). In any case, this large-scale lithospheric structure characterised by thickening and thinning suggests that the Iberian-African margin was possibly formed by more than one mechanism. These mechanisms were not necessarily coeval and, hence, accurate time constraints are needed in order to improve our knowledge of the evolution of the study area.

Both the thinning and the thickening of the lithospheric mantle must be associated with deep processes to produce strong strain partitioning in the context of the dynamics of the Eurasia-Africa plate boundary. In this framework, convective removal or delamination (**Fig. 6.18**) seems to be an unsuitable

candidate given the small shortening affecting the Atlas Mountains (e.g. Teixell et al., 2003) and the absence of evidence for large lithospheric roots in the past. Moreover, the tectonic style of the four main structural units (Betics-Rif orogen, Alboran Basin, Gulf of Cadiz, and Atlas Mountains) requires a more complex mechanism.

The lateral extent of the imaged lithospheric thickening as well as its NE-SW orientation sheds some doubts on an eastward subduction beneath Gibraltar with a slab roll-back to the west (**Fig. 6.18**) as invoked by some authors, either active (Gutscher et al., 2002) or extinguished (Lonergan and White, 1997). Furthermore, the stress orientations of the earthquakes in the crust and upper mantle do not suggest a relation between those earthquakes and an active eastward subduction process (Stich et al., 2005). A plausible slab-retreating model should incorporate tear and asymmetric roll-back of the subducting slab to fit the present-day observed lithosphere geometry in a way similar to that proposed by Spakman and Wortel, (2004).

Chapter 7

SUMMARY

7. SUMMARY

The main objective of this thesis is of methodological nature; the development of numerical methods to determine the lithospheric structure combining geopotential, lithostatic and heat transport equations. In this context, three main goals were achieved:

1) Development of a numerical code to compute Bouguer anomalies from publicly available free air satellite-derived data in both continental and marine areas.

2) Development of a method to calculate a first order lithospheric structure using elevation and geoid anomaly as input data.

3) Development of a 3D interactive code to perform lithospheric forward modelling, integrating surface heat flow (SHF), elevation, gravity and geoid anomalies.

A last but not least important goal was the application of the developed numerical codes to the Gibraltar Arc System (GAS) region with the aim of obtaining a 3D image of its lithospheric structure. The precise knowledge of the present day lithospheric geometry is a key parameter to understand the origin and evolution of the GAS region, where several, even partially opposite, geodynamic models have been proposed. In the following, we summarize the main conclusions obtained in the previous chapters.

7.1. FA2BOUG: A FORTRAN 90 CODE TO COMPUTE BOUGUER ANOMALY FROM GRIDDED FREE AIR ANOMALY

In Chapter 3 we presented FA2BOUG, a FORTRAN 90 code to compute Bouguer anomaly specially intended to work with global elevation and free air data bases. The program is designed to calculate in both continental and oceanic areas.

As an example of application, a complete Bouguer anomaly map of the GAS region was produced combining available land and satellite-derived data processed with FA2BOUG. Positive Bouguer anomaly values are found in the Atlantic oceanic domain (240-300 mGal), central and eastern Alboran Basin (40-

160 mGal) and SW Iberian Peninsula (>40 mGal). Major negative Bouguer anomalies are located beneath the west Alboran Basin (<-40 mGal), the Betics (<-120 mGal), the Rif and Rharb Basin (<-120 mGal), and the Atlas Mountains (<-120 mGal).

As expected, the maximum terrain corrections (Bullard C) are concentrated at sea floor accidents, continental slopes and mountainous areas, where steeper topographic gradients occur. The average of Bullard C corrections is 0.75 mGal with a standard deviation of 4 mGal, being 90 % of the values comprised in the interval (-5.88, 7.28) mGal. Terrain corrections are more widespread distributed in marine than in continental areas. The inner zone contribution and the curvature (Bullard B) correction must be taken in to account to achieve a 1 mGal correction accuracy. The topography of the distant zone beyond 20 km has a noticeable effect in terrain corrections, particularly in offshore areas with elevated bathymetric gradients (>10 mGal).

From the comparison of ETOPO2 and the high resolution SRTM as input DEM for the terrain correction computation, we infer that the use of the lower resolution DEM tends to underestimate the terrain correction, being this misfit higher for increasing terrain correction values (> 24 mGal locally). Therefore, the accuracy of the terrain correction will be strongly dependent on the resolution of the DEM used, at least for rugged topography areas.

7.2. ELEVATION AND GEOID ANOMALY INVERSION: 1D APPROACH

The method presented in Chapter 4, based on the combination of elevation and geoid anomaly data, allows for rapid calculation of the crustal and lithospheric thickness over large regions under the assumption of local isostasy, thermal steady state, linear density gradient for the crust, and temperature dependent mantle density.

Regions with remarkable lateral crustal and/or lithospheric mantle density heterogeneities would require a specific modelling to refine the result. Despite of this, the major features of the lithospheric structure are well reproduced using a four-layer model even for such a very complex tectonic region as the studied area.

Steady state thermal modelling overestimates the actual lithospheric thickness in regions of lithospheric thinning, and underestimates it where the lithosphere is thickened. Therefore, the lithospheric thickness variations presented must be considered as a lower limit.

The effect of introducing the thermal field and a linear density gradient in the crust in our model, with respect to constant crust and lithospheric mantle densities, leads to an increment of the Moho depth ranging from 10% to 40% for E<0, and to a moderate increment or even decrease for E>0 (-5% to +10%). The variations in lithospheric thickness are less important for most of the study area (-5 % to +5 %).

7.3. GEO3Dmod

In Chapter 5 we presented GEO3Dmod, a computer program that allows for interactive 3D lithospheric forward modelling integrating SHF, elevation, gravity and geoid anomalies. The program consists of two modules: GEO3Dmod and GEO3Dmod_INTF. The code is written in FORTRAN 90, uses the graphical library PGPLOT (http://www.astro.caltech.edu/~tjp/pgplot/), and is available for both Linux and Windows platforms.

GEO3Dmod resolves the direct problem, i.e. given a lithospheric model (a set of layers with different properties), it calculates the 3D thermal and density structure as well as the associated geophysical observables (elevation, gravity and geoid anomalies, and SHF).

GEO3Dmod_INTF is a graphical interface designed to visualize and interactively modify the lithospheric structure according to the differences between calculated and measured geophysical observables, i.e. the results from GEO3Dmod.

To test the program, we used a number of synthetic models composed of crust, lithospheric mantle, sea water and asthenosphere. As a benchmark, we have checked that the 3D calculations reproduce the 1D value for long wavelength features. For the geoid anomaly, we find that the wavelength necessary to achieve 90% of the 1D value is about 10 times the length of the mass dipole. For the gravimetric anomalies, the 1D approach implies a null free air anomaly, i.e. the contribution of the topography is exactly cancelled with that due to the density contrast at depth (e.g. Moho). However, in the 3D approach this is not true. For

an isostatically crustal compensated topography of 2 km and –4 km, we find that the wavelengths necessary to reduce the free air anomaly to 20 mGal are 800 km, and 550 km, respectively. Regarding the 2D approach, several test performed illustrated the importance of choosing the correct direction (perpendicular to the strike of the body) when performing 2D modelling.

With the aim of investigating the effect of the lateral variations in the LAB depth, two synthetic tests were performed: crustal overcompensation (i.e. lithospheric thickening), and crustal undercompensation (i.e. lithospheric thinning). The condition of local isostasy changes the Moho depth by about ±4 km with respect to the case of a flat LAB. For the overcompensated topography (lithospheric thickening), the temperature at the Moho (and, hence, the average lithospheric mantle density) and SHF are little changed with respect to a flat LAB model. Conversely, the temperature at the Moho and SHF are noticeably increased for an undercompensated model (lithospheric thinning). The lithospheric thickening is associated with a decrease of the free air, Bouguer and geoid anomalies. Conversely, the lithosphere thinning leads to an increment of all potential fields.

The heat production model used (constant or exponentially decreasing) affects the temperature distribution mainly at crustal levels. The exponentially decreasing model leads to a cooler crust in comparison with the constant model and, therefore, to a higher average lithospheric mantle density. This density difference affects the geoid anomaly but does not have a significant effect on gravity anomalies.

7.4. LITHOSPHERIC STRUCTURE OF THE GIBRALTAR ARC SYSTEM

In Chapter 6 we applied GEO3Dmod to the Gibraltar Arc System region using as initial geometry of the Moho and the LAB the 1D model obtained using elevation and geoid anomaly (Chapter 4).

For the 3D model, eight different layers were considered according to their density, thermal conductivity, heat production, and thermal expansion coefficient:

1) Neogene and Quaternary Sediments in the Alboran Basin (NQSA), with a density of 2350 kg/m^3.

2) Upper Sedimentary (US) layer with a density of 2200 kg/m^3, which covers almost the entire Atlantic oceanic domain as well as the Rharb and Guadalquivir Basins.

3) Accretionary Wedge Sediments (AWS) formed by the imbrications of Triassic to upper Miocene sediments, including also sediments of different ages with a similar density (2400 kg/m^3).

4) Upper-Middle Crust (UMC) with an average density of 2700 kg/m^3.

5) Lower Crust (LC) with a density of 2920 kg/m^3.

6) Intermediate Crust (IC) with average properties between the upper-middle and lower crust, which can replace the upper-middle crust (SW Iberian Massif) or the whole crust, playing the role of a transitional crust (east Alboran Basin).

7) Peridotites located in two small areas in both the Betics and the Rif with a density of 3100 kg/m^3.

8) Lithospheric mantle with a temperature-dependent density.

The application of the model to the GAS region yields a crustal and lithospheric structure that coincides fairly well with previous analyses based on seismic experiments, regional tomography, and integrated modelling. The main features of the geophysical observables have been satisfactorily modelled. The fit is achieved based on the dominant long wavelength part of the geophysical observables. Local features that are out of the scope of this study affect the shorter wavelength part.

The whole Atlas Mountains seem to be affected by lithospheric thinning (60-90 km), but this feature is more conspicuous in its southern part, the Anti Atlas Variscan domain, and to the north, in the Middle Atlas. The eastern branch of the Atlas does not seem to be much affected by this lithospheric thinning.

The strongest LAB topography gradients are present in the northern, southern and eastern limits of the thick lithosphere imaged beneath the Gulf of Cadiz, the Betics and the Rif (170-210 km). These regions coincide with the contact between the Iberian Variscan Massif and the Betic chain in the north, the contact between the Middle Atlas and the external Rif domain to the south, and the contact between the Betic-Rif orogen and the Alboran Basin to the east. The

amplitude differences in the LAB depth of the 3D model are stronger in comparison with the 1D model, since the 1D model tends to smooth the LAB undulations.

The rough topography of the LAB suggests that the mantle contribution to the isostatic balance is not negligible, as confirmed by the isostatic residual anomaly map calculated for the GAS region.

In the Alboran Basin, we found that, assuming a well-constrained crustal structure, it is not possible to fit simultaneously elevation and geoid anomaly. Changing the lithospheric thickness led to two end-member models in the context of a mantle with homogeneous properties everywhere.

The presence of the SW-NE oriented zone of lithospheric thinning affecting the High, Anti and Middle Atlas and extending to the eastern Alboran Basin, as well as the parallel thick lithosphere zone extending along the western Betics, eastern Rif, Rharb Basin, and Gulf of Cadiz, put severe constraints on the proposed geodynamic models. Slab tear and asymmetric roll-back could be a plausible mechanism to explain the lithospheric thickening, whereas lateral asthenospheric flow would cause the lithosphere thinning. An alternative mechanism responsible for the lithospheric thinning could be the presence of a hot magmatic reservoir derived from a deep ancient plume centred in the Canary Island, and extending as far as Central Europe.

7.5. FUTURE WORK

Two of the main simplifications assumed in this thesis are: a) a compositionally homogeneous upper mantle, and b) an isothermal sublithospheric mantle (i.e. asthenosphere). This implies that the density of the asthenosphere is constant everywhere, and that lateral variations in the thermophysical properties other than those arising from temperature variations, are not accounted for. Despite the success of this method to describe the first-order features of the lithosphere, the neglect of compressibility, phase changes, and compositional heterogeneities within the upper mantle leads to inconsistencies when comparing the modelled density with results from tomography, xenoliths, and thermodynamic data. Under some circumstances, it also creates artificial density contrasts across the Moho and the LAB that can potentially affect the interpretation of gravity and geoid anomalies.

In accordance with this, future work should include:

a) Implementation of realistic thermophysical properties within the lithospheric and asthenospheric mantle. This could be accomplished either by prescribing representative mineral assemblages for mantle lithologies (e.g. peridotite, lherzolite, etc.), or by incorporating a self-consistent thermodynamic model to obtain equilibrium mineral assemblages as function of pressure, temperature, and bulk composition. This could also provide the necessary parameters to calculate seismic velocities, which can be used to make helpful comparisons with seismic information.

b) Phase changes within the upper mantle. Two solid-state phase transformations (aluminium phases) exist within the depth range of interest: plagioclase-spinel (~30 km depth) and spinel-garnet (~60 km depth). For typical upper mantle compositions, these phase changes can produce density jumps of ~1.35% (plag-spinel) and 0.9% (spinel-garnet). Since both transformations take place at relatively shallow depths, they can potentially affect the gravity modelling.

c) Temperature variations in the sublithospheric (quasi-adiabatic) mantle. Tomography studies suggest that temperature variations also exist below the lithospheric mantle. Although these thermal anomalies are generally thought to be <~ 120 ºC, they are enough to significantly change the integrated buoyancy of individual mantle columns, exerting therefore a certain influence on isostasy calculations.

d) In this work, the compensation level (i.e. the depth at which no lateral changes in pressure take place) has been taken in the asthenosphere. However, thermal and pressure changes are likely to occur at such depths, leading to buoyancy changes. Therefore, future work should incorporate the use of a deeper compensation level. The 410-km mantle discontinuity is a suitable candidate.

Appendix A

REFERENCE LITHOSPHERIC COLUMN: ESTIMATE FROM CONSTANT CRUSTAL AND LITHOSPHERIC MANTLE DENSITY

A. REFERENCE LITHOSPHERIC COLUMN: ESTIMATE FROM CONSTANT CRUSTAL AND LITHOSPHERIC MANTLE DENSITY

The geoid anomalies in eq. 4.11 are calculated with respect to a reference lithospheric column. This reference column serves to calibrate the zero level for the geoid anomalies, and should be selected in such way that physically meaningful results are obtained in the scope of our four-layered lithospheric model. Thus, we require two conditions to be satisfied:

a) Existence of the lithospheric mantle layer, i.e. $z_L > z_c$ everywhere in the model.

b) Existence of the crust layer, in case of submerged points, i.e. $|E| < z_c$ if $E<0$.

The second condition is only applied when $E<0$. The topographic load can only increase the crustal thickness, i.e. for $E>0$ the smallest Moho depth corresponds to z_{cREF} when $E=0$.

The analysis of these two requirements is difficult in the context of a temperature-dependent lithospheric mantle density and a linear density gradient in the crust, due to the non-linearity of equations 4.10 and 4.11. On the other hand, this test becomes easier if we assume constant densities for the crust and the lithospheric mantle. This will allow us to estimate a reasonable reference lithospheric column provided that the two aforementioned conditions, a) and b), are satisfied. In this approach we derive a criterion to select an appropriate reference level for geoid anomalies, N_0, and, therefore, a reference column. Our aim is to express the conditions a) and b) in terms of only one variable, N_0, rather than two (z_{cREF}, z_{LREF}).

If we consider a constant value for the crust and lithospheric mantle densities, the isostatic geoid anomaly expressed in eq. 4.11 becomes:

$$N = -\frac{\pi G}{g}\left[\rho_w E^2 + \left(z_c^2 - E^2\right)\rho_c + \left(z_L^2 - z_c^2\right)\rho_m + \left(z_{\max}^2 - z_L^2\right)\rho_a\right] + N_0 \qquad \text{(A1)}$$

The isostatic equilibrium can be expressed as:

$$z_c = \frac{\rho_a L_0 + E\cdot\left(\rho_c - \rho_w\right) + z_L\cdot\left(\rho_m - \rho_a\right)}{\rho_m - \rho_c} \qquad \text{(A2)}$$

Note that eq. A2 is formally equal to eq. 4.2, but now, we have a constant density for the crust and the lithospheric mantle, considered as model parameters, instead of average values. If we solve the system of equations formed by (A1) and (A2) we obtain the depth of the LAB as a function of elevation and geoid anomaly:

$$z_L = \frac{1}{\rho_a - \rho_c}\left(\kappa + \sqrt{\frac{\rho_m - \rho_c}{\rho_m - \rho_a}\left(\kappa^2 - (\rho_a - \rho_c)\left[E^2(\rho_w - \rho_c) + z^2{}_{\max}\rho_a + (N - N_0)\frac{g}{\pi G}\right]\right)}\right) \qquad \text{(A3)}$$

where

$$\kappa = \left(\rho_a L_0 + E(\rho_c - \rho_w)\right)$$

Thus, eqs. A2 and A3 give us the depths of the Moho and the LAB which fit simultaneously elevation and geoid anomaly, for constant crustal and lithospheric mantle densities. We now discuss the fulfilment of conditions (a) and (b). For this, we express (a) and (b) in terms of N_0:

a) $N_0 > N_{0c}$

where

$$N_{0c}(E,N) = \frac{\pi G}{g}\left(E^2(\rho_w - \rho_c) + z^2{}_{\max}\rho_a - \frac{\kappa^2}{\rho_a - \rho_c}\right) + N \qquad \text{(A4)}$$

b) $N_0 > \overline{N_{0c}}$ if $E<E_0$ ($E_0<0$)

where

$$\overline{N_{0c}}(E,N) = \frac{\pi G}{g}\left(\frac{\rho_m - \rho_w}{\rho_m - \rho_a}E\left[2\rho_a L_0 + (\rho_a - \rho_w)E\right] + z^2{}_{\max}\rho_a + \frac{(\rho_a L_0)^2}{\rho_m - \rho_a}\right) + N$$

$$E_0 = -\frac{1}{\rho_a - \rho_w}\left(\rho_a L_0 + \sqrt{\frac{\rho_m - \rho_a}{\rho_m - \rho_w}\left((\rho_a L_0)^2 - (\rho_a - \rho_w)\left[z^2{}_{\max}\rho_a + (N - N_0)\frac{g}{\pi G}\right]\right)}\right)$$

(A5)

$N_{0c}, \overline{N_{0c}}$ are critical values for the geoid reference level below which no physically meaningful solution exists. In the first case, condition a), N_{0c} corresponds to the reference level for which the root in (A3) is equal to zero (i.e. non existence of lithospheric mantle layer). In the second case, condition b), is referred only to offshore points with a bathymetry deeper than $E_0(N, N_0)$. E_0 is a critical value for bathymetry with the following physical meaning: given N and a reference level N_0 (derived previously applying condition a), E_0 is the bathymetry for which the crustal thickness is 0. That is, if $E<E_0$, is not possible to find a lithospheric column with a layer crust that simultaneously fits elevation and geoid anomaly. The value of E_0 is calculated setting in (A1) and (A2) $z_c = -E_0$ and using an N_0 value satisfying condition a), i.e. $z_L>z_c$ everywhere in the model. Hence, for the points in which ($E<E_0$) we evaluate $\overline{N_{0c}}$, that is, the reference level for which $z_c = -E$ in (A3). Considering a reference level value higher than $\overline{N_{0c}}$ assures that $z_c>|E|$.

Consequently, for a given set of elevation and geoid anomaly data (i.e. a study area) the procedure to evaluate the reference level is:

1) Evaluate N_{0c} from eq. A4 for all the points and select a reference level according to condition a), i.e. $N_0>N_{0c}$.

2) If there are any offshore points in which $E<E_0$, evaluate $\overline{N_{0c}}$ for those points from A5, and select a reference level according to condition b), i.e. $N_0 > \overline{N_{0c}}$.

3) Calculate the lithospheric reference column associated with the N_0 value selected in steps 1) and 2), using eqs. A2 and A3 for a vanishing geoid anomaly and elevation.

REFERENCES

REFERENCES

Afonso, J.C., Ranalli, G. and Fernàndez, M., 2005. Thermal expansivity and elastic properties of the lithospheric mantle: results from mineral physics of composites. Physics of Earth and Planetary Interiors, 149: 279-306.

Anderson, D.L., 1989. Theory of the Earth. Blackwell Scientific Publications, Boston, UK.

Anguita, F. and Hernán, F., 2000. The Canary Islands origin: a unifying model. Journal of Volcanology and Geothermal Research, 103: 1-26.

Artemieva, I.M. and Mooney, W.D., 2001. Thermal thickness and evolution of Precambrian lithosphere: A global study. Journal of Geophysical Research, 106 (B8): 16387-16414.

Ayala, C., Fernàndez, M., Torne, M. and Pous, J., 1996. Two-dimensional geoid modelling: Some remarks on Chapman's algorithm. Geophysical Journal International, 127 (2): 542-544.

Ayarza, P., Alvarez-Lobato, F., Teixell, A., Arboleya, M.L., Teson, E., Julivert, M. and Charroud, M., 2005. Crustal structure under the central High Atlas Mountains (Morocco) from geological and gravity data. Tectonophysics, 400(1-4): 67-84.

Banda, E. and Ansorge, J., 1980. Crustal structure under the central and eastern part of the Betic Cordillera. Geophysical Journal of the Royal Astronomical Society, 63: 515-532.

Banda, E., Gallart, J., García-Dueñas, V., Dañobeitia, J. and Makris, J., 1993. Lateral variation of the crust in the Iberian Peninsula New evidence from the Betic Cordillera. Tectonophysics, 221: 51-66.

Banerjee, P., 1998. Gravity measurements and terrain corrections using a digital terrain model in the NW Himalaya. Computers & Geosciences, 24(10): 1009-1020.

Barranco, L.M., Ansorge, J. and Banda, E., 1990. Seismic refraction constraints on the geometry of the Ronda peridotitic massif (Betic Cordillera, Spain). Tectonophysics, 184: 379-392.

Berástegui, X., Banks, C., Puig, C., Taberner, C., Waltham, D. and Fernàndez, M., 1998. Lateral diapiric emplacement of Triassic evaporites at the southern margin of the Guadalquivir Basin, Spain. In: A. Mascle, C. Puigdefàbregas, H.P. Luterbacher and M. Fernàndez (Editors), Cenozoic Foreland Basins of Western Europe. Geological society Special Publications, London, pp. 49-68.

Berndt, C., 2002. Residual Bouguer satellite gravity anomalies reveal basement grain and structural elements of the Voring Margin, off Norway. Norwegian Journal of Geology, 82: 283-288.

Bijwaard, H. and Spakman, W., 2000. Non-linear global p-wave tomography by iterated linearized inversion. Geophysical Journal International, 141: 71-82.

Bijwaard, H., Spakman, W. and Engdahl, E.R., 1998. Closing the gap between regional and global travel time tomography. Journal of Geophysical Research, 103 (B12): 30055-30078.

Blais, J.A.R. and Ferland, R., 1984. Optimization in gravimetric terrain corrections. Canadian Journal of Earth Sciences, 21: 505-515.

Blanco, M.J. and Spakman, W., 1993. The P-wave velocity structure of the mantle below the Iberian Peninsula: Evidence for a subducted lithosphere beneath southern Spain. Tectonophysics, 221: 13-34.

Booth-Rea, G., Ranero, C., Martínez-Martínez, J.M. and Grevemeyer, I., 2007. Crustal types and Tertiary tectonic evolution of the Alborán Sea, western Mediterranean. Geochemistry Geophysics Geosystems, 8(Q10005): doi:10.1029/2007GC001639.

Bowin, C., 1983. Depth of principal mass anomalies contributing to the Earth's Geoidal Undulations and gravity anomalies. Marine Geodesy, 7: 61-100.

Bowin, C., 2000. Mass anomalies and the structure of the Earth. Physics and Chemistry of the Earth, 25 (4): 343-353.

Buforn, E. and Coca, P., 2002. Seismic moment tensor for intermediate depth earthquakes at regional distances in the Southern Spain. Tectonophysics, 356: 49-63.

Buforn, E., Udías, A. and Madariaga, R., 1991. Intermediate and deep earthquakes in Spain. Pure and Applied Geophysics, 136: 375-393.

Calvert, A., Sandvol, E., Seber, D., Barazangi, M., Roecker, S., Mourabit, T., Vidal, F., Alguacil, G. and Jabour, N., 2000. Geodynamic evolution of the lithosphere and upper mantle beneath the Alboran Region of the Western Mediterranean: Constraints from travel time tomography. Journal of Geophysical Research, 105: 10871-10898.

Carbó, A., Muñoz-Martín, A., Llanes, P. and Álvarez, J., 2003. Gravity analysis offshore the Canary Islands from a systematic survey. Marine Geophysical Researches, 24 (1 - 2): 113-127.

Carlson, R.W., Pearson, D.G. and James, D.E., 2005. Physical, chemical, and chronological characteristics of continental mantle. Reviews of Geophysics, 43: RG1001.

Casas, A. and Carbó, A., 1990. Deep structure of the Betic Cordillera derived from the interpretation of a complete Bouguer anomaly map. Journal of Geodynamics, 12: 137-147.

Chapman, M., 1979. Techniques for interpretation of geoid anomalies. Journal of Geophysical Research, 84 (B8): 3793-3801.

Cloetingh, S., van der Beek, P.A., van de Rees, D., Roep, T.B., Biermann, C. and Stephenson, R.A., 1992. Flexural interaction and the dynamics of Neogene extensional basin formation in the Alboran-Betic region. Geo-Marine Letters, 12: 66-75.

Coblentz, D., Richardson, R. and Sandiford, M., 1994. On the gravitational potential of the Earth's lithosphere. Tectonics, 13 (4): 929-945.

Cogbill, A.H., 1990. Gravity terrain corrections calculated using digital elevation models. Geophysics, 55: 102-106.

Comas, M.C., Dañobeitia, J.J., Álvarez-Marrón, J. and Soto, J.I., 1997. Crustal reflections and structure in the Alboran Basin: Preliminary results of the ESCI-Alboran survey. Revista de la Sociedad Geológica de España, 8: 529-542.

Contrucci, I., Klingelhoefer, F., Perrot, J., Bartolomé, R., Gutscher, M.-A., Sahabi, M., Malod, J. and Rehault, J.-P., 2004. The crustal structure of the NW Moroccan continental margin from wide-angle and reflection seismic data. Geophysical Journal International, 159: 117-128.

Cserepes, L., Christensen, U.R. and Ribe, N.M., 2000. Geoid height versus topography for a plume model of the Hawaiian swell. Earth and Planetary Science Letters, 178: 29-38.

Dewey, J.F., 1988. Extensional collapse of orogens. Tectonics, 7: 1123-1139.

Docherty, C. and Banda, E., 1995. Evidence for the eastward migration of the Alboran Sea based on regional subsidence analysis: A case for basin formation by delamination of the subcrustal lithosphere? Tectonics, 14 (4): 804-818.

Doin, M.P., Fleitout, L. and McKenzie, D., 1996. Geoid anomalies and the structure of continental and oceanic lithospheres. Journal of Geophysical Research, 101(B7): 16,119-16,135.

Farr, T.G. et al., 2007. The Shuttle Radar Topography Mission. Reviews of Geophysics, 45 (RG2004): doi: 10.1029/2005RG000183.

Featherstone, W.E. and Dentith, M.C., 1997. A geodetic approach to gravity data reduction for geophysics. Computers & Geosciences, 23 (10): 1063-1070.

Fernàndez, M., Berástegui, X., Puig, C., García-Castellanos, D., Jurado, M.J., Torné, M. and Banks, C., 1998a. Geophysical and geological constraints on the evolution of the Guadalquivir foreland basin, Spain. In: A. Mascle, C. Puigdefàbregas, H.P. Luterbacher and M. Fernàndez (Editors), Cenozoic Foreland Basins of Western Europe. Geological society Special Publications, London, pp. 29-48.

Fernàndez, M., Marzán, I., Correia, A. and Ramalho, E., 1998b. Heat flow, heat production, and lithospheric thermal regime in the Iberian Peninsula. Tectonophysics, 291: 29-53.

Fernàndez, M., Marzán, I. and Torne, M., 2004. Lithospheric transition from the Variscan Iberian Massif to the Jurassic oceanic crust of the Central Atlantic. Tectonophysics, 386: 97-115.

Fernández-Ibañez, F., 2007. Sismicidad, reología y estructura térmica de la corteza en el Arco de Gibraltar. Phd Thesis.Universidad de Granada, Granada, 211 pp.

Fernández-Ibáñez, F., Soto, J.-I., Zoback, M.D. and Morales, J., 2007. Present-day stress field in the Gibraltar Arc (western Mediterranean). Journal of Geophysical Research, 112(B08404): doi:10.1029/2006JB004683.

Flis, M.F., Butt, A.L. and Hawke, P.J., 1998. Mapping the range front with gravity - are the corrections up to it? Exploration Geophysics, 29: 378-383.

Forsberg, R., 1985. Gravity field terrain effect computations by FFT. Journal of Geodesy., 59: 342-360.

Frizon de Lamotte, D., Andrieux, J. and Guézou, J.C., 1991. Cinématique des chevauchements néogènes dans l'Arc bético-rifain: discussion sur les modèles géodynamiques. Bulletin de la Société Géologique de France, 162 (4): 611-626.

Frizon de Lamotte, D., Crespo-Blanc, A., Saint-Bézar, B., Comas, M., Fernàndez, M., Zeyen, H., Ayarza, P., Robert-Charrue, C., Chalouan, A., Zizi, M., Teixell, A., Arboleya, M.-L., Alvarez-Lobato, F., Julivert, M. and Michard, A., 2004. TRANSMED Transect I. In: W. Cavazza, F. Roure, W. Spakman, G.M. Stampfli and P. Ziegler (Editors), The TRANSMED Atlas - The Mediterranean region from crust to mantle. Springer, Berlin Heidelberg.

Fullea, J., Fernàndez, M. and Zeyen, H., 2006. Lithospheric structure in the Atlantic-Mediterranean transition zone (southern Spain, northern Morocco): a simple approach from regional elevation and geoid data. Comptes Rendus Geoscience, 338: 140-151.

Fullea, J., Fernàndez, M., Zeyen, H. and Vergés, J., 2007. A rapid method to map the crustal and lithospheric thickness using elevation, geoid anomaly and thermal analysis. Application to the Gibraltar Arc System and adjacent zones. Tectonophysics, 430: 97-117.

Galindo-Zaldivar, J., Jabaloy, A., Gonzalez-Lodeiro, F. and Aldaya, F., 1997. Crustal structure of the central sector of the Betic cordillera (SE Spain). Tectonics, 16(1): 18-37.

Gallardo-Delgado, L.A., Pérez-Flores, M.A. and Gómez-Treviño, E., 2003. A versatile algorithm for joint 3D inversion of gravity and magnetic data. Geophysics, 68: 949.

García-Castellanos, D., 2002. Interplay between lithospheric flexure and river transport in foreland basins. Basin Research, 14 (2): 89-104.

Garcia-Castellanos, D., Fernández, M. and Torne, M., 2002. Modeling the evolution of the Guadalquivir foreland basin (southern Spain). Tectonics, 21(3): 10.1029/2002TC001339.

Giese, P. and Jacobshagen, V., 1992. Inversion tectonics of intracontinental ranges: High and Middle Atlas. Geologische Rundschau 81(1): 249-259.

González, A., Córdoba, D., Vegas, R. and Matias, L.M., 1998. Seismic crustal structure in the southwest of the Iberian Peninsula and the Gulf of Cadiz. Tectonophysics, 296(3-4): 317-331.

González-Fernández, A., Córdoba, D., Matias, L.M. and Torne, M., 2001. Seismic crustal structure in the Gulf of Cadiz (SW Iberian Peninsula). Marine Geophysical Researches, 22: 207-223.

Götze, H.-J. and Lahmeyer, B., 1988. Application of theree-dimensional interactive modeling in gravity and magnetics. Geophysics, 53(8): 1096-1108.

Gràcia, E., Dañobeitia, J., Verges, J., Bartolomé, R. and Córdoba, D., 2003. Crustal architecture and tectonic evolution of the Gulf of Cadiz (SW Iberian margin) at the convergence of the Eurasian and African plates. Tectonics, 22(4): 1033, doi: 10.1029/2001TC901045.

Granet, M., Wilson, M. and Achauer, U., 1995. Imaging a mantle plume beneath the French Massif Central. Earth and Planetary Science Letters, 136: 281-296.

Grevemeyer, I., 1999. Isostatic geoid anomalies over mid-plate swells in the Central North Atlantic. Journal of Geodynamics, 28: 41-50.

Griffin, W.L., O'Reilly, S.Y. and Ryan, C.G., 1999. The composition and origin of sub-continental lithospheric mantle. In: Y. Fei, C.M. Berkta and B.O. Mysen (Editors), Mantle petrology: Field observations and high-pressure experimentation: A tribute to Francis R. (Joe) Boyd. The Geochemical Society.

Gurria, E. and Mezcua, J., 2000. Seismic tomography of the crust and lithospheric mantle in the Betic Cordillera and Alboran Sea. Tectonophysics, 329 (1-4): 99-119.

Gutscher, M.-A., Malod, J., Rehault, J.-P., Contrucci, I., Klingelhoefer, F., Mendes-Victor, L. and Spakman, W., 2002. Evidence for active subduction beneath Gibraltar. Geology, 30: 1071-1074.

Hager, B.H., 1983. Global isostatic geoid anomalies for plate and boundary layer models of the lithosphere. Earth and Planetary Science Letters, 63: 97-109.

Hager, B.H., Clayton, R.W., Richards, M.A., Comer, R.P. and Dziewonski, A.M., 1985. Lower mantle heterogeneity, dynamic topography and geoid. Nature, 313: 541-545.

Hammer, S., 1939. Terrain correction for gravimeter stations. Geophysics, 4: 184-194.

Hastings, D.A. and Dunbar, P.K., 1999. Global Land One-kilometer Base Elevation (GLOBE) Digital Elevation Model, Documentation, Volume 1.0. Key to Geophysical Records Documentation (KGRD) 34.

Hatzfeld, D., 1976. Étude sismologique et gravimétrique de la structure profonde de la mer d'Alboran: Mise en évidence d'un manteau anormal. Comptes Rendus de l'Academie des Sciences - Series IIA - Earth and Planetary Science, 5: 483-500.

Hatzfeld, D. and the Working Group for Deep Seismic Sounding, 1978. Crustal Seismic profiles in the Alboran Sea - Preliminary results. Pure and Applied Geophysics, 116: 167-180.

Haxby, W.F. and Turcotte, D.L., 1978. On isostatic geoid anomalies. Journal of Geophysical Research, 83: 5473-5478.

Hayford, J.F. and Bowie, W., 1912. The effect of topography and isostatic compensation upon the intensity of of gravity. U.S. Coast and Geodetic Survey special publication, 10.

Heiskanen, W.A. and Moritz, H., 1967. Physical Geodesy, San Francisco, 364 pp.

Heller, D.-A. and Marquart, G., 2002. An admittance study of the Reykjanes Ridge and elevated plateaux between the Charlie-Gibbs and Senja fracture zones. Geophysical Journal International, 148: 65-76.

Hildenbrand, T., Kucks, R., Hamouda, M. and Bellot, A., 1988. Bouguer gravity map and related filtered anomaly maps of Morocco. U. S. Geological Survey Open-File Report, 88-517: 15.

Hoernle, K., Zhang, Y.-S. and Graham, D., 1995. Seismic and geochemical evidence for large-scale mantle upwelling beneath the eastern Atlantic and western and central Europe. Nature, 374 (2): 34-39.

Hwang, C., Wang, C.-G. and Hsiao, Y.-S., 2003. Terrain correction computation using Gaussian quadrature. Computers & Geosciences, 29: 1259-1268.

Iribarren, L., Vergés, J., Camurri, F., Fullea, J. and Fernàndez, M., 2007. The structure of the Atlantic-Mediterranean transition zone from the Alboran Sea to the Horseshoe Abyssal Plain (Iberia-Africa plate boundary). Marine Geology, 243 (1-4): 97-119.

Jiménez-Munt, I. and Negredo, A., 2003. Neotectonic modelling of the western part of the Africa–Eurasia plate boundary: from the Mid-Atlantic ridge to Algeria. Earth and Planetary Science Letters, 205 (3-4): 257-271.

Kane, M.F., 1962. A comprehensive system of terrain corrections using a digital computer. Geophysics, 27 (4): 445-462.

Ketalaar, A.C.R., 1987. Terrain correction for gravity measurements, using a digital terrain model (DTM). Geoexploration, 24(2): 109-124.

Kiefer, W.S. and Kellogg, L.H., 1998. Geoid anomalies and dynamic topography from time-dependent, spherical axis mantle convection. Physics of Earth and Planetary Interiors, 106: 237-256.

Lachenbruch, A.H. and Morgan, P., 1990. Continental extension, magmatism and elevation; formal relations and rules of thumb. Tectonophysics, 174: 39-62.

LaFehr, T.R., 1991. An exact solution for the gravity curvature (Bullard B) correction. Geophysics, 56: 1178-1184.

Le Stunff, Y. and Ricard, Y., 1995. Topography and geoid due to lithospheric mass anomalies. Geophysical Journal International, 122: 982-990.

Leaman, D.E., 1998. The gravity terrain correction - practical considerations. Exploration Geophysics, 29: 467-471.

Lemoine, F.G., D. E. Smith, L. Kunz, R. Smith, E. C. Pavlis, N. K. Pavlis, S. M. Klosko, D. S. Chinn, M. H. Torrence, R. G. Williamson, C. M. Cox, K. E. Rachlin, Y. M. Wang, S. C. Kenyon, R. Salman, R. Trimmer, R. H. Rapp and Nerem, R.S., 1998.

The development of the NASA GSFC and NIMA joint geopotential model. In: J. Segawa, H. Fujimoto and S. Okubo (Editors), Gravity, Geoid, and Marine Geodesy, International Association of Geodesy Symposium. Springer-Verlag, Berlin, pp. 461-469.

Li, X. and Götze, H.-J., 2001. Tutorial. Ellipsoid, geoid, gravity, geodesy, and geophysics. Geophysics, 66 (6): 1660-1668.

Litto, W., Jaaidi, E.B., Medina, F. and Dakki, M., 2001. Etude sismo-estructurale de la marge nord du bassin du Gharb (avant-pays rifain, Maroc): Mise en évidence d'une distension d'âge miocène tardif. Eclogea Geologicae Helvetiae, 94: 63-73.

Lonergan, L. and White, N., 1997. Origin of the Betic-Rif mountain belt. Tectonics, 16 (3): 504-522.

Lopez, H.R.B., 1990. FORTRAN program for automatic terrain correction on gravity measurements. Computers & Geosciences, 16 (2): 237-244.

Luis, J.F., Miranda, J.M., Galdeano, A. and Patriat, P., 1998. Constraints on the structure of the Azores spreading centre from gravity data. Marine Geophysical Researches, 20 (3): 157-170.

Ma, X.Q. and Watts, D.R., 1994. Terrain correction program for regional gravity surveys. Computers & Geosciences, 20(6): 961-972.

Makris, J., Demnati, A. and Klussmann, J., 1985. Deep seismic soundings in Morocco and a crust and upper mantle model deduced from seismic and gravity data. Annales Geophysicae., 3: 369-380.

Marone, C., van der Lee, S. and Giardini, D., 2004. Three-dimensional upper mantle S-velocity model for the Eurasia-Africa plate boundary region. Geophysical Journal International, 158: 109-130.

McMillan, W.D., 1958. The theory of potential. Theoretical mechanics. Dover, New York, 469 pp.

Medialdea, T., Suriñach, E., Vegas, R., Banda, E. and Ansorge, J., 1986. Crustal structure under the western end of the Betic Cordillera (Spain). Annales Geophysicae, 4: 457-464.

Medialdea, T., Vegas, R., Somoza, L., Vazquez, J.T., Maldonado, A., Diaz-del-Rio, V., Maestro, A., Cordoba, D. and Fernandez-Puga, M.C., 2004. Structure and evolution of the "Olistostrome" complex of the Gibraltar Arc in the Gulf of Cadiz (eastern Central Atlantic): evidence from two long seismic cross-sections. Marine Geology, 209(1-4): 173-198.

Meghraoui, M., Morel, J.L., Andrieux, J. and Dahmani, M., 1996. Tectonique plio-quaternaire de la chaîne tello-rifaine et de la mer d'Alboran. Bulletin de la Société Géologique de France, 167: 143-159.

Mezcua, J., Gil, A. and Benarroch, R., 1996. Estudio Gravimétrico de la Península Ibérica y Baleares. Instituto Geográfico Nacional, Madrid 14 pp y 2 mapas.

Mezcua, J. and Rueda, J., 1997. Seismological evidence for a delamination process in the lithosphere under the Alboran Sea. Geophysical Journal International, 129: F1-F8.

Missenard, Y., Zeyen, H., Frizon de Lamotte, D., Leturmy, P., Petit, C., Sébrier, M. and Saddiqi, O., 2006. Crustal versus asthenospheric origin of the relief of the Atlas Mountains of Morocco. Journal of Geophysical Research, 111 (B03401): doi:10.1029/2005JB003708.

Moore, W.B. and Schubert, G., 1997. Venusian crustal and lithospheric properties from non linear regressions of highland geoid and topography. Icarus, 128: 415-428.

Nagy, D., Papp, G. and Benedek, J., 2000. The gravitational potential and its derivatives for the prism. Journal of Geodesy, 74: 552-560.

Negredo, A.M., Bird, P., Sanz de Galdeano, C. and Buforn, E., 2002. Neotectonic modeling of the Ibero-Maghrebian region. Journal of Geophysical Research, 107 (B11): 2292, doi: 10.1029/2001JB000743.

Nowell, D.A.G., 1999. Gravity terrain corrections-an overview. Journal of Applied Geophysics, 42: 117-134.

Ockendon, J.R. and Turcotte, D.L., 1977. On gravitational potential and field anomalies due to thin mass layers. Geophysical Journal of the Royal Astronomical Society, 48: 479-492.

Olivier, R.J. and Simard, R.G., 1981. Improvement of the conic prism model for terrain correction in rugged topography. Geophysics, 46: 1054-1056.

Panasyuk, S.V. and Hager, B.H., 2000. Models of isostatic and dynamic topography, geoid anomalies, and their uncertainties. Journal of Geophysical Research, 105(B12): 28199-28209.

Parker, R.L., 1996. Improved Fourier terrain correction: Part II. Geophysics, 61: 365-372.

Parsons, B. and Sclater, J.G., 1977. An analysis of the variations of ocean floor bathymetry and heat flow with age. Journal of Geophysical Research, 82: 803-827.

Platt, J.P. and Vissers, R.L.M., 1989. Extensional collapse of thickened continental lithosphere: A working hypothesis for the Alboran Sea and Gibraltar arc. Geology, 29: 299-302.

Platt, J.P., Whitehouse, M.J., Kelley, S.P., Carter, A. and Hollick, L., 2003. Simultaneous extensional exhumation across the Alboran Basin: Implications for the causes of late orogenic extension. Geology, 31: 251-254.

Polyak, B.G., Fernàndez, M., Khutorskoy, M.D., Soto, J.I., Basov, I.A., Comas, M.C., Khain, V.Y., Alonso, B., Agapova, G.V., Mazurova, I.S., Negredo, A., Tochitsky, V.O., Linde, J.d.l., Bogdanov, N.A. and Banda, E., 1996. Heat flow in the Alboran Sea, western Mediterranean. Tectonophysics, 263: 191-218.

Poudjom Djomani, Y.H., O'Reilly, S.Y., Griffin, W.L. and Morgan, P., 2001. The density structure of subcontinental lithosphere through time. Earth and Planetary Science Letters, 184 (3-4): 605-621.

Ramdani, F., 1998. Geodynamic implications of the intermediate-depth earthquakes and volcanism in the intraplate Atlas Mountains. Physics of Earth and Planetary Interiors, 108: 245-260.

Rimi, A., Chalouan, A. and Bahi, L., 1998. Heat flow in the westernmost part of the Alpine Mediterranean system (the Rif, Morocco). Tectonophysics, 285: 135-146.

Ritter, J.R.R., Jordan, M., Christensen, U. and Achauer, U., 2001. A mantle plume below the Eifel volcanic fields, Germany. Earth and Planetary Science Letters, 186: 7-14.

Sandiford, M. and Powell, R., 1990. Some isostatic and thermal consequences of the vertical strain geometry in convergent orogens. Earth and Planetary Science Letters, 98: 154-165.

Sandwell, D.T., Johnson, C.L., Bilotti, F. and Suppe, J., 1997. Driving forces for limited tectonics on Venus. Icarus, 129: 232-244.

Sandwell, D.T. and MacKenzie, K.R., 1989. Geoid Height Versus Topography for Oceanic Plateaus and Swells. Journal of Geophysical Research, 94 (B6): 7403-7418.

Sandwell, D.T. and Renking, M.L., 1988. Compensation of swells and plateaus in the North Pacific: No direct evidence for mantle convection. Journal of Geophysical Research, 93 (B4): 2775-2783.

Sandwell, D.T. and Smith, W.H.F., 1997. Marine gravity anomalies from GEOSAT and ERS-1 satellite altimetry. Journal of Geophysical Research, 102: 10039-10054.

Schmidt, S. and Götze, H.-J., 1999. Integration of data constraints and potential field modelling — an example from southern lower Saxony, Germany. Physics and Chemistry of the Earth, Part A: Solid Earth and Geodesy, 24, (3): 191-196.

Schubert, G., Turcotte, D.L. and Olson, P., 2001. Mantle convection in the Earth and planets. Cambridge Univ. Press. UK, pp 956.

Seber, D., Barazangi, M., Ibenbrahim, A. and Demnati, A., 1996a. Geophysical evidence for lithospheric delamination beneath the Alboran Sea and Rif-Betic Mountains. Nature, 379: 785-790.

Seber, D., Barazangi, M., Tadili, B.A., Ramdani, F., Ibenbrahim, A. and Sari, D.B., 1996b. Three-dimensional upper mantle structure beneath the intraplate Atlas and interplate Rif Mountains of Morocco. Journal of Geophysical Research, 101(B2): 3125-3138.

Seber, D., Sandvol, E., Sandvol, C., Brindisi, C. and Barazangi, M., 2001. Crustal model for the Middle East and North Africa region: Implications for the isostatic compensation mechanism. Geophysical Journal International, 147: 630-638.

Simancas, J.F., Carbonell, R., González Lodeiro, F., Pérez Estaún, A., Juhlin, C., Ayarza, P., Kashubin, A., Azor, A., Martínez Poyatos, D., Almodóvar, G.R., Pascual, E., Sáez, R. and Expósito, I., 2003. Crustal structure of the transpressional Variscan Orogen of SW Iberia: SW Iberia deep seismic reflection profile (IBERSEIS). Tectonics, 22(6): 1062.

Simons, M., Hager, B.H. and Solomon, S.C., 1994. Global variations in the geoid/topography admittance of Venus. Science, 264: 798-803.

Smith, D.A., 2000. The gravitational attraction of any polygonal shaped vertical prism with inclined top and bottom faces. Journal of Geodesy, 74: 414-420.

Smith, W.H.F. and Sandwell, D.T., 1994. Bathymetry prediction from dense satellite altimetry and sparse shipborne bathymetry. Journal of Geophysical Research, 99: 21803-21824.

Snopek, K. and Casten, U., 2006. 3GRAINS: 3D Gravity Interpretation Software and its application to density modeling of the hellenic subduction zone. Computers & Geosciences, 32(5): 592-603.

Soto, J.I., Comas, M.C. and de la Linde, J., 1996. Espesor de sedimentos en la cuenca de Alborán mediante una conversión sísmica corregida. Geogaceta, 20(2): 382-385.

Spakman, W. and Wortel, M.J.R., 2004. A tomographic view on western Mediterranean geodynamics. In: W. Cavazza, F. Roure, W. Spakman, G.M. Stampfli and P. Ziegler (Editors), The TRANSMED Atlas - The Mediterranean region from crust to mantle. Springer, Berlin Heidelberg, pp. 31-52.

Stich, D. Mancilla, F.L. and Morales, J., 2005. Crust-mantle coupling in the Gulf of Cadiz (SW-Iberia). Geophysical Research Letters, 32 (L13306): doi:10.1029/2005GL023098.

Strang van Hees, G., L., 2000. Some elementary relations between mass distributions inside the Earth and the geoid and gravity field. Journal of Geodynamics, 29: 111-123.

Swick, C.H., 1942. Pendulum gravity measurements and isostatic reductions. U. S. Coast and Geodetic Survey special publication, 232.

Talwani, M., Worzel, J.L. and Landisman, L., 1959. Rapid computations for two-dimensional bodies with application to the Mendocino submarine fracture zone. Journal of Geophysical Research, 64: 49-59.

Tapley, B., Ries, J., Bettadpur, S., Chambers, D., Cheng, M. and Condi, F., 2005. An improved Earth gravity field model from GRACE. Journal of Geodesy, 79: 467-478.

Teixell, A., Arboleya, M.-L., Julivert, M. and Charroud, M., 2003. Tectonics and topography of the central High Atlas (Morocco). Tectonics, 22 (5): 1051, doi:10.1029/2002TC001460.

Teixell, A., Ayarza, P., Zeyen, H., Fernàndez, M. and Arboleya, M.-L., 2005. Effects of mantle upwelling in a compressional setting: the Atlas Mountains of Morocco. Terra Nova, 17: 456-461.

Torne, M. and Banda, E., 1992. Crustal thinning from the Betic Cordillera to the Alboran Sea. Geo-Mar. Lett., 12: 76-81.

Torne, M., Fernàndez, M., Carbonell, J. and Banda, E., 1995. Lithospheric transition from continental to oceanic in the West Iberia Atlantic Margin. In: E. Banda, M. Torne and M. Talwani (Editors), Rifted Ocean-Continent Boundaries. Kluwer Acad. Pub., Dordrecht, pp. 247-263.

Torne, M., Fernàndez, M., Comas, M.C. and Soto, J.I., 2000. Lithospheric structure beneath the Alboran Basin: Results from 3D gravity modeling and tectonic relevance. Journal of Geophysical Research, 105 (B2): 3209-3228.

Tsoulis, D., 2001. Terrain correction computations for a densely sampled DTM in the Bavarian Alps. Journal of Geodesy, 75 (5-6): 291-307.

Turcotte, D.L. and Schubert, G., 1982. Geodynamics. Application of continuum physics to geological problems. John Wiley & Sons, New York, 450 pp.

Verzhbitsky, E.V. and Zolotarev, V.G., 1989. Heat flow and the Eurasian-African plate boundary in the eastern part of the Azores-Gibraltar fracture zone. Journal of Geodynamics, 11(3): 267-273.

Watts, A.B., Platt, J.P. and Buhl, M.L., 1993. Tectonic evolution of the Alboran Sea Basin. Basin Research, 5: 153-177.

Wessel, P., 1993. Observational constraints on models of the Hawaiian Hot Spot Swell. Journal of Geophysical Research, 98 (B9): 16095-16104.

Whitman, W.W., 1991. A microgal approximation for the Bullard B-earth's curvature-gravity correction. Geophysics, 56 (12): 1980-1985.

Wieczorek, M.A. and Zuber, M.T., 2004. Thickness of the Martian crust: Improved constraints from geoid-to-topography ratios. Journal of Geophysical Research, 109 (E01009): doi: 10.1029/2003JE002153.

Wigger, P., Asch, G., Giese, P., Heinsohn, W.-D., El Alami, S.O. and Ramdani, F., 1992. Crustal structure along a transverse across the Middle and High Atlas Mountains derived from seismic refraction studies. Geologische Rundschau., 81: 237-248.

Wortel, M.J.R. and Spakman, W., 2000. Subduction and slab detachment in the Mediterranean-Carpathian Region. Science, 290: 1910-1917.

Zeck, H.P., 1996. Betic-Rif orogeny: subduction of Mesozoic Tethys lithosphere under eastward drifting Iberia, slab detachment shortly before 22 Ma, and subsequent uplift and extension tectonics. Tectonophysics, 254(1-2): 1-16.

Zeyen, H., Ayarza, P., Fernàndez, M. and Rimi, A., 2005. Lithospheric structure under the western African-European plate boundary: A transect across the Atlas Mountains and the Gulf of Cadiz. Tectonics, 24(TC2001): doi:10.1029/2004TC001639.

Zeyen, H. and Fernàndez, M., 1994. Integrated lithospheric modeling combining thermal, gravity, and local isostasy analysis: Application to the NE Spanish Geotransect. Journal of Geophysical Research, 99: 18089-18102.

Zhou, S. and Sandiford, M., 1992. On the stability of isostatically compensated mountain belts. Journal of Geophysical Research, 97(B10): 14207-14221.

Zouhri, L., Lamouroux, C. and Buret, C., 2001. La Mamora, charnière entre la Meseta et le Rif : son importance dans l'évolution géodynamique post-paléozoïque du Maroc. Geodinamica Acta, 14(6): 361-372.

RESUMEN EN ESPAÑOL

1. INTRODUCCIÓN

1.1 TRABAJOS PREVIOS

La modelización detallada de la estructura actual de la litosfera es de gran importancia para comprender la evolución de la Tierra en el marco de la tectónica de placas. La litosfera está compuesta por la corteza y una porción del manto superior. La estructura de la corteza es relativamente bien conocida: observaciones de campo y pozos proporcionan información directa de la parte más superficial de la corteza, mientras que los métodos sísmicos ofrecen información fiable a profundidades superiores, llegando hasta la discontinuidad corteza-manto. Desgraciadamente, se tiene un conocimiento pobre del manto litosférico y hay pocas observaciones directas disponibles. La modelización numérica que toma la información proporcionada por los diversos observables geofísicos, es decir, elevación, anomalías de gravedad y geoide, y flujo de calor superficial (SHF), constituye una manera sencilla y de coste relativamente bajo de mejorar nuestro conocimiento del manto litosférico y puede complementar a otras técnicas indirectas, como la tomografía sísmica.

Diversos trabajos han contemplado la modelización directa de la litosfera, y hay varios códigos numéricos disponibles. Zeyen y Fernández (1994) presentaron un algoritmo 2D para determinar la estructura térmica en régimen estacionario de la litosfera incorporando un análisis isostático y gravimétrico. En trabajos posteriores incorporaron también la anomalía de geoide en el algoritmo para obtener una mejor imagen de la estructura litosférica profunda. Sin embargo, la aproximación 2D solo es apropiada cuando las variaciones litosféricas en dirección perpendicular al perfil son pequeñas en comparación con las variaciones a lo largo del perfil. Otros trabajos ofrecen un marco 3D para modelizar la estructura litosférica usando diferentes conjuntos de datos. 3GRAINS es un programa que permite una modelización 3D interactiva de la distribución de densidades en la litosfera usando las anomalías gravimétricas (Snopek y Casten, 2005). IGMAS es una herramienta 3D para interpretar datos de geoide, gravedad y magnetismo que utiliza una aproximación poliédrica para modelizar la estructura litosférica (Götze y Lahmeyer, 1988; Götze y Schmidt, 1999). Sin embargo, las herramientas 3D de modelización anteriormente mencionadas no incorporan la distribución de temperaturas, que es un parámetro clave para modelizar la densidad del manto (e.g. Parsons y Sclater, 1977; Schubert et al., 2001).

Para comprobar la validez de los códigos numéricos desarrollados en esta tesis, se ha seleccionado una zona relativamente bien conocida y estudiada: el Sistema Arco de Gibraltar (GAS). Tradicionalmente se ha considerado que el GAS comprendía la Cuenca de Alborán, el orógeno Betico-Rifeño y el Golfo de Cádiz. Sin embargo, en esta tesis consideraremos que las montañas adyacentes del Atlas podrían jugar un papel importante en la evolución geodinámica de la zona. Así pues, y en el marco de esta tesis, consideraremos que el GAS, en un sentido lato, está compuesto por la Cuenca de Alborán, el orógeno Betico-Rifeño, el Golfo de Cádiz y el Atlas.

Numerosos estudios se han llevado a cabo en el GAS: perfiles de reflexión/refracción sísmica (Banda et al., 1993; Comas et al., 1997; Simancas et al., 2003), tomografía sísmica (e.g. Blanco y Spakman, 1993; Bijwaard et al., 1998; Calvert et al., 2000; Marone et al., 2004), modelización gravimétrica (e.g. Torne et al., 2000; Gràcia et al., 2003) y flujo de calor (Polyak et al., 1996; Fernàndez et al., 1998b; Rimi et al., 1998). A pesar de todos estos trabajos, muchos aspectos permanecen oscuros, fundamentalmente el modo en que se resuelve la transición entre una litosfera oceánica Jurásica en el dominio Atlántico y una litosfera oceánica Neógena en la Cuenca de Argelia. Además, el origen y formación del margen Sudibérico y Norteafricano es todavía asunto de debate y hay varios modelos geodinámicos propuestos, algunos incluso mutuamente excluyentes, basados en diferentes datos geológicos y geofísicos: subducción Neógena asociada a un slab roll back (Frizon de Lamotte et al., 1991; Lonergan y White, 1997), subducción activa (Gutscher et al., 2002), delaminación (e.g. Seber et al., 1996a; Mezcua y Rueda, 1997; Calvert et al., 2000), colapso convectivo (Platt y Vissers, 1989; Platt et al., 2003), desprendimiento de slab (Zeck, 1996; Wortel y Spakman, 2000) o slab roll-back y desgarro litosférico (Spakman y Wortel, 2004).

1.2 OBJETIVOS

El objetivo principal de esta tesis es de naturaleza metodológica: el desarrollo de métodos numéricos para determinar la estructura litosférica combinando las ecuaciones geopotenciales, litostáticas y de transporte de calor. El producto final debería ser una herramienta 3D útil para analizar la litosfera integrando de manera consistente el campo térmico, la elevación, el flujo de calor superficial y las anomalías gravimétricas y del geoide. En este sentido, cuatro puntos importantes son:

1) Desarrollo de un código numérico para calcular la anomalía de Bouguer tanto en zonas marinas como continentales a partir de datos satelitales de anomalía de aire libre públicamente disponibles.

2) Desarrollo de un método para determinar una primera aproximación de la estructura litosférica utilizando como datos de partida la elevación y la anomalía del geoide.

3) Desarrollo de un código 3D interactivo que permita la modelización directa de la litosfera integrando SHF, elevación y las anomalías gravimétricas y del geoide.

4) Obtención de una imagen 3D de la geometría litosférica independiente de la tomografía sísmica para mejorar el conocimiento que se tiene de la estructura profunda actual del GAS y comparar con los diferentes modelos geodinámicos propuestos para explicar su origen.

1.3 ESTRUCTURA DE LA TESIS

En el Capítulo 2 se resumen brevemente los aspectos teóricos relacionados con el contenido de la tesis: la corteza y la litosfera terrestres, el campo gravitatorio, el geoide, el campo térmico y la isostasia.

En el Capítulo 3 se introduce la zona de estudio, el Sistema del Arco de Gibraltar (GAS), desde un punto de vista geológico y geofísico. Los principales aspectos estructurales se esbozan en el marco geológico. También se analizan mapas de elevación, anomalía de aire libre y anomalía del geoide. Se presenta el programa FA2BOUG que permite determinar la anomalía de Bouguer tanto en tierra como en mar usando como dato de partida anomalías de aire libre satelitales. El programa es utilizado, junto con los datos de tierra disponibles, para producir un mapa de la anomalía de Bouguer completa del GAS.

En el Capítulo 4 se desarrolla un método que permite una estimación rápida de los grosores corticales y litosféricos a partir de la combinación de datos de elevación y anomalía del geoide. En el método se asume isostasia local, estado térmico estacionario, un gradiente lineal de densidad para la corteza y una densidad dependiente de la temperatura para el manto. El modelo litosférico resultante sirve como entrada para el modelo 3D desarrollado en capítulos posteriores.

En el Capítulo 5 se presenta GEO3Dmod, un programa de ordenador que permite realizar modelización litosférica 3D directa, integrando SHF, elevación,

anomalías gravimétricas y ondulación del geoide. El programa tiene dos módulos. El primero (GEO3Dmod) resuelve el problema directo, es decir, dado un modelo litosférico (un conjunto de cuerpos con diferentes propiedades), calcular los observables geofísicos asociados a través de la distribución 3D de densidades y temperaturas de la litosfera. El segundo módulo (GEO3Dmod_INTF) es una interfaz gráfica diseñada para visualizar y modificar la estructura litosférica de acuerdo a las diferencias entre observables geofísicos calculados y medidos.

GEO3Dmod se aplica en el Capítulo 6 al GAS para obtener un modelo litosférico 3D regional de la zona de estudio integrando gravedad, geoide, elevación y SHF. Los resultados obtenidos son discutidos en el contexto de los diferentes modelos geodinámicos propuestos para explicar el origen y evolución del GAS.

En el Capítulo 7 se hace un sumario de las conclusiones más importantes obtenidas en los capítulos precedentes y se muestran posibles líneas de trabajo futuro.

2. FUNDAMENTOS

En esta tesis se integran los siguientes observables geofísicos para modelizar la estructura litosferica: Elevación, anomalías gravimétricas, ondulación del geoide y flujo de calor superficial (SHF). La idea es aprovechar la información complementaria que estos observables nos pueden ofrecer.

2.1 DEFINICIONES GENERALES: CORTEZA Y LITOSFERA TERRESTRES

La corteza es la capa más externa y ligera de la Tierra y está caracterizada por rocas con velocidades de onda P menores que 7.6 km/s y, en general, por densidades inferiores a 3100 kg/m^3. La corteza continental se divide usualmente en dos capas: una corteza superior con velocidades sísmicas de onda P comprendidas entre 4.5 y 6.4 km/s y densidades entre 2670 y 2810 kg/m^3, y una corteza inferior con valores comprendidos entre 6-7.5 km/s y 2850-2950 kg/m^3. La corteza oceánica está compuesta por una capa grabroica con velocidades típicas entre 6.6 y 7.2 km/s, cubierta por pillow lavas basálticas y diques laminados con una velocidad promedio de 4.5 km/s. En general, existe una capa sedimentaria de baja velocidad cuyas densidades varían en un amplio espectro (2000-2600 kg/m^3).

La litosfera es la capa externa de la Tierra que se comporta de manera rígida y es la unidad fundamental de la tectónica de placas. Comprende la corteza y una porción del manto superior. No hay una manera única de definir la litosfera. Dependiendo de las propiedades geofísicas que se estudien, puede definirse sísmica, térmica, mecánica, y químicamente. Sísmológicamente, la litosfera se define como el material de alta velocidad que queda por encima de la zona de baja velocidad del manto superior. Térmicamente, la litosfera es la parte del manto superior en la que los procesos conductivos de transmisión de calor predominan sobre los convectivos. La litosfera mecánica puede definirse como una capa no afectada por la convección que tiene lugar bajo ella, en escalas de tiempo geológicas. Desde un punto de vista geoquímico, la discontinuidad litosfera-astenosfera es la máxima profundidad a la cual se tienen granates pobres en Y (<10 ppm). En esta tesis adoptaremos una definición térmica de la litosfera, cuya base vendría definida por una isoterma. Como resultado de esto, y de acuerdo a la ec. 2.1, la densidad del manto litosférico disminuye linealmente con la profundidad. Aunque esta aproximación ha permitido describir correctamente, a primer orden, la estructura térmica de los diferentes dominios litosféricos, no

considera los efectos de la compresibilidad y la composición. Dado que los observables geofísicos relevantes usados en esta tesis solamente dependen de los contrastes de densidad y no de los valores absolutos, la compresibilidad, si los gradientes de presión son moderados, es un efecto de segundo orden. Los cambios composicionales pueden resultar en variaciones significativas de las propiedades termofísicas. De este modo, la definición adoptada para la litosfera solamente es válida cuando la estructura química de la misma no varíe significativamente en la región modelizada.

2.2 CAMPO GRAVITATORIO

El campo gravitatorio terrestre nos proporciona información de las variaciones laterales de densidad en el interior de la Tierra. Con un buen grado de aproximación, la Tierra puede ser descrita por un elipsoide de revolución equipotencial. El campo gravitatorio producido por este elipsoide de referencia se denomina campo normal o teórico. La superficie real equipotencial de la Tierra coincidente con el nivel medio de los océanos es el geoide. El potencial de gravedad terrestre puede descomponerse en un potencial normal o teórico asociado al elipsoide de referencia, y un potencial anómalo (ec. 2.3). Tanto las anomalías gravimétricas como la ondulación o anomalía del geoide están referidas al campo normal producido por el elipsoide de referencia.

2.2.1 Anomalías gravimétricas

Las anomalías gravimétricas (Δg) son la diferencia entre la gravedad medida sobre el (o reducida al) geoide, g, y la gravedad normal o teórica en un punto sobre el elipsoide de referencia (proyección del punto de medida a lo largo de la normal al elipsoide), γ. La gravedad medida directamente contiene diversos efectos que deben corregirse para obtener las anomalías gravimétricas. Así, se aplican diferentes correcciones: mareas terrestres, deriva instrumental, latitud, aire libre y topografía. Cuando se aplican las cuatro primeras correcciones se obtiene la anomalía de aire libre (Δg_{FA}), que está fuertemente correlacionada con la topografía en longitudes de onda cortas. La corrección de aire libre tiene en cuenta si el punto de medida de la gravedad está por encima o por debajo del elipsoide de referencia asumiendo el gradiente vertical de la gravedad. La anomalía de Bouguer (Δg_B) resulta de corregir la anomalía de aire libre por el efecto de la topografía circundante. El objetivo de la corrección de Bouguer es eliminar todas las componentes no geológicas de la gravedad para reasaltar las variaciones de masa en el interior de la Tierra. La corrección de Bouguer

completa está compuesta de tres partes: la lámina de Bouguer (Bullard A), que aproxima la topografía por una lámina infinita horizontalmente de densidad constante y espesor igual a la elevación en el punto de medida; la corrección por curvatura (Bullard B), que reemplaza la lámina de Bouguer por una capa esférica del mismo espesor hasta una distancia de 166.735 km; y la corrección por el terreno (Bullard C), que considera el efecto de la topografía circundante por encima y por debajo de la elevación del punto de cálculo (Nowell, 1999). La corrección por el terreno es siempre positiva para puntos por encima del nivel del mar, mientras que en los océanos puede ser positiva o negativa. De las tres partes que componen la corrección de Bouguer completa, la corrección por el terreno es la más costosa y la que más tiempo requiere para su ejecución.

2.2.2 Anomalía del geoide

El geoide es la superficie equipotencial de la Tierra que coincide con el nivel medio del mar y contiene, idealmente, toda la masa de la Tierra. La anomalía u ondulación del geoide es la distancia entre el geoide y el elipsoide de referencia. En los océanos, las variaciones del geoide pueden determinarse directamente a través de altimetría satelital. En tierra, el geoide debe determinarse por métodos indirectos. La fórmula de Stokes (ec. 2.9) permite calcular la ondulación del geoide en función de las anomalías gravimétricas en superficie en el marco de la aproximación esférica. La anomalía del geoide es inversamente proporcional a la distancia a las masas anómalas, y se ve afectado por variaciones laterales de densidad situadas en un amplio rango de profundidades, desde la frontera núcleo-manto hasta la corteza. En general, no es posible descomponer el campo gravitatorio terrestre en sus diversas fuentes causativas. Sin embargo, estudios globales muestran que las anomalías del geoide con longitudes de onda mayores que 4000 km son producidas por contrastes de densidad situados en niveles sublitosféricos (Bowin, 1983).

2.3 CAMPO TÉRMICO

El calor puede ser transferido de cuatro maneras: conducción, advección, convección y radiación. La conducción de calor implica la transmisión de energía cinética entre átomos o moléculas vecinas. El transporte de calor por advección ocurre debido a movimientos de masa, independientemente del origen de ese movimiento. La convección es una forma particular de advección en la cual el movimiento se debe específicamente a las diferencias de flotabilidad. La radiación implica transporte de calor por radiación electromagnética. La principal

característica de la litosfera, desde un punto de vista térmico, es el predominio de los procesos conductivos sobre los convectivos. En el resto del manto la convección es el principal mecanismo de transporte de calor. Las principales contribuciones a la producción radiogénica de calor provienen del decaimiento radiactivo de los isótopos U^{238}, Th^{232} y K^{40}. La distribución en profundidad de los elementos productores de calor es escasamente conocida, y hay varios modelos propuestos dependiendo de las litologías, edades, o historia tectónica de las rocas. En esta tesis, y por razones de simplicidad, hemos seleccionado dos modelos de distribución de elementos radiogénicos en la corteza: constante y decrecimiento exponencial. Para el manto litosférico, en el contexto de esta tesis, hemos asumido que la producción de calor es despreciable.

El flujo de calor superficial, SHF, es una medida de la energía liberada por la Tierra por unidad de área y por unidad de tiempo. En los océanos, el SHF es aproximadamente inversamente proporcional a la raíz cuadrada de la edad del suelo marino. En los continentes, el valor promedio del SHF es aproximadamente 60 mW/m^2, un valor bajo en comparación con el promedio para los océanos (70-75 mW/m^2). Dos fuentes contribuyen al SHF: la producción radiogénica de calor, fundamentalmente en la corteza, y el flujo de calor basal proveniente de la astenosfera. En los continentes, estas dos contribuciones parecen ser de magnitud comparable, mientras que en los océanos la producción de calor es baja y el SHF está correlacionado con el espesor litosférico.

2.4 ISOSTASIA

Si consideramos un modelo de Tierra plana, la isostasia local implica que una serie de columnas verticales (la litosfera) flota libremente sobre un líquido no viscoso (la astenosfera), de modo que la presión no varíe lateralmente por debajo de un cierto nivel de compensación. La isostasia local es una formulación alternativa del principio de Arquímedes del equilibrio hidrostático. En el contexto de la isostasia local, la elevación es una medida de la flotabilidad de las columnas litosféricas de acuerdo a la ecuación 2.20. La isostasia local es una buena aproximación para largas longitudes de onda topográficas. Sin embargo, para longitudes de onda cortas, parte de la carga puede ser soportada elásticamente por la litosfera.

3. REGIÓN DEL SISTEMA DEL ARCO DE GIBRALTAR: CONTEXTO GEOLÓGICO Y GEOFÍSICO

3.1 MARCO GEOLÓGICO

Al este del punto triple de las Azores y hasta el Banco del Gorringe, el límite entre las placas Euroasiática y Africana en el Atlántico es una falla transformante asísmica bien definida por las anomalías magnéticas y la batimetría. Sin embargo, hacia el este, en la transición Atlántico-Mediterráneo, cambia a un límite de placas transpresivo difuso abarcando una amplia zona de deformación activa (e.g. Meghraoui et al., 1996; Negredo et al., 2002; Jiménez-Munt y Negredo, 2003). La región del sistema del Arco de Gibraltar (GAS) comprende, en un sentido amplio, varias estructuras: el orógeno arqueado Bético-Rifeño, la cuenca interior extensiva de Alborán, las cuencas de antepaís del Guadalquivir y el Rharb, el sistema frontal de acreción del Golfo de Cádiz, y el Atlas (**Fig. 3.1**). Las cadenas de las Béticas y el Rif están formadas por rocas metamórficas de las Zonas Internas, una cobertera de margen pasivo de las Zonas Externas, las unidades Flysch, y las cuencas neógenas de antepaís e intra-montañosas. Las Zonas Internas están formadas por rocas paleozoicas y triásicas apiladas durante la compresión del Terciario, seguida por un evento extensivo iniciado en el Mioceno. Las Zonas Externas se corresponden con las secuencias de los palomárgenes del SO de Iberia y NO del Maghreb. Las unidades Flysch están formadas por turbiditas marinas profundas. La Cuenca de Alborán está caracterizada por una tectónica extensiva limitada por un amplio sistema de fallas extensivas a lo largo del Arco de Gibraltar. El relleno sedimentario es marino y el basamento está constituido por sedimentos paleozoicos continentales que sufrieron metamorfismo durante la orogenia alpina. En su parte central el basamento está formado por rocas volcánicas. El rifting y exhumación progresiva del dominio de Alborán tuvieron lugar desde, al menos, el Mioceno Inferior hasta el Tortoniense Inferior. La topografía y línea de costa toman su forma actual durante el Plio-Pleistoceno. La columna sedimentaria está formada fundamentalmente por pizarras, areniscas y margas de edades comprendidas entre el Aquitaniense-Burdigaliense hasta la actualidad (Torne et al., 2000, y referencias en el interior). La Cuenca del Guadalquivir es la cuenca de antepaís de las Béticas centrales y occidentales. El basamento está compuesto por rocas del Paleozoico y Mesozoico. La cuenca se formó por flexión litosférica debida a

la carga de cabalgamientos y, probablemente, a una carga adicional producida por engrosamiento litosférico. La cuenca está rellena de sedimentos miocenos cubiertos por sedimentos plio-cuaternarios que progradan hacia el oeste. El flanco sur de la cuenca está rellenado por diapiros laterales de evaporitas del Triásico (García-Castellanos et al., 2002, y referencias en el interior). La Cuenca del Rharb es la cuenca de antepaís del Rif. Su basamento se compone de rocas paleozoicas del Hercínico y materiales mesozoicos. Su flanco sur está condicionado por fallas hercínicas que generan horsts y grabens, rellenos con secuencias del Mioceno-Plioceno cubiertas por sedimentos cuaternarios. El sector norte presenta un basamento paleozoico con una cobertera mesozoica flexionada durante el emplazamiento de la carga de cabalgamientos provenientes del Rif (Zohuiri et al., 2001). Las unidades estructurales que forman las Béticas y el Rif tienen su continuación bajo el Golfo de Cádiz. Cabe destacar la presencia de grandes masas alóctonas caracterizadas por reflexiones sísmicas caóticas en el frente del Arco de Gibraltar. Dichas masas caóticas miocenas reciben diferentes nombres: "cuerpo caótico gigante", "unidades alóctonas" o "complejo olistostrómico", y pueden dividirse en dos unidades: una cuña de acreción presente en el talud continental del Golfo de Cádiz formada por la imbricación de sedimentos triásicos del Mioceno superior, y una unidad gravitacional submarina en la llanura abisal de la Herradura (Zeyen et al., 2005; Iribarren et al., 2007, y referencias en el interior). El Atlas es una cadena intra-continental situada en el antepaís del orógeno Rif-Tell en el norte de África, que se extiende más de 2000 km en dirección SO-NE desde Marruecos hasta Argelia y Túnez. Está compuesto por rocas paleozoicas, mesozoicas y cenozoicas plegadas y fracturadas, y tiene picos a más de 4 km de altura. El Atlas es el resultado de la inversión tectónica de una cuenca extensiva mesozoica. Desde el Cenozoico hasta la actualidad, el Atlas ha experimentado compresión asociada con la convergencia hacia el NO de África hacia Europa. El acortamiento, que afecta al basamento pre-mesozoico y a la cobertera mesozoico-cenozoica, es del 15-24 %. Cabe destacar asimismo la presencia de rocas ígneas triásicas y jurasicas, así como de un volcanismo alcalino del Terciario y Cuaternario (Ayarza et al., 2005, y referencias en el interior).

3.2 OBSERVABLES GEOFÍSICOS

Los observables geofísicos son magnitudes que se pueden medir o determinar en la superficie de la Tierra, y que nos proporcionan información de las propiedades del interior del planeta. En esta tesis se han utilizado los

siguientes observables: elevación, anomalía del geoide, anomalías gravimétricas de aire libre y Bouguer, y flujo de calor superficial (SHF).

3.2.1 Elevación

Los datos de elevación provienen de la base global ETOPO2 V9.1 (Smith y Sandwell, 1994; Sandwell y Smith, 1997; Hastings y Dunbar, 1999) (**Fig. 3.2**). La topografía supera localmente los 3000 m y los 2000 m en las Béticas y el Rif, respectivamente, si bien la elevación media es de 1000-1500 m para las Béticas, y de 500-1000 m para el Rif. El Atlas presenta una elevación media de 2000 m, superándose localmente los 4000 m. En la Cuenca de Alborán, la batimetría aumenta distalmente y en dirección este, alcanzándose profundidades de más de 2000 m en la transición a la Cuenca de Argel. En el Océano Atlántico se alcanzan profundidades de más de 4500 m en las llanuras abisales. También cabe destacar la presencia de estructuras contractivas que se elevan 3000-4000 m sobre el suelo marino.

3.2.2 Anomalía del geoide

Los datos de anomalía del geoide provienen del modelo global de armónicos esféricos EGM96 (Lemoine et al., 1998) (**Fig. 3.3**). Las longitudes de onda superiores a 4000 km han sido eliminadas para retener la componente litosférica de la anomalía del geoide. Cabe destacar los valores negativos que afectan al Golfo de Cádiz, Béticas occidentales, Cuenca del Guadalquivir, Rif y Cuenca del Rharb (<-6 m), y el fuerte máximo que se observa en el Atlas (>15 m).

3.2.3 Anomalía de aire libre

En **Fig. 3.4** se muestra un mapa de anomalía de aire libre del GAS. Los datos vienen de la recopilación global de altimetría satelital de Sandwell y Smith (1997). En Marruecos, los datos de Hildenbrand et al., (1988) han sido mallados para encajar con los datos de altimetría. En la Península Ibérica destacan valores positivos en las Béticas internas (>60 mGal), el basamento hercínico al oeste de la Cuenca del Guadalquivir (>80 mGal) y las inmediaciones del Cabo de San Vicente (>100 mGal). La Cuenca del Guadalquivir muestra una anomalía negativa NE-SO (<-60 mGal). En la parte occidental Cuenca de Alborán hay un mínimo de forma arqueada (<-100 mGal) relacionado con la presencia de sedimentos. En África, el Atlas muestra valores positivos (> 140 mGal), mientras que la Cuenca del Rharb se caracteriza por valores negativos (<-100 mGal). En el dominio Atlántico se encuentran los máximos de anomalía del Banco del

Gorringe (>350 mGal) y Coral Patch (>220 mGal), y los mínimos del Banco del Guadalquivir (>120 mGal), Golfo de Cádiz (<-100 mGal) y Oeste del margen norteafricano (<-160 mGal).

3.2.4 Anomalía de Bouguer

La anomalía de Bouguer se obtiene aplicando las correcciones de la lámina de Bouguer (Bullard A), curvatura (Bullard B) y terreno (Bullard C) a la anomalía de aire libre. En esta tesis se ha desarrollado un programa en FORTRAN 90 (FA2BOUG) para calcular la anomalía de Bouguer en mar y en tierra. FA2BOUG calcula las correcciones Bullard A, B y C, y distingue varias zonas de cálculo de acuerdo a la distancia horizontal al punto de cálculo y dependiendo de si el punto está en tierra o mar (**Fig. 3.5**). El programa ha sido aplicado al GAS para obtener un mapa de la anomalía de Bouguer completa de toda la zona de estudio mezclando diferentes datos.

Método

La superficie topográfica/batimétrica se divide en una serie de prismas cuadrados verticales de tope plano centrados en cada punto del modelo digital del terreno (DEM). La altura de los prismas es la elevación. FA2BOUG calcula directamente el efecto de la topografía cuya distancia al punto de cálculo sea inferior al límite de la zona distante, R_d, en lugar de calcular por separado la lámina de Bouguer y la corrección por el terreno. La atracción vertical producida por un prisma vertical de cara superior plana viene dada por la ecuación 3.1. Para la corrección por curvatura se ha utilizado la aproximación de Whitman (1991) (ec. 3.2). FA2BOUG trabaja con diferentes zonas de cálculo que pueden ser definidas por el usuario de acuerdo a la distancia al punto de cálculo: zona distante, intermedia e interna. Para puntos de cálculo en tierra el programa ofrece la posibilidad de trabajar con una zona interna detallada adicional para explotar las ventajas de los DEM más detallados disponibles en áreas continentales. Para determinar el valor óptimo del tamaño de la zona intermedia se realizaron varios cálculos (**Table 3.2**), con el resultado de R_i=20 km.

Cálculo en la zona distante ($R_d > R > R_i$):

El paso de malla en la zona distante es Δx_d (**Table 3.1**). Para calcular la atracción vertical de un prisma rectangular recto evitando inestabilidades numéricas, se utiliza la expresión del desarrollo en armónicos esféricos de su potencial (ec. 3.3 y ec. 3.4).

Cálculo en la zona intermedia (Ri > R > Δxi/2):

El paso de malla en la zona intermedia es Δx_i (**Table 3.1**). Para zonas continentales, FA2BOUG ofrece la posibilidad de añadir una nueva zona intermedia más detallada comprendida entre $\Delta x_i/2 > R > \Delta x_{det}/2$, siendo $\Delta x_{det}(<\Delta x_i)$ el paso de malla de la topografía detallada (**Table 3.1**). La atracción gravitatoria producida por los prismas en ambas zonas intermedias se calcula mediante la ecuación 3.1.

Cálculo en la zona interna (R < Δxi/2 ó Δxdet/2):

La zona interna consiste en un cuadrado centrado en el punto de cálculo, de lado Δx_i ó Δx_{det} dependiendo de si la zona intermedia detallada se utiliza en el cálculo o no. La elevación en cada vértice del cuadrado se interpola linealmente utilizando los tres nodos vecinos más próximos y el punto de cálculo (**Fig. 3.5**). La contribución de la zona interna se calcula en dos pasos: primero se evalúa la atracción vertical de un prisma de tope plano con extensión lateral igual al tamaño de la zona interna y altura igual a la elevación en el punto de cálculo; segundo, se divide la zona interna en cuadrantes con pendiente constante desde su vértice hasta el punto de cálculo, es decir, cuartos de un prisma cónico con su eje vertical pasando por el punto de cálculo (**Fig. 3.6**). La atracción vertical producida por un cuarto de prisma cónico viene dada por la ecuación 3.8. El signo de dicha atracción depende de si la elevación es positiva o negativa en el punto de cálculo y en el vértice de la zona interna (**Fig. 3.7 A1-A4**).

Descripción del programa

FA2BOUG requiere dos ficheros de entrada: elevación y anomalía de aire libre (o anomalía de Bouguer corregida por la lámina solamente). Para zonas continentales puede suministrarse opcionalmente un fichero con la topografía detallada de las zonas rugosas. El programa lee del fichero de entrada *parameters.dat* , la variable *det* que indica si el programa debe esperar un fichero con topografía detallada para áreas continentales (*det*=1), o no (*det*=0), los pasos de malla de las zonas intermedia y distante, Δx_i, Δx_d, el paso de malla para el fichero de anomalía de Bouguer de salida, Δx_{Bg}, las densidades de reducción para la corteza y el agua, ρ_c y ρ_w, respectivamente, el número de nodos de las mallas regulares de entrada, N x M, los límites de las zonas intermedia y distante, R_i, R_d , la variable de texto land, que indica si el cálculo debe hacerse para puntos en tierra y mar (land=*'on'*), o solo para puntos en mar (land=*'off'*), y la variable Boug_slab, que indica si la malla de entrada es Bouguer simple (Boug_slab=1) o anomalía de aire libre (Boug_slab=0). Si la opción de topografía detallada está

activada (*det*=1), el fichero de entrada, *parameters.dat*, debe contener los siguientes campos adicionales: los nodos del fichero de topografía detallada, N_{det} x M_{det}, y su paso de malla, Δx_{det}. Los ficheros ASCII de entrada de elevación y anomalía de aire libre, *topo_cart.xyz* and *gravi_cart.xyz*, deben estar en coordenadas cartesianas y tener un paso de malla Δx_i. Adicionalmente se puede suministrar un fichero de topografía detallada, *topo_cart_det.xyz*, en coordenadas cartesianas y con un paso de malla Δx_{det}. Los ficheros de salida de anomalía de Bouguer completa (*Bouguer.xyz*) y simple (*Bouguer_slab.xyz*) están en coordenadas cartesianas y tienen un paso de malla Δx_{Bg} (**Fig. 3.8**).

Resultados: mapa de anomalía de Bouguer del GAS

Con el objetivo de producir un mapa completo de la anomalía de Bouguer del GAS se han integrado diferentes datos. En la Península Ibérica los datos de anomalía de Bouguer completa provienen del Instituto Geográfico Nacional (Mezcua et al., 1996). En Marruecos, los datos de anomalía de Bouguer simple de Hildenbrand et al. (1988) han sido mallados para ajustar los datos de altimetría antes de aplicarles la corrección por el terreno. En el mar y en el resto de África la anomalía de Bouguer ha sido calculada usando FA2BOUG con los parámetros de entrada listados en **Table 3.1**, y la anomalía de aire libre satelital de la compilación de Sandwell and Smith (1997). El mapa de anomalía de Bouguer resultante se muestra en **Fig. 3.10**. El dominio oceánico Atlántico está caracterizado por valores positivos (240-300 mGal) con un máximo destacado en el Banco del Gorringe (>360 mGal). En el Golfo de Cádiz hay valores positivos de la anomalía comprendidos entre 0 y 200 mGal de este a oeste. En la parte occidental de la Cuenca de Alborán se observa un mínimo de forma arqueada, mientras que en la parte central los valores están entre 40-120 mGal, aumentando gradualmente hacia el este (>160 mGal). En Iberia cabe destacar el mínimo de anomalía bajo las Béticas (<-120 mGal), y los valores positivos en el SO de la Península (>40 mGal). En África, el valor de fondo de la anomalía es, en general, negativo, destacándose la presencia de dos mínimos en el Rif y Cuenca del Rharb por una parte, y en el Atlas por la otra (<-120 mGal).

Discusión

En **Fig. 3.11** se muestra un mapa de la corrección por el terreno (Bullard C) para la zona de estudio. En tierra, las máximas correcciones están presentes en el Atlas (hasta 30 mGal), mientras que el resto de la región las correcciones son <1 mGal. En mar las correcciones están más repartidas y se alcanzan amplitudes de >20 mGal, fundamentalmente en los taludes continentales y accidentes batimétricos. El efecto de la zona distante (topografía más allá de 20 km del

punto de cálculo) resulta en una componente de larga longitud de onda con amplitudes >10 mGal en algunos accidentes topográficos. (**Fig 3.12**). La corrección por curvatura va desde >4 mGal en las llanuras abisales Atlánticas hasta <-4 mGal en las partes más elevadas del Atlas (**Table 3.4**). De la comparación de ETOPO2 con el DEM de alta resolución SRTM como entradas de topografía al programa, se concluye que el uso de DEMs de baja resolución tiende a subestimar la corrección por el terreno, siendo este desajuste mayor cuanto más elevada sea la corrección por el terreno. Así, la precisión de la corrección topográfica es fuertemente dependiente de la resolución del DEM usado, al menos para zonas de topografía muy irregular (**Fig. 3.13**).

3.2.4 Flujo de calor superficial (SHF)

Los datos de SHF utilizados en esta tesis provienen de: Fernàndez et al., (1998) en la Península Ibérica, Polyak et al., (1996) en la Cuenca de Alborán, Verzhbitsky y Zolotarev (1989) en el Atlántico, cerca del Banco del Gorringe, y Rimi et al., (1998) en Marruecos. En **Fig 3.14** se muestra un mapa con la localización de las medidas disponibles. En la parte norte del Golfo de Cádiz y la Cuenca del Rharb los datos presentan una gran dispersión debido a la circulación de fluidos, con un valor promedio de 70 mW/m^2. Los valores decrecen a 40-50 mW/m^2 en las partes central y meridional del Golfo de Cádiz. En el Alto Atlas las pocas mediciones están en torno a 60 mW/m^2. El Rif se caracteriza por valores comprendidos entre 50 y 90 mW/m^2. Los valores más altos de flujo de calor de la zona de estudio se encuentran en la parte oriental de la Cuenca de Alborán (100-120 mW/m^2). En el SO de Iberia un máximo de 80 mW/m^2 centrado en la faja pirítica es la característica mejor definida.

4. INVERSIÓN CONJUNTA DE ELEVACIÓN Y GEOIDE: APROXIMACIÓN 1D

4.1 INTRODUCCIÓN

En este capítulo se presenta un método sencillo para determinar automáticamente en 1D el grosor de la corteza y la litosfera utilizando elevación y anomalía del geoide, acopladas con la temperatura, bajo condiciones de equilibrio térmico e isostasia local. En esta aproximación se considera un modelo de cuatro capas compuesto por corteza, manto litosférico, agua (ρ_w =1030 kg/m^3) y astenosfera (**Fig. 2.1**). Para la densidad de la corteza se asume un gradiente vertical positivo lineal para simular el incremento usual de la densidad debido a la presión y a cambios mineralógicos. En el caso del manto litosférico se utiliza una densidad dependiente de la temperatura, lo que resulta en un gradiente lineal negativo.

4.2 MÉTODO

Si la isostasia local se cumple y la longitud de onda de las variaciones laterales de densidad es grande en comparación a su profundidad, entonces la anomalía del geoide, para un modelo de Tierra plana, es proporcional al momento dipolar de la distribución vertical de masas anómalas (ec. 4.1). La profundidad de la base de la corteza, z_c, y de la litosfera, z_L, se relaciona con la elevación bajo isostasia local según la ecuación 4.2. Para la densidad del manto litosférico se considera una dependencia lineal con la temperatura a través del coeficiente lineal de expansión térmica (ec. 4.3). La geoterma estacionaria para la corteza asumiendo temperatura y flujo de calor fijos en la superficie y en la base de la corteza, respectivamente, viene dada por la ecuación 4.4. La temperatura en el Moho puede expresarse en función de los grosores cortical y litosférico, la elevación y otros parámetros térmicos (ec. 4.8). La densidad media del manto litosférico, resultante de la integración de la ecuación 4.3, depende linealmente de la temperatura en el Moho (ec. 4.9). La formulación generalizada de la isostasia incorporando el campo de temperaturas, expresada por la ecuación 4.10, se obtiene combinando las ecuaciones 4.9 y 4.8 con la 4.2. La anomalía del geoide para nuestro modelo de litosfera con cuatro capas, en el cual la densidad de la corteza varía linealmente con la profundidad, y la densidad del manto litosférico es dependiente de la temperatura, viene expresada por la ecuación 4.11. La resolución conjunta de las ecuaciones 4.10 y 4.11, fijando los parámetros de la

densidad de la corteza, nos permite determinar la densidad promedio del manto litosférico (a través de la temperatura en el Moho) y las profundidades de la base de la corteza y la litosfera que ajustan simultáneamente la elevación y la anomalía del geoide bajo isostasia local. Para resolver el sistema de ecuaciones formado por ec. 4.10 y ec. 4.11 se adopta el siguiente esquema iterativo:

1) Estimar los valores iniciales de z_c y z_L asumiendo densidades constantes para la corteza y el manto litosférico (Appendix A).

2) Usar el valor inicial de z_c para calcular la profundidad de la base de la litosfera que satisface la ecuación de isostasia local acoplada con el campo térmico (ec. 4.10).

3) Calcular la temperatura en el Moho como función de z_c y z_L de los pasos anteriores usando la ecuación 4.8.

4) Calcular la anomalía del geoide con la ec. 4.11 usando las variables litosféricas z_c, z_L y temperatura en el Moho determinadas en los pasos anteriores.

5) Restar la anomalía del geoide calculada de la medida para obtener una anomalía del geoide residual. Dependiendo del signo del residuo, el valor inicial de z_c es incrementado o disminuido, y se repiten los pasos del 2) al 5) hasta que la anomalía del geoide residual sea tan pequeña como se desee.

4.3 SENSIBILIDAD DEL MÉTODO

Para realizar un análisis de la sensibilidad del algoritmo presentado se introducen los diagramas elevación-geoide (E-N): superficies que representan en los ejes de elevación y geoide las variables litosféricas calculadas (las profundidades del Moho y el LAB). Se han considerado dos modelos de producción de calor en la corteza: constante y exponencial decreciente (**Table 4.1**). Un parámetro clave en la metodología presentada es el nivel de referencia considerado para el geoide, que depende de la configuración de la columna litosférica de referencia empleada. A su vez, el rango de soluciones con sentido físico en el espacio E-N depende de la columna litosférica de referencia escogida. Dos condiciones deben cumplirse: a) la existencia de la capa del manto litosférico, es decir $z_L>z_c$, y b) la existencia de la capa de la corteza, es decir $|E|<z_c$ if $E<0$ (Appendix A).

Las principales conclusiones que pueden extraerse de los diagramas E-N presentados en **Figs. 4.1 y 4.2** son: i) un incremento en la elevación, manteniendo la anomalía del geoide constante, implica una corteza y litosfera gruesas, y

viceversa; ii) el espesor cortical afecta fundamentalmente a la elevación, especialmente para E>0, mientras que el espesor del manto litosférico tiene una fuerte influencia en la anomalía del geoide, particularmente para E<0; iii) las diferencias en la densidad media del manto litosférico entre los modelos de producción de calor constante y exponencial decreciente, son importantes para E>0. En **Fig. 4.2** se muestran diagramas E-N de la variación inducida (incertidumbre) en z_c y z_L por el error RMS típico de los datos de elevación y anomalía del geoide. Para la corteza, en E>0 la incertidumbre está comprendida entre (0.5-2) km, estando los valores más altos restringidos a las zonas de elevada N. Para E<0 las incertidumbres en z_c van de 2 km a 4 km. La incertidumbre en el espesor litosférico para E>0 es <10 km en casi todas partes excepto para valores de N elevados. Para E<0 la incertidumbre está entre 6 y 15 km, excepto para N elevada.

El nivel de referencia del geoide, N_0, depende de la columna de referencia. En general, cuanto más gruesa sea la litosfera de la columna de referencia considerada, mayores serán los espesores corticales y litosféricos obtenidos. Si se varía ±1 km el grosor cortical de la columna de referencia (lo cual implica una variación de ±9 km debido a la isostasia local), N_0 cambia aproximadamente ±1.5 m. Este cambio en N_0 produce cambios en los grosores de corteza y litosfera calculados <1.5 km en la corteza, y < 15 km en la litosfera (**Fig. 4.3**). Con respecto a la variación en los parámetros térmicos dentro de rangos físicamente razonables, z_L disminuye de forma aproximadamente lineal para valores crecientes del coeficiente de expansión térmica, y decrecientes de la producción radiogénica de calor. La profundidad del Moho varía <1 km debido a la variación de los parámetros térmicos, mientras que la conductividad térmica asumida para el manto no afecta significativamente ni z_c ni z_L.

4.4 RESULTADOS DE LA MODELIZACIÓN

El método presentado de inversión de elevación y geoide ha sido aplicado al GAS con los parámetros listados en **Table 4.1**.

4.4.1 Corteza

La profundidad del Moho calculado a partir de los datos de elevación y anomalía del geoide se muestran en **Fig. 4.5 A**. La profundidad del Moho es <16 km en la parte más oriental de la Cuenca de Alborán, hacia la Cuenca de Argelia. En la parte central de Alborán el Moho se mantiene relativamente constante a una profundidad de 20-18 km, mientras que cerca del Estrecho de Gibraltar la

profundidad es de unos 32 km. Bajo las Béticas el grosor cortical es 34-36 km, reduciéndose abruptamente al sur, hacia la Cuenca de Alborán. En el SO de la Península Ibérica es de 28-30 km. En el norte de África, el Rif y el Atlas presentan una corteza gruesa, con profundidades del Moho >36 km y >38 km, respectivamente. En el dominio Atlántico, la profundidad del Moho es 12-16 km en las llanuras abisales y 26-32 km en la región del Golfo de Cádiz. Los resultados obtenidos son consistentes con los trabajos previamente realizados, con algunas diferencias en las partes central y oriental de la Cuenca de Alborán, al NO del margen marroquí y en la parte central del Golfo de Cádiz.

4.4.2 Manto litosférico

Los resultados obtenidos para el grosor de la litosfera se muestran en **Fig. 4.5 B**. Cabe destacar la orientación NE-SO de las estructuras litosféricas obtenidas, dibujándose dos zonas alargadas con una litosfera relativamente adelgazada separadas por una región de litosfera gruesa. El adelgazamiento afecta al SO de Iberia (~95 km), el Atlas y la parte oriental de la Cuenca de Alborán (80-90 km). La zona de litosfera gruesa se encuentra bajo el Golfo de Cádiz y la Cuenca del Rharb (>160 km). Este engrosamiento prosigue en dirección NE-SO, afectando a las Béticas occidentales y el NO del margen Atlántico marroquí (130-140 km). Hacia el cratón africano, la litosfera se engruesa progresivamente hasta alcanzar espesores >180 km. Los resultados obtenidos son consistentes con los trabajos anteriores, excepto en la Cuenca de Alborán, donde otros estudios encuentran una litosfera unos 35 km más delgada que la presentada en **Fig. 4.5 B**.

4.5 DISCUSIÓN

4.5.1 Hipótesis y discrepancias con modelos previos

El método presentado en éste capítulo se basa en tres hipótesis principales: i) régimen térmico estacionario; 2) isostasia local; 3) dos capas con gradientes verticales lineales de densidad, y dos capas con densidades constantes (agua y astenosfera). La modelización asumiendo estado estacionario tiende a sobreestimar el grosor litosférico en zonas recientemente adelgazadas y a subestimarlo en zonas engrosadas. Así pues, las variaciones de espesor litosférico obtenidas deben considerarse como una cota inferior. Las variaciones introducidas por considerar el gradiente lineal de densidad en la corteza y el campo térmico, con respecto a asumir densidades constantes en corteza (2780 kg/m^3) y manto (3245 kg/m^3) (Fullea et al., 2006) son: para la corteza, incremento de z_c del 10-40 % para E<0 e incremento moderado o incluso

disminución (-5% a 10%) para E<0; para el manto litosférico las variaciones son < ±5%.

En la parte oriental de la Cuenca de Alborán los grosores cortical y litosférico obtenidos exceden considerablemente los valores propuestos por resultados previos (Hatzfeld, 1976; Hatzfeld, 1978; Torne y Banda, 1992; Polyak et al., 1996; Fernàndez et al., 1998b; Torne et al., 2000). Para las partes central y oriental de la Cuenca de Alborán se ha considerado un modelo alternativo compuesto de tres capas: Corteza de densidad 2680 kg/m^3, un manto litosférico anómalo entre 18 y 30 km de profundidad de 3200 kg/m^3 y un manto litosférico estándar de 3300 kg/m^3 (**Fig. 4.6**). La presencia de esta capa sub-cortical de baja densidad reduce la profundidad de la base de la litosfera a unos 65 km. Una de las limitaciones del método presentado es que considera una sola capa para la corteza, de manera que, por ejemplo, la presencia de importantes acumulaciones sedimentarias en el Golfo de Cádiz, donde la corteza obtenida es más gruesa que la observada por la sísmica (González-Fernández et al., 2001), no se ve reflejada.

4.5.2 Comparación con la tomografía sísmica

Teniendo en cuenta las hipótesis hechas, la estructura litosférica obtenida refleja los cambios laterales más importantes en corteza y litosfera. Los resultados obtenidos sugieren que tanto la corteza como la litosfera se engruesan bajo el Estrecho de Gibraltar, las Béticas y el Rif, lo cual es consistente con la tomografía sísmica (Blanco y Spakman, 1993; Bijwaard y Spakman, 2000; Calvert et al., 2000; Spakman y Wortel, 2004). El adelgazamiento litosférco bajo el Atlas y la Cuenca de Alborán también se aprecia en la tomografía como una capa de baja velocidad situada aproximadamente entre 40 y 100 km de profundidad (Blanco y Spakman, 1991; Seber et al., 1996b; Calvert et al, 2000; Gurría y Mezcua et al., 2000). De acuerdo a nuestros resultados, sin embargo, el engrosamiento litosférico afecta también a la Cuenca del Rharb, al Golfo de Cádiz y, en menor medida, al NO del margen marroquí. Este resultado es particularmente interesante debido a la limitada resolución de los modelos tomográficos en el Golfo de Cádiz y al NO del margen marroquí, dada la distribución inconveniente de estaciones y eventos.

5. MODELIZACIÓN NUMÉRICA 3D DE LA LITOSFERA: GEO3Dmod

5.1 INTRODUCCIÓN

En este capítulo se presenta un programa de ordenador que permite modelizar interactivamente, en 3D, la litosfera, integrando SHF, elevación, anomalías gravimétricas y ondulación del geoide. El programa consiste en dos módulos: el primero, GEO3Dmod, que resuelve el problema directo, y el segundo, GEO3Dmod_INTF, que permite la modificación interactiva de la estructura litosférica de acuerdo a los resultados arrojados por el primer módulo (**Fig. 5.1**).

5.2 GEO3Dmod

Este módulo es un algoritmo que permite realizar una modelización directa 3D, calculando las distribuciones de temperatura, presión y densidad, la elevación (asumiendo isostasia local), el geoide, las anomalías de aire libre y Bouguer, y el SHF, para un modelo litosférico dado. GEO3Dmod permite trabajar con varias capas (cuerpos) con diferentes propiedades físicas: densidad, coeficiente de expansión térmica, coeficiente de presión, producción de calor y conductividad térmica. Cada cuerpo está definido entre dos superficies límite sucesivas, cada una de las cuales está definida en todo el espacio del modelo.

5.2.1 Campo de temperaturas

GEO3Dmod usa un esquema de diferencias finitas (FD) para resolver la ecuación térmica 3D en estado estacionario en un volumen rectangular que representa a la litosfera con las siguiente condiciones de contorno: temperatura fija en la parte superior (T_s) e inferior (T_a) de la litosfera, y flujo de calor horizontal nulo en las fronteras verticales del modelo (ec. 5.1). Para el esquema de diferencias finitas, el modelo se discretiza en una malla 3D con N_x, N_y y N_z nodos en los ejes X, Y y Z, respectivamente. Los pasos de malla son Δx, Δy y Δz (**Fig. 5.3**). Para resolver el sistema lineal de ecuaciones se ha seleccionado un esquema iterativo de mínimos cuadrados.

5.2.2 Presión, densidad y elevación

Una vez que las temperaturas en el modelo son conocidas, GEO3Dmod calcula la presión y las densidades del modelo de acuerdo a las ecuaciones 5.8, 5.12 y 5.13.

5.2.3 Anomalías de gravedad y del geoide

Una vez que la distribución de densidades en conocida, GEO3Dmod calcula las anomalías de gravedad y del geoide. El programa considera una serie de prismas rectos rectangulares de techo plano centrados en los nodos de la malla de diferencias finitas. Cada columna litosférica se descompone en una serie de prismas verticales de acuerdo al número de capas existentes en dicha columna (**Fig. 5.4**). Las anomalías de gravedad y del geoide en cada punto de la superficie del modelo se calculan agregando el efecto de cada prima individual de acuerdo a las ecuaciones 5.14 y 5.15. Para evitar efectos de borde, los prismas situados en los límites del modelo son extendidos 10^6 km. Para la gravedad, el promedio de las anomalías calculadas se ajusta al promedio de los datos, ya que se trata de anomalías relativas. En el caso de la anomalía del geoide, pequeñas perturbaciones de la isostasia local en los bordes pueden dar lugar a una componente regional de larga longitud de onda. Así, es necesario eliminar una componente regional restando el plano que mejor ajusta (en el sentido de mínimos cuadrados) el geoide calculado.

5.2.4 Descripción del programa

En **Fig. 5.5** se muestra un esquema general de la estructura de ficheros y directorios utilizados por GEO3Dmod. GEO3Dmod realiza sus cálculos usando un sistema de coordenadas cartesiano con el origen situado en la esquina sudeste del modelo. El programa lee del fichero de entrada *GEO3Dmod.info* las dimensiones horizontales del modelo, L_x(km), L_y(km), la topografía máxima, E_{max}(km), el número de nodos en los ejes X, Y y Z, N_x, N_y, N_z, el paso de malla vertical, Δz(km), la variable *topo*, que indica si el programa debe usar como entrada la topografía filtrada (*topo*=0) o sin filtrar (*topo*=1), la variable *temp_calc*, que indica si se desea realizar el cálculo térmico (*temp_calc*=1) o no (*temp_calc*=0), y las temperaturas fijadas en la parte superior, T_s, e inferior de la litosfera, T_a, (**Table 5.1**). GEO3Dmod lee el número de capas definidas y sus propiedades en el fichero *layers.info* (**Fig. 5.5 panel superior**). En **Fig. 5.6** se muestra un fichero de ejemplo. Cada cuerpo definido en *layers.info* debe tener asociado un fichero ASCII en el directorio **layers_xy**, llamado *layer*i*.xyz*, donde i es el número de capa definido en *layers.info*. El fichero *layer*i*.xyz* representa la

interfaz entre los cuerpos i e i+1 (**Fig. 5.7**). El programa también requiere los ficheros de entrada: *geoid_obs.xyz*, *FA_obs.xyz*, *Boug_obs.xyz*. Los ficheros de salida, *elev_calc.xyz, geoid.xyz, FA.xyz, Boug.xyz, T_moho.xyz, HF.xyz, dens.xyz, pres.xyz* y *T.xyz*, se escriben en el directorio **OUT_xyz**.

5.3 GEO3Dmod_INTF

GEO3Dmod_INTF es una interfaz gráfica que permite visualizar y modificar interactivamente los resultados de la modelización directa llevada a cabo por GEO3Dmod. Los cambios en la geometría litosférica se llevan a cabo modificando las superficies que definen las capas en secciones verticales sucesivas. El programa interpola linealmente a lo largo y a través de los perfiles para reconstruir las superficies de las capas modificadas.

5.3.1 Funciones principales de GEO3Dmod_INTF

Las opciones de GEO3Dmod_INTF se pueden clasificar en tres grupos: visualización, modificación y datos adicionales. La pantalla principal del programa está dividida en dos partes: a la derecha se muestra un mapa topográfico de la zona de estudio; a la izquierda se muestra el número de capas definidas así como un menú con las diferentes opciones disponibles (**Fig. 5.8**).

Opciones de visualización

El programa ofrece dos posibilidades para visualizar la geometría 3D del modelo litosférico: secciones 2D verticales y mapas en planta. La opción *EXTRACT PROFILE (p)* permite extraer secciones 2D de la estructura litosférica y los observables geofísicos calculados, seleccionando los extremos del perfil mediante el ratón (**Fig. 5.9**). También es posible realizar un cálculo 2D de las anomalías del geoide, aire libre y Bouguer, y 1D de la elevación por medio de la opción *CROSS SECTION (k)* (**Fig. 5.10**). La opción *BODY PLOT* permite obtener un mapa en planta del espesor de las capas tanto por pantalla (*b*) como en un fichero post script (*s*) (**Fig. 5.11**). El mapa en planta de la pantalla principal (topografía, inicialmente) puede cambiarse por cualquiera de los diferentes observables geofísicos usando la opción *CHANGE OBS (c)* (**Fig. 5.12**).

Opciones de modificación

La geometría litosférica se cambia modificando las capas que definen las fronteras de las diferentes capas en perfiles verticales sucesivos. Esto se hace mediante la opción *MODIFY REGION (m)* (**Fig. 5.14**). GEO3Dmod_INTF realiza una interpolación lineal a lo largo de cada perfil modificado y,

posteriormente, otra interpolación lineal (perpendicular) entre los perfiles modificados. El usuario trabaja con datos 2D, mientras que el programa realiza la interpolación de la estructura 3D final. La opción *ADD NEW LAYER (a)* permite al usuario introducir una nueva capa dentro del modelo preexistente (**Fig. 5.15**). La opción *JOIN TWO LAYERS (j)* permite unir dos superficies consecutivas, y puede ser usada para eliminar una capa, o partes de una capa. La opción *LAYER HIERARCHY (h)* comprueba (y corrige si es necesario) que el orden entre dos superficies sucesivas sea el correcto. La opción *SMOOTH LAY (i)* permite suavizar una superficie seleccionada.

Opciones de datos adicionales

La opción *LABELS (l)* permite al usuario introducir etiquetas (es decir, texto localizado en un punto caracterizado por su longitud, latitud y profundidad) que describan información geofísica previa. Las etiquetas se escriben en el fichero *labels.dat* (**Fig. 5.16**)**.** La opción *REFERENCE POINTS (r)* permite definir interactivamente unos polígonos o áreas de referencia que pueden usarse para marcar las estructuras que se quieren modificar. Las intersecciones entre los perfiles verticales y las áreas de referencia son proyectadas sobre los perfiles verticales usados en la opción *MODIFY REGION* (**Fig. 5.17**). La información referente a los puntos de referencia se almacena en los ficheros: *ref_points.info* y *ref_points.dat*.

5.3.2 Descripción del programa

En **Fig. 5.5** se muestra un esquema general de los ficheros y archivos utilizados por GEO3Dmod_INTF. El programa lee del fichero de entrada *info.dat* las coordenadas de la zona de estudio, *lon_min, lon_max, lat_min, lat_max*, y el paso de malla en grados decimales, *p_m*. También son necesarios los ficheros de elevación, *elev.xyz*, y línea de costa, *coast_prev.xy*. Opcionalmente el programa puede leer los ficheros *labels.dat, ref_points.info* y *ref_points.dat* (**Fig. 5.5 panel inferior**). Los ficheros con los observables geofísicos, si están presentes, deben estar en el directorio **GEO_DATA**. GEO3Dmod_INTF lee el número de capas y sus propiedades en el mismo fichero que el módulo de la modelización directa: *layers.info*. Cada capa definido en dicho fichero debe tener asociado un fichero ASCII en el directorio **layers** llamado *layer*i*.xyz*, donde i es el número que identifica a la capa en el fichero *layers.info* (**Fig. 5.5 panel inferior**).

5.4 MODELOS SINTÉTICOS: CÁLCULOS 1D, 2D Y 3D

En la aproximación 1D se asume que las estructuras litosféricas se extienden de manera infinita horizontalmente. Un caso típico de aproximación 1D es la isostasia local (ecs. 2.7 y 5.13). En el caso de la gravimetría, la aproximación 1D implica que el efecto de las anomalías de masa solo depende de su grosor y contraste de densidad. Para la anomalía del geoide, la aproximación 1D viene dada por las ecuaciones. 4.1 y 4.11. La aproximación 2D asume que los cuerpos geológicos se extienden infinitamente a lo largo de la dirección perpendicular a la sección modelizada. Dicha aproximación es razonablemente válida si las estructuras geológicas son más de cinco veces más grandes en dirección perpendicular al perfil modelizado que a lo largo del propio perfil. En otro caso, la aproximación 3D debe usarse. Para comprobar los resultados del programa, se han utilizado diferentes modelos sintéticos de cuatro capas: corteza, manto litosférico, agua y astenosfera (**Table 5.2 y Table 5.3**).

5.4.1 Comparación entre las aproximaciones 3D y 1D

Una condición que debe satisfacerse es recuperar el valor 1D para longitudes de onda topográficas suficientemente grandes. En **Fig. 5.19** se muestra el cociente entre la anomalía del geoide 3D y 1D como función de la longitud de onda de la topografía para dos modelos sintéticos. La longitud de onda necesaria para alcanzar el 90 % del valor 1D es de aproximadamente diez veces la longitud del dipolo de masa. En **Fig. 5.20** se muestra la anomalía de aire libre para dos modelos sintéticos en función de la longitud de onda de la topografía. Para las longitudes de onda cortas el efecto de la topografía predomina sobre el contraste más profundo de densidad corteza-manto. Para longitudes de onda suficientemente grandes la anomalía tiende a cero. Con el objeto de ilustrar el contraste entre las aproximaciones 3D y 1D, se han calculado en 3D los observables geofísicos asociados al modelo litosférico obtenido mediante inversión 1D de elevación y anomalía del geoide presentado en el capítulo 4 (**Fig. 4.5 A y B**). En **Fig. 5.21** se muestran las diferencias entre los observables geofísicos calculados y medidos. La elevación calculada es, en general, consistente con la medida, particularmente en zonas de gradiente suave, donde las temperaturas en las aproximaciones 1D y 3D son similares (**Fig. 5.21 D**). Los residuales de las anomalías gravimétricas presentan un mayor contenido en altas frecuencias en comparación con la anomalía del geoide. Los residuales positivos (excesos de masa) de aire libre, Bouguer y anomalía del geoide están presentes en áreas donde el modelo 1D predice una litosfera gruesa, y viceversa (**Fig. 5.21 A-**

C), lo cual nos indica que las variaciones laterales obtenidas en el modelo 1D invirtiendo elevación y anomalía del geoide están subestimadas.

5.4.2 Comparación entre las aproximaciones 3D y 2D

En la aproximación 2D se asume que los cuerpos geológicos se extienden infinitamente en dirección perpendicular al perfil modelizado. Para un bloque isométrico de topografía, las diferencias entre los cálculos 2D y 3D son notables si la longitud de onda de la topografía es de 100 km (**Fig. 5.22 A**), reduciéndose considerablemente si la longitud de onda se aumenta a 600 km (**Fig. 5.22 B**). Para el bloque de topografía con longitudes de onda de 1000 km y 100 km en los ejes x e y, respectivamente (**Fig. 5.23**), la aproximación 2D es válida cuando se corta la estructura a lo largo de su dimensión más corta (eje y) (**Fig. 5.23 A y C**), siendo las diferencias 2D-3D obvias a lo largo del eje x (**Fig. 5.23 B y D**).

5.4.3 Campo térmico. Litosfera sobre/sub-compensada

En todos los modelos sintéticos anteriores la densidad del manto litosférico se asumía constante, pero, en general una densidad dependiente de la temperatura representa una mejor aproximación a la realidad. En este apartado se consideran modelos sintéticos con densidad dependiente de la temperatura en el manto (**Table 5.3**) y longitud de onda suficientemente grande como para evitar las diferencias 2D-3D (**Fig. 5.24**). El modelo de producción de calor utilizado (constante o exponencialmente decreciente) afecta a la temperatura a niveles corticales fundamentalmente, siendo los cambios en las anomalías de aire libre y Bouguer poco significativas. La anomalía del geoide es ~1.5 m más baja para el modelo de producción de calor decreciente exponencialmente con respecto al constante (**Fig. 5.24 A y B**). Si el contraste de densidad litosfera-astenosfera se incluye en el balance isostático, el Moho cambia ±4 km con respecto a los modelos con LAB plano (**Table 5.3**). Para el modelo de topografía sobre-compensada (engrosamiento litosférico), la temperatura en el Moho y el SHF se ven poco afectados con respecto al modelo con LAB plano, mientras que para el modelo sub-compensado ambas variables térmicas se ven notablemente incrementadas (**5.24 C y D**). En el modelo que representa un engrosamiento litosférico, las anomalías de aire libre, Bouguer y geoide disminuyen en comparación con el modelo con LAB plano (**Fig. 5.24 C**). Por el contrario, en el caso del modelo que reproduce un adelgazamiento litosférico, las anomalías aumentan de valor, si bien el cambio es menor que en el caso de engrosamiento litosférico debido a la mayor influencia del contraste de densidad corteza-manto con respecto al contraste litosfera-astenosfera (**Fig. 5.24 D**).

6. APLICACIÓN DE GEO3DMOD AL SISTEMA DEL ARCO DE GIBRALTAR

6.1 INTRODUCCIÓN

En este capítulo se aplica el programa de modelización GEO3Dmod a la región del Sistema del Arco de Gibraltar (GAS) con el objectivo de obtener un modelo litosférico 3D regional, integrando gravedad, geoide, elevación y flujo de calor superficial.

6.2 DESCRIPCIÓN DEL MODELO 3D

Para modelizar el GAS se han utilizado ocho cuerpos diferentes, de acuerdo a su densidad, conductividad térmica, producción de calor y coeficiente de expansión térmica (**Table 6.1**).

6.2.1 Sedimentos

Se han utilizado tres tipos de sedimentos: sedimentos neogeno-cuaternarios en la Cuenca de Alborán (NQSA) (**Fig. 6.1**); capa de sedimentos poco consolidados (2200 kg/m^3) en el dominio oceánico Atlántico y las cuencas del Rharb y el Guadalquivir (US) (**Fig. 6.2**); cuña de acreción en el Golfo de Cádiz formada por la imbricación de sedimentos del Triásico al Mioceno superior, incluyendo asimismo sedimentos de otras edades con densidades similares (AWS) (**Fig. 6.3**).

6.2.2 Corteza

En la mayor parte del modelo la corteza está dividida en dos capas: una corteza media-superior (UMC) de densidad promedio 2700 kg/m^3, y una corteza inferior (LC) de densidad promedio 2920 kg/m^3. En algunas áreas se ha utilizado una corteza con propiedades intermedias entre la corteza media-superior e inferior (IC), que puede sustituir a la corteza media-superior o funcionar como una corteza transicional (**Figs. 6.4, 6.5 y 6.7**). También se ha considerado la presencia de cuerpos mantélicos intracorticales en dos pequeñas áreas en las Béticas y el Rif (**Fig. 6.6**)

6.2.2 Manto litosférico

Para el manto litosférico se ha considerado una densidad dependiente de la temperatura (**Fig. 6.8**).

6.3 RESULTADOS DE LA MODELIZACIÓN

En **Fig. 6.9** se muestran los valores residuales de los observables geofísicos para el modelo 3D. Dicho modelo es el preferido después de varios ajustes en un proceso de error y ensayo. Las características principales de los observables geofísicos se reproducen adecuadamente, exceptuando el valor calculado de la anomalía del geoide en la Cuenca de Alborán, que es 1-3.5 m más alto que el valor observado (**Fig. 6.9 A**).

6.3.1 Perfiles litosféricos

Para mostrar mejor la estructura obtenida se han seleccionado ciertos perfiles litosféricos, algunos de ellos coincidentes con modelos 2D previos (**Fig. 6.10**). El perfil P1 va dirección E-O, empieza en el dominio oceánico Atlántico, cruza el Golfo de Cádiz, el Estrecho de Gibraltar, la Cuenca de Alborán, y termina en la transición a la Cuenca de Argelia (**Fig. 6.10**). En la corteza cabe destacar la presencia de una importante acumulación de sedimentos no consolidados (~2 km) y pertenecientes a la cuña de acreción formada por la imbricación de sedimentos del Triásico al Mioceno superior (~8 km) bajo el Golfo de Cádiz. La corteza inferior desaparece en la parte central de la Cuenca de Alborán, dando lugar a una corteza continental adelgazada cubierta por sedimentos neógenos y cuaternarios. Hacia el este, la corteza se adelgaza aun más (<12 km) dando lugar a una corteza transicional o continental oceanificada. La litosfera tiene un espesor normal en el dominio oceánico Atlántico (100-110 km), engrosándose fuertemente bajo el Estrecho de Gibraltar (~200 km). En las partes central y oriental de la Cuenca de Alborán la litosfera se adelgaza abruptamente alcanzándose valores de <50 km de profundidad del LAB (**Fig. 6.11 A**). Los perfiles P2, P3 y P4 parten del dominio Atlántico y atraviesan en dirección NO-SE el margen continental marroquí. El P2 empieza en el Golfo de Cádiz y cruza la parte norte del Alto Atlas cerca del contacto con el Medio Atlas, siendo paralelo al Perfil II de Teixell et al. (2005). El P3 cruza la parte central del Alto Atlas, el Anti Atlas, y es coincidente con el perfil 3 en Missenard et al. (2006), y similar al perfil 1 en Teixell et al. (2005). El P4 cruza la terminación occidental de la parte central del Alto Atlas, el Anti Atlas, y coincide con el perfil 2 en Missenard et al. (2006). Los perfiles P2, P3 y P4 finalizan al NO del Sahara (**Fig. 6.10**). La corteza pasa de unos 15 km en el dominio Atlántico a unos 28 km en la Meseta. A lo largo de la parte central del Alto Atlas la profundidad del Moho varía entre 34-36 km en sus partes occidental y media, hasta 38-40 km (**Figs. 6.11 C y D**) en la transición al Medio Atlas (**Fig. 6.11 B**). La litosfera es relativamente

gruesa al NO del margen Atlántico marroquí (150-160 km), adelgazándose bajo la parte central del Alto Atlas (90-80 km) y Anti Atlas (<70 km) y engrosándose de nuevo en el NO del Sahara (160-220 km) (**Figs. 6.11 B, C y D**). El perfil P5 corre paralelo a la transecta de Zeyen et al. (2005), es decir, NNO-SSE, empezando en el SO del Macizo Ibérico, cruzando el Golfo de Cádiz, el antepaís del Rif, el Medio y Alto Atlas, y finalizando en el cratón del Sahara (**Fig 6.10**). La profundidad del Moho es de unos 32 km en el SO de Iberia, 32-34 km bajo la Cuenca del Rharb, aumentando a > 36 km en el contacto entre el Medio y el Alto Atlas. El LAB se sitúa a >210 km bajo la parte oriental del Golfo de Cádiz, Cuenca del Rharb y Rif, adelgazándose a <90 km en el Medio Atlas (**Fig. 6.11 E**). El perfil P6 va en dirección NNO-SSE partiendo del Macizo Ibérico, cruzando las Béticas, la parte central de la Cuenca de Alborán, la parte oriental del Alto Atlas y finalizando en el cratón del Sahara (**Fig. 6.10**). La profundidad del Moho es >34 km bajo las Béticas, adelgazándose hasta 16-18 km en la parte central de la Cuenca de Alborán, donde la corteza inferior está ausente. En el continente africano la corteza tiene un grosor de 35-40 km, con >36 km bajo la parte oriental del Alto Atlas. La profundidad del LAB presenta valores normales en el Macizo Ibérico (100 km), se engruesa hasta >170 km bajo las Béticas y se adelgaza hasta 70 km en la parte central de la Cuenca de Alborán. Hacie el SE, en el cratón del Sahara, se alcanzan valores de hasta 230 km de profundidad (**Fig. 6.11 F**).

De acuerdo al modelo 3D, todo el Atlas parece estar afectado por un adelgazamiento litosférico, siendo éste más intenso en el Anti y Medio Atlas. La rama oriental del Atlas no parece estar particularmente adelgazada. Los mayores gradientes litosféricos se hallan en los contactos entre el Macizo Ibérico y las Béticas al norte, entre el Medio Atlas y el dominio externo del Rif al sur, y entre el orógeno Betico-Rifeño y la Cuenca de Alborán al este (**Fig. 6.12**).

6.2.2 Temperatura en el Moho y flujo de calor superficial

En **Fig. 6.13 A** se muestra un mapa de la temperatura en la Moho calculada para el modelo 3D. Las áreas continentales de Iberia y África presentan temperaturas > 480 ºC. En las zonas marinas la temperatura es más baja: <200 ºC en la corteza oceánica de las llanuras abisales Atlánticas, y <340 °C en la corteza continental adelgazada de la Cuenca de Alborán. En África, las temperaturas son altas en la parte central del Alto Atlas (760-830 ºC), Medio Atlas (690-760 ºC) y Anti Atlas (830-900 ºC), y algo más moderadas en el Rif (550-620 ºC). En el SO del macizo Ibérico los valores son altos pero moderados (<690 ºC). El flujo de calor superficial calculado se muestra en **Fig. 6.13 B**. En el continente africano el

SHF es bajo en el Rif (50-65 mW/m^2) y elevado en el Alto Atlas (65-80 mW/m^2), Medio Atlas (65-70 mW/m^2) y Anti Atlas (>80 mW/m^2). Para las zonas sumergidas, el SHF es mínimo en las llanuras abisales Atlánticas (<45 mW/m^2), y extremadamente alto en la parte oriental de la Cuenca de Alborán (>90 mW/m^2), donde está presente la corteza más delgada del modelo 3D. El SHF en el SO de Iberia (50-65 mW/m^2), a pesar de las temperaturas relativamente elevadas en el Moho, es moderado debido a la baja producción de calor de la corteza modelizada en la zona.

6.4 DISCUSIÓN

6.4.1 Comparación entre los modelos 1D y 3D

Las principales discrepancias entre el modelo 1D y el 3D en la corteza se sitúan en el Golfo de Cádiz, en la Cuenca de Alborán, en el SO del Macizo Ibérico y NO del margen marroquí (**Fig. 6.14 A**). En el modelo 1D obtenido mediante la inversión de elevación y anomalía del geoide se asume que la corteza está representada por una única capa de densidad uniforme. De esta forma, las discrepancias 1D-3D se explican por la imposibilidad del modelo 1D de reproducir los cambios laterales de densidad de la corteza producidos por sedimentos, cambios en las litologías etc. El modelo 3D incorpora estos cambios laterales de acuerdo a estudios previos. En el caso del manto litosférico, las principales diferencias 1D-3D se encuentran en la Cuenca del Rharb, Béticas y Golfo de Cádiz, donde el espesor litosférico obtenido en el modelo 3D es hasta 50 km mayor que el obtenido en el 1D mediante inversión. Por el contrario, el modelo 3D muestra una litosfera más delgada bajo el Atlas, el SO del Macizo Ibérico y la Cuenca de Alborán (**Fig. 6.14 B**). Las diferencias de amplitud de la profundidad del LAB son mayores para el modelo 3D que para el 1D. Por otra parte, las ondulaciones indeseables de pequeña longitud de onda del modelo 1D han sido eliminadas en el modelo 3D.

En la Cuenca de Alborán, el valor predicho por el modelo 3D es 1-3.5 m más alto que el valor observado (**Fig. 6.9 A**). Si se asume que el espesor y densidad de la corteza son bien conocidos, es necesario reducir el grosor litosférico para disminuir la anomalía del geoide. Varias pruebas realizadas indican que no es posible ajustar a la vez la anomalía del geoide y la elevación, con los parámetros corticales asumidos, en esta zona. En **Fig. 6.15** se muestra un modelo alternativo extremo en el que la anomalía del geoide se ha ajustado adelgazando unos 10 km la base de la litosfera, con el resultado de que la elevación calculada se ha incrementado en unos 300 m. En este caso, efectos

térmicos no estacionarios y variaciones composicionales podrían estar afectando al manto litosférico y sublitosférico (astenosfera).

6.4.2 Análisis de sensibilidad

Las variaciones del espesor litosférico están fundamentalmente controladas por la elevación y la anomalía del geoide, ya que ambos observables geofísicos son sensibles a variaciones de densidad en niveles profundos. Para analizar la sensibilidad de los diferentes observables hemos realizado la siguiente prueba: reducir la amplitud de la topografía del LAB en un 30% para suavizarla (**Fig. 6.16 A**), y modificar la profundidad del Moho en un 10 % (< 4 km) (**Fig. 6.16 B**) intentando mantener un buen ajuste de los observables geofísicos (**Fig. 6.16 C**). Los resultados muestran que este modelo alternativo no es capaz de reproducir adecuadamente la elevación ni las anomalías de Bouguer y el geoide. Así, las variaciones de la topografía del LAB del modelo 3D son necesarias para explicar los observables geofísicos, si se asume que la estructura cortical está relativamente bien determinada (±10 %).

6.4.3 Estructura cortical: análisis isostático

La anomalía isostatical residual (IRA) se calcula eliminando el efecto gravimétrico de las masas de compensación isostáticas. La IRA debería ser nula si el balance isostático fuera perfecto de acuerdo al modelo de compensación isostática escogido. En **Fig. 6.17** se muestra un mapa de la IRA de la zona de estudio, calculado asumiendo un modelo de compensación en corteza Airy-Heiskanen. Los valores residuales negativos en la parte occidental de la Cuenca de Alborán, la Cuenca del Rharb, el Golfo de Cádiz y el NO del margen marroquí, pueden ser explicados parcialmente por la acumulación de sedimentos (Torne at al, 2000; Medialdea et al., 2004; Iribarren et al, 2007), así como por el engrosamiento litosférico (**Fig. 6.8**), el cual sugeriría que la compensación isostática se alcanza a niveles subcorticales. Los valores residuales positivos en la parte oriental de la Cuenca de Alborán, Medio y Anti Atlas, podrían deberse a un adelgazamiento litosférico como el que se observa en el modelo 3D (**Fig. 6.8**). En el caso del SO del macizo Ibérico, la anomalía residual negativa se debería en parte al moderado adelgazamiento litosférico (**Fig. 6.8**), así como a una elevada densidad cortical (Fernández et al., 2001; Fernàndez et al., 2004) que no es tenida en cuenta por el modelo de compensación isostática, el cual asume un contraste de densidad igual para toda la corteza.

6.4.4 Modelos Geodinámicos

El engrosamiento litosférico bajo el Arco de Gibraltar y el adelgazamiento adyacente en la Cuenca de Alborán han dado lugar a diferentes modelos geodinámicos relacionados con el colapso convectivo (e.g. Dewey, 1988; Platt y Vissers, 1989; Platt et al., 2003), delaminación (Seber et al., 1996a; Mezcua y Rueda, 1997; Calvert et al., 2000), subducción Neógena asociada a un slab roll back (Frizon de Lamotte et al., 1991; Lonergan y White, 1997), subducción activa (Gutscher et al., 2002), desprendimiento de slab (Zeck, 1996; Wortel y Spakman, 2000) o slab roll-back y desgarro litosférico (Spakman y Wortel, 2004) (**Fig. 6.18**). Todos estos modelos incluyen el hundimiento de una litosfera fría y densa, y la presencia de material de baja velocidad de onda P/caliente, poco denso o incluso astenosférico bajo la Cuenca de Alborán. La mayor parte de estos modelos no incluye, sin embargo, el adelgazamiento litosférico bajo el Atlas como parámetro importante de cara a explicar la evolución del GAS.

Esencialmente hay dos tipos de teorías para explicar el adelgazamiento litosférico bajo el Atlas. Algunos autores han propuesto que el adelgazamiento litosférico bajo el Atlas y la Cuenca de Alborán está causado por una entrada de material astenosférico relacionada con la dinámica de placas entre Eurasia y África. Dicha entrada estaría inducida por el desgarro y el slab roll-back (Spakman y Wortel, 2004; Teixell et al., 2005), o bien por una delaminación litosférica (Ramdani et al., 1998). Otro grupo de trabajos propone que el adelgazamiento litosférico podría ser debido a la erosión térmica producida por un ascenso del manto independiente de la dinámica de placas Eurasia-África (Anguita y Hernán, 2000; Zeyen et al., 2005; Missenard et al., 2006). En este sentido algunos autores han señalado la relación entre el volcanismo de las Islas Canarias y el volcanismo Neógeno y Cuaternario presente en el Atlas, sugiriendo la presencia de un reservorio de magma sublitosférico bajo toda la región (Anguita y Hernán, 2000, y referencias en el interior). Dicho reservorio sería un remanente de una antigua y profunda pluma, y el volcanismo se canalizaría a través de un sistema de fracturas heredado de la extensión Triásica y Jurásica.

Los resultados obtenidos en la modelización 3D indican que tanto la corteza como la litosfera se engruesan bajo el Estrecho de Gibraltar, las Béticas y el Rif, en consonancia con las anomalías de velocidad indicadas por estudios tomográficos (Blanco y Spakman, 1993; Bijwaard y Spakman, 2000; Calvert et al., 2000; Spakman y Wortel, 2004). Sin embargo, el engrosamiento litosférico parece continuar hacia el SO, abarcando el NO del margen marroquí, la Cuenca del Rharb y el Golfo de Cádiz, sin una contrapartida aparente en la corteza (**Figs.**

6.7 y 6.8). Hacia el sur hay un marcado adelgazamiento litosférico bajo el Atlas que se extiende hacia la parte oriental de la Cuenca de Alborán. El adelgazamiento litosférico en el Atlas es oblicuo a la rama de origen tectónico del orógeno, el Alto Atlas, donde el relieve es debido fundamentalmente a la deformación intracontinental asociada al régimen compresivo entre Iberia y África durante el Eoceno tardío y el Cuaternario. La litosfera que separa los adelgazamientos de la Cuenca de Alborán oriental y el Medio Atlas presenta un grosor normal de 110-120 km. La alineación paralela SO-NE de los engrosamientos y adelgazamientos litosféricos sugiere que ambas estructuras están relacionadas con procesos profundos en el marco de la dinámica del límite entre las placas Eurasiática y Africana. En este contexto la erosión convectiva o la delaminación no parecen candidatos apropiados dado el poco acortamiento observado en el Atlas (e.g. Teixell et al., 2003) y la falta de evidencia de grandes raíces litosféricas en el pasado. Además, el estilo tectónico de las cuatro unidades tectónicas principales (orógeno Bético-Rifeño, Cuenca de Alborán, Golfo de Cádiz y Atlas) requiere un mecanismo más complejo. La extensión lateral y la orientación del engrosamiento litosférico arrojan algunas dudas sobre una posible subducción hacia el este con slab roll-back hacia el Oeste. Además, la orientación de los esfuerzos de los terremotos en la corteza y manto superior no sugiere una relación entre dichos terremotos y una subducción hacia el este activa (Stich et al., 2005). Un modelo posible de retirada de slab debería incorporar desgarro y slab roll-back asimétrico para ajustar la estructura litosférica actual (Spakman y Wortel, 2004)

7. SUMARIO

El principal objetivo de esta tesis es de naturaleza metodológica: el desarrollo de métodos numéricos para determinar la estructura litosférica combinando las ecuaciones geopotenciales, litostática y de transporte de calor. Tres objetivos principales alcanzados en este sentido son:

1) Desarrollo de un código numérico para determinar la anomalía de Bouguer en tierra y mar a partir de datos de anomalía de aire libre satelital públicamente disponibles.

2) Desarrollo de un método para determinar a primer orden la estructura litosférica a partir de la elevación y la anomalía del geoide.

3) Desarrollo de un código 3D interactivo para modelizar la litosfera integrando elevación, anomalías gravimétricas y del geoide, y flujo de calor superficial.

Por último, pero no menos importante, los códigos numéricos desarrollados se han aplicado al GAS, con el objetivo de determinar su estructura litosférica.

7.1 FA2BOUG: CÓDIGO EN FORTRAN 90 PARA DETERMINAR LA ANOMALÍA DE BOUGUER A PARTIR DE MALLAS DE ANOMALÍA DE AIRE LIBRE

En el Capítulo 3 se presentó un código en FORTRAN 90 para calcular la anomalía de Bouguer en tierra y mar especialmente diseñado para trabajar con datos globales de elevación y anomalía de aire libre. Como ejemplo de aplicación se produjo un mapa de la anomalía de Bouguer del GAS combinando datos disponibles en tierra y datos satelitales procesados mediante FA2BOUG. Valores positivos de la anomalía de Bouguer caracterizan el dominio oceánico Atlántico (240-300 mGal), la parte oriental y central de la Cuenca de Alborán (40-160 mGal) y el SO de la Península Ibérica (>40 mGal). Las principales anomalías negativas están situadas en la parte occidental de la Cuenca de Alborán (<-40 mGal), las Béticas (<-120 mGal), el Rif y la Cuenca del Rharb (<-120 mGal), y el Atlas (<-120 mGal). De la comparación de ETOPO2 con el DEM de alta resolución SRTM como entradas de topografía al programa, se concluye que el uso de DEMs de baja resolución tiende a subestimar la corrección por el terreno, siendo este desajuste mayor cuanto más elevada sea la corrección por el terreno. Así, la precisión de la corrección topográfica es fuertemente dependiente de la resolución del DEM utilizado, al menos para zonas de topografía muy irregular.

7.2 INVERSION DE GEOIDE Y ELEVACIÓN: APROXIMACIÓN 1D

El método basado en la combinación de elevación y anomalía del geoide asumiendo isostasia local, estado térmico estacionario, y un gradiente lineal vertical de densidad para la corteza y el manto litosférico (cf. Capítulo 4), permite un cálculo rápido de los grosores corticales y litosféricos para regiones extensas. Dadas las hipótesis simplificadoras, las variaciones del grosor litosférico calculadas deben considerarse como un límite inferior. Las variaciones que introducen el gradiente lineal de densidad en la corteza y la densidad dependiente de la temperatura en el manto litosférico, con respecto a asumir densidades constantes en corteza (2780 kg/m^3) y manto (3245 kg/m^3) (Fullea et al., 2006) son: para la corteza, incremento de z_c del 10-40 % para E<0 e incremento moderado o incluso disminución (-5% a 10%) para E<0; para el manto litosférico las variaciones son < ±5%.

7.3 GEO3Dmod

En el Capítulo 5 se presentó GEO3Dmod: un programa que permite la modelización interactiva de la litosfera integrando elevación, anomalías de gravedad y del geoide, y SHF. El programa consta de dos módulos: GEO3Dmod y GEO3Dmod_INTF. GEO3Dmod resuelve el problema directo, es decir, a partir de un modelo litosférico dado, calcula la distribución 3D de densidades y temperaturas y los observables geofísicos asociados. GEO3Dmod_INTF es una interfaz gráfica diseñada para visualizar y modificar interactivamente la estructura litosférica de acuerdo con las diferencias entre los observables geofísicos calculados y los medidos. Para comprobar la validez del programa se utilizaron una serie de modelos sintéticos.

7.4 ESTRUCTURA LITOSFÉRICA DEL SISTEMA DEL ARCO DE GIBRALTAR (GAS)

En el Capítulo 6 se aplicó GEO3Dmod al GAS usando como geometría inicial del Moho y el LAB el modelo 1D obtenido mediante inversión de elevación y anomalía del geoide (cf. Capítulo 4). Para el modelo 3D se utilizaron ocho cuerpos diferentes de acuerdo a su densidad, conductividad térmica, producción de calor y coeficiente de expansión térmica:

1) Sedimentos neógenos y cuaternarios en la Cuenca de Alborán (NQSA) con una densidad de 2350 kg/m^3.

2) Sedimentos poco consolidados (US), que cubren prácticamente el dominio oceánico Atlántico así como las cuencas del Rharb y del Guadalquivir, con una densidad de 2200 kg/m^3.

3) Sedimentos de la cuña de acreción (AWS) formados por la imbricación de sedimentos del Triásico al Mioceno superior, incluyendo también sedimentos de edades diferentes con una densidad similar (2400 kg/m^3).

4) Corteza media-superior (UMC) con una densidad promedio de 2700 kg/m^3.

5) Corteza inferior (LC) con una densidad de 2920 kg/m^3.

6) Corteza intermedia (IC) con propiedades promedio entre la corteza media-superior y la inferior, que puede reemplazar a la corteza media-superior o funcionar como corteza de transición.

7) Peridotitas localizadas en dos pequeñas áreas en las Béticas y el Rif con una densidad de 3100 kg/m^3.

8) Manto litosférico con una densidad dependiente de la temperatura.

La aplicación del modelo a la zona del GAS da lugar a una estructura litosférica que coincide razonablemente bien con trabajos anteriores basados en experimentos de sísmica, tomografía sísmica regional, otras modelizaciones previas, así como con los observables geofísicos medidos. Todo el Atlas parece estar afectado por un adelgazamiento litosférico, si bien este adelgazamiento es más notable al sur en el Anti Atlas, y al norte en el Medio Atlas. La rama este del Atlas no parece estar significativamente afectada por el adelgazamiento. Los gradientes más fuertes del LAB están presentes al norte, sur y este del engrosamiento litosférico observado bajo el Golfo de Cádiz, las Béticas y el Rif. La topografía irregular del LAB sugiere que la contribución litosférica al balance isostático no es despreciable, como confirma el mapa de anomalía isostática residual calculado para el GAS. La presencia de adelgazamientos y engrosamientos litosféricos con una orientación similar (SO-NE) permite restringir los modelos geodinámicos propuestos. Un modelo de desgarro de slab con roll-back asimétrico podría explicar el engrosamiento litosférico, estando el adelgazamiento litosférico causado por la entrada lateral de un flujo astenosférico. Un modelo alternativo para explicar el adelgazamiento litosférico sería la presencia de un reservorio magmático proveniente de una antigua y profunda pluma centrada en las Islas Canarias que llegaría hasta la Europa central.

7.5 TRABAJO FUTURO

Dos de las principales simplificaciones asumidas en esta tesis son: a) manto superior composicionalmente homogéneo, y, b) manto sublitosférico

(astenosfera) isotermo. Dichas simplificaciones implican que la densidad de la astenosfera es igual en todas partes y que las variaciones laterales de las propiedades termofísicas que no provienen de variaciones de temperatura son despreciables. A pesar del éxito de la metodología presentada para describir las variaciones principales de la litosfera, despreciar la compresibilidad, cambios de fase y heterogeneidades composicionales en el manto superior puede dar lugar a inconsistencias al comparar la densidad modelizada con la tomografía, los xenolitos y los datos termodinámicos. Así, el trabajo futuro debería incluir:

a) Implementación realista de las propiedades termofísicas en el manto litosférico y sublitosférico. Esto permitiría calcular velocidades sísmicas y comparar con la tomografía sísmica.

b) Cambios de fase en el manto superior.

c) Variaciones de temperatura en el manto sublitosférico.

d) Cambiar el nivel de compensación isostático para tener en cuenta las variaciones de la flotabilidad del manto superior inducidas por los puntos anteriores.